

Corrosion behaviour of X65 carbon steel under flowing conditions

By

Mustafa Abdulhamza Hashim

Submitted in accordance with the requirements for the degree of
Doctor of Philosophy

The University of Leeds
School of Mechanical Engineering
Institute of Functional Surfaces

April 2017

The candidate confirms that the work submitted is his own and that appropriate credit has been given where reference has been made to the work of others.

This copy has been supplied on the understanding that it is copyright material and that no quotation from the thesis may be published without proper acknowledgement.

© 2017 The University of Leeds and Mustafa A. Hashim

To my father.

Acknowledgements

First and foremost, I would like to express my deep gratitude to Prof. Nik Kapur and Prof. Anne Neville for all the supervision and encouragement they have provided throughout this research.

I would also like to thank my colleagues and friends at the school of mechanical engineering for their support.

A big thanks go to the technical staff at the iFS (the lab finest), in particular, Jordan, Andrew, Mick and Paul for fixing my test section whenever it broke and for providing the samples, solutions and other technical support whenever it needed.

A big thanks go to my beloved wife Sarah, my father and mother, to my dear brother and sister for believing in me and their endless support.

Abstract

This thesis presents the outcome of a systematic study carried out to establish an understanding of the influence of flow conditions on the corrosion behaviour of X65 carbon steel in CO₂ saturated environments. An assessment of both the corrosion behaviour of uncovered and film-covered surfaces of X65 is made under different flow conditions.

All the experiments under flowing conditions were conducted using a newly designed flow loop. This was designed to provide a platform to study the effect of flow parameters and the physical/chemical properties of the solution on corrosion behaviour. A range of wall shear stresses that were gradually increased throughout the test section could be achieved and corrosion rate could be monitored *in-situ*.

Firstly the corrosion behaviour of an uncovered surface under flowing conditions was examined at two values of solution pH of 6.6 and 4 at two temperatures 50°C and 80°C. Such an approach enabled the investigation of the effect of flow parameters (described by wall shear stress, Reynold's number, mass transfer coefficient, and water chemistry/properties) on the corrosion behaviour of the X65 carbon steel.

The results enabled the effect of these parameters on the corrosion to be unravelled and it demonstrated how a combination of these parameters may influence the corrosion rate. Furthermore, the parameter with which the corrosion rate shows a direct correlation at each pH level was determined. Furthermore, the influence of the flowing conditions on the Rate Determining Step (RDS) of the cathodic reduction process at pH 4 & 6.6 solution was investigated; the data analysis at temperatures 50°C & 80°C and pH 4 showed a threshold of a diffusion boundary layer thickness, at which the reduction reaction switches from diffusion-controlled to mixed diffusion and charge-transfer controlled.

The second part of this study was the corrosion behaviour of the FeCO₃ film-covered surface. Prior to the corrosion rate tests, the protective film was formed using static conditions in a high-pressure CO₂ autoclave at different immersion times. The outcome of the formation tests series revealed the critical time required to achieve the optimum thickness of the iron carbonate film. The corrosion rate and film stability tests in static and flowing conditions were evaluated. Iron carbonate film stability was determined under static conditions through corrosion rate measurement and

topography analysis of the protected surface at pH values of 6.6 and 4, at two temperatures of 50°C and 80°C.

The outcome of the static tests showed that the stability of the iron carbonate film is a function of the solution chemistry and temperature. The critical pH level at which the formed corrosion product film starts to show clear sign of dissolution in static conditions was evaluated at both temperatures.

The stability of the iron carbonate film was further investigated under flowing conditions in a range of shear stress values of 10 to 655 Pa. The wall shear stress levels where the protectiveness of the film starts to reduce were determined at both temperatures 50°C and 80°C. The film removal mechanisms were identified; the removal process was a strong function of mass transfer. The nature of the film after exposure to shear stress was evaluated using SEM/EDX and XRD. The removal mechanisms of the protective film were determined.

The thesis contributes to the current debate of how flow would effect a carbon steel corrosion behaviour in the CO₂ environment, and in particular how flow would affect corrosion in the absence/presence of an iron carbonate film.

Table of Contents

Acknowledgements	iv
Abstract	v
Table of Contents	vii
List of Tables.....	xii
List of Figures	xiii
Nomenclature	xix
Chapter 1. Introduction	1
1.1 Aim and objectives of this study.....	5
1.2 Outline of this project.....	6
Chapter 2. Mechanism of CO ₂ corrosion.....	8
2.1 Corrosion in the oil and gas industry	8
2.1.1 CO ₂ corrosion.....	9
2.1.2 CO ₂ corrosion mechanism	10
2.1.3 Anodic reaction	11
2.1.4 Cathodic reactions.....	12
2.2 Types of CO ₂ corrosion.....	14
2.2.1 Uniform corrosion.....	14
2.2.2 Localised corrosion	15
Chapter 3. Literature review	17
3.1 Introduction.....	17
3.2 The structure of formed films	17
3.2.1 Iron carbide Fe ₃ C film.....	18
3.2.2 Iron carbonate FeCO ₃ films	19
3.2.3 Iron carbonate plus iron carbide Fe ₃ C +FeCO ₃ films	20
3.3 Theory of iron carbonate FeCO ₃ formation	20
3.3.1 Iron carbonate formation rate.....	21
3.3.2 Parameters affecting the formation of iron carbonate films.....	22
3.3.2.1 Temperature effect.....	22
3.3.2.2 Microstructure effect	26
3.3.2.3 Species concentration effect	27
3.3.2.4 pH effect	29
3.4 Flow effect on the corrosion behaviour of protected/unprotected carbon steel.....	30
3.4.1 Turbulent Flow.....	32

3.4.2	Flow velocity.....	33
3.4.3	Mass transfer rate effect	35
3.4.4	Shear stress effect.....	36
3.4.5	Film removal mechanisms	38
3.4.6	Erosion effect on film removal	39
3.4.7	Mechanical film removal by hydrodynamic forces	41
3.4.8	Chemical-mechanical film removal	43
3.5	Mechanical properties of FeCO ₃ films	44
3.6	Summary	46
Chapter 4.	Flow parameter calculations and CFD simulation	49
4.1	Introduction	49
4.2	Flow parameter calculations	49
4.3	Tafel slope calculations.....	51
4.4	Computational Fluid Dynamics (CFD) technique	52
4.5	Simulation Process	52
4.5.1	Pre-processing	53
4.5.2	CFD Solver	53
4.5.3	CFD Post processing.....	53
4.6	Navier-Stokes equations.....	53
4.7	Finite Element Method (FEM).....	54
4.8	Boundary conditions	55
4.9	Turbulence model.....	55
4.10	Test section CFD simulation.....	56
Chapter 5.	Methodology and test procedure	63
5.1	Introduction	63
5.2	Materials preparation	63
5.3	Samples preparation for the protected test	63
5.3.1	Samples preparation for the protected surface test.	64
5.4	Experimental design.....	64
5.4.1	Flow loop design and testing procedure.....	64
5.4.1.1	The tank.....	65
5.4.1.2	The loop.....	65
5.4.1.3	The pump.....	66
5.4.1.4	The test section	66
5.4.1.5	The electrolyte solution	68

5.4.1.6	The electrochemical measurement	68
5.4.1.7	High-pressure autoclave test procedure	69
5.4.1.8	Mass loss testing procedure.....	70
5.4.2	Static conditions test procedure	70
5.4.3	Electrochemical measurements under static conditions.....	71
5.5	Surface analysis.....	71
5.5.1	Scanning Electron Microscopy (SEM) & Energy Dispersive X-ray (EDX).....	71
5.5.2	X-ray Diffraction (XRD).....	72
5.5.3	Surface roughness	73
5.1	Summary	73
Chapter 6.	Results of X65 carbon steel bare surface under flowing conditions at pH 6.6	74
6.1	Introduction.....	74
6.2	Test matrix	74
6.3	X65 carbon steel corrosion behaviour under flowing conditions at 50°C and pH 6.6	75
6.3.1	Corrosion rate as a function of time at temperature 50°C and pH 6.6.....	76
6.3.2	Corrosion rate as a function of flow at 50°C and pH 6.6	81
6.3.2.1	Cathodic polarisation curves under flowing conditions at pH 6.6 and temperature 50°C.....	83
6.4	X65 carbon steel corrosion behaviour under flowing conditions at 80°C and pH 6.6	85
6.4.1	Corrosion rate as a function of time at temperature 80°C and pH 6.6.....	85
6.4.2	Corrosion rate as a function of flow at 80°C and pH 6.6	88
6.4.2.1	Cathodic sweep under flowing conditions at pH 6.6 and temperature 80°C	91
6.5	Summary	92
Chapter 7.	Results of X65 carbon steel bare surface under flowing conditions at pH 4	94
7.1	Introduction.....	94
7.2	Test matrix	94
7.3	X65 carbon steel corrosion behaviour under flowing conditions at 50°C and pH 4	95
7.3.1	Corrosion rate as a function of time at temperature 50°C and pH 4	95
7.3.2	Corrosion rate as a function of flow at 50°C and pH 4	98

7.3.2.1	Cathodic sweep under flowing conditions at pH 4 and temperature 50°C	99
7.4	X65 carbon steel corrosion behaviour under flowing conditions at 80°C and pH 4	102
7.4.1	Corrosion rate as function of time at temperature 80°C and pH 4	102
7.4.2	Corrosion rate as a function of flow at 80°C and pH 4	104
7.4.2.1	Cathodic polarisation curves under flowing conditions at pH 4 and temperature 80°C	106
7.5	Summary	110
Chapter 8.	Results of X65 carbon steel protected surface under flowing conditions at temperature 50°C	111
8.1	Introduction	111
8.2	Film formation rate as a function of various immersion times	111
8.3	Protective film removal under static conditions.....	116
8.4	Protective film removal under flowing conditions.....	119
8.4.1	Flow effects on the protective film removal	121
8.4.2	Mechanical effect of the flow (erosion) on the film removal	128
8.5	Summary	129
Chapter 9.	Results of X65 carbon steel protected surface under flowing conditions at 80°C	130
9.1	Introduction	130
9.2	Iron carbonate FeCO ₃ film formation	130
9.3	Protective films removal under static conditions.....	131
9.4	Protective film removal under flowing conditions at 80°C and the critical pH.....	136
9.4.1	Flow effect on the protective film removal.....	138
9.5	Summary	143
Chapter 10.	Overall Discussion	144
10.1	Introduction	144
10.2	What controls the corrosion of the unprotected surface of X65 under flowing conditions and pH 6.6?	144
10.2.1	Flow sensitivity of the corrosion rate.....	144
10.2.2	How the flow and channel geometry influence the corrosion rate.....	149
10.2.3	Temperature effect on the corrosion rate	152
10.3	An understanding of the effect of flow on the corrosion behaviour at pH 4 environment.....	153

10.3.1	How the mass transfer coefficient controls the corrosion behaviour.....	155
10.4	Understanding to the corrosion behaviour of protected surfaces.....	160
10.4.1	In static conditions	160
10.4.2	In flowing conditions	161
10.5	The critical shear stress at temperature 50°C and 80°C	164
10.6	A categorisation of the corrosion behaviour of the protective surface throughout the 24 hr immersion time	164
10.7	How durable is the iron carbonate layer, and what are the removal mechanisms?	166
10.7.1	At temperature 50°C.....	166
10.7.2	At 80°C.....	169
Chapter 11.	Conclusions and recommendations for future work	171
11.1	Corrosion behaviour of X65 carbon steel under flowing conditions and temperature 50°C & 80°C.....	171
11.1.1	At pH 6.6.....	171
11.1.2	At pH 4.....	172
11.2	Corrosion behaviour of the protected X65 carbon steel under static and flowing conditions.....	173
11.2.1	At 50°C.....	173
11.2.2	At 80°C.....	174
11.3	Recommendations for future work.....	175
References	177
Appendix A	189
Appendix B	195

List of Tables

Table 3-1 The parameters that were considered to study the corrosion behaviour of carbon steel under flowing conditions.....	48
Table 5-1. Elemental composition of X65 steel (wt. %) [209].....	64
Table 5-2. Tests sequence: Gasket thickness (test section height) and flow rates	67
Table 6-1. Test matrix of the corrosion tests at pH 6.6.....	74
Table 6-2. Cross section dimensions at each sample in the flow direction (flow cell height × channel width). The wall shear stress generated at each sample calculated using empirical equations at temperature 50°C and pH 6.6.....	76
Table 6-3. A comparison between the wall shear stress calculated from empirical and numerical calculations.....	78
Table 6-4. Cross section dimensions at every sample along the flow direction & Flow cell height (gasket thickness) and the calculated wall shear stress generated at each sample at temperature 80°C and pH 6.6.....	85
Table 7-1. Test matrix of the corrosion tests at pH 4.....	94
Table 8-1. Formation test matrix.....	112
Table 8-2. Static conditions test matrix.....	116
Table 8-3. Tests sequence details for 50°C temperatures: Flow cell heights and flow rates.....	119
Table 8-4. Cross section dimensions at every sample along the flow direction & flow cell height (gasket thickness) and the wall shear stress generated at each sample at temperature 50°C.....	120
Table 8-5. Test matrix of flowing condition test at temperature 50°C	121
Table 9-1. Test matrix of flowing condition test at a temperature of 80°C.	137
Table 9-2. Cross section dimensions at every sample along the flow direction & Flow cell height (gasket thickness) and the wall shear stress generated at each sample at temperature 80°C.....	138
Table 10-1. Summary of the studies in literature related to the corrosion flow sensitivity at high pH conditions.....	145

List of Figures

Figure 1-1. Causes of Pipeline failure in 2011 [19]	2
Figure 2-1. Pipeline degradation due corrosion attack [46].....	8
Figure 2-2. Uniform corrosion form [19].....	15
Figure 2-3. Localised corrosion [75, 76].....	16
Figure 2-4. Morphology of pitting [77].....	16
Figure 3-1. Protective and non-protective structures of the combination of Fe ₃ C and FeCO ₃ [10]	18
Figure 3-2. SEM image of a cross-section of the iron carbonate film formed on the surface at temperature 80°C, pH 6.6 and Fe ⁺² concentration 250 ppm [109]	23
Figure 3-3. Gao et al [89] study outcome of the temperature effect on the iron carbonate film porosity: a- at 75°C b- at 90°C	25
Figure 3-4. Akeer et al [16] corrosion rate of different carbon steel microstructure as a function of flowing conditions, temperature 80°C and pH 6.6 at 30 Pa for first 48 hrs, and to 535 Pa for the left of the test period.	26
Figure 3-5. Neville et al [107]. The effect of the Ca ²⁺ concentration in the bulk solution on the precipitation rate of calcium carbonate on the surface:.....	28
Figure 3-6. Pipeline failure due to CO ₂ corrosion in flowing conditions [127].	31
Figure 3-7. (a) Laminar flow (b) turbulent flow [131].....	32
Figure 3-8. Slaimana et al [26] study outcome of the effect of the flow turbulence on the limiting current density at temperatures: 30°C, 45°C, and 60°C	33
Figure 3-9 Villarreal et al [25] corrosion rate as a function of flowing conditions at 1% of NaCl, saturated with CO ₂ , temperature 40°C.	34
Figure 3-10. Nestic [14] study of the effect of the flow velocity on the corrosion rate at pH 4 & 6 at temperature 80°C.....	35
Figure 3-11. Wall shear stress profile on the pipeline wall [19].....	37
Figure 3-12. Schematic of turbulent eddy mechanism for downstream undercutting of erosion-corrosion pits [156]	40
Figure 3-13. Ruzic et al [22] SEM images of the mechanical removal due to flow hydrodynamic a: at 7000 rpm b- at 10000 rpm	42
Figure 4-1. The initial test section CFD model.....	57
Figure 4-2. Shear stress profile at given inlet velocities	58
Figure 4-3. The final test section model geometry	59
Figure 4-4. Shear stress profile on the test section using the modified model at a flow velocity.....	60

Figure 4-5. CFD simulation to the pressure drop across the test section at different inlet flow velocities.	60
Figure 4-6. CFD simulation of:.....	62
Figure 5-1. Flow loop layout and design	65
Figure 5-2. Test section 3D design: (a) Exploded view; (b) Assembled view	66
Figure 5-3. Top view of flow of flow cell & width details cross the samples	67
Figure 5-4. (a) Schematic of the autoclave & (b) photo of high-pressure autoclaves setup.	69
Figure 5-5. Image of (a) Carl Zeiss EVO MA15 SEM & (b) TM3030 Bench Top SEM.....	72
Figure 5-6. Examples of EDX mapping on the cross-section of the corrosion product on the X65 carbon steel surface exposed to the CO ₂ environment.	72
Figure 5-7. Procedures of experimental structure.	73
Figure 6-1. Electrochemical impedance spectroscopy (EIS) graph of the solution resistance at the first & fifth samples under 50°C, pH 6.6 and 3% NaCl solution.....	75
Figure 6-2. CFD simulation of the wall shear stress distribution across the test section at inlet velocity 3.27 m/s and gasket thickness 2mm.....	77
Figure 6-3. Corrosion rate as a function of time under wall shear stress range of 1.6 to 5.66 Pa at temperature 50°C and pH 6.6. Using flow rate 34 l/min and gasket thickness 15mm	78
Figure 6-4. Corrosion rate as a function of time under wall shear stress range of 9 to 30 Pa at temperature 50°C and pH 6.6. Using 32.5 l/min flow rate and 6mm gasket thickness	79
Figure 6-5. Corrosion rate as function of time under wall shear stress range of 30 to 100 Pa at temperature 50°C and pH 6.6.....	80
Figure 6-6. Corrosion rate as function of time under wall shear stress range of 120 to 410 Pa at temperature 50°C and pH 6.6.....	81
Figure 6-7. Corrosion rate as a function of shear stress – pH 6.6, 50°C and 3% NaCl.	82
Figure 6-8. Corrosion rate as a function of Reynold`s number – pH 6.6, 50°C and 3% NaCl.	82
Figure 6-9. Corrosion rate as a function of $v^{1.75} * D^{-0.25}$ – pH 6.6, 50°C and 3% NaCl.	83
Figure 6-10. Cathodic sweep for points A & B at temperature 50°C, pH 6.6	84
Figure 6-11. Cathodic sweeps carried out at temperature 50°C, pH 6.6 for wall shear stress/flow velocity: a- 1.35 to 4.75 Pa b- 7.65 to 25.5 Pa c-120 to 410 Pa.....	84
Figure 6-12. Corrosion rate as function of time under wall shear stress range of 1.35 to 4.75 Pa at temperature 80°C and pH 6.6.....	86

Figure 6-13. Corrosion rate as function of time under wall shear stress range of 7.65 to 26.5 Pa at temperature 80°C and pH 6.6.....	86
Figure 6-14. Corrosion rate as function of time under wall shear stress range of 25.5 to 87 Pa at temperature 80°C and pH 6.6.....	87
Figure 6-15. Corrosion rate as function of time under wall shear stress range of 100 to 340 Pa at temperature 80°C and pH 6.6.....	88
Figure 6-16. Corrosion rate as a function of flow shear stress – 6.6 pH, 80°C and 3% NaCl.	89
Figure 6-17. Corrosion rate as a function of Reynold`s number – 6.6 pH, 80°C and 3% NaCl.	89
Figure 6-18. Points C & D: The effect of the samples on each other corrosion rates.	90
Figure 6-19. Corrosion rate as function of flow velocity – pH 6.6, 80°C and %3 NaCl.....	91
Figure 6-20. Cathodic sweep of point C & D at temperature 80°C, pH 6.6	91
Figure 6-21. Cathodic sweeps carried out at temperature 80°C, pH 6.6 for wall shear stress/flow velocity: a- 7.65 to 25.5 Pa b- 25.5 to 87 Pa c-100 to 340 Pa.....	92
Figure 7-1. Corrosion rate as function of time under wall shear stress range of 1.6 to 5.66 Pa at temperature 50°C and pH 4.....	96
Figure 7-2. Corrosion rate as function of time under wall shear stress range of 9 to 30 Pa at temperature 50°C and pH 4.....	96
Figure 7-3. Corrosion rate as function of time under wall shear stress range of 30 to 100 Pa at temperature 50°C and pH 4.....	97
Figure 7-4. Corrosion rate as function of time under wall shear stress range of 120 to 410 Pa at temperature 50°C and pH 4.....	97
Figure 7-5. Corrosion rate as a function of flow shear stress – pH 4, 50°C and %3 NaCl.....	98
Figure 7-6. Corrosion rate as a function of Reynold`s number – pH 4, 50°C and %3 NaCl.	99
Figure 7-7. Cathodic sweep carried out at temperature 50°C and pH 4 for a- points: Points A & B b- Points C & D.....	100
Figure 7-8. Cathodic sweeps carried out at temperature 50°C and pH 4 for wall shear stress/flow velocity: a- 8.9 to 30 Pa b- 30 to 100 Pa c- 120 to 410 Pa.....	101
Figure 7-9. Corrosion rate as function of time under wall shear stress range of 1.35 to 4.75 Pa at temperature 80°C and pH 4.....	102
Figure 7-10. Corrosion rate as function of time under wall shear stress range of 7.65 to 25.5 Pa at temperature 80°C and pH 4.....	103
Figure 7-11. Corrosion rate as function of time under wall shear stress range of 25.5 to 87 Pa at temperature 80°C and pH 4.....	103

Figure 7-12. Corrosion rate as function of time under wall shear stress range of 100 to 340 Pa at temperature 80°C and pH 4.....	104
Figure 7-13. Corrosion rate as a function of flow shear stress –pH 4, 80°C and 3% NaCl.....	105
Figure 7-14. Corrosion rate Vs Reynold`s number – pH 4, 80°C and 3% NaCl.....	106
Figure 7-15. Cathodic sweep carried out at temperature 80°C, pH 4 for points:....	107
Figure 7-16. Cathodic sweeps carried out at temperature 80°C, pH 4 for wall shear stress/flow velocity: a- 1.35 to 4.75 Pa b- 7.65 to 25.5 Pa.	108
Figure 7-17. Cathodic sweeps carried out at temperature 80°C, pH 4 for wall shear stress/flow velocity: a- 25.5 to 87 Pa b- 100 to 340 Pa.	109
Figure 8-1. Corrosion behaviour of X65 under CO ₂ pressure 100 bar and temperature 60°C as function of time	112
Figure 8-2. SEM images of the corrosion products morphology and thickness the X65 carbon steel surface formed at temperature 60°C and 100 bar CO ₂ pressure	113
Figure 8-3. SEM images of the corrosion products morphology and thickness the X65 carbon steel surface formed at temperature 60°C and 100 bar CO ₂ pressure for immersion time: a- 96 hrs b- 192 hrs	114
Figure 8-4. SEM image and XRD pattern of the formed films at conditions of CO ₂ saturated water at temperature 60°C and partial pressure 100 bar for 48 hours.....	115
Figure 8-5. Corrosion rates of the covered surface with protective films at different pH values & temperature 50°C for 24 hrs.....	116
Figure 8-6. SEM images of the protective films on the X65 carbon steel surface at 50C after 24 hrs exposure to a- pH 4 b- pH 5 c- pH 5.5.....	118
Figure 8-7. 3D analysis to the protected films surface roughness	120
Figure 8-8. Corrosion rates of the protected surface under different levels of wall shear stress at pH 5.5 & temperature 50°C for 24 hrs.....	122
Figure 8-9. Surface and cross-section SEM images of the protective films after 24 hrs exposure to flowing conditions with various wall shear stresses: a- 655 Pa b- 300 Pa c- 171 Pa d- 65 Pa.....	125
Figure 8-10. Element mapping profile of the cross-section of the iron carbonate films after exposure to 655 Pa shear stress.....	126
Figure 8-11. Surface and cross-section SEM images of the protective films after 24 hrs exposure to flowing conditions with various wall shear stresses: a- 37 Pa b- 18 Pa.....	126
Figure 8-12. SEM images to the surface and cross-section of the protective films after 24 hrs exposure to 10 Pa wall shear stress at different zoom.	127
Figure 8-13. Corrosion rate at 655 Pa as a function of time, temperature 50°C, pH 6.9.....	128

Figure 8-14. SEM images of the top view of the surface and the cross-section after 24 hrs exposure to wall shear stress 655 Pa at temperature 50°C and pH 6.9.....	129
Figure 9-1. SEM & EDS analysis image of the surface and the cross-section of the iron carbonate films after the formation test.....	131
Figure 9-2. Corrosion rates of the covered surface with protective films at different pHs & temperature of 80°C for 24 hr.....	132
Figure 9-3. SEM images of the protective films on the X65 carbon steel surface at temperature of 50°C after 24 hrs exposure to a- pH 4 b- pH 5 c- pH 5.5.....	134
Figure 9-4. SEM images of protective films on the X65 carbon steel surface at 80°C after 24 hrs exposure to pH 6 solution.....	135
Figure 9-5. Corrosion rates of the covered surface with protective films at pH 6 and temperature of 80°C for 48 hrs exposure time.	135
Figure 9-6. SEM image of the protective films surfaces at pH 6 & 80°C temperature for 48 hrs.	136
Figure 9-7. Corrosion rates of the protected surface under different levels of wall shear stress at pH 6, temperature 80°C and for 24 hrs.....	139
Figure 9-8. Surface and cross-section SEM images of the protective films after 24 hrs exposure to flowing conditions with various wall shear stresses at temperature of 80°C.....	141
Figure 9-9. Surface and cross-section SEM images of the protective films after 24 hrs exposure to flowing conditions with wall shear stresses 35 & 16 Pa at temperature of 80°C.....	142
Figure 10-1. Data of corrosion rate as function of flow at temperature 20°C and 1% NaCl, from Nesic et al [60].....	146
Figure 10-2. Data of corrosion rate as a function of flow and surface roughness at temperature 25°C and pH > 6, from Ferreira et al [27].....	147
Figure 10-3. The data of the corrosion rate as a function of flow velocity from current study at pH 6.6: 50°C (Black dots) and 80°C (Green dots)	148
Figure 10-4. Reynold`s number effect and channel geometry on the corrosion behaviour at temperature 50°C and pH 6.6.....	150
Figure 10-5. Sketch shows how the flow parameters and properties influence the corrosion rate.....	151
Figure 10-6. A diagram illustrates how the temperature affects the corrosion behaviour.....	152
Figure 10-7. Mass transfer coefficient as a function of the wall shear stress at points A, B, C and D at pH 4 & temperature 50°C.....	156
Figure 10-8. Corrosion rate as function of mass transfer coefficient at pH 4 and temperature 50°C calculated using the limiting current density.....	156
Figure 10-9. Mass transfer coefficient as function of the wall shear stress at pH 4 & temperature 50°C.....	158

Figure 10-10. Corrosion rate as function of mass transfer coefficient at pH 4 and temperature 80°C calculated using the limiting current density.....	158
Figure 10-11. Mass transfer coefficient as function of the wall shear stress of points E & F at pH 4 & temperature 80°C	159
Figure 10-12. SEM image of the surface and cross-section of the protective film after 24 hrs exposure in pH 5.5 solution	161
Figure 10-13. Gaps/holes on the surface of the protective film at shear stress 655 Pa, 50°C and pH 5.5	162
Figure 10-14. SEM images from a- Data from Ruzic et al [22] show gaps on the surface as consequence of mechanical removal from at 10,000 rpm (466 Pa) b- from this thesis, shows the surface after exposure to 655 Pa at 50°C c- from this thesis, at 592 Pa at 80°C	163
Figure 10-15. A categorisation of the corrosion behaviour of the protective surface throughout a 24 hrs immersion time.....	165
Figure 10-16. Data show the effect of mass transfer on the dissolution of the protective film from a- Yang et al [39] b- Ruzic et al [23] c- the current study	167

Nomenclature

τ	Flow shear stress	N/m ²
ΔG	Gibbs free energy	kJ * mol ⁻¹
ρ	Fluid's density	kg/m ³
D_h	Hydraulic diameter of the flow cell	m
v	Flow velocity	m/s
C_f	Dean Friction factor	dimensionless
μ	Fluid viscosity	kg/m-s
D	Diffusion coefficient at given temperature	m ² /s
D_{ref}	Diffusion coefficient of H ⁺ at 20°C = 9.31×10^{-9} *	m ² /s
T_{ref}	Reference temperature 293	K
S_c	Schmitt number	dimensionless
K_m	Mass transfer coefficient	m/s
δ_m	Diffusion boundary thickness	m
L_c	Characteristic length	m
a & b	empirical constants	dimensionless
ϵ	Surface roughness	m
R	Universal gas constant	8.3143 J/(mol * K)
T	Absolute temperature	K
a_c & a_a	Apparent transfer coefficients	dimensionless
F	Faraday constant	(96,490 C/mol)
β_c & β_a	Tafel slope constants	mV/decade
B	Stern Geary constant	mV/decade

*Nesic et al 1996

Chapter 1. Introduction

Corrosion can be defined as a process through which metals revert to their natural stable state [1-7] due to the fact that metals are thermodynamically unstable. Most metals found and processed from mineral/ore to the metallic state will increase their energies, except for some precious metals (gold, silver and platinum) which are found in their metallic state [2]. Therefore unstable metals with high energy will react to form a system that is thermodynamically more stable [3]. Metals return to their natural oxidation states through chemical reactions with the environment which can be divided into oxidation and reduction processes [1]. Corrosion is an electrochemical reaction involving charge and mass transfer through the “corrosion cell”. The complexity of the electrochemical reaction depends on the anodic material (corroded), the corrosion solution and the cathodic reaction, in general, the electrochemical reactions can split into two or more reduction and oxidation reactions [4].

The impact of corrosion on industry and the environment has been viewed in both financial and environmental terms. It has the potential to impact on pollution and affects both capital and operational expenditure. Studies show that the annual cost of corrosion related damage in the U.S. is approximated by \$276 billion [8]. Capital expenditure operating expenses relating to the failure of the pipeline are estimated. In the oil and gas industry, 22% of the failures are associated with corrosion reactions, Figure 1-1 shows the percentage of pipeline failures in 2011 and more than half of these failures are caused by sweet corrosion [1-7, 9].

Gibbs free energy (ΔG) is the main driving force in the corrosion process. ΔG is the change in the free energy between the corroded metal and the environment. The ΔG value must be negative for the corrosion process to proceed [5, 6].

Pipelines are widely used to transport crude oil and its products, as they are both economic and efficient for delivering large volumes of products [10]. Due to low costs and good mechanical properties, carbon steel alloys are the most commonly used material to manufacture oil and gas pipelines [11, 12]. However, within the long line transportation and subsea flowlines, there is often a highly corrosive environment giving the tendency for an increased risk of failure [13]. Failure due corrosion is one of the main threats in oil transportation pipelines; water present in the oil production process combined with other soluble corrosive gases such as carbon dioxide creates an environment which initiates the corrosion process [5]. Erosion due particle impingement is an additional threat to the pipeline integrity. However, this study focused on the internal corrosion due to an electrochemical reaction between the surface of the steel and the aqueous CO₂ solution, and how the flowing conditions affect the process. To initiate corrosion attack on a steel surface the aqueous CO₂ solution should be in contact with the steel surface. Within these physical & chemical conditions, CO₂ corrosion will occur [10, 14, 15]. An understanding of the corrosion mechanism and attack on oil transport pipelines is vital to the operation of oil industry transmission lines [16]. To minimise the high cost and the effect of corrosion in the oil industry and environment, the kinetics of CO₂ corrosion at different flow conditions have been investigated in depth [10] 2003, [6] 1991, [5] 2006, [17] 1978, [18] 2015. However, due to the complexity of the corrosion behaviour under CO₂ saturated conditions, these phenomena are not fully understood [13].

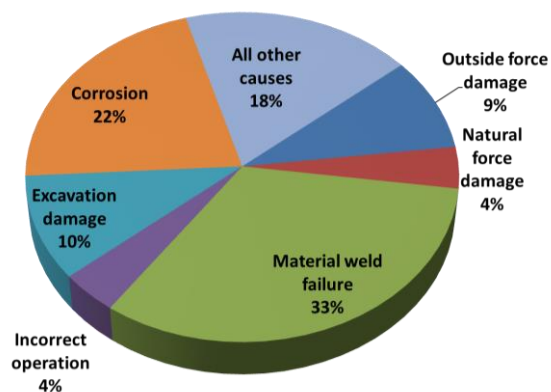


Figure 1-1. Causes of Pipeline failure in 2011 [19]

Kermani et al [10] in 2003 proposed that the effect of fluid flow on corrosion is yet to be understood and that the flow dynamics, if present, adds more complexity to the prediction process of the corrosion rate. Today there are still several aspects related to flow effects on corrosion that are not fully understood. Efrid [20] proposed that wall shear stress and mass transfer of the species involved in the corrosion process are the parameters by which the effect of the flow of corrosion products is determined. Furthermore, Ruzic et al [21-23] studied the effect of flowing conditions on the corrosion rate and film stability. The findings showed that flow velocity is the parameter which governs the flow pattern and that high velocity leads to an increase in the mass transfer of species from/towards the steel surface, resulting in an increase of corrosion rate. However, Palacios et al [24] studied the effect of flow velocity on the corrosion rate in single-phase flow with a constant pH value; the author noticed that the corrosion rate decreased when a greater fluid velocity was applied, but the corrosion rate increased again at higher flow velocities. Villarreal et al [25], showed an initial increase in corrosion rate with increasing flow velocity, and then the corrosion rate slightly declined at a higher fluid velocity. This was attributed to the mechanism of the cathodic species reduction, where, at low velocity, the reduction process is controlled by mass transfer rate. At higher velocities, the reduction of the cathodic species becomes under activation-control. In addition, at much higher flow velocities the author observed a rapid increase in corrosion rate, which was attributed to the possible removal of the protective films from the surface resulting in further corrosion attack on the carbon steel surface. The standard flow velocity for liquids 1-3 m/s and 5-15 m/s for gases. Therefore, for this study, the range of velocities was selected between 0.6 to 13.75 m/s, in order to investigate the effect of the flow (aqueous CO₂ solution) on the corrosion behaviour within the expected flow velocities in oil and gas industry.

Slaimana et al [26], conducted a study to investigate the effect of Reynold`s number on the corrosion rate at different temperatures. The authors found that the flow intensity had a significant effect on the corrosion rate. This effect was dependent on the solution temperature and flow velocity. Ferreira et al [27] carried out research to understand the effect of flow conditions and the surface properties on mild steel corrosion behaviour in a CO₂ environment using Rotating Cylinder Electrode (RCE). They showed that mild steel corrosion rate increases with surface roughness and flow velocity.

Carbon steel is not a Corrosion Resistant Alloy (CRA) and can undergo severe corrosion attack if it is exposed to a corrosive environment such as an aqueous CO₂ solution or organic acids. Nevertheless, carbon steel can display self-corrosion protection if a protective corrosion film can form on its surface as a consequence of the electrochemical reaction between the bulk solution and the surface. Therefore, carbon steel pipelines can be operated safely when iron carbonate FeCO₃ films form on the internal surface of the pipeline in the presence of aqueous CO₂ solutions [28]. The protective films can act as a diffusion barrier that hinders the diffusion of corrosive species to/from the steel surface and slows down the corrosion process [29]. The degree of the protection depends on the structure and the coverage of the protective films on the surface; fully covered surfaces with dense and compact iron carbonate films provide higher protection than scattered uneven covered surfaces with porous films [10].

The physical properties of the films are highly dependent on the formation conditions. CO₂ partial pressure is one of these conditions that can influence the protective film structure [30]. Nesic et al [31] suggested that under low CO₂ partial pressure conditions, it is not easy to form a fully-protective iron carbonate layer in a short period of time. However, using a high-pressure autoclave reduces the time required to form dense and compact protective films, by increasing the concentration of dissolved CO₂ in the water, and consequently increasing the precipitation rate of iron carbonate films. This is attributed to the increase in supersaturation level at the surface due to fast iron dissolution. The film formation rate will be accelerated on the surface resulting in a dense and less porous iron carbonate film in a relatively short exposure time. Cabrini et al [32] conducted a study to investigate the corrosion behaviour of carbon steel and the formation of protective films under high partial pressure CO₂ conditions. The outcome confirmed that film formation under high CO₂ partial pressure and at 60°C is dense, with a compact structure and it fully covered the surface.

Many studies have been carried out to investigate the effect of flowing conditions on the protective film stability [21-23, 33]. Wall shear stress was considered as the primary factor for the mechanical film removal (i.e. film removal due to the mechanical effect of the flow) [34-36]. However, it is thought that critical shear stress values are too small to be the cause of the mechanical removal disruption [21]. The intensities of the near-wall turbulence also have a very influential role in the removal

process [37]. Dawson et al [38] examined the protective film removal under hydrodynamic conditions. The outcome of the study confirmed that hydrodynamic force has an influence on the removal of the film. Furthermore, Yang et al [39] studied the chemical dissolution of the protective films in aqueous CO₂ solution. The conclusions were that the key parameter of the dissolution process is the level of undersaturation and the change of the flow velocity does not have a major effect on iron carbonate dissolution.

To be able to predict CO₂ corrosion rates in flow conditions, it is important to establish an understanding of the influence of the flow on the corrosion behaviour of the carbon steel at a different range of temperatures and pH levels. The pH range of the water associated with the oil and gas production is between 4 to 6 [40] and the stability of the protective films within this range of pH solutions under static and flowing conditions was investigated. In addition to the study of the corrosion behaviour of the unprotected surface of the X65 carbon steel at CO₂ saturated environment. X65 carbon steel was selected for this study (X grade carbon steel), due to the wide usage of this grade in water and oil transportation pipelines for the excellent strength, low costs and weldability [15].

1.1 Aim and objectives of this study

The first part of this work introduces an understanding of the corrosion behaviour of the carbon steel under flowing conditions, 50°C and 80°C and pH values of 4 and 6.6. The second part, investigates the stability of the protective film under flowing conditions, to assist in the determination of the operation limitation of wall shear stress and fluid properties for safe operation without the removal of the protective film. The wall shear stress as a parameter was selected to study the effect of flow on the corrosion rate. Knowing that wall shear stress is a function of velocity, fluid properties and Re (via friction factor), makes the wall shear stress a valid parameter to represent the flowing conditions [20].

This will help to establish a threshold of flowing conditions at different temperatures and pH values, at which the low corrosion of the protected surface is maintained, and obtain an understanding to the possible removal mechanisms of the protective film. Therefore, the main objectives of this research are:

To evaluate the corrosion behaviour of the carbon steel under static and flowing conditions in CO₂ saturation conditions. This was achieved by:

- Design and development of a flow loop to generate a realistic flow across the samples. To simulate the flowing conditions in the pipelines transportation industry.
- Assessing the corrosion behaviour using in-situ investigation of the unprotected surface of X65 carbon steel under flowing conditions at different pH and temperature levels.

Study the formation of the protective films as a function of time under high CO₂ pressure, to determine the critical time immersion to form dense and compact iron carbonate films FeCO₃. This was done by:

- Examining the effect of static and flowing conditions on the protective film corrosion/removal at different pH and temperature levels.
- Identifying the removal mechanisms of the protective film under static and flowing conditions at different temperatures.

1.2 Outline of this project

Chapter 2 includes a description of the fundamental theories of the CO₂ corrosion behaviour of the carbon steel and illustrates the different corrosion mechanisms and reactions.

Chapter 3 includes the review of the studies in the literature related to the corrosion behaviour of the protected/unprotected carbon steel surface under flowing conditions.

Chapter 4 describes the sample materials and preparation steps followed by the steps of the flow loop design. Surface analysis techniques used to examine the surface and cross-section of the sample prior and after the tests are described.

Chapter 5 details the description of the Computational Fluid Dynamics (CFD) simulation steps of the flow through the test section at different fluid properties and different test section geometries. The outcome of the CFD simulation is compared to the outcome of the analytic calculations of the flow parameters. The outcome of both the CFD and the analytic calculations were used to select the exact dimensions for the test section to generate the required flow characteristics.

Chapter 6 illustrates the first results of corrosion behaviour of the unprotected surface of the X65 carbon steel under flowing conditions of wall shear stress and pH 6.6. The effect of temperature was examined on the corrosion rate.

Chapter 7 presents the outcome of the corrosion behaviour tests of the unprotected surface of the X65 carbon steel as a function of wall shear stress at pH 4 and temperatures 50°C and 80°C. It is well documented that the corrosion rate tends to differ in behaviour as a function of the temperature range (i.e. low temperatures < 60°C and high temperature $\geq 80^\circ\text{C}$) because of the film formation [10, 11]. Therefore 50°C and 80°C were chosen for this study to examine how the corrosion behaviour under flowing conditions will differ at these two levels of temperatures. This part of the research considers the influence of the high concentration of the diffusion-controlled species at pH 4 on the corrosion behaviour under flowing conditions.

Chapter 8 describes the results of the procedure of the film under high CO₂ pressure. The immersion time to obtain the maximum thickness of protective film with compact and dense structure was determined. The second part investigates the stability of the protective film under flowing conditions by understanding the corrosion behaviour of the iron carbonate covered the surface of X65 carbon steel under static and flowing conditions at different pH and wall shear stress levels at 50°C.

Chapter 9 describes the stability of the protective films under static and flowing conditions at 80°C, illustrates how the corrosion behaviour of the protective films exhibited different behaviour than at 50°C. The critical pH in static conditions and the critical wall shear stress in flowing conditions at 80°C were determined. The possible removal mechanisms were identified at 80°C and solution pH equal to the critical level in static conditions. Several surface analyses were adopted to examine the topology of the surface and cross-section of the protective films such as SEM, element mapping profile, XRD and EDS used to identify the chemical composition of the protective films on the X65 carbon steel surface.

Chapter 10 is composed the discussion of all the main findings in the previous result chapters. The discussion chapter highlights the main findings and compares it to the related experimental data in the literature.

Chapter 11 presents the main conclusions and the recommend test procedures for future work.

Chapter 2. Mechanism of CO₂ corrosion

2.1 Corrosion in the oil and gas industry

The demand for the hydrocarbon resources has increased in the last few decades due to the development of the global demand for energy. To meet that demand, oil/gas companies are required to work in harsher environments; at greater depths and at higher temperatures, pressures and in more severe acidic conditions. This has elevated the challenges in this industry, both in terms of the material performance in such harsh environments and the ability to predict the operational life of the materials in these conditions [41-45].

The oil and gas industry extensively uses carbon steel, stainless steel and other metallic materials in its transport pipelines, drilling heads and operating plants. The degradation of the steel alloys affects almost every component and operational stage in the oil/gas field. From drilling, casings to production units and pipeline transmission; corrosion is considered to be a major concern within the oil/gas industry further research of corrosion at such conditions is needed to establish a clear understanding of the kinetics and mechanisms [45].

The capital cost and the mechanical properties make carbon steel a very common alloy in the oil/gas industry, although within multi-phase long line transportation and subsea flowlines there is a highly corrosive environment while the tendency for increased risk of failure [13]. Corrosion, therefore, remains the main operational and economic threat affecting the environment and the cost of the production. Figure 2-1 shows the damage inside pipelines as result of corrosion attack.



Figure 2-1. Pipeline degradation due corrosion attack [46]

The most prevalent forms of corrosion attack in the oil and gas industry are hydrogen sulphide corrosion (sour corrosion) and carbon dioxide corrosion (sweet corrosion) which can cause severe corrosion of completion strings.

Carbon steel corrosion can be observed in different forms, and many factors can influence the corrosion process such as the concentration of oxygen. It plays such an important role in corrosion and is not normally present in produced waters. It is only at the drilling stage that oxygen contaminated fluids are first introduced. If drilling muds and seawater are left untreated of contamination and oxygen, this will corrode not only well casings but also drilling equipment, pipelines and mud handling equipment [43-45].

Many failures in industry result from CO₂ corrosion of carbon steel and low alloy steel due to the lack of predictive capability and full understanding of the formation and parameters which are controlling sweet corrosion.

Carbon steel is one of the main materials used in the oil and gas pipeline transportation industry. It is not resistant to internal corrosion caused by CO₂, H₂S and organic acids, but iron carbonate films formed on the surface may give some resistance to carbon steel in some operational cases. The reason for the high usage of these materials with a relatively low level of corrosion resistance is the costs of supply, construction and repair when compared to other alloys like stainless steels and Ni-based alloys costs [45, 47, 48].

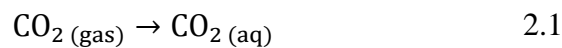
2.1.1 CO₂ corrosion

CO₂ corrosion was first recorded in the US Oil/gas industry in the 1940s [49]; carbon and low alloy steels were widely associated with this kind of corrosion attack due to their expanding use within the industry [6]. CO₂ gas is not corrosive by itself at the range of temperatures in the oil and gas production, but an aqueous solution of CO₂ promotes an electrochemical reaction between the steel substrate and the aqueous phase [48]. CO₂ gas is soluble in water and also soluble in hydrocarbon phases, therefore, hydrocarbon reservoirs can provide a ready reservoir of CO₂ dissolved in the phases [1, 4, 50, 51].

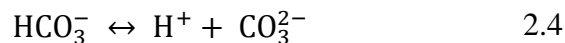
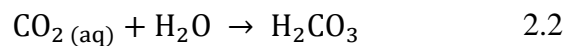
2.1.2 CO₂ corrosion mechanism

CO₂ corrosion in carbon steel is widely investigated. However, the complexity of this phenomenon requires further elucidation. Researchers proposed various mechanisms for the CO₂ corrosion process. However, most of these mechanisms occur at specific conditions and offer inadequate knowledge of the CO₂ corrosion process if any of these conditions change [10].

The basic CO₂ corrosion reaction mechanisms have been well understood and supported by many researchers through the work done over the past six decades. The major chemical reactions include CO₂ dissolution and hydration to form carbonic acid as shown in following reactions;



When dissolved in water, CO₂ is hydrated to give carbonic acid, a weak acid compared to other mineral acids since it dissociates in several steps as in 2.3 and 2.4.



Some of the chemical reactions are very fast compared with other simultaneous reactions, thereby preserving the chemical equilibrium throughout the solution [52]. In other words, when chemical reactions proceed quickly, other slower processes (such as electrochemical reactions or diffusion) can create high/low local concentration zones of ions near the surface. In both ways, the chemical reactions occurring in the solution can significantly influence the rate of electrochemical reactions at the steel surface and the rate of corrosion. At high local concentrations of species, the solubility limit is exceeded and precipitation of surface films can occur [41, 42]. In a precipitation process, heterogeneous nucleation occurs first on the surface of the steel or within the pores of an existing film since homogeneous nucleation in the bulk requires a much higher concentration of the species. Nucleation is followed by crystalline film growth. Under certain conditions, surface films become very protective and reduce the rate of corrosion by forming a diffusion barrier for the species involved in the corrosion reaction and by covering the steel surface [51, 53]

In CO₂ corrosion, when the concentrations of Fe²⁺ and CO₃²⁻ ions exceed the solubility limit in the solution, they combine to form solid iron carbonate FeCO₃ film;



CO₂ concentration in the aqueous solution increases the corrosion rate of the carbon steel by increasing the rate of the hydrogen-evolution reaction:



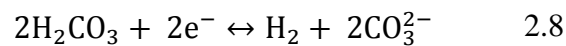
Hydrogen evolution rate cannot exceed the rate of mass transfer limit at which the H⁺ ions are transported to the surface from the bulk solution [52].

The presence of H₂CO₃ can increase the corrosion rate in two possible ways:

Firstly, the dissociation of H₂CO₃ according to reaction 2.7 becomes an additional source for H⁺ ions which are subsequently reduced due to the hydrogen-evolution reaction.



Secondly, there is a suggestion that direct-reduction of H₂CO₃ at the steel surface can increase the corrosion rate, according to reaction 2.8 [41-44, 47, 48, 50, 54, 55].



2.1.3 Anodic reaction

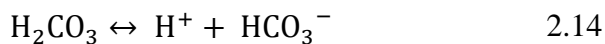
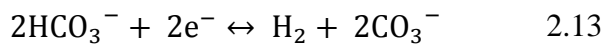
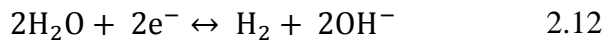
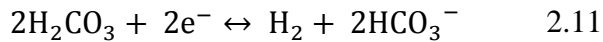
The anodic reaction in the CO₂ corrosion involves the dissolution of the iron of the steel into the aqueous CO₂ solution as Fe²⁺. The reaction of the iron dissolution is associated with electron release. The typical anodic reaction can be illustrated as:



As results of the corrosion process, two electrons are released from reaction 2.9. The released electrons will be consumed in the cathodic reaction, which is balanced with the anodic reaction and occurs at the same rate of the anodic reaction [56, 57].

2.1.4 Cathodic reactions

Five possible cathodic reactions may occur on the sample surface [11, 40, 58, 59] one or a combination of these reactions can cause the corrosion current.



A large number of studies have been and continue to be conducted to achieve an understanding of the cathodic reaction pathway and the conditions that control reduction of the cathodic species on the metal surface. Previous studies proposed that at high pH levels the main cathodic reaction is the direct reduction of the carbonic acid H_2CO_3 [40, 60, 61] as first proposed by de Waard et al [62] reaction 2.11. At $\text{pH} < 7$ many studies [40, 63, 64] proposed that the main cathodic reactions are the reduction of H^+ reaction 2.10 and the direct reduction of the carbonic acid H_2CO_3 reaction 2.11. The authors referred their assumption to thermodynamic and kinetic obstacles that prevent the other two cathodic reactions from taking place. Ogundele et al [57], carried out a study to investigate the corrosion behaviour of mild steel in a CO_2 saturated environment, the outcome of the study showed that the direct reduction of the bicarbonate ion reaction 2.13 is the main source of the cathodic current.

The author conducted the study at conditions of CO_2 partial pressure 7 bar and temperature 95°C . A follow-up study by, Burstein et al [65] excluded the direct reduction of bicarbonate ion from the possible cathodic reactions on mild steel surface under low acidity conditions. The author explained his conclusion by the high negative overpotential required to reduce the bicarbonate ion. Other authors attribute the elimination of the direct reduction of bicarbonate ion to its slow chemical reaction kinetics compared to the other species (i.e. H^+ , H_2CO_3 and H_2O) [59]. Dugstad's [11] findings confirmed the limited contribution of the bicarbonate ion reduction to the cathodic current density. He attributed that to the low dissociation constant of bicarbonate compared to the other cathodic species with a higher dissociation constant. Direct reduction to water is also eliminated for similar reasons, as it requires

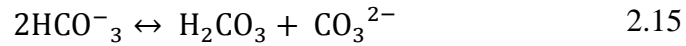
a high negative overpotential and water is considered to be a poor proton/hydrogen ion donor [11, 59].

Recently there were some studies suggesting another possible cathodic reaction known as (Hydrogen buffering effect). These studies [66-68] show that direct reduction of carbonic acid has a limited effect on the cathodic current. Tran et al [66] in his recent study, investigated the cathodic reaction mechanism on the sample surface using an experimental approach. The author used two pH solutions 4 & 5 at different CO₂ partial pressures (1 & 10 bar) to study the influence of the carbonic acid concentration on the cathodic reaction under these pH solutions. The results showed that the concentration of the carbonic acid has a very limited effect on the charge transfer current difference over the range of pH 4 & 5 and for this reason the author concluded the main reduction reaction on the surface was associated with what is known as “Hydrogen buffering effect”, reaction 2.14. At the hydrogen buffering effect reaction, the carbonic acid acts solely as an additional source of H⁺ to the hydrogen reduction process on the sample surface.

Later, Kahyarian et al [67] proposed that the direct reduction of H₂CO₃ on the mild steel surface has a limited effect on the corrosion current. Remita et al [68] conducted a study to investigate the effect of hydrogen buffering, by comparing the reduction of the cathodic species under in CO₂ saturation environment and N₂ purged solution with the same pH; the study results showed that, if the carbonic acid reduced directly on the surface the local pH near the surface will increase in CO₂ saturated solution leading to a decrease in corrosion rate in comparison to the N₂ purged solution. The outcome of the tests confirmed that was not the case, therefore the author attributed the corrosion behaviour to the hydrogen buffering effect from the carbonic acid.

Hydrogen buffering effect is not a new assumption; Hurlen et al [69] in 1984 reported that the additional cathodic current can be a result of H⁺ reduction provided by the carbonic acid. The author suggested that the reduction of carbonic acid on the surface has a negligible effect on the cathodic current.

Dugstad [18] in 2015 reported that at high pH ≥ 6 aqueous CO₂ solutions, the concentration of bicarbonate acid increases to approximately ~300 times the concentration of carbonic acid [67]; under these conditions, another reaction becomes a possibility’ (reaction 2.15) which is known as carbonic acid regeneration.



Carbonic acid regeneration from bicarbonate reserved in the bulk solution was proposed by Turgoose et al [70] in his study in 1992. Where an increase in bicarbonate in the bulk solution at high pH was observed followed by depletion again near the surface associated with an increase in carbonic acid; the author described this behaviour as a disproportionation reaction. Nevertheless, no further details are available in the literature regarding this assumption.

2.2 Types of CO₂ corrosion

CO₂ corrosion exhibits itself in different forms. The process and mechanism of the corrosion are highly influenced by the environment. The initiation of each type of CO₂ corrosion required specific conditions, which control the rate, size and the shape of the corrosion product formation.

2.2.1 Uniform corrosion

Uniform corrosion or also known as general corrosion, is a type of corrosion (degradation) is the most common form of corrosion [71]. Figure 2-2 shows the typical form of metal degradation from the surface due to uniform corrosion attack. General corrosion caused a uniform metal deterioration (loss) from the exposed metal surface. The prediction and measurement of uniform corrosion are relatively easy, therefore it is not the main cause of corrosion failure within the industry [72]. Uniform corrosion progress and development are functions of the solution properties and the physical characteristics of the environment [73].



Figure 2-2. Uniform corrosion form [19]

2.2.2 Localised corrosion

Localised corrosion occurs at confined areas of the metal surface. The rest of the metal surface shows lower rates of corrosion. The high corrosion rate zones are usually unprotected and exposed to a corrosive environment, the rest of the metal surface shows a higher degree of protection. Sun et al [74], investigated the localised corrosion behaviour under different conditions. The authors concluded that localised corrosion occurs when the surface of the metal is not fully protected, the corrosion rate decrease at the areas where the protective films are present in the compact structure, whereas the non-protected areas generate greater corrosion rate due to the exposure of the bare metal to the corrosive environment. The localised corrosion attack initiated as consequence of the uneven distribution of the protective films on the metal surface.



Figure 2-3. Localised corrosion [75, 76]

Pitting corrosion is a form of localised corrosion, pitting corrosion is a serious threat to many alloys. Pitting corrosion has two separate phases of initiation and propagation, Figure 2-4 shows the morphology of the pitting corrosion.

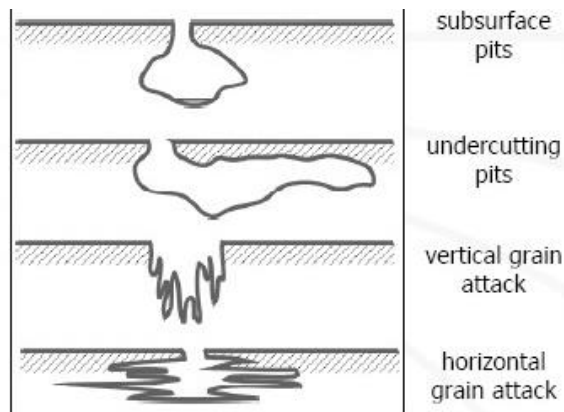


Figure 2-4. Morphology of pitting [77]

The rate of this form of corrosion is determined by the penetration rate at the attacked areas, where the pit depth and size are an indication of the rate of pitting corrosion. The pit size can be classified as deep or shallow, depending on the size of the attacked area. Pitting factor is another way to describe the depth of pitting, which is the ratio of the depth of the deepest pit to the average of the reduction of the metal surface as determined by using mass loss technique [1, 78, 79].

Chapter 3. Literature review

3.1 Introduction

A reliable understanding of the corrosion behaviour under flowing conditions is extremely important in pipelines design and construction. Water chemistry in terms of pH and salinity are other key considerations for pipeline materials selection. Any failure in the oil/gas transportation pipelines due to corrosion can cause devastating consequences to public health and the environment, adding to financial losses and disturbances in production and delivery schedules. Pipeline material selection depends on the physical properties and flows characteristics of the transported fluid. With regards to the presence of CO₂ or H₂S aqueous solution for over moderate distances, carbon steel is the most common material of choice for its favourable mechanical properties, availability, relatively low cost, and the ability to form a corrosion product to cover the surface [80, 81]. However, under solution conditions of high water content, high temperature and pressure, high flow velocities/wall shear stress and low pH environments other corrosion resistant alloys such as stainless steels and duplex stainless steels are preferable than carbon steel [82, 83].

3.2 The structure of formed films

The common use of carbon steel alloys in the manufacturing of the oil/gas pipeline transmission is attributed to its ability to forms a protective film which acts as a barrier to prevent the transport of the corrosion species to/from the metal surface [84, 85]. Nevertheless, corrosion products can be categorised as protective and non-protective, depending on the morphology, composition and the structure of the films [86]. The effect of the film structure on the corrosion process was investigated within a range of temperatures $\leq 150^{\circ}\text{C}$ in water containing CO₂. Film morphology is an important indication to predict the corrosion behaviour of the metal surface [29, 87-90]. There are three main film types:

- Iron carbide (Fe₃C) film.
- Iron carbonate (FeCO₃) film.
- Iron carbonate plus iron carbide (Fe₃C + FeCO₃) film.

Figure 3-1 illustrates typical structures of the corrosion films. The formation rate of these films is greatly influenced by the physical and chemical properties of the environment. Therefore the corrosion behaviour of the carbon steel is determined by the structure, stability and adherent of these films [91].

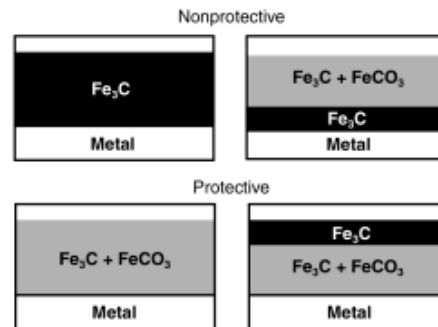


Figure 3-1. Protective and non-protective structures of the combination of Fe_3C and FeCO_3 [10]

3.2.1 Iron carbide Fe_3C film

Iron carbide films form at all temperatures. Iron carbide films form due to an anodic dissolution of carbon steel which leads to a preferred dissolution of the ferrite phase and leaves the cementite (Fe_3C) phase which is conductive [10]. The Fe_3C film structure can be fragile and porous, and flow conditions can remove these films. Also, a tougher cementite can form at fast flow rates in a low CO_2 partial pressure environment; this film consists mainly of Fe_3C with some constituents of alloying elements from the steel [92]. Reducing the flow velocity increases the amount of Fe_3C , and the empty cementite network forms a conductive porous sponge layer, very adherent, with a metallic-to-black appearance. The Fe_3C film influences the corrosion process and increases the corrosion rate by a significant factor of 3 to 10, by playing a number of roles [10, 93, 94]:

- Galvanic coupling:

The conductive Fe_3C can support cathodic reactions with iron and thus galvanic contact between the two can accelerate the dissolution of iron by accelerating the cathodic reaction. The cathodic reactions at the Fe_3C film will change the local chemical properties of the solution.

- Local acidic sites:

Cathodic reactions can occur in general at Fe_3C sites, thus separating the anodic and cathodic corrosion reactions. This results in changes in the solution composition with the aqueous phase at cathodic sites becoming more alkaline and that of the anodic regions more acidic. This can cause internal localized acidification and increase corrosion rate on the metal surface.

- Fe^{2+} enrichment:

The dissolution of the ferrite phase at the metal surface leads to a gradient in concentration of the Fe^{2+} at the metal surface. This increases the local supersaturation of iron carbonate and promotes the formation of such films.

The formation of Fe_3C can, therefore, reduce the corrosion rate, depending on its manner of formation and its concentration within the film structure. It promotes the formation of FeCO_3 films, to offer a degree of protection. This contrasts with, Fe_3C providing local acidification and promoting galvanic corrosion and hence an increased rate of attack [10, 93-95].

3.2.2 Iron carbonate FeCO_3 films

For the mitigation of corrosion of carbon steel in the CO_2 environment, FeCO_3 or siderite is the most important film that can form. Film formation is strongly dependent on the thermodynamics and kinetics of FeCO_3 precipitation [59]. Supersaturation of the solution has a major influence in the role in FeCO_3 film growth and its morphology. A high supersaturation of FeCO_3 is necessary to form protective films, especially at low temperatures [10, 41-43, 45, 47, 48, 50, 54, 55, 62, 96, 97].

The properties of the iron carbonate scales such as the adherence and thickness depend on the metal microstructure; the steel microstructure comparing pearlite/ferrite promotes the formation of an adherent scale [98, 99]. FeCO_3 reduces the corrosion rate by reducing and practically sealing the porosity of the film and can lead to coverage of the metal surface by its precipitation. This eliminates the diffusion fluxes of the species involved in the cathodic process and, therefore, can limit its electrochemical activity.

There is a general agreement in the literature that increasing the temperature $\geq 80^{\circ}\text{C}$ would improve the protectiveness of the FeCO_3 scale as well as its adhesion, hardness and that the higher the temperature, the greater the protectiveness [10, 41-43, 45, 47, 48, 50, 54, 55, 62, 96-99]

3.2.3 Iron carbonate plus iron carbide $\text{Fe}_3\text{C} + \text{FeCO}_3$ films

This type of film is the most common film found on carbon and low-alloy steel surfaces in CO_2 containing environments. During CO_2 corrosion of carbon steels, the Fe_3C phase is cathodic (corrosion resistant) and may combine within the FeCO_3 film. The structure of the film then depends on where and when the FeCO_3 precipitation takes place. On one hand, if it occurs directly and integrates within the carbide phase, then a protective and stable film will form that can often withstand high fluid flow conditions. On the other hand, the initial formation of a cementite layer on the surface followed by partial FeCO_3 sealing, close to or beyond the external limit of cementite can lead to a non-protective film. If the cementite phase effectively sealed the iron carbonate layer formed in contact with the metal surface, an incomplete sealing or a partial dissolution of FeCO_3 anywhere else is not detrimental and the corrosion film remains protective [10, 100].

The structure of the mixed film plays an important role in the formation and breakdown of protective carbonate film. This is influenced by the carbon content and the size and distribution of carbides, which therefore is dependent of the microstructure of steel [10].

3.3 Theory of iron carbonate FeCO_3 formation

Iron carbonate film is the main naturally occurring protection barrier in pipelines against CO_2 corrosion attack. The formation and growth of these films on the steel surface are controlled by the precipitation rate. In order to initiate the precipitation process, the solution must be supersaturated [59]. The mechanism of the iron carbonate film formation is a complicated process. Many theories have been proposed to describe steps involved in the formation process, and the possible factors which may affect the growth rate. Kazmierczak et al [101] referred to some of these factors as an influential effect on the film growth, such as that of species diffusion, adsorption of the film to the substrate, loss of water of hydration and reactions near to the

substrate surface. Nancollas [102] referred to the supersaturation of the solution as driving force for the formation of the film. Nancollas work confirmed that the initial stages of nucleation, which are contained in the reactant species, are not fully understood. Kazmierczak et al [101] did not believe that the ratio of bulk solution concentration to the equilibrium concentration is the driving force in protective film formation process.

Slowing down one or a combination of these factors can reduce growth rate. Therefore, researchers divided the growth theories into two groups depending upon the growth rate governing factor; theory of diffusion control and theory of surface reaction control [84].

Greenberg and Tomson [103, 104], proposed that the kinetics and precipitation of iron carbonate are highly temperature sensitive, in which the rate limited process is governed by the temperature. In other words, at elevated temperatures $\geq 150^{\circ}\text{C}$ the precipitation is diffusion limited, however, at lower temperatures, precipitation is either surface reaction or mass transfer limited. Later, Tomson investigated the precipitation and kinetics of iron carbonate with Greenberg [103]. Their results confirmed the previous findings of Nancollas [102] and Nielsen [105] in which they considered the surface reaction as rate limited rather than the diffusion of the species.

3.3.1 Iron carbonate formation rate

Iron carbonate formation involves several chemical reactions governed by various conditions such as temperature, pressure, ion concentration and flow conditions. The study of iron carbonate formation kinetics centres on the investigation of these effects on the chemical reaction rates which produce the iron carbonate film. Despite the importance of iron carbonate precipitation and dissolution kinetics, the literature on these processes is rather limited [104].

Hunnik et al [106], investigated the precipitation kinetics of FeCO_3 and introduced the scaling tendency concept which they defined as the ratio between the precipitation of iron carbonate film and the corrosion rate. When this ratio increased more than the critical value (i.e. the precipitation rate is higher than the corrosion rate), the iron carbonate grew and offered protection to the surface. They observed that the ratio declined in steel with low carbon content, this observation agreed with the findings of Dugstad [12, 106], when he concluded that steel with $\geq 0.15\%$ carbon content can

form a carbide network on the surface which increases the supersaturation level near the surface leading to a protective layer being formed, despite the bulk solution condition remaining undersaturated.

Dugstad et al [29] confirmed the previous findings of [12], where the presence of the iron carbide film on the surface of high carbon content steel accelerates the formation of iron carbonate film. Moreover, these findings illustrated the effect of temperature on iron carbonate and carbide formation in high carbon steel content. At temperature $\geq 80^{\circ}\text{C}$ the iron carbonate film forms on the surface, and becomes a substrate to the carbide films; however, at a temperature of 60°C carbide films form beneath the iron carbonate and cause a high corrosion threat to the steel surface [107].

Ueda et al [108] explained further the effect of iron carbide formation on the FeCO_3 stability. Ueda used J55 and N80 steel with 0.52% and 0.23% carbon content respectively at a temperature below 80°C . Results showed that J55 steel had better local corrosion resistance than 0.23% carbon N80 steel. The author attributed this behaviour to the effect of the iron carbide structure on the species concentration near the metal surface, resulting in iron carbonate formation within the carbide films. Furthermore, lamellar iron carbide increased the FeCO_3 adhesion bond to the surface. However, the situation in the N80 steel is much different. The homogeneous formation of iron carbide on the surface acts as a cathodic site reducing the adhesion bond of FeCO_3 to the surface, becoming an interface between the iron carbonate and the surface and leads to severe corrosion attack [108].

3.3.2 Parameters affecting the formation of iron carbonate films

3.3.2.1 Temperature effect

Dugstad [29] explained the effect of temperature on the iron carbonate kinetics. At temperature $> 60^{\circ}\text{C}$ a high precipitation rate leads to a reduction in supersaturation. These conditions produce dense and crystalline films that provide high protection to the surface. At temperatures $< 40^{\circ}\text{C}$ a low precipitation rate is observed and high relative supersaturation can exist due to the dissolution of iron carbonate. These conditions are likely to produce a porous, weak adherent and non-crystalline film. Dugstad suggested, that in order to get a dense and high protective film at low temperature, the supersaturation level near the steel surface must increase. The author

added that the high supersaturation level found near the surface can be attributed to the corrosion products, which prevent the movement of the reactant toward the bulk solution. A process balance is maintained between the corrosion and the precipitation rates.

Nesic et al [109] investigated the kinetics of iron carbonate films and confirmed the influence of supersaturation and temperature on the film kinetics, where at high supersaturation, high precipitation rate was observed and a layer of iron carbonate was formed. However, the corrosion process can cause voids within or under the iron carbonate layer leading to porous sites and increasing the corrosion rate. Nesic explained that this behaviour is likely to occur at low tendency ratio conditions (Hunnik ratio [106]) (i.e. the temperature of $> 60^{\circ}\text{C}$ and low pH levels). Figure 3-2 shows the outcome of a FeCO_3 formation test conducted by Nesic et al [109]. The SEM image highlights the thickness of the iron carbonate film and the visible porosity and voids underneath the formed layer.

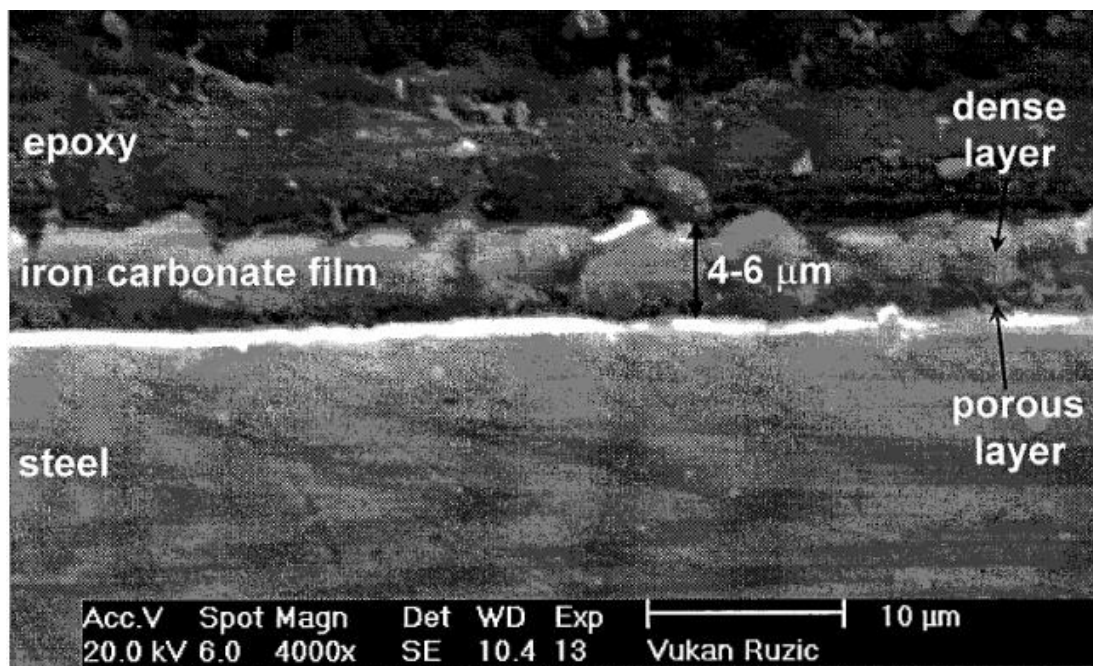


Figure 3-2. SEM image of a cross-section of the iron carbonate film formed on the surface at temperature 80°C , pH 6.6 and Fe^{+2} concentration 250 ppm [109]

These voids can occur at any level of supersaturation when the iron carbonate covers the surface, the corrosion continues under these films creating voids that Nesic called “film undermining”.

However, when the rate of precipitation is more than the corrosion rate, ongoing precipitated films fill these voids once they are created. At low precipitation rates, these voids grow further and cause spalling and porosity to the layer. Netic proposed that using the solution species concentrations near the steel surface in Hunnik's [106] ratio offered an indication of the iron carbonate growth, rather than considering the bulk solution chemistry in this ratio. Netic called this version of scaling tendency ratio "surface scaling tendency or SST". The SST ratio can be very different from the one obtained by using bulk chemistry (Hunnik's [106] ratio). Netic attributed these possible differences to the variation of the scaling tendency with time as the precipitation and corrosion rates changed.

The author's experimental results at temperature 80°C confirmed that the consideration of the high supersaturation parameter of the bulk solution solely as an indication of protective film formation is lacking in accuracy.

The study by Dugstad [11] confirmed his previous findings, that the supersaturation is the main driving force for film precipitation. However, Dugstad concluded that whether nucleation or crystal growth processes dominate the precipitation, depends on the relative supersaturation. At low relative supersaturation, crystal growth is faster than nucleation leading to the formation of large crystals distributed on the metal surface. However, at high relative supersaturation, crystal nucleation dominates the precipitation process, resulting in substantially smaller crystals being formed. High temperature and supersaturation result in high precipitation rates, leading to the formation of a dense iron carbonate layer. At lower temperatures, a significant reduction in precipitation rate occurs. Under these conditions, if the steel surface is descaled or cleaned, a protective film is not expected to form. In this case, a stagnant period is necessary to elevate the supersaturation level at the metal surface in order to initiate film formation and the deposition of the FeCO_3 on the surface.

Sun et al [84] found that high temperature and stagnant solution conditions lead to iron carbonate layers which were dense. Sun illustrated how the stagnant conditions can increase the ferrous carbonate concentration which leads to elevating the precipitation rate at relatively low temperatures of 60°C. Furthermore, at high temperatures $\geq 80^\circ\text{C}$ the main source of the ferrous ions forming a FeCO_3 layer is the bulk solution, however, at low temperatures the source is the dissolution of the films and the corrosion at the metal surface.

Gao et al [89] in their interesting research investigated the growth mechanism of iron carbonate films of X65 steel surface under various temperatures and exposure times. A duplex layer structure of iron carbonate films was observed, which is a thin line that divides the protective layer into two layers; the outer is thin and the inner is thicker, which suggests a two-phase structure. At temperature 75°C and 108h exposure, only a single layer structure is observed on the surface. The porosity of the formed film was an inverse function of the temperature, at a high temperature of 90°C the porosity of the iron carbonate film decreased with time, however, at 75°C, it took approximately threefold the time at 90°C to achieve a similar porosity level as shown in Figure 3-3.

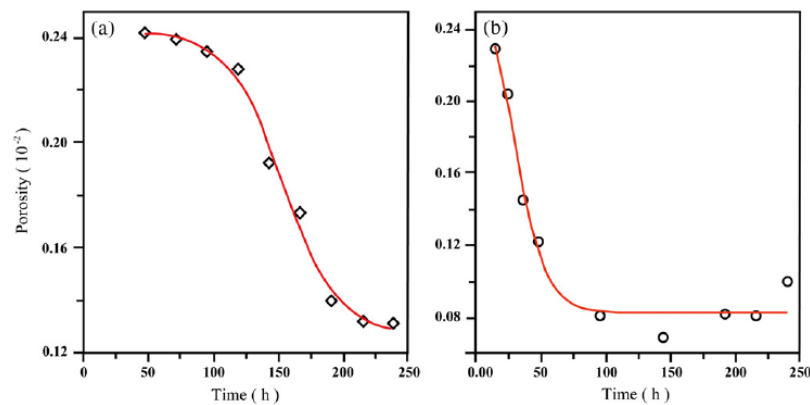


Figure 3-3. Gao et al [89] study outcome of the temperature effect on the iron carbonate film porosity: a- at 75°C b- at 90°C

Temperature accelerated the kinetics of FeCO₃ precipitation, making it more protective. The solubility of the iron carbonate film depends on temperature. To achieve supersaturation, FeCO₃ precipitates at high pH and/or high concentration of Fe²⁺. However, when the temperature is increased, the pH value necessary to initiate the FeCO₃ precipitate will decrease. For example, at 80°C FeCO₃ starts precipitation on steel surface only if the pH is ~ 6.0. At 120°C, the iron carbonate precipitates at pH ~ 4.0 which is a significant reduction in pH value [110].

Hassan et al [111], investigated the formation of the protective films under flowing conditions at different temperatures and pH levels. The authors employed rotating disk electrode (RDE). The outcome of the study confirmed that iron carbonate formation favoured high temperature and high pH environment. Under flowing conditions, the formation rate of the protective films decreased as a function of the flow velocity.

3.3.2.2 Microstructure effect

Previous studies by Dugstad [11, 29] referred to the effect of iron carbide on the iron carbonate protectiveness and explained how these brittle films can promote the formation of FeCO_3 , Dugstad concluded that quenched and tempered low carbon steel needs stagnant periods to initiate the film forming process under low supersaturation and temperature conditions, where ferritic-pearlitic steel forms a carbide network on the surface and iron carbonate films can form on that substrate [11].

Farelas et al [112]; studied the effect of iron carbide on the formation of protective films. In this research, the findings showed a porous carbide layer formed at the early stage of corrosion on the X65 steel surface. Carbide films act as a diffusion barrier for the reactant species, which leads to elevating the pH and the saturation levels, resulting in iron carbonate formation and precipitation within and as a substrate of the carbide films. The microstructure of the X65 steel contains Fe_3C prompts the stability of the iron carbide, making it hard to dissolve. Other steel microstructure phases, e.g. ferrite which is subject to dissolution, act as sources of ferrous ions at the steel surface or bulk solution. The author used another steel sample with a ferritic-pearlitic microstructure to confirm his findings with X65 steel. Higher corrosion rates were observed which resulted in the formation of thick iron carbide layer. The stagnant conditions inside the porous increased solution saturation and pH level promoted the formation of iron carbonate layers. However, the formation of iron carbonate and iron carbide layers were faster in the case of ferrite-pearlite steel than X65, despite the similarity in composition.

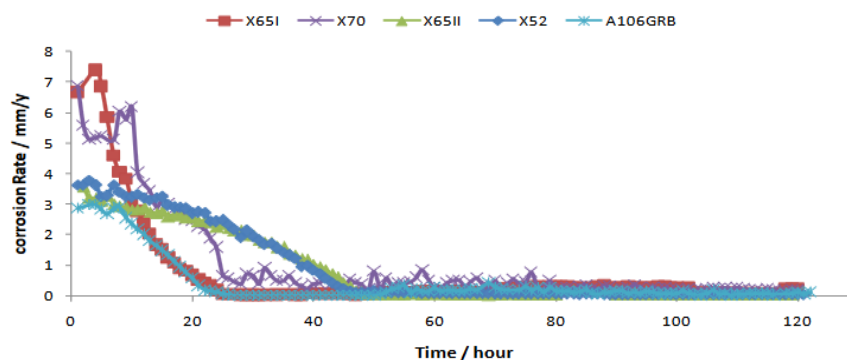


Figure 3-4. Akeer et al [16] corrosion rate of different carbon steel microstructure as a function of flowing conditions, temperature 80°C and pH 6.6 at 30 Pa for first 48 hrs, and to 535 Pa for the left of the test period.

Gao et al [89] explained the effect of iron carbide and ferrite phases in the steel microstructure on the films growth, where, iron carbide can increase the corrosion rate, and ferrite is subject to dissolution, resulting in an eroded surface. The authors observed a galvanic cell between the eroded ferrite as an anode and the iron carbide as a cathode, which was proposed as a possible mechanism of iron carbonate precipitation. Gao, et al findings are in agreement with the Dugstad et al [12] study about the influence of relative supersaturation on the nucleation and crystal growth of iron carbonate film. Akeer et al [16], carried out an investigation to understand the corrosion behaviour of the different microstructure of carbon steel under flowing conditions, using a thin channel flow loop at a high temperature of 80°C and pH 6.6. The flowing conditions were two wall shear stresses level 30 & 535 Pa. The author concluded that corrosion behaviour of the carbon steel was varied as a function of the microstructure and the wall shear stress. Figure 3-4 shows the corrosion behaviour in the study of Akeer, carbon steels with tempered martensite (X65I & X70) exhibited higher corrosion rates than the hot rolled steel with pearlite and ferrite (X65II & X52) microstructures. The corrosion rate then dropped rapidly as a consequence of iron carbonate formation on the metal surfaces. After 48 hrs the wall shear stress increased to 535 Pa to examine the effect of the flow on the stability of the protective film.

Liu et al [113], investigated the effect of the microstructure of the carbon steel on the corrosion behaviour, the outcome of their study confirmed the presence of martensitic and ferritic crystalline structures which promote the formation of the protective film. Guo et al [114], studied the effect of the microstructure on the corrosion behaviour of the high strength low alloy steel. The author concluded that acicular ferrite enhances the corrosion resistance due to the increase the steel toughness, however, steel with martensitic structure exhibited a lower corrosion rate as consequence of the protective film formation.

3.3.2.3 Species concentration effect

The results of Sun et al [84] showed an agreement with findings of Nesic et al [109] regarding the kinetics of iron carbonate film. They confirmed that the iron carbonate formation process reduces the species concentration near the steel surface; however, the diffusion of iron ions from the bulk solution and the corrosion occurring within the iron carbonate porous and voids increases the concentration of the species at the

metal surface. Taking into consideration that the rate of films precipitation is much faster than the rate of species diffusion from the bulk solution to the metal surface, the precipitation becomes diffusion-controlled.

Sun observed an interesting behaviour of iron carbonate growth. It was found that the thickness of the iron carbonate layer formed on steel surface in the absence of an inhibitor was four times thicker than a layer formed in the presence of the inhibitor. The authors attributed this behaviour to the Fe^+ concentration and the solution chemistry at the surface which is high in case of the absence of the inhibitor and low when the inhibitor is present. This confirms the suggestion of Sun; that the corrosion within voids or beneath the porous film and the species movement from the bulk solution, increases the precipitation rate by replenishing the consumed ions at the metal surface. Moreover, iron carbonate film forms on a bare surface faster and thicker because corrosion leads to a much higher supersaturation near the metal surface than the bulk solution which leads to a high precipitation rate. Neville et al [107], investigated the formation of calcium carbonate scales on both the bulk solution and on the metal surface. Neville referred to the importance of the supersaturation as the driving force for films formation, and the value of the supersaturation ratio governs the formation kinetics. Also, that high supersaturation increases precipitation rate of the film on the surface. Furthermore, Neville's findings confirmed that supersaturated solution enhanced the coverage of the films formed on the substrate surface as shown in Figure 3-5.

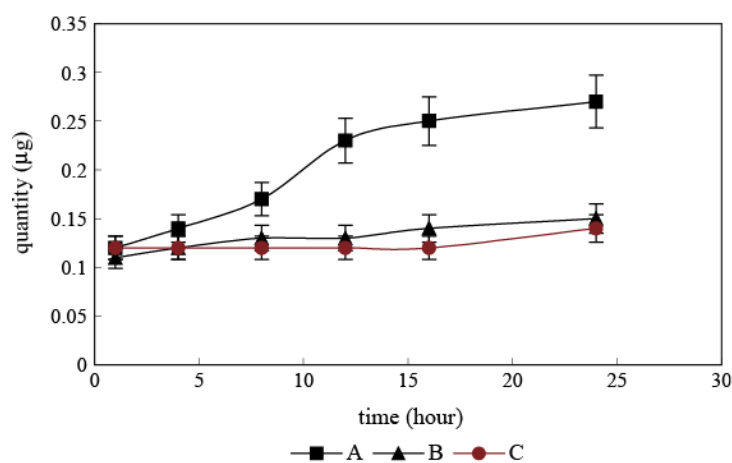


Figure 3-5. Neville et al [107]. The effect of the Ca^{2+} concentration in the bulk solution on the precipitation rate of calcium carbonate on the surface:
A- 1440 mg/l B- 720 mg/l C- 350 mg/l

Nafday et al [115] investigated the formation of iron carbonate in acetic acid conditions. The findings suggest that high concentration of Fe^+ at the metal surface not only increases the precipitation rate but also produces a dense protective layer with a significant reduction in corrosion rate within a shorter time than a low concentration of Fe^+ at the steel surface in similar conditions.

These findings agree with the previous work and confirm the importance of the species concentration at the metal surface in the formation of the protective layer. Nafday concluded that at high pH conditions the presence of free organic acids has no effect on the formation of the protectiveness of the layer. However, the concentration of the organic acid has a major effect on the corrosion rate of the bare steel surfaces.

Kennell et al [116], investigated the growth of the corrosion product at a CO_2 aqueous solution. His findings confirmed the dependency of the precipitation rate on the temperature which agreed with several previous studies [103, 107, 117, 118]. Kennell found that CO_2 partial pressure parameter affected both precipitation process of the nucleation and the growth of the film. Dense and compact films were formed at high CO_2 partial pressure due to the initial increase in corrosion rate, and the supersaturation increase as consequent. However, the amount of iron carbonate film was not sufficient to establish a protective layer on the surface, despite the high iron ions concentration due to the (additional Fe^{2+} added to the CO_2 aqueous solution prior to the test). The authors attributed this behaviour either to the local acidification or physical hindrance. Nevertheless, at room temperature the precipitation rate is extremely low regardless of the species concentration; it is well known that the precipitation rate is highly temperature dependent.

3.3.2.4 pH effect

Previous studies have shown the effectiveness of the pH level on the corrosion behaviour of the carbon steel and the formation of the protective films on the surface [110, 119]. It has been confirmed by experimental results [120, 121] that corrosion rate is a strong function of the pH. Fajardo et al [122], studied the corrosion behaviour of the mild steel under different pH and temperature levels, the outcome showed a significant increase in corrosion rate at low pH conditions due to the high availability of the mass diffusion species in the bulk solution. Solution acidity represented by pH level not only affect the corrosion rate, it has a strong influence on the formation

process of the protective films. High pH environment increases the supersaturation level by decreasing the solubility of the iron carbonate crystals [31, 123]. Nestic et al [109] investigated the growth of the iron carbonate film. The outcome of the study confirms the effect of the pH on the corrosion rate of the mild steel and the formation of the protective films. Whereas at high pH solution the solubility of the FeCO_3 decreased leading to an increase the precipitation rate of the protective films. The Dugstad [11] study showed the influence of the pH on the formation process. By monitoring the Fe^{2+} concentration as a function of the pH level, the author found that the solubility of Fe^{2+} decreased by a factor of 5 if the pH increased from 4 to 5, and by a factor of 100 when the pH went up from 5 to 6.

Berntsen et al [87] investigated the CO_2 corrosion mechanism at high $\text{pH} \geq 7$ and room temperature $\sim 20^\circ\text{C}$ on X65 steel samples. The outcome confirmed that; the formation of iron carbonate is extremely slow and at the film size of around 1-2 μm , no carbide was observed on the surface, despite the corroded surface which indicated the amount of the metal removed due to the corrosion. High supersaturation was used to overpower the low-temperature effect on the precipitation rate, however, the protectiveness of the iron carbonate layer was low regardless of the continuous buffering. The Berntsen findings confirmed the outcome of the Dugstad studies [12, 29] that carbide presence is a key parameter for iron carbonate formation. Tanupabrungsun et al [110] investigated the effect of the pH solution on the CO_2 corrosion products at elevated temperatures, Their findings agreed with previous studies [100, 124] in which the pH has a major effect on the corrosion rate, and high influence on the FeCO_3 formation. High pH value decreases the corrosion rate in the system by reducing both the H^+ ions concentration in solution and the solubility of FeCO_3 resulting with supersaturation and a high precipitation rate.

3.4 Flow effect on the corrosion behaviour of protected/unprotected carbon steel

Transportation pipelines in oil and gas production are important in industry. Pipelines transport mixtures of oil, gas and water from the reservoirs to the refinery units or/and a single-phase transport to export platforms. Corrosion threat on the steel surface depends on several factors, which can then be divided into chemical and physical parameters. Flow conditions of the fluid are important physical parameters [125].

To understand the influence of fluid flow on the steel surface corrosion in a CO₂ containing environment both physical and chemical factors should be considered. For instance, to initiate a corrosion attack on steel surface the aqueous CO₂ solution should be in contact with the steel surface; within these physical & chemical conditions, CO₂ corrosion will occur [10, 126].

These factors are highly affected by the flow conditions inside the transmission pipelines of oil product (containing water cut) and varied depending on the velocity of the fluid and the water rate within the fluid. Figure 3-6 shows CO₂ corrosion attack on a transmission pipeline of natural gas under flowing conditions.

The effect of flow on CO₂ corrosion of the protected/unprotected carbon steel surface is still debatable. Kermani et al [10] proposed that the effect of the fluid flow on the corrosion is yet to be understood, and that, the flow dynamic if present adds more complexity to the prediction process of the corrosion rate.

The parameter that is currently favoured for determining the effect of flow on corrosion rate and film formation/stability is the wall shear stress at the pipe wall. Although there is limited reported data on the upper limits of the shear stress, a figure of 100 Pa for carbon steel above which disruption to surface films becomes a concern, is considered by some as appropriate [10, 94].

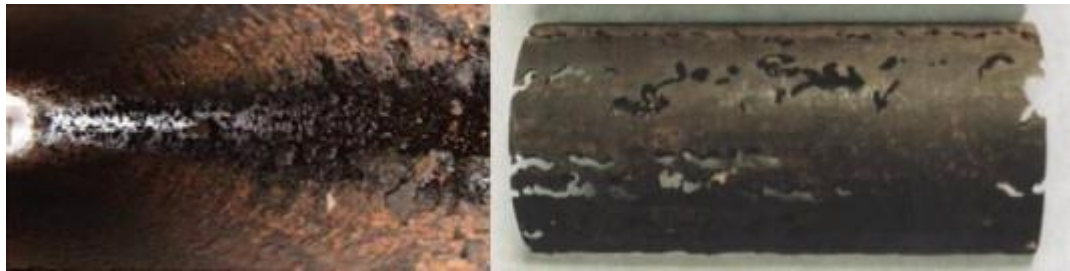


Figure 3-6. Pipeline failure due to CO₂ corrosion in flowing conditions [127].

Wall shear stress and the mass transfer of the species involved in corrosion process are the parameters by which the effect of the flow of corrosion products is determined [20]. Corrosion rate can be affected by the fluid movement to the steel surface. It is similar to a relative motion between the surface and the fluid motion layers. Velocity is the parameter which governs the flow pattern; high velocity leads to an increase in the mass transfer of species from/toward the steel surface, resulting in an increase of corrosion rate [21-23, 33, 128].

3.4.1 Turbulent Flow

Fluid flow can be divided into two types, laminar and turbulent illustrated in Figure 3-7. In the field, it is unlikely that laminar flow will be present and turbulent flow is the most common type of flow. In the turbulent flow, nonparallel velocity vectors and fluctuations occur in the boundary layers [128]. In viscous flow, Reynold`s number “Re” is a dimensionless number used to describe the flow intensity, and to predict the flow velocity at which turbulence occurs. High Reynold`s number means higher flow turbulence [129, 130].

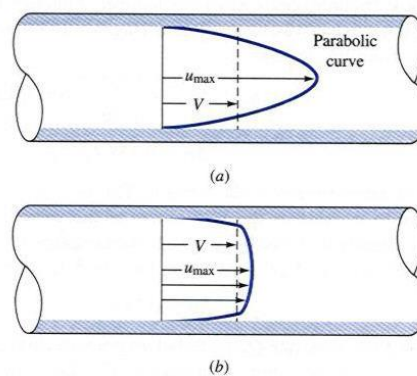


Figure 3-7. (a) Laminar flow (b) turbulent flow [131]

High-velocity flow leads to a turbulent flow in the pipelines. This type of flow can be divided into two parts; first, the turbulent core where the mean velocity is constant and the boundary layer represents the interface between the fluid and the pipe wall. Within this layer all the interaction between the surface and the fluid occurs from species mass transfer and stress changes; moreover, turbulent boundary layers influence the film formation and growth on the steel surface, and mechanical removal may occur within this layer [132].

Slaimana et al [26], carried out an investigation to study the effect of flow turbulence on the corrosion behaviour at different temperatures. The results showed the corrosion rate is a function of the flow intensity. High corrosion rate was recorded at high flow turbulence and temperatures. Although no further details were given to explain how Reynold`s number influences the corrosion rate. In Figure 3-8 the limiting current density (y-axis) is a function of temperature, Reynold`s number and time. Limiting current density is a strong function of the diffusion rate of the cathodic species to/from the metal surface.

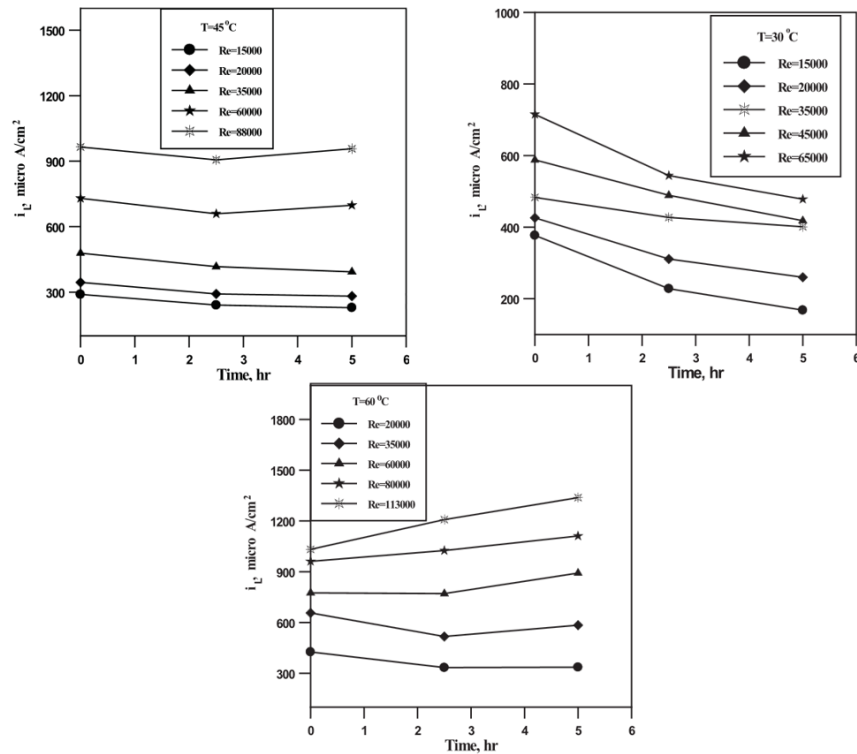


Figure 3-8. Slaimana et al [26] study outcome of the effect of the flow turbulence on the limiting current density at temperatures: 30°C, 45°C, and 60°C

3.4.2 Flow velocity

A large amount of research has been reported to investigate the corrosion behaviour of carbon steel under a wide range of flow conditions. In general corrosion rate increases with the flow velocity. Villarreal et al [25] proposed that, despite an initial increase in corrosion rate with the velocity, the corrosion rate slightly declines at higher fluid velocity as shown in Figure 3-9.

The author attributed that, to the species involved in the corrosion processes, which are transferred by flow movement have less influence on the corrosion than electrochemical reactions at the surface. The author added that corrosion rate showed a significant increase at higher velocities due to an increase in the films mechanical removal.

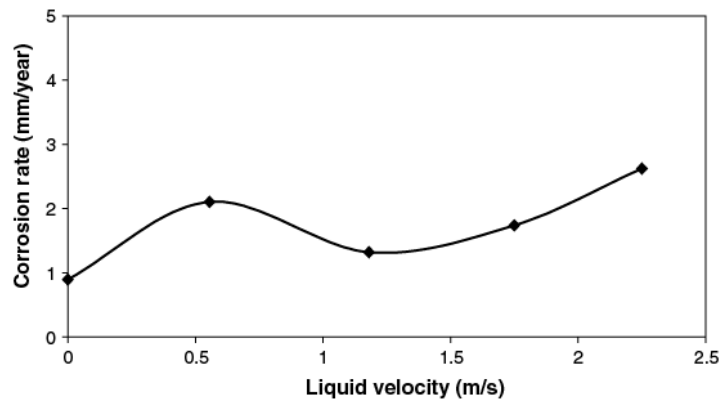


Figure 3-9 Villarreal et al [25] corrosion rate as a function of flowing conditions at 1% of NaCl, saturated with CO₂, temperature 40°C.

Palacios et al [24] suggested in their work a similar observation, at single-phase flow with pH value maintained at 3.4; the author noticed that the corrosion rate decreased when a greater fluid velocity was applied, but the corrosion rate increases again after that. Furthermore, the study by Videm [133] showed some passivity on the steel surface even with high fluid velocity as 20m/s. Palacios [24] attributed Videm's findings to the steel microstructure, whereas his work confirmed that steel with pearlitic-ferritic microstructure can easily form protective layers and offer passivity despite the turbulent flow conditions where a steel with martensitic microstructure requires a low flow dynamic to maintain an iron carbonate layer. Ferreira et al [27], investigated the corrosion behaviour under flowing conditions at high pH environment and room temperature.

The author simulated the flowing conditions by using a Rotating Cylinder Electrode RCE rig. The investigation concluded that corrosion rate of the carbon steel increases with the flow velocity and directly proportional to the surface roughness of the samples, although tests conditions were limited by low flow velocity and high pH solution. Later on, Ferreira et al [90] conducted another a series of tests to study the effect of the flow on the corrosion behaviour of the carbon steel using Thin Channel Flow Cell (TCFC). Corrosion rate increased as a function of the flow at all cases, however flowing conditions also promoted the formation of a protective film at flow velocity 3.5 m/s at CO₂ partial pressure 2 bar and temperature of 80°C. Nestic [14] investigate the effect of the flow velocity (up to 2.5 m/s) on the CO₂ corrosion of carbon steel, the outcome showed a rapid increase in corrosion rate as function of the

flow velocity at pH 4, however at pH 6 the corrosion rate showed no significant increase in the same range of flow velocities as shown in Figure 3-10.

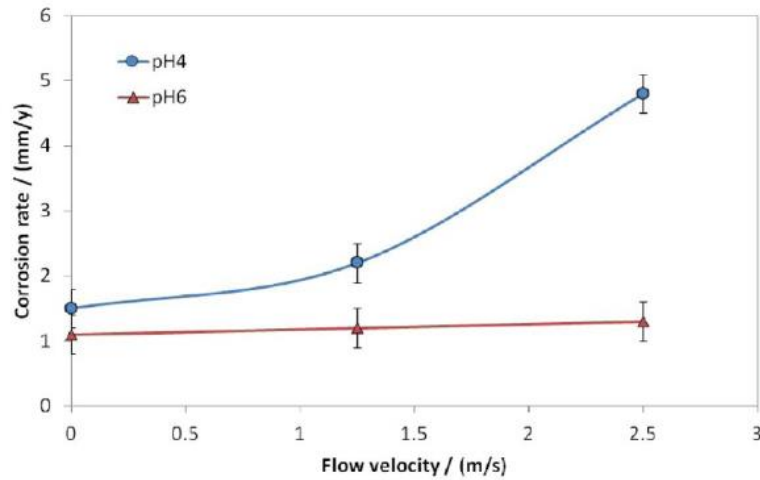


Figure 3-10. Nestic [14] study of the effect of the flow velocity on the corrosion rate at pH 4 & 6 at temperature 80°C

Zara et al [134] studied the effect of flowing conditions on the corrosion rate of the carbon steel at CO₂ saturated environment, the outcome showed a rapid increase in the corrosion rate with flow velocity. The author attributed the increase in the corrosion rate to the high flow turbulence associated with the high flow velocity. Another study by Barmatov et al [135] investigated the effect of the flow velocity on the corrosion rate using RCE rig, the author reported that at high flow velocity the corrosion rate of the X65 carbon steel showed a rapid increase.

3.4.3 Mass transfer rate effect

Mass transfer in corrosion can be defined as the movement of the species involved in the reaction toward and/or from the substrate to bulk solution, due to the non-equilibrium condition between the solution and the metal surface [136]. The mass transfer of the reactant species effect on the corrosion rate can be via two mechanisms;

- The transfer of species involved in corrosion to the steel surface.
- Transport of the dissolved corrosion films away from the metal.

Flow velocity can play a significant role in the mass transfer process. High fluid velocity increases the rate of the species movement toward/away from the bulk solution, especially within turbulent flow [137, 138].

Nesic [14] attributed that to the turbulent flow effect on the species movement to/from the mass transfer boundary layer, the author added that hydrogen ion reduction in CO₂ corrosion on mild steel surfaces is highly influenced by turbulent flow. Fluid velocity increases the mass transfer of H⁺ ions to the surface to precede the reduction reaction and to buffer the H⁺ concentration at the surface. In addition, this leads to a reduction of the pH near the surface and therefore an increase in corrosion rate. Wang et al [139] suggested that the effect of turbulent flow on CO₂ corrosion can be attributed to the increase of mass transfer of species from/to the metal surface, where the turbulent flow increases the transport of the cathodic reaction species H⁺ from the bulk solution to the surface.

Other reduction reactions which involve other cathodic species e.g. H₂CO₃ are less dependent on the flow regime and mass transfer, as proposed by Wang et al [139]. Nesic et al [14, 139] stated, that the slow H₂CO₃ hydration reaction plays a significant role in the determination of reduction species concentration at the surface. Therefore, at high CO₂ partial pressure condition (pCO₂ >5 bar), the cathodic reaction will be mainly through the H₂CO₃ reduction, which means less influence of mass transfer on the corrosion rate. However, Nesic proposal opposed a previous study by Denpo et al [140] where it showed an influence of flow regime on CO₂ corrosion rate even at high CO₂ partial pressures. The outcome of Tran et al and Remita et al studies [66, 68] contradicted the direct reduction of the carbonic acid as possible cathodic reduction reaction and proposed another reduction mechanism known as hydrogen buffering effect.

Mass transfer of the positive iron ions Fe⁺ can highly affect corrosion rate. A turbulent flow increases Fe⁺ mass transfer toward the bulk solution decreasing Fe⁺ concentration at the steel surface; in these conditions forming iron carbonate layer on the surface becomes harder. Furthermore, the effect of Fe⁺ ions mass transfer on the corrosion rate can be greater when it occurs in accompanying with a decrease in the pH at steel surface [14].

3.4.4 Shear stress effect

Several studies have been carried out to investigate the mechanical effect of flow on pipeline walls and the adherent films on it [25, 128, 133]. Several mechanical/chemical interactions between the pipe wall and the fluid during the flow

take place, e.g. chemical dissolution and species mass transfer. Mechanical interactions have a significant role in the corrosion process. With single-phase flow, wall shear stress is one of the main mechanical force which can be imposed during a turbulent flow in the pipelines.

Iron carbonate film presence on the surface create a rough surface. Under flowing conditions, rough surface creates near wall micro-turbulences, thinning the boundary layer and increases the wall shear stress, which may produce porous sites. Porous sites are the typical environment for corrosion cells and can lead to further scale removal and exposure of the steel surface to highly corrosive conditions [84, 141].

Practically shear stress must be at the high level to break the adherent force between the films and the substrate. Researchers have studied this phenomenon for many decades, starting with Efirid [142]. His research indicated that the mean shear stress generated by the flow of seawater on metal surfaces could be enough to overcome the binding force between the substrate and the scales if it reached a certain level. He called this ‘critical shear stress’ and suggested that mean wall shear stress is the main factor in the mechanical removal process.

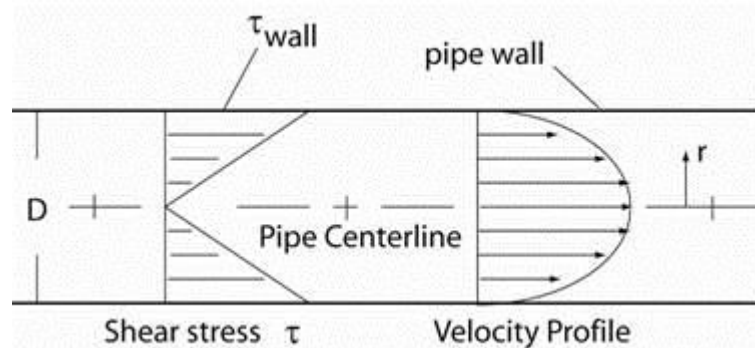


Figure 3-11. Wall shear stress profile on the pipeline wall [19]

Schmitt et al [143], suggested that wall shear stress, caused by the fluid flow cannot at any stage break out the scales from the metal surface solely; Schmitt, supported this claim by experimental results. Later, Schmitt et al [35], confirmed his previous findings, that wall shear stress is an order of magnitude less than the films adherent energy with the surface. However, Schmitt added that theoretically, the critical wall shear stress is enough to initiate a mechanical removal of the protective layer on the surface. According to the outcomes of Yang et al's [144] study, the wall shear stress fluctuating might be the key to determining the governing factors the removal process.

The author found that mass transfer is better correlated with fluctuation wall shear stress than mean wall shear stress.

In a recent study by Nichols's et al [145] investigated the effect of high shear stress on the corrosion processes under moderate to very high shear value (10 to 10,000 Pa) was examined. The author explained the extremely high shear stress level by the possibility of such level of shear stress is high at some stages of the production stages. The outcome of this study highlights the importance of the shear stress as a parameter in determining the corrosion behaviour and the inhibition properties of the inhibitors. Zhang et al [146], carried out a study to examine the corrosion behaviour of N80 carbon steel under static and dynamic conditions. Corrosion rate accelerated as a function of the flowing conditions, the author attributed this behaviour to the shear stress and the turbulent energy applied on the surface preventing the formation of the protective film due to the ongoing mass transfer from/to the surface.

Jiankuan et al [147], studied the effect of the flowing conditions on the corrosion behaviour of the X65 carbon steel under wet CO₂ environment, the outcome showed an increase in corrosion rate as a function of the flowing conditions. A continuous flowing conditions resulted in the formation of the protective film.

Although, many studies were carried out to investigate the effect of the wall shear stress on the corrosion behaviour of the both protected/unprotected surface of the carbon steel, the effect of the wall shear stress as flowing conditions parameter on the corrosion rate, in general, is still lack of investigation in a realistic flowing conditions.

3.4.5 Film removal mechanisms

Carbon steel shows a good corrosion resistance when protective layers are formed on the surface act as diffusion barriers to the reactant species from/to metal surface [148]. However, the level of iron carbonate films protection can be affected by different factors. Physical and chemical parameters can reduce the surface coverage of the protection films by damaging the adherent structure of the iron carbonate layers, resulting in the removal of these films from the surface. This will be followed by an increase in corrosion rate due to the exposure of the steel surface to the aqueous CO₂ solution [10, 23, 88]. Many studies were carried out to investigate the removal of the protective films at different mechanical and chemical conditions [21-23, 33, 100, 104, 141, 149-152]. Fluid flow influences the corrosion rate of the covered surface in

different ways. Below the critical flow intensity, the corrosion rate increases only gradually as a function of the flow intensity. Above this critical flow intensity, the interaction between the fluid and the wall becomes so intense that the shear stress exceeds a limit and leads to the destruction of the protective film, which also prevents the re-formation of the protective films [21, 22]. Flow dynamics can damage the film by applying a mechanical stress when the film is poorly adherent to the surface causing the removal of the protective film and exposing the bare metal surface to the corrosive environment, leading to corrosion attack. Although the removal mechanism in a single and multi-phase flow is not fully understood, it can, however, be due to hydrodynamic effects or chemical dissolution of the protective film [21]. Nevertheless, the mechanism of the removal process of the protective films is still debatable between a mechanical, chemical or synergistic effect of both mechanisms.

A clear distinction should be made between pure CO₂ corrosion and a combined interaction of erosion-CO₂ corrosion. The flow rate of water containing CO₂ has two principal effects on film formation and corrosion rate.

First, it prevents the formation of the protective film and slows down its growth by reducing the local supersaturation Fe²⁺ & CO₃²⁻. Second, flow can damage the film by applying a mechanical stress when the film is poorly adherent to the surface causing a localised corrosion, especially Mesa attack [10, 21].

3.4.6 Erosion effect on film removal

Erosion is the process in which a deformation occurs due to gradual removal of material from the surface by continuous solid particle impingement [153]. Erosion can cause severe damage to the components and this may lead to catastrophic consequences both financially and the integrity of the pipeline. Significant attention has been given to investigate this phenomenon in recent years. The presence of water containing solid particles and CO₂ can develop a chemical/mechanical interaction with the steel. The complexity of the erosion-corrosion process is that the synergism effect is not fully understood, where the total weight loss due to erosion-corrosion is higher than the sum of material loss of both the pure erosion and corrosion process [49, 100, 124, 154, 155]. Figure 3-12 illustrates the effect of the erosion on the protective films when solid particles are present in the solution.

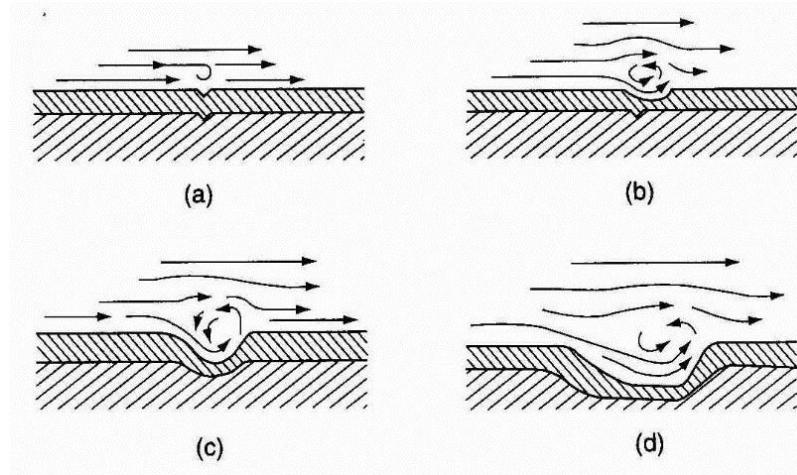


Figure 3-12. Schematic of turbulent eddy mechanism for downstream undercutting of erosion-corrosion pits [156]

Hu et al [15] studied erosion-corrosion to determine the loss of the total material due to pure erosion & corrosion and the synergism between erosion-corrosion under a range of temperature. The author observed the effect of fluid velocity on the ions supersaturation necessary to form the protective layer. The results showed the difficulties in maintaining the supersaturation of corrosion species to form the iron carbonate layer. The fluid dynamic flows the ions away resulting with low supersaturation to form FeCO_3 . Hu concluded that the effect of corrosion enhancing erosion dominates the material loss process.

Ige et al [36], conducted research to study the influence of the erosion-corrosion and flow-induced corrosion on the X65 carbon steel in blank and inhibited conditions using both Rotating Cylinder Electrode RCE and Submerged Impinging Jet SIJ techniques for low and high shear stress tests respectively at temperature 45°C . Ige found that the presence of the inhibitor reduces the material loss, where a significant reduction was observed in inhibited conditions compared with the same parameters in blank condition. In terms of sand loading parameters the authors observed no significant change in degradation when sand loading changed at low flow velocity (low shear stress) however, at higher shear stresses, sand loading has a high influence on the erosion-corrosion rate.

3.4.7 Mechanical film removal by hydrodynamic forces

Many studies have been carried out to investigate the removal mechanism and the effect of flow rate on iron carbonate films. The corrosion process is affected by fluid velocity due to the fact that flow velocity governs the species mass transfer rate by playing an important role in the film removal [157]. A critical wall shear stress was introduced as the defining factor for the mechanical film removal [34-36, 155]. However, it is thought that critical shear stress values are too small to be the cause of the mechanical removal disruption, the intensities of the near wall turbulence also have a very influential role in the removal process. Nesic [37] simulation experiments showed the separation and reattachment of the flow through a sudden pipe expansion leads to increase the flow turbulent at that area, resulting in high rate of mass transfer and weight loss, the author referred the weight loss purely to the corrosion rate. The maximum metal loss was observed at high turbulence areas coupled with mean wall shear stress equal to zero near to the point of flow reattachment. Later Nesic [14] investigated the mechanical removal of the protective film using a Rotating Cylinder Electrode RCE in highly turbulent flow regime. Nesic concluded that shear stresses applied on the film are physically not enough to remove the films by breaking down the adherent bond between the scales and the surface. However, there are some other suggestions from field experience that; hydrodynamic effects are able to remove FeCO_3 scales. The author attributed these suggestions and the results behind them to other factors, e.g. Water chemistry and the presence of organic acids in the environment. Ruzic et al [21, 22], in his work, concluded that the previous works regarding scales removal in flow conditions might be the “missing link”, that is, the determining factor for film removal. Other authors like Schmitt et al [143] proposed that an internal stress which is associated with films growth process known as intrinsic stresses could cause film cracking rather than hydrodynamic forces. Schmitt attributed the film removal to the intrinsic stresses developed from the volume mismatch between the metal surface and the growing FeCO_3 scale; this can cause cracks and failure in the structure of the film. Ruzic et al [21-23], predicted the wall shear stress value at low velocity 7000 rpm (~ 4 m/s) is roughly half of what it is at a high velocity 1000 rpm (~ 6.5 m/s). It also increased by a factor of 5.1 to 5.7 for rough surface films in comparison to smooth surface films, and showed that the instantaneous wall shear stress fluctuations can be three to four times larger in magnitude than the maximum average (mean) value; this magnitude of wall shear

stresses occurs locally and in an intermittent manner in the turbulent flow region. Ruzic suggested that the wall shear stress values (both mean and fluctuating) are too small to be the only determining factor for the mechanical removal of FeCO_3 films in single-phase flows. Figure 3-13 illustrates the top-view appearance of the protective film surface after exposure to flowing conditions from Ruzic et al [22], the author attributed the film removal process to a purely mechanical effect.

Based on the studies by Ruzic et al studies [21-23]; the proposed mechanism of mechanical film removal in single-phase flow using sequence steps that take place:

- Separation from the substrate:

The porous and spongy structure of the iron carbonate gives the film a spring-like behaviour. The wall shear stress is not sufficient to remove the film from the surface; instead, severe fatigue caused by local fluctuating quantities such as velocity and wall shear stress fluctuations apply a dynamic mechanical stress (vibration), leading to the films separation from the substrate once the adhesive strength of the film is exceeded.

- Crack opening and widening

Surface roughness increases at the crack site enhancing the local levels of turbulence and leading to further film detachment and separating from the metal surface.

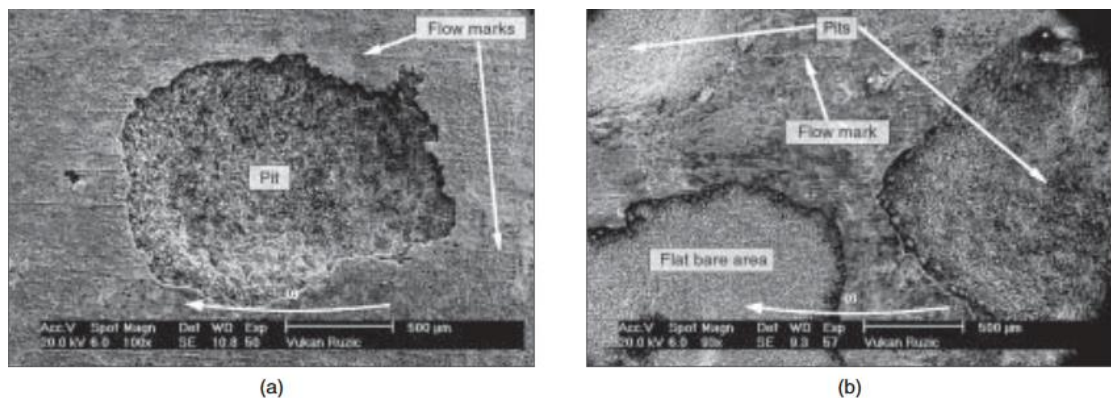


Figure 3-13. Ruzic et al [22] SEM images of the mechanical removal due to flow hydrodynamic a: at 7000 rpm b- at 10000 rpm

3.4.8 Chemical-mechanical film removal

Iron carbonate FeCO_3 film formed on mild steel generally provides satisfactory protection from potentially destructive internal pipeline corrosion in the oil and gas production and transportation industry. However, they can be damaged chemically by dissolution and mechanically by hydrodynamic forces.

In multi-phase flow systems such as in solid particle (sand) and water in CO_2 environments, it is clear that the mechanical impact forces of the sand particles are capable of removing the protective films [158].

However, some studies associate film removal in single-phase flow through pipelines with chemical dissolution and reported that in typical velocities $<10\text{m/s}$ the mechanical stress cannot remove the films because their value was considered too small to overcome the film's strength [22]. Malka et al [124] confirmed that the mean wall shear stress is insufficient to govern the removal process; the author added that local turbulence and internal stress accompanied by significant fluctuation quantities play a major role in mechanical removal, however under turbulent flow conditions a synergism between the mechanical and chemical effect cause the film removal process.

The FeCO_3 dissolution reaction is a chemical dissolution process take the following reaction path [95]:



The protective films dissolve when subjected to an unsaturated solution where $S < 1$.

S = Saturation and is expressed as:

$$S = \frac{[\text{Fe}^{2+}][\text{CO}_3^{2-}]}{K_{SP}} \quad 3.2$$

Where the denotes equilibrium concentration of the species, and K_{SP} is the solubility product dependent on solution ionic strength and temperature.

Yang et al [39] studied the dissolution of iron carbonate films in CO_2 corrosion conditions. They used a suitable iron carbonate formation temperature and pH with high supersaturation solution with Fe^{2+} to accelerate the formation of the protective film. The findings revealed a clear easy dissolution of the iron carbonate films subjected to the undersaturated solution at low pH after 15hrs exposure.

Yang went further by examining the effect of flow velocity on the dissolution process. The saturation level decreased to an undersaturated condition by lowering the pH of the solution. This initiated the dissolution process where a mass loss was observed within 3 hrs of exposure to a solution of a pH 3.8. The author concluded out of their experiments that the key parameter of the dissolution process is the level of undersaturation, and the change of the flow velocity does not have a major effect on iron carbonate dissolution. This observation proposes that the dissolution process is surface reaction controlled rather than mass transfer rate dependent [39].

In pipeline transportation of oil and gas, the value of pH varies from 4 to 6 [40]. It is important to understand the influence of the physical and chemical properties of the solution on the corrosion behaviour of the bare and protected surface of the carbon steel, under static and flowing conditions. The study by Neilson et al [159] study showed that chemical and mechanical removal processes combined may cause more damage than if they acted separately. Dissolution leads to losing the adherent of the film grains, subjecting them to mechanical removal.

Ruzic et al [22, 23, 124] proposed that the Mechanical and chemicals removal were acting separately. However, film dissolution (chemical removal) was more important and effective than mechanical film removal under same conditions.

3.5 Mechanical properties of FeCO₃ films

High strength, adherent and dense film formation on the surface will decrease the anodic reaction by creating a diffusion barrier to the anodic species moving toward the bulk solution. Anodic reactions are likely to occur in areas where the protective layer does not fully cover the surface or flaw sites, where anodic species are readily transported from the surface. Therefore, the combination of high cathodic/anodic reactions in split areas within the protective layer leads to high local corrosion rates in these areas [10].

Since the strength of the protective films significantly affects the corrosion rate, the mechanical properties of these layers should be considered as important factors governing the corrosion process. By understanding the films properties it may give a mechanism for the threat prediction on the surface and provide the researchers in this field the means to improve the protectiveness of the layer against the harsh corrosive environment not only chemically but also mechanically.

A limited literature is available regarding the mechanical properties of CO₂ corrosion products, specifically the fracture mechanical properties. Until the early-mid 90s, most of the conducted work in this field investigated the corrosion process at elevated temperatures and the properties of iron oxides and Ni-based alloys at extreme temperatures e.g. Johnson [160], Jervis [161], Hancock [162]. In general, corrosion scales are brittle and show failures due to any extrinsic and intrinsic stresses that exceed their strength limit; scales detachment from the surface leaves uncovered sites on the metal surface, allowing corrosion to proceed. Moreover, fluid flow can make the damage more severe by creating a micro-turbulence within these areas widening the spalling site and preventing the layer from forming a replacement film. [163]. Schmitt et al [143], conducted research to examine the mechanical strength of the protective films, by measuring Young's modulus E , surface fracture energy γ , and yield stress. Schmitt assessed the value of these parameters by adopting other oxides strength parameters, which shared similar atomic construction with iron carbonate, i.e. MgO, FeO, Fe₃O₄, and MnCO₃. The author described how to measure the surface fracture energy but had not used it to calculate the exact force of iron carbonate surface required to mechanically remove the films. However, he assessed its value through the same technique mentioned above by using a confirmed value of other oxides which are chemically similar to iron carbonate. Schmitt proposed through his work that thinner scales are likely to hold higher strain before failure and that scales shape plays a highly important role in crack resistance and in the strength of the scales.

Later Schmitt et al [35] investigated the mechanical properties of CO₂ corrosion products and the effect of it on the corrosion rate. However in his work Schmitt used different methods & tests than his previous work [143] to measure the exact values of the mechanical properties of the protective film. The author used the 4-point loading test to determine the fracture stress and fracture strain of the scales. The 4-PLT test is widely accepted in stress and strain measurement [164]. Using the obtained values from both studies [143] and [35], Schmitt, observed a variation in fracture surface energies along the scales length; the variation between the elastic adherent and brittle spalling, where at a length less than 10 μ m an elastic adherent is dominating, whereas with scales above 10 μ m length Schmitt observed a rapid decrease toward a brittle spalling.

3.6 Summary

To date, an adequate understanding of the effect of the flowing conditions on the corrosion behaviour of the uncovered surface has not been achieved. This is partly due to the complexity of the process through which flow parameters interact with each other, and how a combination of these parameters influence the corrosion behaviour of the carbon steel in CO₂ saturated environment. The effect of the flowing conditions on the stability and the removal mechanisms of the iron carbonate film is also lacking a clear comprehension. This can be attributed to the difference in film formation conditions prior to the tests, the unrealistic flow profile, and the study limitation on one or two (physical or chemical) parameters and neglecting the overall effect of the flowing conditions parameters.

In the review presented in this chapter, several studies have investigated the corrosion behaviour under flowing conditions from different perspective and approaches. However, more studies are needed to establish guidelines for the corrosion behaviour of carbon steel under flowing conditions. Despite the numerous studies carried out to investigate the influence of the flow on the CO₂ corrosion, there is no general consensus on which parameter (physical or chemical) has a direct relationship with corrosion rate, and describes the corrosion behaviour of the carbon steel as directly proportional. In addition to, how the flow parameters such as (Reynold`s number, wall shear stress, and flow velocity) correlate with each other and influence the corrosion rate. And how the channel geometry can govern that influence.

An understanding of the corrosion behaviour of the protected surface is not fully achieved. Two proposals are present in the literature to explain the removal mechanism, mass transfer controlled and/or surface reaction controlled. A limited number of systematic studies have been carried out to determine the removal process of the protective film, as a function of pH and temperature at both static and flow conditions. To establish whether the same removal mechanisms observed at low temperature extend to a higher temperature at both conditions static and flowing.

Table 3-1 summaries some of the work in literature carried out to investigate the corrosion behaviour of uncovered and covered surface of carbon steel in CO₂ saturated conditions, the table presents details of which parameter each study considered to investigate the corrosion behaviour, in comparison to the current study (highlighted in red at the end of the table). It is clear that most of the previous research

did not necessarily employ all the physical and chemical flow parameters to study the corrosion behaviour. However, it studied the corrosion as a function of one or two of these parameters and considered the other parameters are constant, therefore the effect of the other flow parameters, solution properties and channel geometry on the corrosion behaviour was not fully understood.

The study, temperature, CO ₂ concentration in water	Flow velocity	Shear stress	Mass transfer	Flow turbulence (Re)	Channel geometry	Species concentration (F ²⁺ or H ⁺)	Microstructure	Film formation rate	Film removal (Chemical)	Film removal (Mechanical)	Film removal (Chemical + mechanical)
Slaimana et al [26] 2010, T 30-60°C, , 10 ⁻⁴ mol/l				20K to 113K							
Videm [133] 1987, T 60-90°C, , 10 ⁻⁴ mol/l	1 to 6 m/s										
Ferreira et al [27, 90] 2015, T 25°C, 10 ⁻⁴ mol/l	0 to 1200 rpm			~3K							
Nesic [14] 2012, To 50-80°C, 10 ⁻⁴ mol/l	0 to 2.5 m/s										
Zara et al [134] 2015, T 25-80°C, , 10 ⁻⁴ mol/l	0 to 2000 rpm										
Barmatov et al [135] 2015, T 80°C, , 10 ⁻⁴ mol/l	5 to 6000 rpm			0 to 150K							
Denpo et al [140] 1993, T 80°C, 4×10 ⁻³ mol/l	2 to 17 m/s										
Efird [142] 1977, T 50°C, 10 ⁻⁴ mol/l	0 to 18	0 to 700 Pa									
Schmitt et al [143] 1996, T 80°C, 5×10 ⁻⁴ mol/l	2 m/s										
Schmitt et al [35] 1999, T 80°C, 5×10 ⁻³ mol/l		350 Pa									
Nichols et al [145] 2017, T 90°C, 10 ⁻⁴ mol/l,		Up to 1000 Pa									
Zhang et al [146] 2017, T 60°C, 8×10 ⁻⁴	2 m/s	3.5 Pa									
Ruzic et al [22, 23, 141] 2006-2007, T 80°C, 10 ⁻⁴ mol/l,	7000 to 1000 rpm	229 to 466 Pa									
Yang et al [33, 39] 2010-2013, T 80C, 10 ⁻⁴ mol/l,	0.6 to 2.9 m/s										
Dugstad [11, 12, 29] 1994, 1998, 2006, T 20-90°C, 10 ⁻⁴ mol/l,	0.1 to 13 m/s										
Farelas et al [112] 2013, T 80°C, 10 ⁻⁴ mol/l,	0.5 m/s										
Akeer et al [16] 2013, T 80°C, 10 ⁻⁴ mol/l		30 & 525 Pa									
Liu et al [113] 2015, T 75°C, 10 ⁻⁴ mol/l,											
Neville et al [107] 2005, , 10 ⁻⁴ mol/l	600 to 3600 rpm										
The current study	0.6 to 13.75 m/s	1.3 to 655 Pa		35K to 125K							

Table 3-1 The parameters that were considered to study the corrosion behaviour of carbon steel under flowing conditions

Chapter 4. Flow parameter calculations and CFD simulation

4.1 Introduction

In this chapter, the calculations of the flow parameters using empirical correlations and the CFD simulation of the flow profile are reported. The wall shear stress values were calculated using empirical correlations. The goal was to generate a range of low to high shear stresses in the range of 1 to 450 Pa, this range was assessed by the previous work conducted in CO₂ saturated environments [16, 35, 151]. The first part of this chapter describes the calculations of the flow parameters via numerical correlations. The second part of this chapter presents the Computational Fluid Dynamics (CFD) technique and how it is used to simulate the flowing conditions through the test section. The CFD simulation results were used to assess profiles of the flow parameters such as the flow velocities across the samples.

4.2 Flow parameter calculations

Flow parameters throughout the test section were calculated using empirical relations. The aim was to calculate the flow characteristics (i.e. velocity, Reynold`s number and shear stress) at given flow rate and flow cell geometries. The test section geometries that were varied the width of the test section at each sample and the thickness of the test section.

The flow shear stresses on the sample surfaces were determined by using Dean`s formula (for a rectangular duct flow) [165] to calculate the friction factor.

$$C_f = 0.073 \times Re^{-0.25} \quad 4.1$$

However, covered surfaces with iron carbonate films are treated as rough surfaces, where the friction factor for the rough surfaces was determined using the Colebrook equation [60, 166]. This equation was rewritten and simplified [152] to calculate the friction factor in a rectangular cross-section flow section.

$$\frac{1}{\sqrt{C_f}} = -4 \log \left\{ \frac{0.27 \times \epsilon}{D_h} + \left(\frac{7}{Re} \right)^{0.9} \right\} \quad 4.2$$

where the Reynold`s number is given by

$$Re = \frac{D \times v \times \rho}{\mu} \quad 4.3$$

The characteristic length D for rectangular cross-section channel in equation 4.3 is equal to the value of the hydraulic diameter which can be calculated by equation 4.9 [167-169].

This allows the wall shear stress to be calculated using:

$$\tau = \frac{C_f \times v^2 \times \rho}{2} \quad 4.4$$

All the values of the wall shear stress employed in this study were calculated from the correlation in equation 4.4. This equation is widely used in literature to calculate the wall shear stress across the samples on rectangular cross-section flow loops [16, 151, 165, 170]

The diffusion coefficient is calculated from the Stokes-Einstein equation [40]

$$D = D_{ref} \times \frac{T}{T_{ref}} \times \frac{\mu_{ref}}{\mu} \quad 4.5$$

and the mass transfer coefficient is described using the Sleicher and Rouse mass transfer correlation [40, 171, 172].

$$\frac{K_m \times L_c}{D} = 5 + 0.015 \times Re^a \times Sc^b \quad 4.6$$

The values of a and b are ~0.87 and ~0.33 respectively [173]. Equation 4.6 was not used to calculate mass transfer coefficients, as these can be determined experimentally using the limiting current density (see paragraph 10.3.1). Equation 4.6 is a semi-empirical expression to represent a mass transfer coefficient in fully developed flow, and over wide fluid properties. Other forms exist, where there is a developing flow profile (e.g. Coulson & Richarson Vol 1 [174]).

Schmitt number is given by [40]

$$Sc = \frac{\mu}{\rho \times D} \quad 4.7$$

Finally, the thickness of the diffusion boundary layer and the hydraulic diameter are given by

$$\delta_m = \frac{D}{K_m} \quad 4.8$$

$$D_h = \frac{4A}{2P} \quad 4.9$$

Where P is the wetted perimeter of the cross-section (width + height).

4.3 Tafel slope calculations

Corrosion rates were measured using the Linear Polarisation Resistance (LPR) technique. The initial values of the Tafel slope constants used in the LPR to measure the corrosion rate were 120 mV/decade for both the cathodic (β_c) and anodic (β_a) resulting with Stern Geary constant B equal to 26. However, the final reading of the corrosion rate was corrected based on theoretical β_c and β_a values. The cathodic and anodic Tafel slope was calculated from Zheng et al [175] which was also reported by [31, 40].

$$\beta_c = \frac{2.303 \times R \times T}{a_c \times F} \quad 4.10$$

$$\beta_a = \frac{2.303 \times R \times T}{a_a \times F} \quad 4.11$$

The apparent transfer coefficients a_c & a_a values are 0.5 and 1.5 respectively for the cathodic and the anodic reactions [52].

Stern Geary constant B is given by Stern Geary equation [112, 176]

$$B = \frac{\beta_a \times \beta_c}{2.3 (\beta_a + \beta_c)} \quad 4.12$$

Therefore the actual corrosion rate can be calculated by:

$$\text{The actual C.R mm/y} = \frac{\text{The measured corrosion rate}}{26} \times B \quad 4.13$$

4.4 Computational Fluid Dynamics (CFD) technique

Computational Fluid Dynamics (CFD) is a technique to solve the set of numerical equations that describe fluid flow. Several equations are governing the flow-simulating process [177]. For Newtonian fluid dynamics, the well-known Navier-Stokes equations are the main numerical laws to simulate fluid flow characteristics in the given conditions [178]. CFD experiments play a major role in aerospace and fluid flow applications by validating and finding an approximation solution of the numerical laws that govern the flow regime providing an adequate and cost & time-effective results rather than full-scale tests [179]. Navier–Stokes equations are partial differential equations. Due to their complexity, these equations were solved analytically under simplified conditions [180]. Computational fluid dynamic methods use approximate solutions by replacing the partial differential equations with sets of algebraic equations that can be solved by computational analysis [181]. The CFD method is computing power dependent, where the improvement of the accuracy of the results is accompanied by the development of both the computing system software and hardware [182].

The CFD methods have developed in a way which has become part of a wide range of scientific research in the field of fluid dynamics and design in industry, resulting in significant reductions in fluid flow test costs. Moreover, CFD allows research and testing the fluid flow under conditions which are not possible to create or to measure experimentally in the field or lab [183]

4.5 Simulation Process

To simulate a fluid flow through certain domains, several steps are involved in the process to construct the model. For fluid dynamic simulation, the first step is building the geometry of the model and selecting the domain material. The volume is divided into small fragments known as mesh, with the size of the mesh governing the accuracy of the simulation results. The boundary conditions of the domain define the conditions of the fluid (generally) at the extremities of the domain. These represent the physical condition of the experiment. The flow analysis then computes the behaviour within the domain environment. The results of the simulation will depend on the meshing accuracy, geometry, and the precision of the boundary conditions [184]. Thus CFD process in overall is a three steps procedure [185-187]:

4.5.1 Pre-processing

Pre-processing consists of defining the geometry of the flow cell. To determine the domain of interest, the test section geometry was built and developed using Solidworks software. The domain is divided into smaller segments using, a grid known as mesh generation “fine mesh”. The boundary conditions including the physical and chemical properties of the fluid were defined and fed to the model (density and viscosity of 3% NaCl water at 50°C and inlet velocity of 3.25 m/s).

4.5.2 CFD Solver

This step involves solving the numerical equations which are controlling the flow characteristics; the mesh which was generated in the pre-processing stage defines the points on the geometry at which the governing equations are solved. Several methods are used to solve the flow equations such as finite element, finite difference, and spectral methods. However; the finite element method was selected to process the simulation part of this project represented by COMSOL software [188]. This is due to several facts that the finite element method divides the domain into elements with small areas which produce what is known as mesh for the whole domain.

This will facilitate the solving process by avoiding the simplifying steps of the geometry of curved edges. Moreover, in the FEM, the values of unknown functions can be approximated inside of each element [186].

4.5.3 CFD Post processing

In this step, the results of the analysis of the flow cell model are represented as colours, contour plots, and graphical representations from which the values of the flow properties can be obtained.

4.6 Navier-Stokes equations

Navier-Stokes equations provide general definition and description to the fluid flow; these equations describe how the velocity, pressure, temperature, and density of a fluid in motion are related. These equations are generally too complicated to be solved analytically, therefore the researchers conducted further simplifications and

approximations to the equation set that is possible to solve. Over the last few decades, the researchers and industry employed various techniques such as finite element, finite volume, and finite difference to solve Navier-stokes equations, allowing a significant increase in the application of CFD within industry and research [186, 189].

4.7 Finite Element Method (FEM)

The Finite Element Method is a powerful method for solving Partial Differential Equations (PDE) within scientific research and industry including the field of fluid flow [190]. Other methods are on the field to solve PDE like finite difference/volume methods; however, the FEM has several advantages over other methods that make it superior in solving partial differential equations. FEM offers easy solutions for complex geometries, using a grid of nodes with various shapes forming what it's known as a mesh. Finite element method is a numerical technique consisting of the following essential specifications [191-193]:

- I. The domain is divided into small areas known as elements to form a grid over the continuum field; these elements are varied in size, they can be triangular or curved shapes depending on the domain geometry. Each node or element area represents a function to solve during the solver stage. Therefore FEM can solve complex geometries

However, the Finite Difference Method (FDM) needs a structured grid, and therefore the mesh is limited to the regular shape of mesh cells, which increase the complexity of the simulation [194].

- II. The FEM solves the PDEs by converting them to ordinary differential equation (ODEs), using an integral form of the PDE rather than looking for the solution of these equations itself. Whereas FDM provides solutions for the functions at grid points only using algebraic equations. Therefore FEM with respect to the easy solution and accuracy has a great advantage on the FVM and FDM [195].
- III. FEM obtained strong momentum in solving the PDEs in the 1960s and 1970s [196]. However, the FDM introduced during the last three decades as a new method to solve the partial differential equations [197]

4.8 Boundary conditions

Boundary conditions are an important concept for CFD simulations. The dependent variables in the solver equations are required to be identified with valid values within the **boundary of the model geometry** [198]. The initial boundary conditions and the input parameters for CFD simulation included:

- I. An inlet velocity range up to 5 m/s was selected. This range of flow velocity was chosen based on the theoretical calculations in order to identify the flow velocities range required to generate the targeted wall shear stress across the samples on the test section. Knowing that the aim is to generate shear stresses in the range of up to ~1 to 450 Pa this value was defined in the literature as a high shear stresses [16, 36].
- II. The following CFD simulation run carried out to identify the pressure inside the test section that is associated with maximum inlet velocity (1 to 4 m/s) required to generate the targeted flow parameters of this project. To use these data as a reference during the flow loop parts.
- III. The inlet and outlet diameters are 16.5mm equal to the diameter of the high-pressure hoses used to fit through the inlet and outlet of the test section in the flow loop.
- IV. The test section thickness is 2mm. The theoretical calculations of the wall shear stress profile were based on a 2mm test section height.
- V. Outlet: Environment gauge pressure was 0 Pa.
- VI. The fluid properties are incompressible flow and temperature is 50°C.
- VII. Flow type: Turbulent flow.

4.9 Turbulence model

Processing a CFD model usually consists of four main stages: geometry, grid generation, setting-up the boundary conditions, solving and post-processing the results. The complexity of the CFD process is highly dependent on the degree of the flow turbulence. The main difficulty in turbulence flow CFD is to capture and solve every scale of the fluid motion, which requires super-computers power [199, 200]. The turbulence is dominant over all other flow regimes in any fluid flow domain. Therefore to reduce the complexity of the CFD process without affecting the accuracy of the results, the sub-grid turbulent motion present in the fluid flow will be modelled

and introduced to the field as a turbulence model [201]. Reynold`s averaged Navier-Stokes equations RANs and k- ϵ turbulence model were selected for the current study. The k- ϵ model determines the mechanisms that affect the turbulent kinetic energy per unit mass. [202]. Other turbulence models such as k- ω (k- ω) predict the turbulence by solving the PDEs partial differential equations for two variables, K first is the turbulence kinetic energy, while ω is the specific rate of the turbulence kinetic energy k into internal thermal energy. For comparison purposes, both models were used at the initial stages of the CFD simulations. The simulation results showed the velocity, pressure and wall shear stress profiles of both models were relatively similar. Therefore, the following CFD simulations were conducted using k- ϵ turbulence model for its reasonable accuracy for a wide range of flow where it provides stable calculations for flows with high Reynold`s number [203-205].

4.10 Test section CFD simulation

The main objective of the test section geometry is to provide a gradual decrease in the cross-section area at each sample of the five samples, at which the flow velocity of the 1st sample is always half of the flow velocity at the 5th sample. This design provides a different range of flow velocities/wall shear stresses while the Reynold`s number range is maintained, or different Reynold`s numbers are achieved at a similar range of wall shear stress.

To analyse the model in the COMSOL solver, it was necessary to identify the geometry of the structure by generating the model`s physical geometry using the Solidwork`s designing tools and then import it to COMSOL [188]. The initial model of the test section is shown in Figure 4-1. A CFD simulation run was carried out using this model to examine the wall shear stress profile across the test section. The inlet width is 50mm, the outlet is 10mm, the length of the test section is 300mm and the thickness is 2mm.

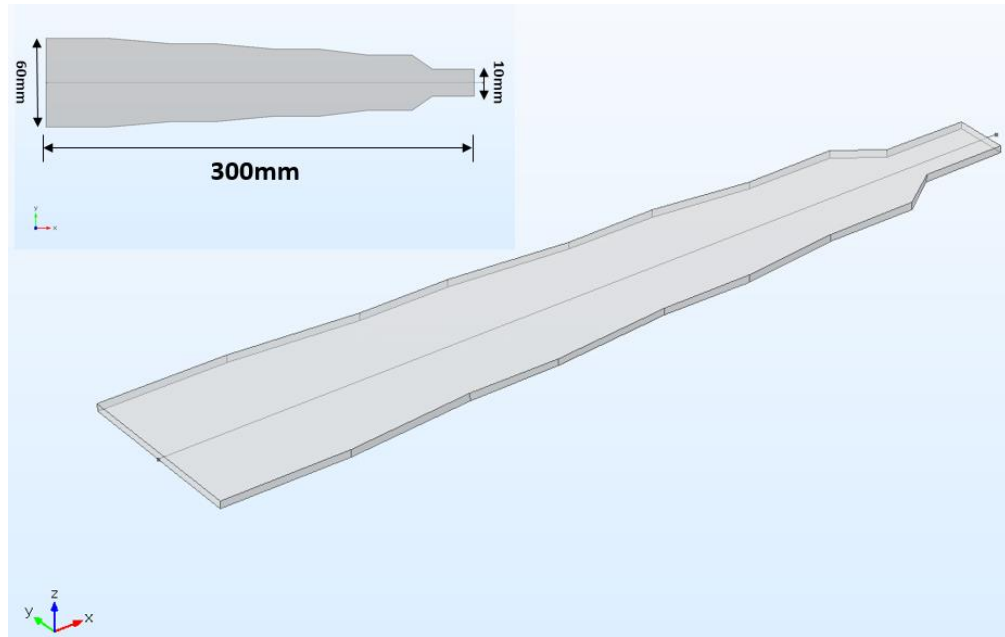


Figure 4-1. The initial test section CFD model

The shear stress profile is shown Figure 4-2. It was clear that the model needs some modification on its geometries. Where the shear stress value is almost constant from the inlet point up to the halfway toward the outlet then the value increases dramatically for all the flow velocities. The aim was to obtain a gradual value of shear stresses along the X direction of the cell flow. Therefore, both the geometry of the cell and the boundary conditions were subjected to several modifications during each of the CFD runs to achieve a compatible flow cell design that provided the desired flow conditions.

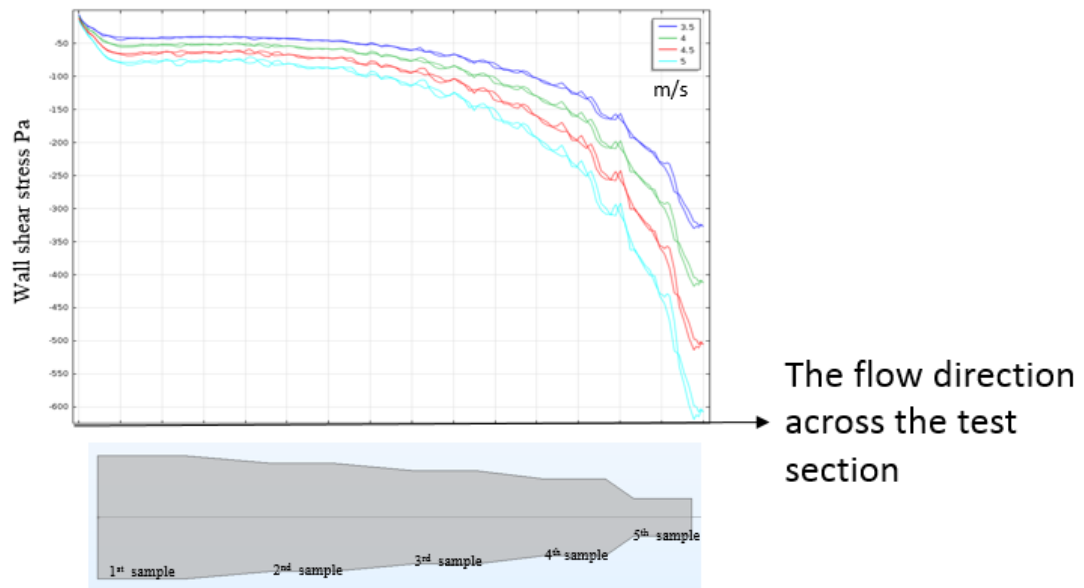


Figure 4-2. Shear stress profile at given inlet velocities

The main changes in the geometry of the test section at this stage were:

- I. Increase the length of test section in the X direction from 300mm to 435mm; in order to enhance the length of the hydrodynamic entrance region to avoid any vortex (core) flow regions and forming a fully developed flow throughout the test section. Also, the increase in test section length provides better space management on the surface of the test section to mount the carbon steel samples at suitable points at which changes in shear stress occur due to the increase in flow velocities. The width of the test section at the inlet side reduced from 60mm to 50mm and the outlet width increased from 10mm to 25mm.
- II. 16.5mm diameter inlet and outlet holes were added to the design. This pipe diameter was selected with respect to the pump specifications and the flow rate to achieve the desired inlet velocity at reasonable pressure.

Based on the CFD results in Figure 4-2 the design was modified by adding more features such as inlet & outlet fits to create a more realistic simulation of the actual geometry of flow cell. In addition, the dimensions of the test section were changed to enhance the shear stresses increasing rate along the X direction. The final model of the test section is shown in Figure 4-3.

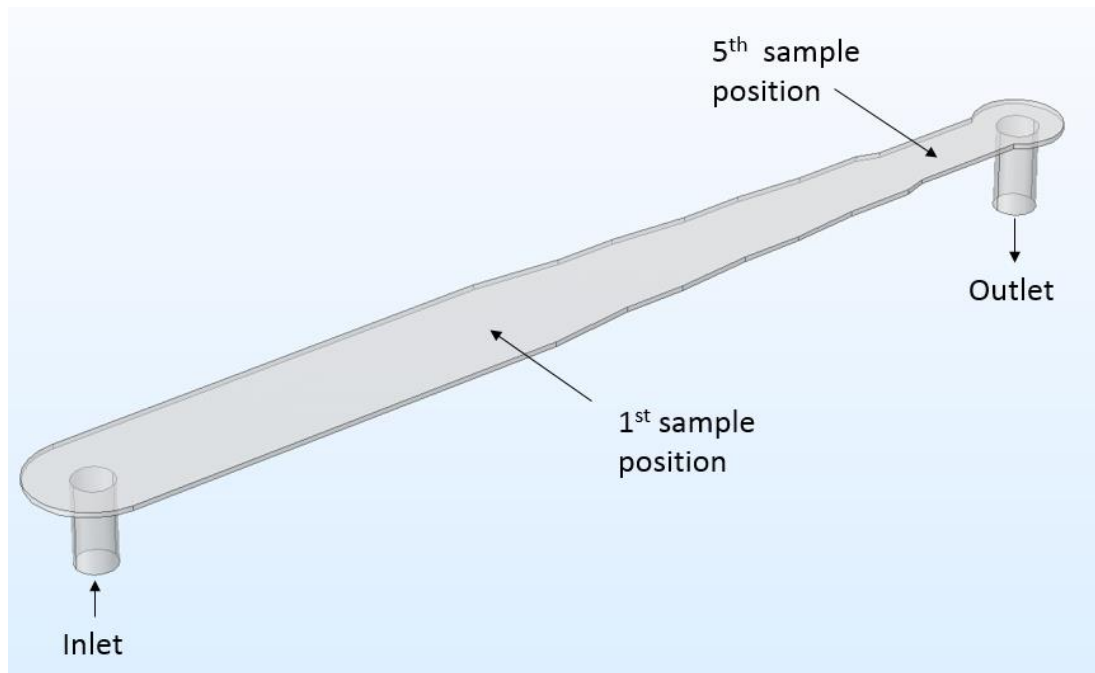


Figure 4-3. The final test section model geometry

Figure 4-4 shows the shear stress values along the X direction (distance from the first sample to the fifth) of the modified test section model at inlet velocities range 1 to 4 m/s. One can observe the changes in the shear stresses contribution along the X-direction of the test section, where the wall shear stress values increased gradually across the test section, which gives the opportunity to examine the carbon steel samples surface at a wider range of shear stress values during the same run of the experiment. The first CFD simulation which was carried out using an inlet velocity range of 1 to 5 m/s showed that a wall shear stress of ~450 Pa (the maximum wall shear stress required in this study) achieved with an inlet velocity of 4 m/s. Therefore, the following CFD runs were limited to maximum inlet velocity up to 4 m/s.

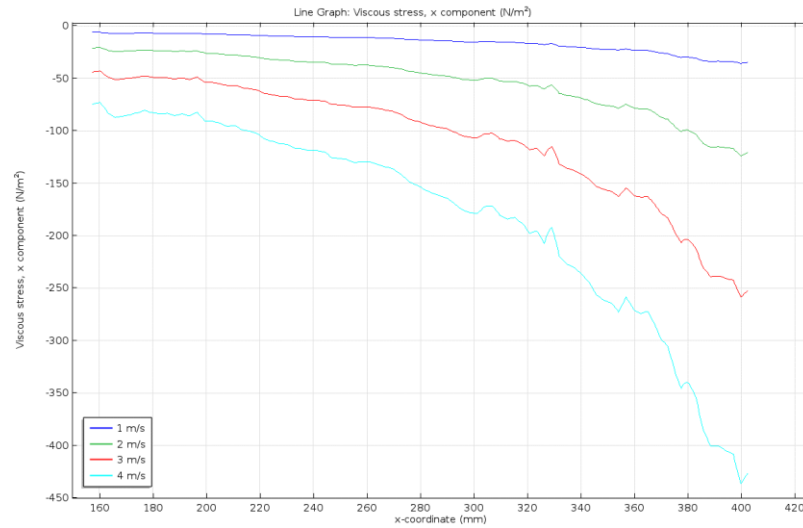


Figure 4-4. Shear stress profile on the test section using the modified model at a flow velocity

Figure 4-5 shows the pressure profile inside the test section under inlet flow velocities 1 to 4 m/s. At maximum inlet velocity of 4 m/s, the highest pressure point is ~ 4.5 bar. Therefore, the flow loop pump model was selected to be capable to be fully operative at > 4.5 bar.

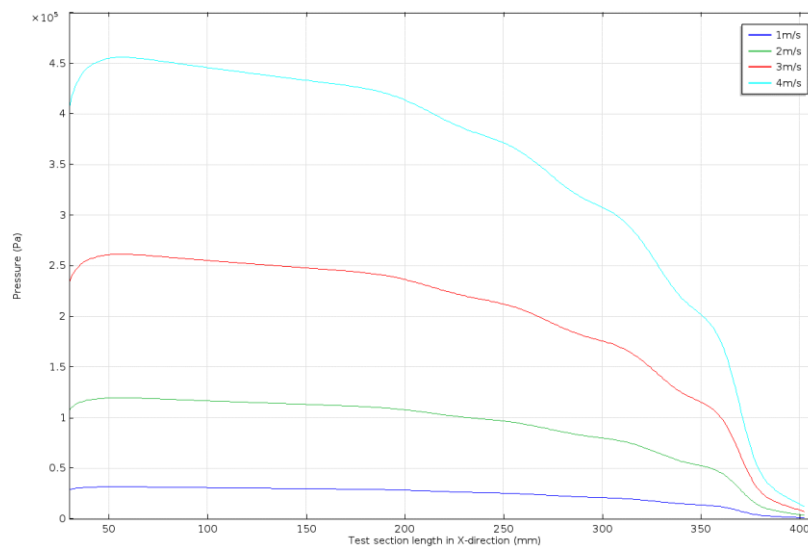
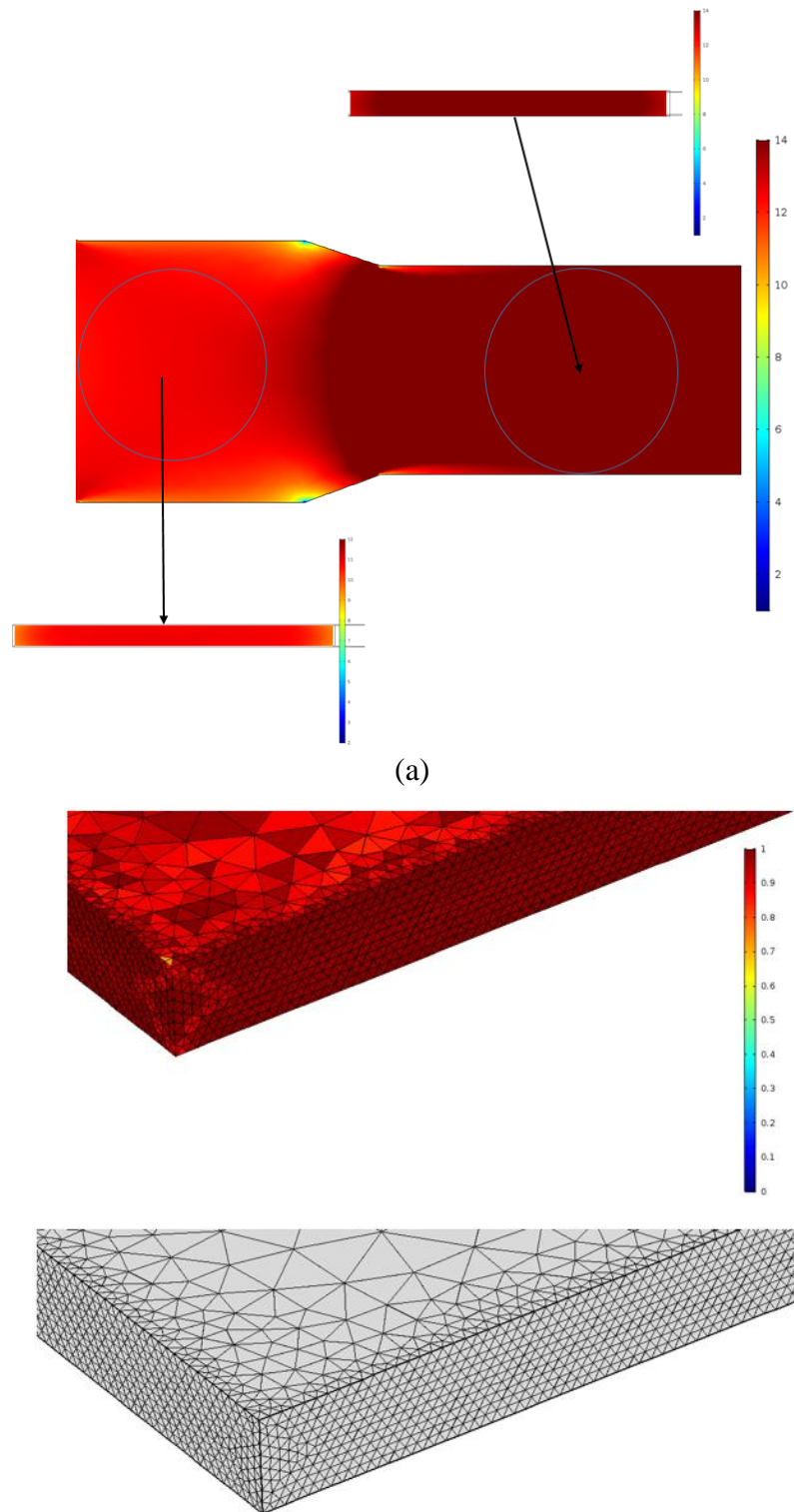


Figure 4-5. CFD simulation to the pressure drop across the test section at different inlet flow velocities.

The results of the CFD experiments were essential in determining the dimensions of the rigs parts and to help accurately select the pump model with specific specifications that matched the flow simulation outcome. The flow bath was designed as a flow between two fixed parallel plates. This technique was selected because it provides

flow conditions that simulate the turbulent flow dynamics in pipelines in the field [206-208] and due to its simple manufacture process. The actual flow geometries consist of three parts; however, this was simplified in the simulation model into one part without comprising the physical dimensions of the flow domains as this will minimise the time required for the processing stages and improve the accuracy of the outcome results by keeping the model simple and without complicated geometries. The inlet and outlet pipe's diameter was designed based on the maximum inlet flow velocity that is required in the future plan of this research and the associated pressure increase, based on the flow simulation results; 16.5mm diameter will keep the pressure within the pump specifications at inlet velocity of ~4 m/s as shown in Figure 4-5. Which gives a 6.75 m/s flow velocity across the 1st sample and 13.5 m/s across the 5th. The 1st and the 5th samples positions are illustrated in Figure 4-3. The flow velocity profiles across the 4th and 5th samples are shown in Figure 4-6 (a). The number of mesh cells in the Z direction (flow cell thickness of 2mm) was 8 cells, the mesh quality across the flow cell geometry between 0.8 to 0.95 as shown in Figure 4-6 (b). No Eddy effect zones were observed across the 4th and 5th samples.



(a)

(b)

Figure 4-6. CFD simulation of:

- (a) Top view of the velocity profile cut plane through the 4th & 5th samples.
- (b) Mesh quality and grid structure.

At flow velocity 11 & 13.75 m/s across the 4th and the 5th samples respectively. Solution density of 1009.62 Kg/m³ and viscosity 5.82×10⁻⁴ Pa*S.

Chapter 5. Methodology and test procedure

5.1 Introduction

This chapter details the experimental procedures used in this work. This chapter also describes the composition of the material used throughout the test series in this research project. The techniques employed to carry out the surface analysis of the morphology and chemical composition of the corrosion product are described.

Firstly, sample preparation steps are described, followed by the flow parameter calculations, then the surface analysis techniques such as Scanning Electron Microscopy (SEM) and X-Ray Diffraction (XRD) used to examine the nature of the surface topography and the crystalline structure after the exposure to the test environment.

5.2 Materials preparation

Sample preparation was carried out using two processes:

- I. For the uncovered surface corrosion rate tests.
- II. For the covered surface with protective film corrosion rate tests.

5.3 Samples preparation for the protected test

The test coupon materials were made from X65 carbon steel for representative of pipe materials used in oil/gas pipeline transmission. X65 carbon steel is widely used in crude oil/oil products transmission pipelines construction for it is high strength, high weldability, low costs and availability. The standard chemical composition is presented in

Table 5-1. The samples were machined down to a cylindrical shape to fit in the sample holder in the test section. The coupon diameter is 25 mm and the samples were 10 mm thick flat circular discs with a surface area 490 mm² exposed to the test environment. During the pre-test preparations, sample surfaces were polished down using 600, 800 and 1200 grit sandpapers respectively and then washed with isopropanol solution and dried using a heat gun. Samples were then stored in a vacuum desiccator until needed.

The test section/cell holder for the cylindrical shape specimen will be discussed in the next chapter.

Table 5-1. Elemental composition of X65 steel (wt. %) [209]

C	Si	Mn	P	S	Cr	Mo	Ni
0.12	0.18	1.27	0.008	0.002	0.11	0.17	0.07
Cu	Sn	Al	B	Nb	Ti	V	Fe
0.12	0.008	0.022	0.005	0.054	0.001	0.057	Bal

5.3.1 Samples preparation for the protected surface test.

Sample preparation for the test series was similar to the bare surface sample preparations detailed in paragraph 5.3. The samples were polished down by 320 and 600 grit sandpapers respectively prior to the test and then washed using isopropanol solution and dried gently using an air gun.

5.4 Experimental design

Three different apparatus were adopted in this study to carry out the tests series:

- I. Flow loop
- II. High-pressure autoclave
- III. Three electrode glass cell

5.4.1 Flow loop design and testing procedure

The corrosion tests were carried out using the newly designed flow loop as explained in Chapter 4. The flow cell was designed to provide a realistic fluid flow simulating the flow dynamics in transport pipelines and to generate a range of flow from low to high flow shear stresses. The flow loop parts consist of a centrifugal pump, tank, a series of high-pressure high-temperature pipes and valves. The layout of the loop is shown in Figure 5-1. An insulated tank fitted with a temperature controller supplies the flow cell via a pump and flow meter monitor. The tank is fitted with facilities to allow CO₂ gas to be bubbled inside the tank prior and during the tests. The

temperature, pH and the pressure of the aqueous solution were monitored by using *in-situ* probes prior and throughout the test period.

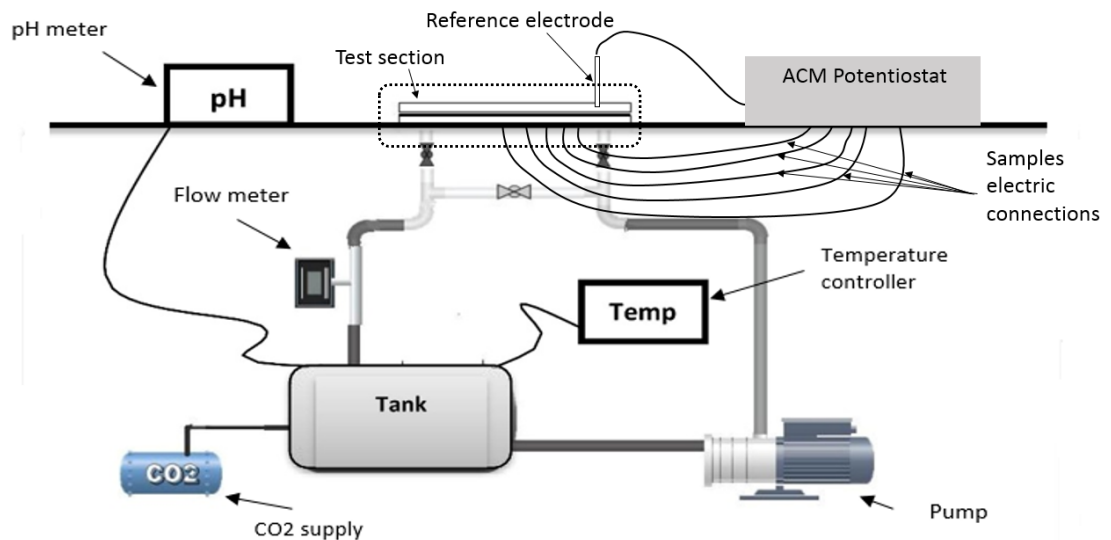


Figure 5-1. Flow loop layout and design

5.4.1.1 The tank

The tank is mainly used for water storage to ensure sufficient fluid supply to the pump to complete the flow loop by refilling the tank from the test section's outlet pipe. The tank capacity is 50L. The tank was made of 316L stainless steel alloy, the tank walls were electrically and thermally isolated from the rest of the flow loop parts to avoid and interference with the electrochemistry measurements. CO₂ gas pipes were attached to the tank via two points to ensure a sufficient and continuous CO₂ supply prior and during the tests, with a vent valve attached to the tank to keep the pressure inside at atmospheric pressure level. Electrical resistance heaters (316L stainless steel) are placed in the tank and immersed in the water. The level of water in the tank is continuously monitored to ensure constant aqueous solution properties and that the electrical heaters are properly covered with water.

5.4.1.2 The loop

The loop was made of a high-pressure high temperature and nonconductive hoses. It is 3 metres long and is thoroughly insulated from the ambient air in the laboratory.

The pipe diameters at the test section inlet and outlet are carefully selected to provide the targeted pressure and flow rate at certain velocities as described in Chapter 4.

5.4.1.3 The pump

The pump used for this research is a MXHL405/B horizontal centrifugal multistage pump. The wetted parts of the pumps are made from corrosion resistant alloys including chrome-nickel- molybdenum stainless steel AISI 316L. The flow rate generated by the pump was controlled via an Easymat 5MT discharge variable speed drive and SU7000 IFM flow meter. The pump operating temperature range was from -15°C to +110°C. The maximum permissible pressure in the pump is 8 bar.

5.4.1.4 The test section

The test section consists of three layers; the base, the middle and the top part. These parts are fitted together using 30 M5 bolts as shown in Figure 5-2. The middle part of the test section was designed to be varied in thicknesses as gasket thickness; 15mm, 6mm, 3mm and 2mm, consequently allowed a wide range of flow velocities and thus different flow shear stresses could be tested. In addition, the flow velocities and wall shear stresses were also controlled via the flow rates of the pump.

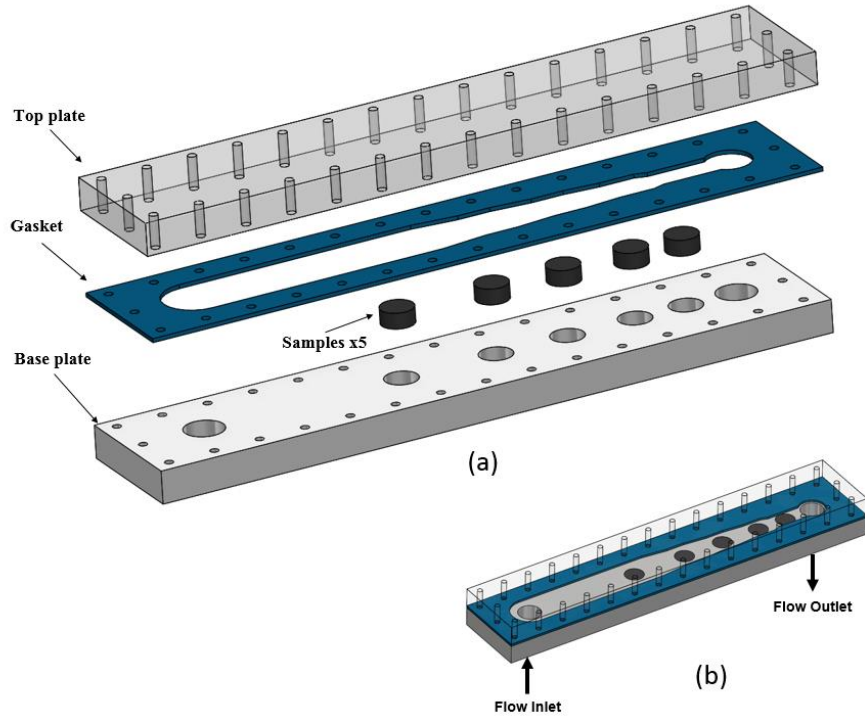


Figure 5-2. Test section 3D design: (a) Exploded view; (b) Assembled view

The width of the flow cell reduces gradually across the samples, starting at the first sample with 50mm width and decreases down to 25mm at the fifth sample, the flow velocity at the fifth sample is always double of the velocity at the first as shown in Figure 5-3.

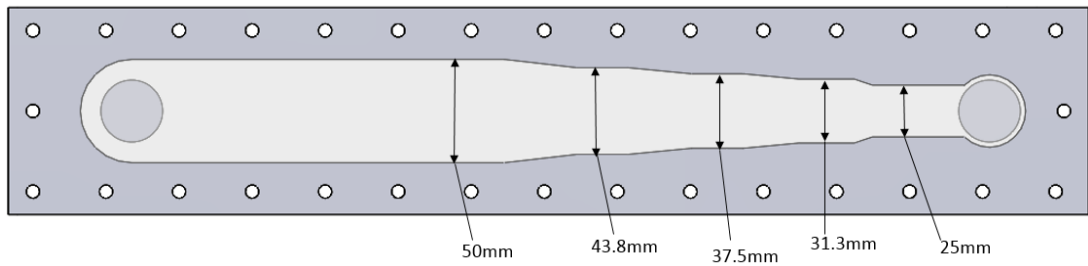


Figure 5-3. Top view of flow of flow cell & width details cross the samples

Therefore, the desired flow velocity and wall shear stress were generated by using a combination of two variables; test section geometry and the flow rates. Table 5-2 shows the sequence of the tests with the details of the test section geometry and the flow rate at each test.

Table 5-2. Tests sequence: Gasket thickness (test section height) and flow rates

Tests Sequence.	Gasket thickness	Flow rate
	mm	l/min
1 st test	15	34.0
2 nd test	6	32.5
3 rd test	3	29.5
4 th test	2	41.5

By using four different gaskets thicknesses it was possible to generate a range of wall shear stresses 1.2 to 410 Pa (calculated using empirical equations as detailed in the following paragraph 4.2) resulting from the gradient increase of the flow velocity from 0.75 to 13.75 m/s. At each test carried out using a specific flow rate and gasket thickness, the five mounted samples on the flow cell were exposed to an accumulated wall shear stress starting on the 1st sample and stepping up in value on each sample up to the 5th sample. The value of this shear stress is a function of the flow cell height (gasket thickness), the width of the channel cross the samples, the flow rate through the flow loop, and the solution temperature.

The X65 carbon steel coupons are fitted on the base part by bolts, to ensure stability during the experiments; a coupons fitting system was designed to avoid any sharp edges that could affect the fluid flow characteristic over/around the coupons. This occurs if the top surfaces of the steel samples are fitted higher or lower than the base part surface of the test section.

The design of the flow cell provided an opportunity to study the effect of flow shear stress on X65 steel corrosion rate. In addition, establishing an understanding of how the other flow parameters such as Reynold`s numbers, mass transfer coefficient and diffusion may govern the influence of wall shear stress on the corrosion behaviour of X65 carbon steel is a principal objective of the study.

5.4.1.5 The electrolyte solution

Deionised water containing 3wt% NaCl (Lab grade Sodium Chloride 99.9% pure) was used as the electrolyte. The solution was deoxygenated by purging with CO₂ gas for an overnight period prior to the electrochemistry test in order to reach minimum oxygen levels in the electrolyte (below 10 ppb) the oxygen levels were monitored prior and after each test using Hannah Portable Dissolved Oxygen meter,

simultaneously, bubbling the solution with CO₂ was continued during the tests. The concentration of the carbonic acid and CO_{2(aq)} in the solution reached and stabilised on 10⁻⁴ and 10^{-2.15} mol/l respectively at conditions of 1 bar of CO₂ partial pressure [59]. Sodium bicarbonate NaHCO₃ was added to the water to adjust the pH to the desired level. Solution temperature and pH were monitored throughout the test period.

5.4.1.6 The electrochemical measurement

The electrochemistry measurements were carried out using a saturated Ag/AgCl electrode was used as reference electrode. For the counter electrode, Platinum wires were custom designed and mounted next to the working electrodes in a way to maintain stable and accurate LPR readings at minimum solution resistance. The LPR technique was employed to monitor the corrosion rates using ACM 12 Gill potentiostat. The start potential of the LPR test was -15mV in the cathodic direction from the open circuit potential and the potential was +15mV to the open circuit potential. The sweeping rate was 10mV per minute. For the purpose of the potentiodynamic sweeps, the samples were subject to a cathodic sweep rate from 15mV to -500mV of the open circuit potential OCP with a scanning rate of 10mV per minute. The AC impedance technique was used to measure the solution resistance under flowing conditions prior to the corrosion rate test. The measurements are carried out over a wide frequency range (100 kHz to 0.01 Hz).

5.4.1.7 High-pressure autoclave test procedure

A high-pressure autoclave system was used to produce protective films. Figure 5-4 shows the layout and the schematic of the autoclave setup. The autoclave design consists of an autoclave container with a capacity of one litre, a series of high-pressure pipes and valves control the CO₂ supply to/from the autoclave, a pressure gauge to monitor the pressure inside the system throughout the test period and temperature controller. Distilled water was purged with CO₂ for at least 12 hours, to ensure a full de-aerated solution and CO₂ saturated solution prior to the formation test.

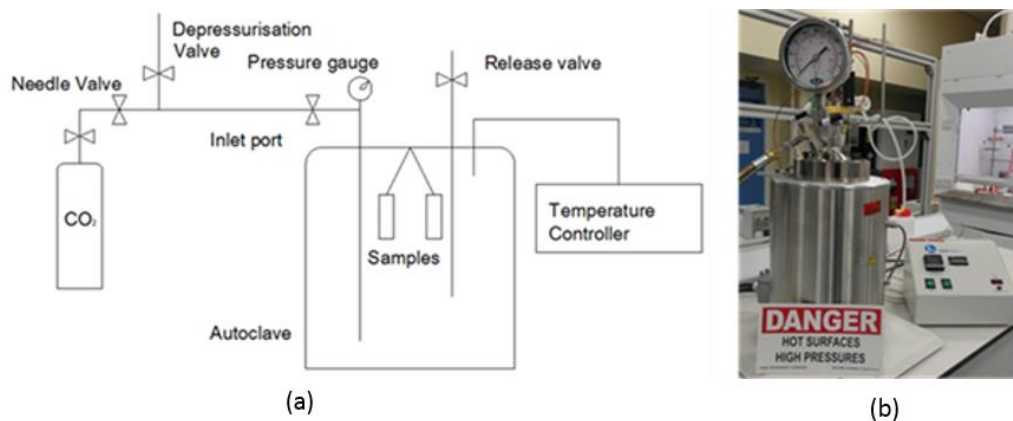


Figure 5-4. (a) Schematic of the autoclave & (b) photo of high-pressure autoclaves setup.

Samples were placed in the autoclave using a samples holder made of PTFE plastic to insulate the samples from the autoclave walls to prevent any possible galvanic effect. The aqueous CO₂ solution was placed inside the autoclave at atmospheric pressure and temperature then the autoclave was sealed. To remove any trace of oxygen inside the system, CO₂ gas was passed through the system pipes and valves. Then the autoclave was pressured with CO₂ gas and heated to the correct pressure and temperature. The system reached the desired pressure and temperature after ~30 min. The formation test was carried out under static conditions. The pH inside the autoclave was calculated using software MultiScale 7.1 package [210, 211] and it was predicted to be ~ 3.2. The measured pH inside the autoclave using a high-pressure pH probe is between ~3.35.

5.4.1.8 Mass loss testing procedure

The sample preparation process for the protective films formation tests is similar to the samples preparation procedure mentioned in section 5.3. During the first five tests, mass loss measurement was used to monitor the formation of the protective films as a function of time. At the end of each test, samples were dried gently using an air gun followed by weight measurement and the removal of the corrosion product using Clark's solution which was prepared based on ASTM Standard G1-03 [212] consisting of 20 g antimony trioxide, 50 g stannous chloride and 1000 ml hydrochloric acid. Subsequently, the samples were rinsed using distilled water and followed by ethanol and dried again with the air gun.

$$CR = \frac{87600\Delta m}{\rho At} \quad 4.1$$

Corrosion rates were measured using weight loss method using Equation 4.1 [213] where CR is the corrosion rate in mm/y, Δm is the weight loss (the difference in the measured mass of the samples prior and after the test), ρ is density of the carbon steel in g/cm^3 , A is the surface area exposed to corrosion in cm^2 and t is the test duration in hours. For more accuracy, each test was repeated at least three times.

5.4.2 Static conditions test procedure

A three-electrode glass cell was used to examine the corrosion rate of the protected carbon steel surface under static conditions. The sample preparation process consists of mounting the samples in a nonconductive resin. The samples were placed carefully into the resin (standard nonconductive) to avoid any contamination to the protective iron carbonate films. 1 litre of distilled water was purged with CO_2 gas for at least 2 hrs prior to the test to ensure a minimum oxygen content in the water, the pH was adjusted to the desired level by adding a sodium bicarbonate NaHCO_3 to the solution. The temperature and the pH level were monitored throughout the test period.

5.4.3 Electrochemical measurements under static conditions

For the electrochemistry measurements, a saturated Ag/AgCl electrode was used as a reference electrode. The LPR technique was employed to monitor the corrosion rates using multi-channel ACM 12 Gill potentiostat. The start potential of the LPR test is -15mV of the open circuit potential and the stop potential is +15mV from the open circuit potential, with sweeping rate 10mV per minute. The test duration is 24 hrs and after that, the samples were taken out, rinsed with distilled water and isopropyl alcohol and gently dried with an air gun and stored in a vacuumed desiccator for further surface analysis.

5.5 Surface analysis

The topography and morphology of the corrosion product surfaces were analysed using a combination of the Scanning Electron Microscopy (SEM), Energy-Dispersive X-ray spectroscopy (EDX), X-ray Diffraction (XRD) and the surface roughness of the

corrosion products were measured using a non-contact method by white light interferometry.

5.5.1 Scanning Electron Microscopy (SEM) & Energy Dispersive X-ray (EDX)

Scanning Electron Microscopy (SEM) was used to analyse the surface morphology of the protective films on the carbon steel surface at different exposure time. The elemental composition of the corrosion products on the surface was identified and quantified using Energy Dispersive X-ray (EDX). Two units of SEM were used in this study:

- I. Carl Zeiss EVO MA15 SEM Figure 5-5(a)
- II. and Hitachi TM3030 Bench Top SEM Figure 5-5(b)

Carl Zeiss EVO MA15 was used when high-resolution SEM images and EDX analysis was required. The analysis was carried out at an accelerating voltage 20 KV (the voltage difference between the anode and the filament, which accelerates the electrons beam toward the anode). The working distance was 8mm. All other SEM surface analysis and images on the protected surface were obtained using Hitachi TM3030 Bench Top SEM.



(a)



(b)

Figure 5-5. Image of (a) Carl Zeiss EVO MA15 SEM & (b) TM3030 Bench Top SEM

EDX analysis was used to characterise the elemental components of the corrosion product, and to identify the distribution of the elements of the corrosion product across the sample surface as shown in Figure 5-6.

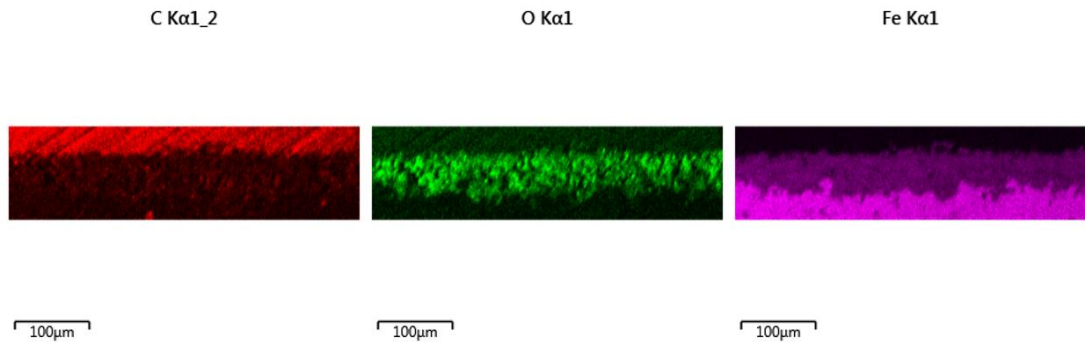


Figure 5-6. Examples of EDX mapping on the cross-section of the corrosion product on the X65 carbon steel surface exposed to the CO₂ environment.

5.5.2 X-ray Diffraction (XRD)

The XRD spectra on the corrosion product surface detected using PANalytical X'pert multi-purpose diffractometer (MPD). The active area was 10 mm x 10 mm programmable divergence slits. Using Cu K α radiation, the scans were carried out over a range of $2\theta = 20$ to 80° with a step size of 0.033 per second. The total scan time is ~50 minutes.

5.5.3 Surface roughness

The surface roughness of the protective films was measured by a non-contact method using NP-FLEX 3D optical microscopy based on white light interferometry. For each sample, three zones were chosen randomly on the surface, each area was 10mm x 10mm. The resolution used 2.5X with a 5mm working distance. Samples surface were first cleaned by distilled water and followed by ethanol and dried again with the air gun prior to the surface roughness measurement.

5.1 Summary

In this chapter, the experimental procedure, the electrochemistry measurement, and the surface analysis methods which are used to study the corrosion behaviour of the X65 carbon steel in the CO₂ saturated environment were described at different conditions. The surface analysis techniques used to **examine the protective film morphology and the topography of the protected surface** of the X65 carbon steel are detailed. Figure 5-7 outlines the structure of the experiments throughout the project.

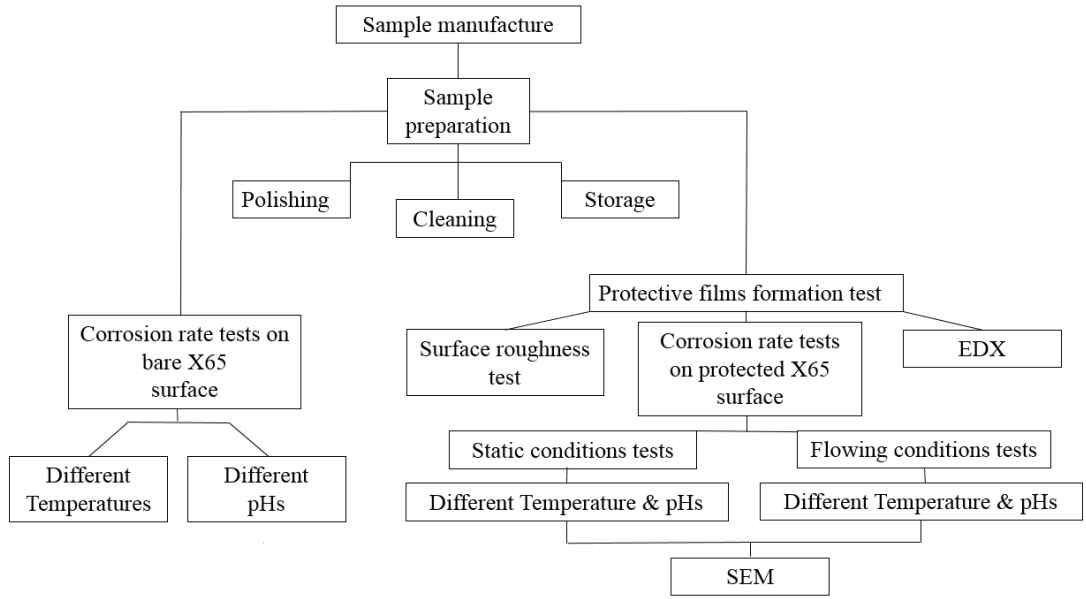


Figure 5-7. Procedures of experimental structure.

Chapter 6. Results of X65 carbon steel bare surface under flowing conditions at pH 6.6

6.1 Introduction

Having an understanding of corrosion mechanisms in oil/gas pipelines is key for material selection, designing and maintenance planning in transmission lines used in the oil and gas industry. A large amount of research has been evidenced in literature to investigate the corrosion behaviour in the oil/gas industry under a wide range of simulated field conditions. These studies were not necessarily conducted under conditions that simulate realistic flow conditions. In this chapter, the outcome of the corrosion rate tests of the bare surface of the X65 carbon steel under flowing conditions at pH 6.6 and temperatures of 50°C and 80°C are presented. The correlation between the shear stress profile and the corrosion rate is presented at a fixed pH level of 6.6. The aim of these experiments is to highlight the importance of considering flow parameters, geometry, solution, and sample conditions when assessing the behaviour of X65 using electrochemical tests.

6.2 Test matrix

Table 6-1 details the test matrix of the unprotected X65 carbon steel surface subject to flowing conditions at pH 6.6

Table 6-1. Test matrix of the corrosion tests at pH 6.6

Solution	pH 6.6	
Temperature °C	50	80
Time (hrs)	Up to 10	
Range of flow velocity (m/s)	0.7 to 13.75	
Range of wall shear stress (Pa)	1.35 to 410	
Solution	3 wt. % NaCl	
Electrochemistry measurement	LPR	

For each test, the electrochemistry measurement continued until the corrosion rates were stabilised, then the test was terminated to ensure the accuracy of the corrosion rate reading. Therefore the duration of the test varied up to 10 hrs depending on the test conditions.

6.3 X65 carbon steel corrosion behaviour under flowing conditions at 50°C and pH 6.6

Prior to the corrosion behaviour tests under flowing conditions, the conductivity of the solution was tested to ensure an accurate corrosion rate reading. The resistance of the solution was examined using the Electrochemical Impedance Spectroscopy (EIS) technique, in order to measure the value of the additional resistance applied by the solution. This value is added as compensated resistance to the polarisation resistance during the corrosion rate in LPR measurements. Initially, two sample positions were selected; the first sample and the fifth sample. If the difference of the solution resistance between these two samples was significant then another test would be carried out to measure the solution resistance on the other three samples. The EIS test carried over a range of frequencies from ~100,000 – 0.01 Hz under temperature 50°C, pH 6.6 and 3% NaCl solution.

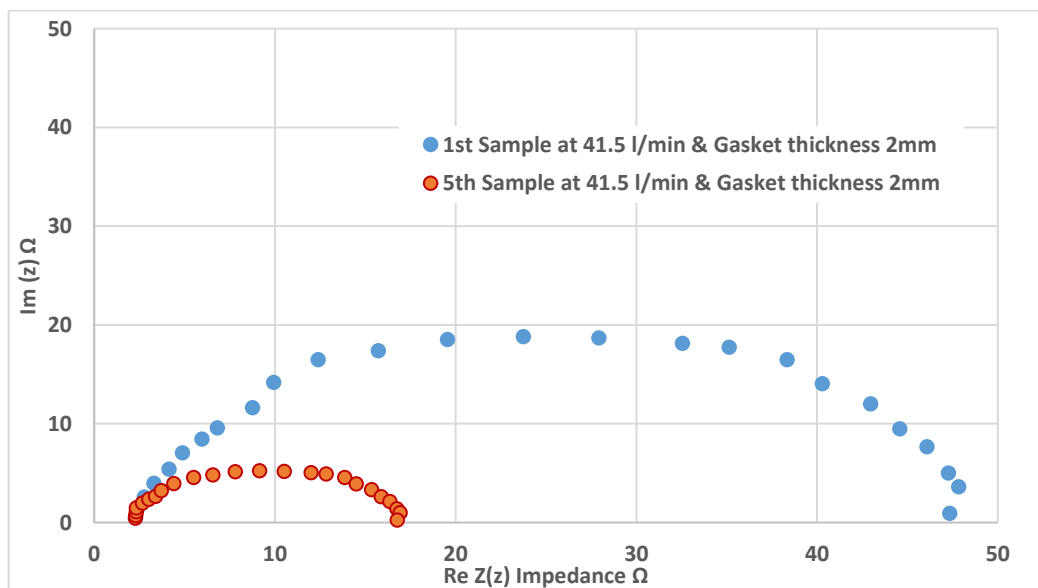


Figure 6-1. Electrochemical impedance spectroscopy (EIS) graph of the solution resistance at the first & fifth samples under 50°C, pH 6.6 and 3% NaCl solution

Each sample surface area is 4.9 cm². Figure 6-1 illustrates the outcome of the EIS test, where it shows the solution resistance at both the first and fifth samples are 3 Ohms for the 4.9cm², it means a ~0.60-0.65 Ohms per cm² respectively, which is low resistance and indicates that the solution resistance values at the other three samples will be similar to this range.

6.3.1 Corrosion rate as a function of time at temperature 50°C and pH 6.6

A series of four tests were carried out to examine the corrosion behaviour of X65 carbon steel as a function of time under flowing conditions. Each test was conducted using a specific flow rate and gasket thickness (flow cell height) as shown in Table 5-2 and Table 6-2.

Table 6-2. Cross section dimensions at each sample in the flow direction (flow cell height × channel width). The wall shear stress generated at each sample **calculated using empirical equations** at temperature 50°C and pH 6.6.

Sample number.	Channel Width (mm)	Wall shear stress on sample			
		1 st test	2 nd test	3 rd test	4 th test
		Gasket thickness: 15mm Flow rate: 34 l/min	Gasket thickness: 6mm Flow rate: 32.5 l/min	Gasket thickness: 3mm Flow rate: 29.5 l/min	Gasket thickness: 2mm Flow rate: 41.5 l/min
1	50.0	1.60 Pa	9.0 Pa	30.0 Pa	120 Pa
2	43.8	2.00 Pa	11.0 Pa	37.5 Pa	152 Pa
3	37.5	2.7 Pa	15.0 Pa	50.0 Pa	200 Pa
4	31.3	3.75 Pa	20.5 Pa	67.0 Pa	275 Pa
5	25.0	5.66 Pa	30 Pa	100 Pa	410 Pa

To generate a range of wall shear stress 1.6 to 410 Pa across the five samples throughout the four tests, the wall shear stress was calculated using equation 4.4. Therefore, the plots of corrosion rate as a function of wall shear stress and time were divided into four graphs. This allows the effects of flow parameters such as the flow turbulence, the geometry of the flow cell and the mass diffusion rate on the corrosion behaviour to be examined.

The flow parameters across the sample surfaces were calculated using the empirical correlation equations 4.1 to 4.8 listed in paragraph 4.2. The calculated wall shear stress values across each sample are detailed in Table 6-2. The calculation details are illustrated in Appendix A. In addition, a CFD simulation was carried out to identify the profile of the flow and the distribution of the parameters across the test section as shown in Figure 4-6.

The model was built as test section thickness of 2 mm and a flow rate 41.5 l/min with inlet flow velocity 3.25 m/s, which is similar to the 4th test conditions shown in Table 6-2. The viscosity and density of the water were selected based on 3% NaCl water properties at 50°C [214]. The wall shear stress distribution across the test section surface (gradually increased from the position of the 1st sample to the 5th) as shown in Figure 6-2. The empirical calculations of the flow parameters showed good agreement with the CFD simulation outcome as shown in Table 6-3.

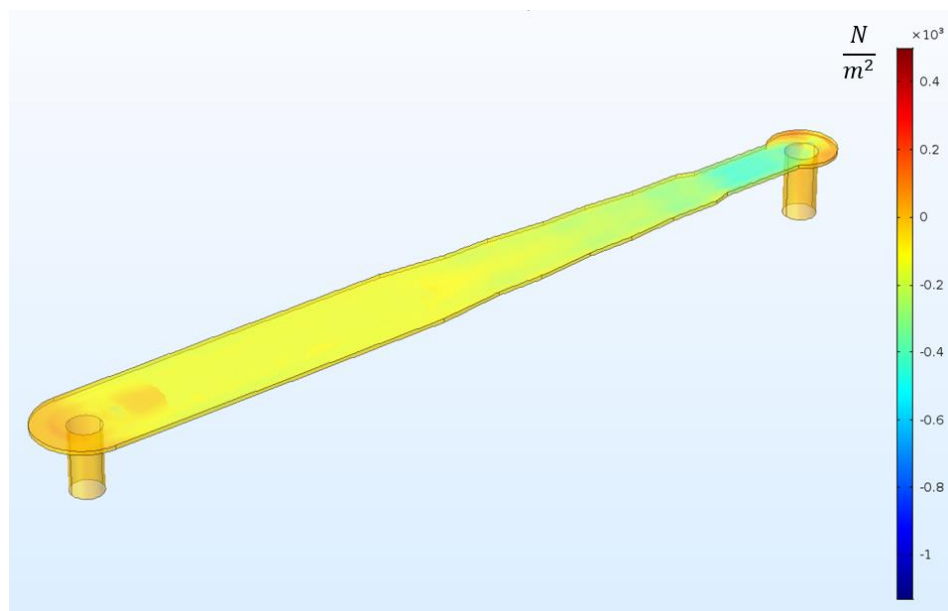


Figure 6-2. CFD simulation of the wall shear stress distribution across the test section at inlet velocity 3.27 m/s and gasket thickness 2mm.

Table 6-3. A comparison between the wall shear stress calculated from empirical and numerical calculations

Sample number	Empirical correlation calculations equation 4.4 (Shear stress Pa)	Numerical simulation results (Shear stress Pa)
1	120	125
2	152	160
3	200	205
4	275	285
5	410	425

Figure 6-3 shows the corrosion behaviour of the X65 carbon steel under flowing conditions as a function of time for a test duration 10 hrs. The tests are carried out under wall shear stress range values from 1.6 to 5.66 Pa. The total surface area of the five samples was $(4.9 \times 5) \text{ cm}^2$ subjected to a water volume of 50 litres contained within the flow loop.

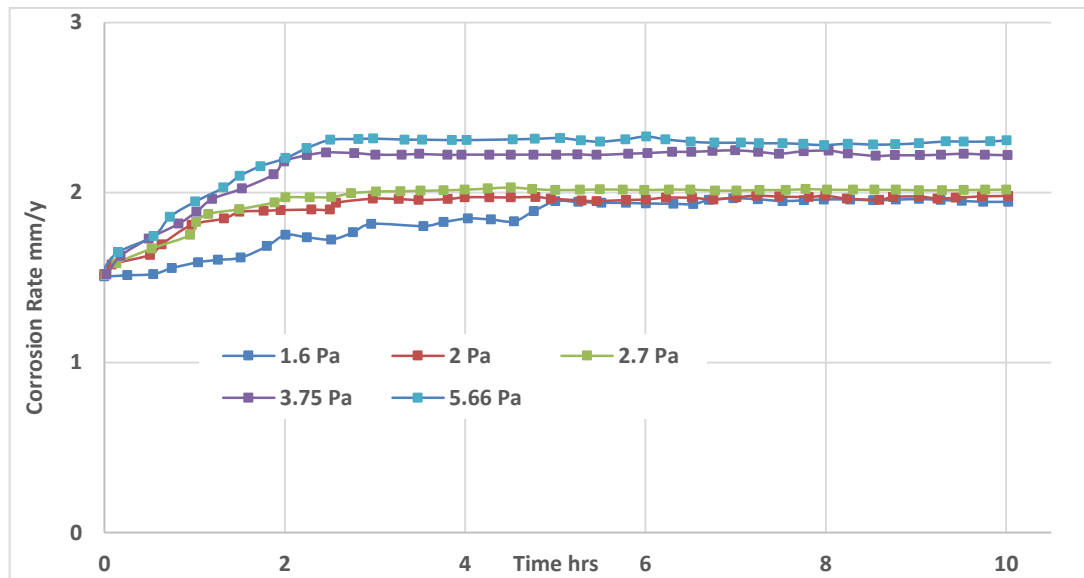


Figure 6-3. Corrosion rate as a function of time under wall shear stress range of 1.6 to 5.66 Pa at temperature 50°C and pH 6.6. Using flow rate 34 l/min and gasket thickness 15mm

The starting value of the corrosion rate was similar in all cases. For all tests, the corrosion rates increased with time and stabilised to steady-state values. In general, as the shear stress increases, the time required to reach the plateau decreases, **since the**

corrosion rate increased with the shear stress, this indicates that the corrosion behaviour is under at least some aspect of a mass diffusion-controlled process.

The corrosion rate at 1.6 Pa increased with time and stabilised after 5 hrs. At 2 and 2.7 Pa, the corrosion rates at both shears stress stabilised after ~3 hrs. However, at high wall shear stresses 3.75 and 5.66 Pa corrosion rate increased up to steady state rate within 2.5 hrs and stayed on that level until the end of both tests.

Figure 6-4 showed the overall shape of the same data for the range of shear stress values of 9 to 30 Pa. The initial corrosion rate at all cases was ~ 2.15 mm/y, which increased with time up to the plateau. However, the final corrosion rate was a function of the applied wall shear stress. At shear stresses 9 to 20.5 Pa corrosion rates increased with time to steady corrosion rates within ~2 hrs. However, the corrosion rate under 30 Pa showed different behaviour, where it took only ~1 hr to reach the steady-state rate.

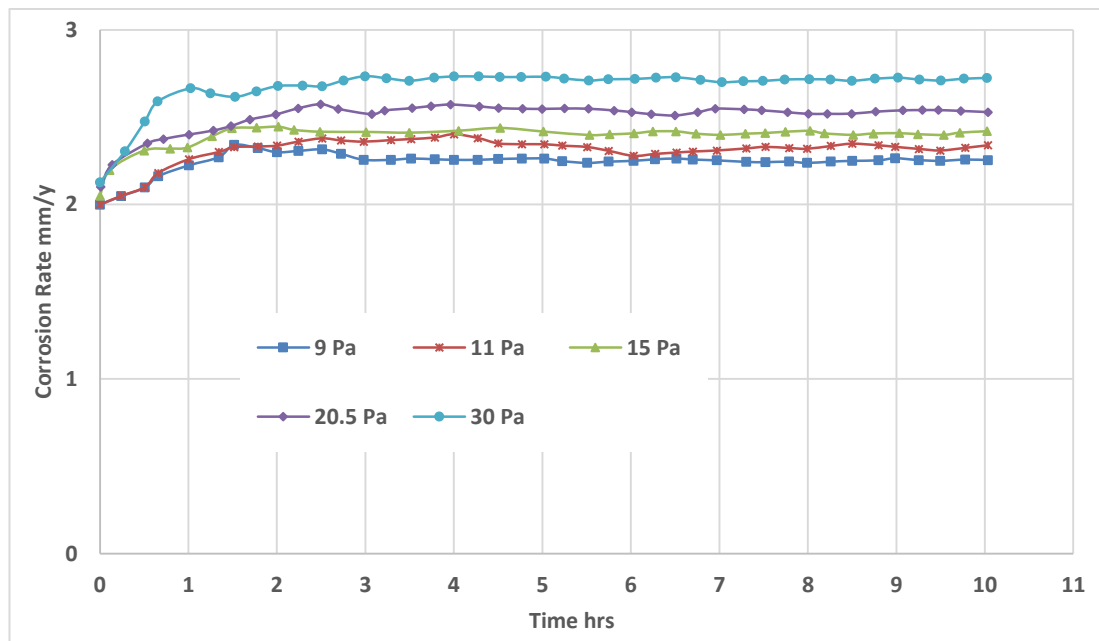


Figure 6-4. Corrosion rate as a function of time under wall shear stress range of 9 to 30 Pa at temperature 50°C and pH 6.6. Using 32.5 l/min flow rate and 6mm gasket thickness

Figure 6-5 shows the corrosion rate of X65 carbon steel surface for higher levels of wall shear stresses of 30, 37.5, 50, 67 and 100 Pa on each of the five samples respectively. The initial corrosion rate under 30 to 67 Pa shear stress was ~2.1 mm/y. However, at 100 Pa the initial corrosion rate was ~2.5 mm/y. The time to reach a

plateau (at which the charge transfer rate between the surface and the solution reaches a steady state condition with the mass transfer rate of the cathodic species) was ~30 minutes lower than the previous test, therefore all tests duration was limited to 5 hrs.

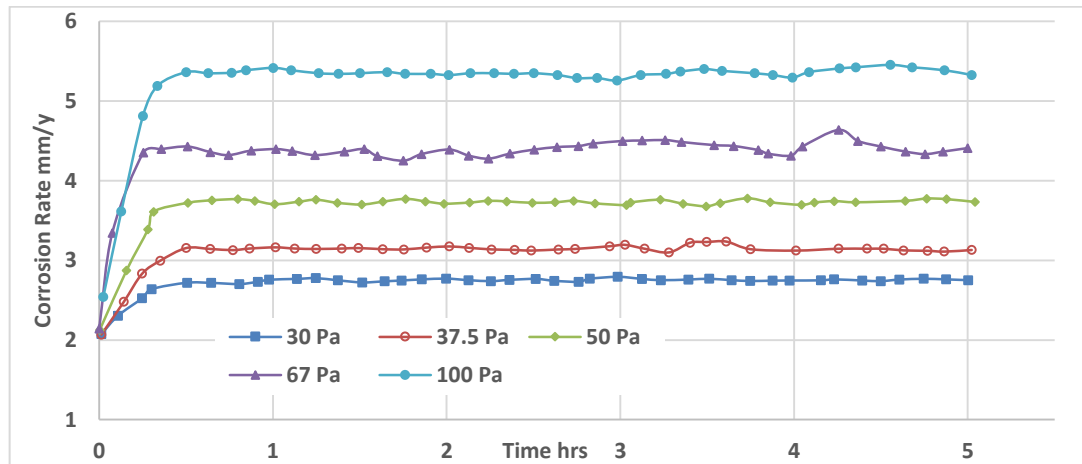


Figure 6-5. Corrosion rate as function of time under wall shear stress range of 30 to 100 Pa at temperature 50°C and pH 6.6

Figure 6-6 illustrates shows the same data for 120 to 410 Pa. The corrosion behaviour of the five samples was similar. However, for shear stress 120 Pa, the initial corrosion rate increased during the first 30 minutes and stabilised to the end of the test. Similar behaviour at shear stress 152, 200 and 275 Pa. This behaviour becomes more significant at the higher wall shear stresses, at 410 Pa corrosion rate increased to steady state value within ~30 minutes of the starting point.

A dependence of corrosion rate on the flow at $\text{pH} \geq 6$ was also observed by Nestic et al [40] who carried out several corrosion tests on carbon steel in CO_2 saturated solutions using RCE and flow loop rigs at a temperature of 20°C.

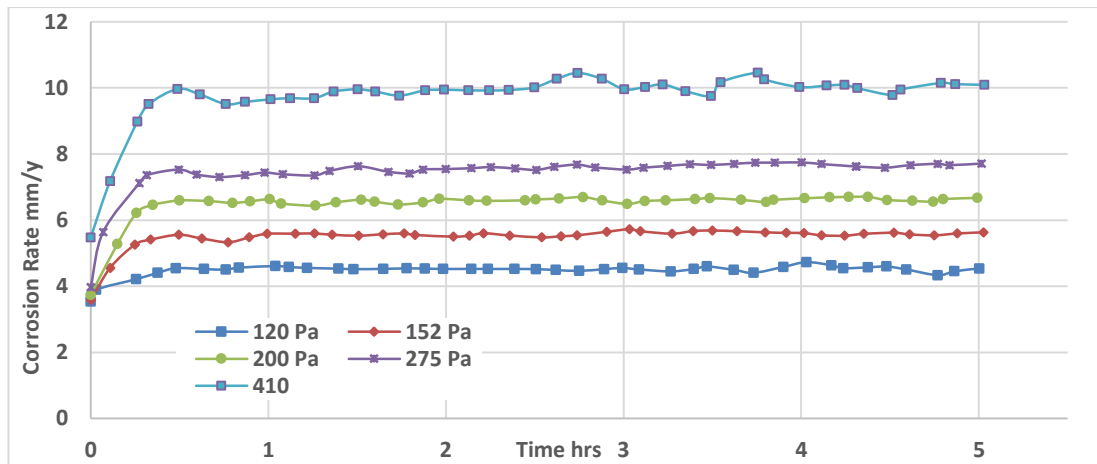


Figure 6-6. Corrosion rate as function of time under wall shear stress range of 120 to 410 Pa at temperature 50°C and pH 6.6

6.3.2 Corrosion rate as a function of flow at 50°C and pH 6.6

Corrosion rate as a function of the wall shear stress at 50°C and pH 6.6 is plotted in Figure 6-7. The data in Figure 6-7 and Figure 6-8 represent the equilibrium values of corrosion reached (steady state values) after the initial corrosion rate increased as a function of time. All the tests were repeated three times and each test was carried out using polished samples prior to the test and new purged CO₂ water. The flow cell design generates an increase in the wall shear stress by 3 fold between the 1st and the 5th sample. From the shape of the curve, it can be seen that corrosion rates showed a clear flow sensitivity and were generally linear with shear stress. Corrosion behaviour as a function of Reynold`s number was more complicated as shown in Figure 6-8. Notwithstanding that Reynold`s numbers on the five samples at this test (red curve) are roughly the same as its values on the five samples subject to 30 to 100 Pa (green curve), the flow sensitivity of the corrosion rate varied between the two curves. Which indicated the participant of another parameter controls the corrosion behaviour other than the flow turbulence and the shear stress. This will be discussed in detail in Chapter 10.

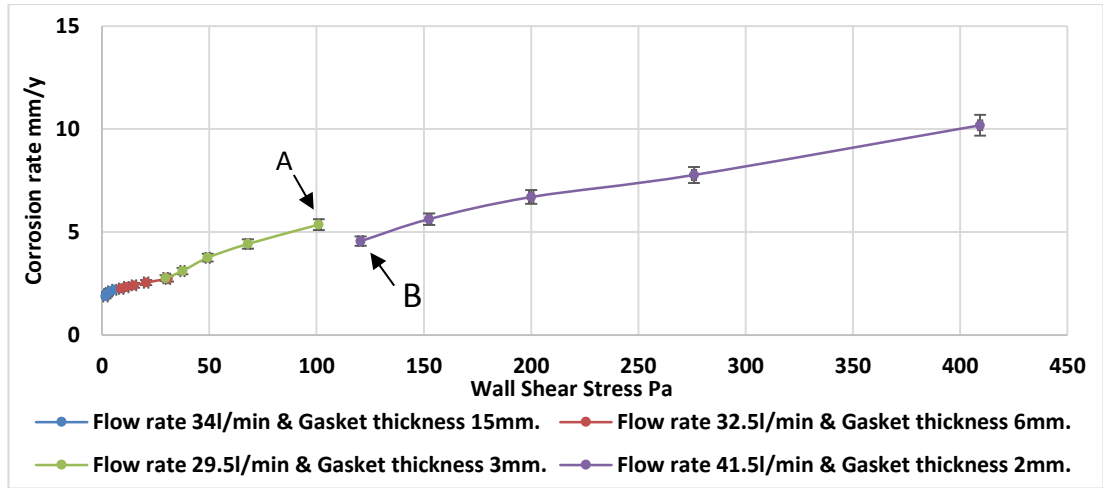


Figure 6-7. Corrosion rate as a function of shear stress – pH 6.6, 50°C and 3% NaCl.

An interesting behaviour is observed at points A & B shown in Figure 6-7 “A” represents the 5th sample mounted on the flow cell and “B” is the 1st sample mounted on the flow cell of the tests that are detailed in Table 6-2. The samples are exposed to a wall shear stresses values of 100 & 120 Pa respectively. Although point B is subjected to a higher wall shear stress than at point A, the corrosion rate at point A is slightly higher than B. From Sleicher and Rouse correlation (equation 4.6), the mass transfer coefficient of the cathodic species is a function of Reynold`s number. Therefore, to understand the diffusion behaviour these species, corrosion rate was plotted as a function of Reynold`s number as shown in Figure 6-8. Corrosion rate as a function of Reynold`s number curves indicates that the higher corrosion rate is associated with the higher flow turbulence (Reynold`s number) at point A than at B.

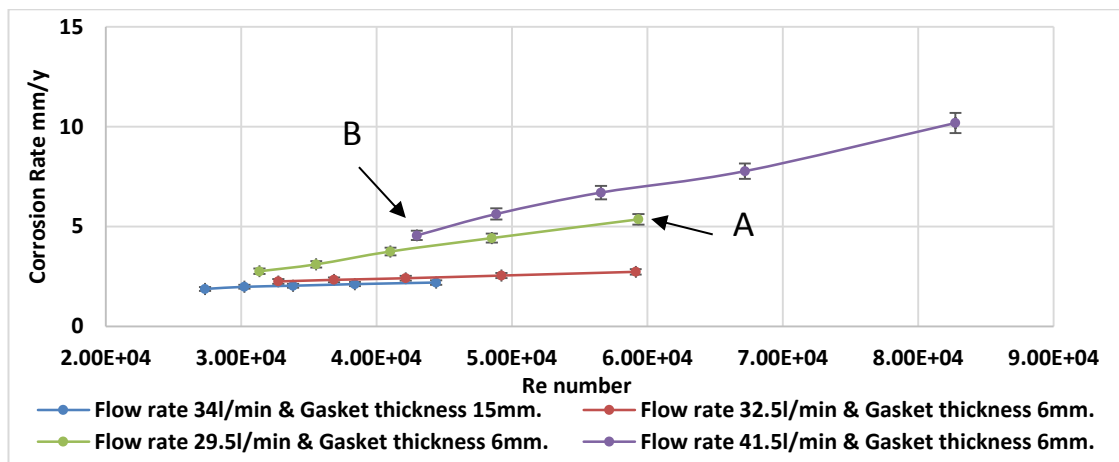


Figure 6-8. Corrosion rate as a function of Reynold`s number – pH 6.6, 50°C and 3% NaCl.

Corrosion rate was plotted versus the wall shear stress represented a function of $(v^{1.75} * D^{-0.25})$, where v is the flow velocity and D is the hydraulic diameter as shown in Figure 6-9. This function was derived by breaking down the wall shear stress (equation 4.4) to velocity and hydraulic diameter. More details are presented in Appendix B section. The overall shape of the curve was similar to the shape of the corrosion rate as a function of wall shear stress shown in Figure 6-7.

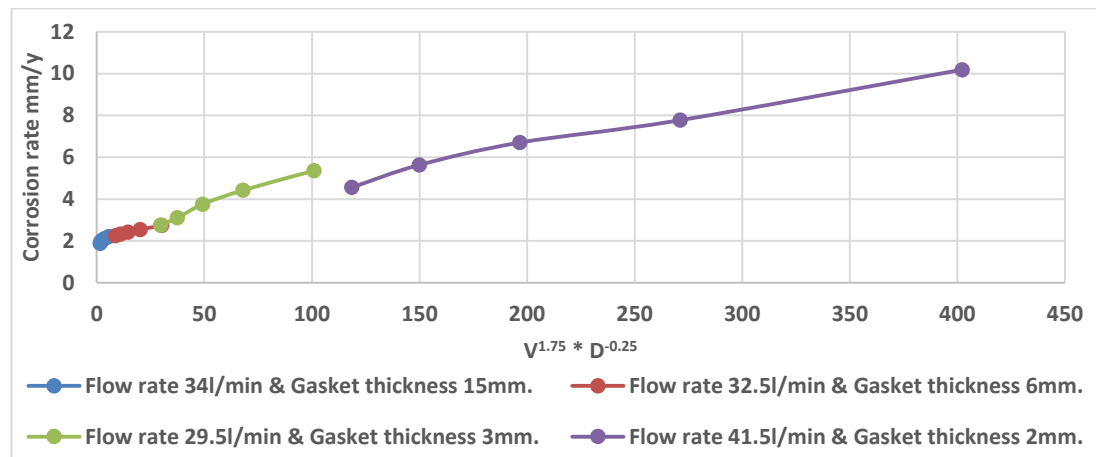


Figure 6-9. Corrosion rate as a function of $v^{1.75} * D^{-0.25}$ – pH 6.6, 50°C and 3% NaCl.

6.3.2.1 Cathodic polarisation curves under flowing conditions at pH 6.6 and temperature 50°C

Potentiodynamic sweeps were conducted at 50°C and pH 6.6 and at different wall shear stresses/flow velocities. The anodic branch showed no dependency on flowing conditions and had no significant effect on the corrosion behaviour; consequently only the cathodic sweep branches are shown. Figure 6-10 presents cathodic polarisation curve for the samples of points A and B in Figure 6-7, it shows that the cathodic current density at A is higher than at B, this indicates that the reduction rate of the cathodic species at point A is higher than at B. High reduction rate at point A agrees well with the corrosion rate measurement shown in Figure 6-7 which shows that corrosion rate at point A is higher than at B.

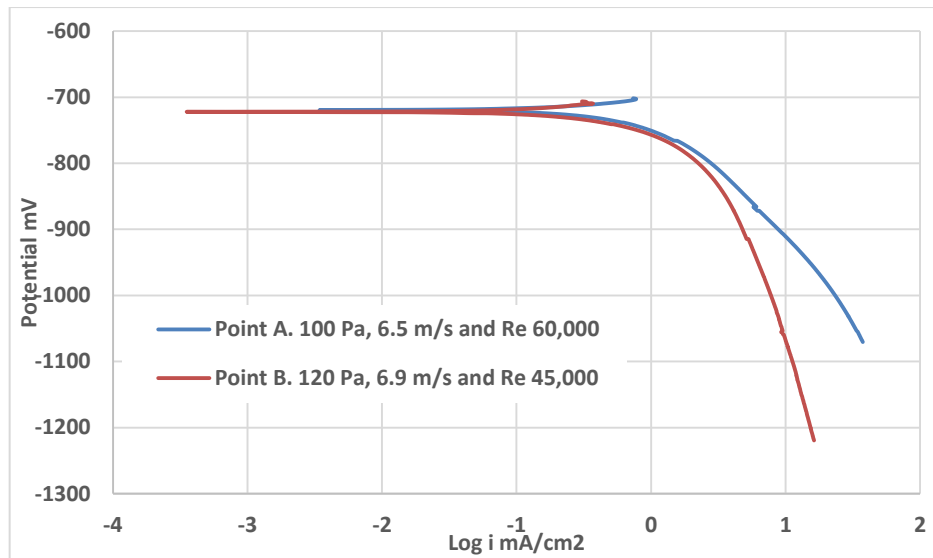


Figure 6-10. Cathodic sweep for points A & B at temperature 50°C, pH 6.6

Cathodic polarisation curves as a function of the shear stress are shown in Figure 6-11. The overall shape of the curves correlates to the corrosion behaviour presented in Figure 6-7. These curves will be discussed further in context of the controlling cathodic reaction in 10.2.1.

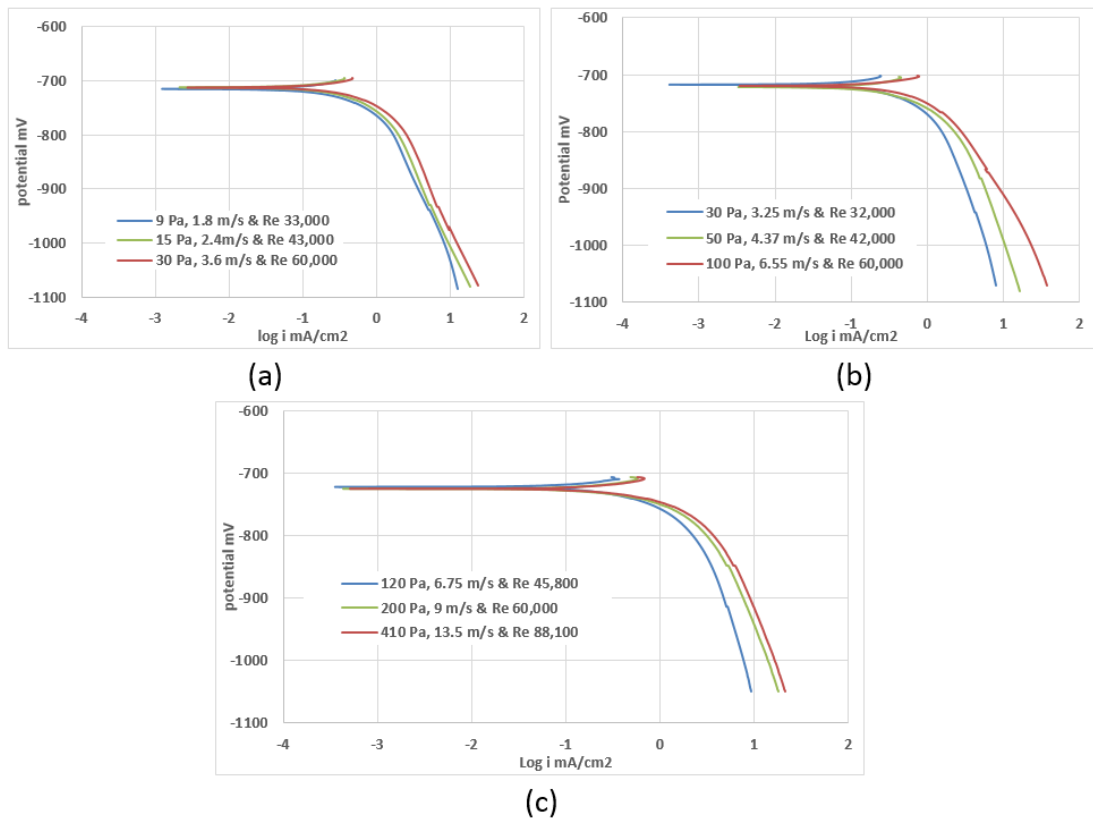


Figure 6-11. Cathodic sweeps carried out at temperature 50°C, pH 6.6 for wall shear stress/flow velocity: a- 1.35 to 4.75 Pa b- 7.65 to 25.5 Pa c-120 to 410 Pa.

6.4 X65 carbon steel corrosion behaviour under flowing conditions at 80°C and pH 6.6

6.4.1 Corrosion rate as a function of time at temperature 80°C and pH 6.6

The corrosion behaviour at pH 6.6 was investigated at a higher temperature of 80°C. Test results are divided into four plots for the same reasons previously explained in 6.3.1. The wall shear stress values and distribution across the samples are detailed in Table 6-4.

Corrosion rates as a function of time under flowing conditions are shown in Figure 6-12. A range of 1.35 to 4.75 Pa wall shear stress was generated across the five samples. The initial corrosion rates of the first three samples subjected to 1.35, 1.7 and 2.25 Pa were similar as shown in Figure 6-12.

Table 6-4. Cross section dimensions at every sample along the flow direction & Flow cell height (gasket thickness) and the calculated wall shear stress generated at each sample at temperature 80°C and pH 6.6.

Sample number.	Channel Width (mm)	Wall shear stress on sample			
		1 st test	2 nd test	3 rd test	4 th test
		Gasket thickness: 15mm Flow rate: 34 l/min	Gasket thickness: 6mm Flow rate: 32.5 l/min	Gasket thickness: 3mm Flow rate: 29.5 l/min	Gasket thickness: 2mm Flow rate: 41.5 l/min
1	50.0	1.35 Pa	7.65 Pa	25.5 Pa	100.0 Pa
2	43.8	1.70 Pa	9.75 Pa	32.3 Pa	127.0 Pa
3	37.5	2.25 Pa	12.75 Pa	42.4 Pa	166.4 Pa
4	31.3	3.1 Pa	17.75 Pa	58.5 Pa	230.0 Pa
5	25.0	4.75 Pa	25.5 Pa	87.0 Pa	340.0 Pa

However, within 1 hr, the corrosion rate of these samples increased as and stabilised at an approximately similar plateau for the next 4 hrs of exposure time. Under higher wall shear stress 3.1 and 4.75 Pa, corrosion rate stabilised after 1 hr and 30 minutes respectively. The variation in the time required to reach a steady state corrosion rate between 3.1 and 4.75 Pa indicating that corrosion rate at the later exhibited higher flow sensitivity than at the former values at this range of wall shear stress.

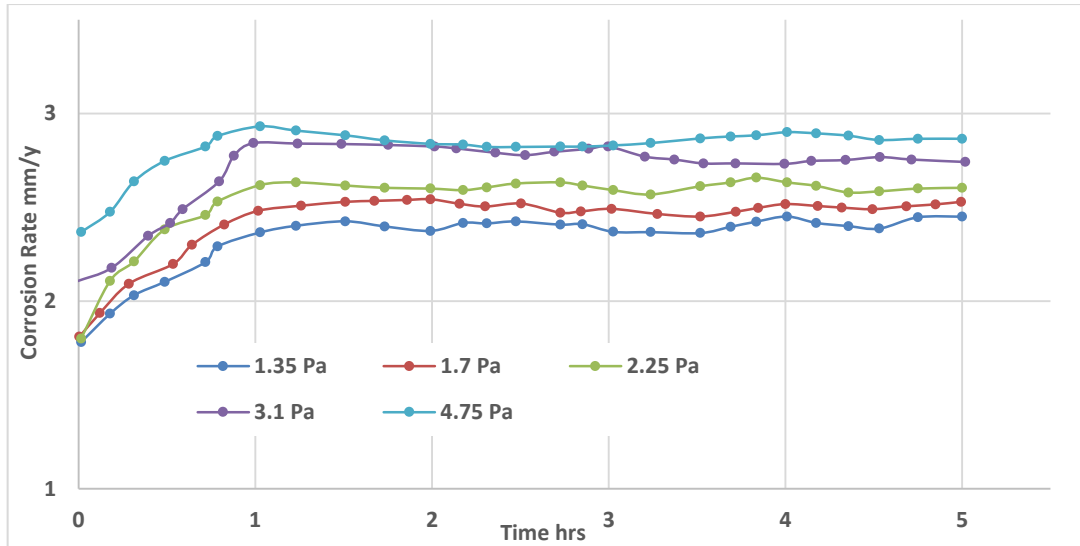


Figure 6-12. Corrosion rate as function of time under wall shear stress range of 1.35 to 4.75 Pa at temperature 80°C and pH 6.6

Corrosion behaviour of five X65 carbon steel subjected to higher shear stresses 7.65 to 26.5 Pa is shown in Figure 6-13. The overall shape of the curves of the first four samples at 7.65, 9.75, 12.75 and 17.75 Pa was similar, however, the initial corrosion rate of each sample was a function of the shear stress, and stabilised on steady-state rate after ~ 30 minutes of the starting point. At wall shear stress 26.5 Pa the corrosion behaviour was different, where the corrosion rate throughout the test duration was stable around the initial value to the end of the test. In general, corrosion behaviour at shear stress range of 7.65 to 26.5 Pa illustrated that the corrosion rates were a strong function of the applied flowing conditions.

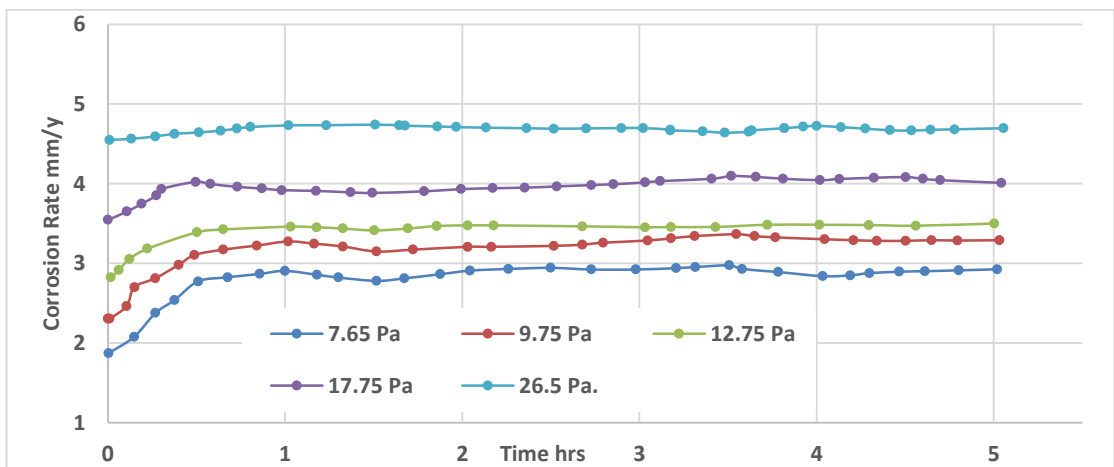


Figure 6-13. Corrosion rate as function of time under wall shear stress range of 7.65 to 26.5 Pa at temperature 80°C and pH 6.6

Figure 6-14 shows the corrosion behaviour in the shear stress range 25.5 to 87 Pa. The overall shape of the curves was similar, where no significant difference in corrosion behaviour was observed. The corrosion rate of all the five samples was at a steady state value throughout the test duration. Nevertheless, corrosion behaviour under wall shear stress 25.5 to 87 Pa was different than previous corrosion behaviours under lower ranges of wall shear stress, since the corrosion rates did not require a stabilisation period and were at a plateau from the starting point.

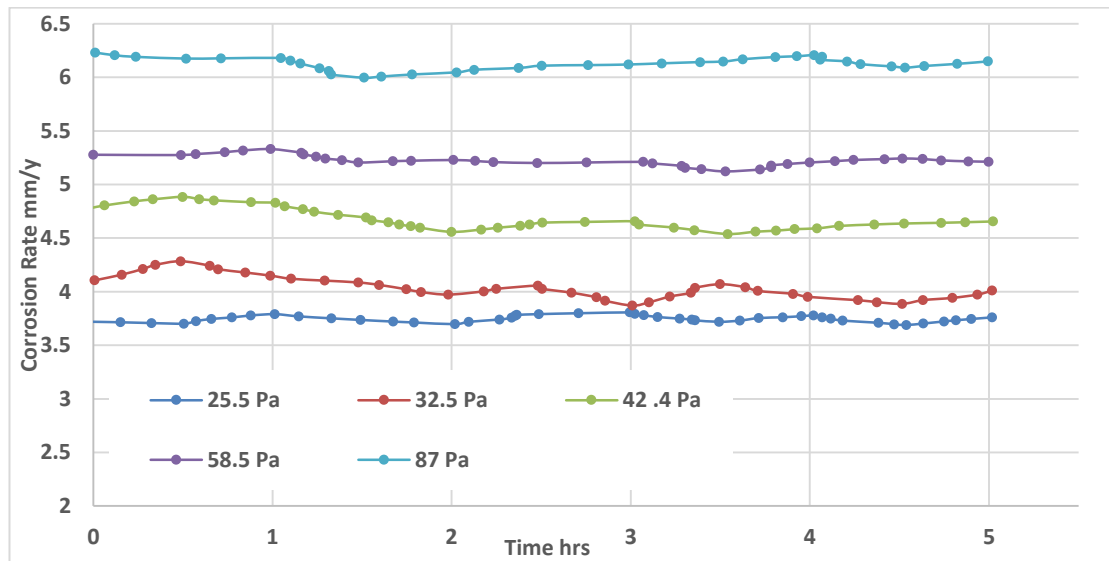


Figure 6-14. Corrosion rate as function of time under wall shear stress range of 25.5 to 87 Pa at temperature 80°C and pH 6.6

The outcome of tests at wall shear stress (7.65 to 26.5 Pa) and (25.5 to 87 Pa) as shown in Figure 6-13 and Figure 6-14 indicated, that at wall shear stress > 26 Pa, corrosion rate exhibited a steady state rate from the starting point, where no increase in corrosion rate above the initial value throughout the test duration.

Similar behaviour occurred at shear stress range 100 to 340 Pa as shown in Figure 6-14. Corrosion rate of the five samples was stable on plateau throughout the 5 hrs exposure to flowing condition with no increase in corrosion rate was recorded as shown in Figure 6-15.

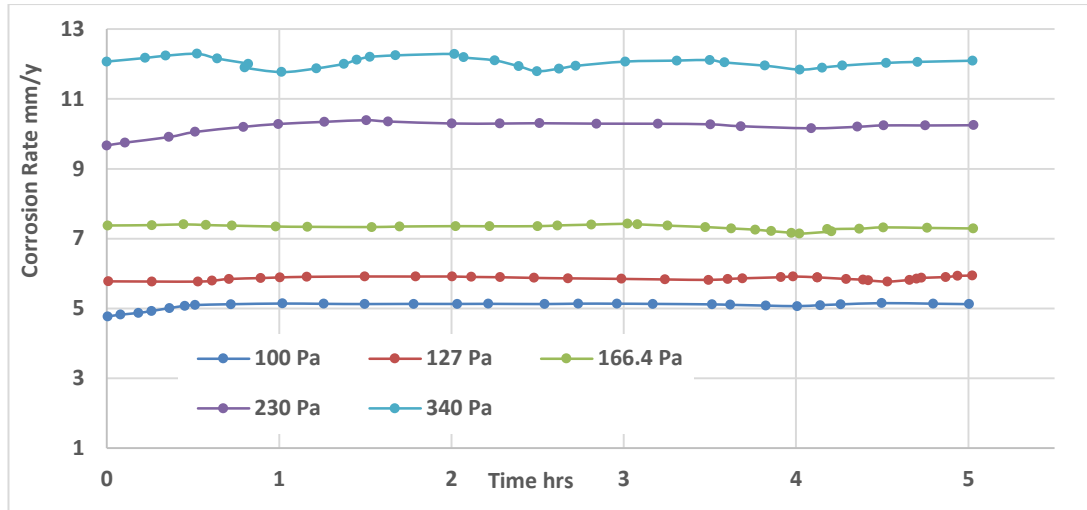


Figure 6-15. Corrosion rate as function of time under wall shear stress range of 100 to 340 Pa at temperature 80°C and pH 6.6

6.4.2 Corrosion rate as a function of flow at 80°C and pH 6.6

Corrosion behaviour of the X65 carbon steel surface was examined as a function of wall shear stress at 80°C. Different rates and channel dimensions were applied in order to investigate the effect of Reynold`s number on the corrosion behaviour. The flow parameters were calculated using Equations 5-1 to 5-10. Table 6-4 shows the outcome of the empirical calculations of the wall shear stress across the five mounted samples on the test section. Further details of the flow parameters calculations are listed in Appendix A.

Figure 6-16 shows the effect of wall shear stress on the corrosion rate at fixed pH 6.6 and 80°C. A gradual increase in wall shear stress of 1.35 to 340 Pa was generated on the X65 steel. Corrosion rate increased as function of the wall shear stress up to ~ 26 Pa, at this wall shear stress two different corrosion rates were recorded; 4.5 mm/y at point A which is the fifth sample on the test section represented as red curve, and 3.8 mm/y at point B represent the first sample of the test showed as green curve. Figure 6-17 illustrates the relationship between the corrosion rate and Reynold`s number across the five samples at each test as detailed in Table 6-4. From the curves Reynold`s number at points A ~89,500 and at point B ~ 47,500 this shows that the turbulence level at point A is significantly higher than at point B.

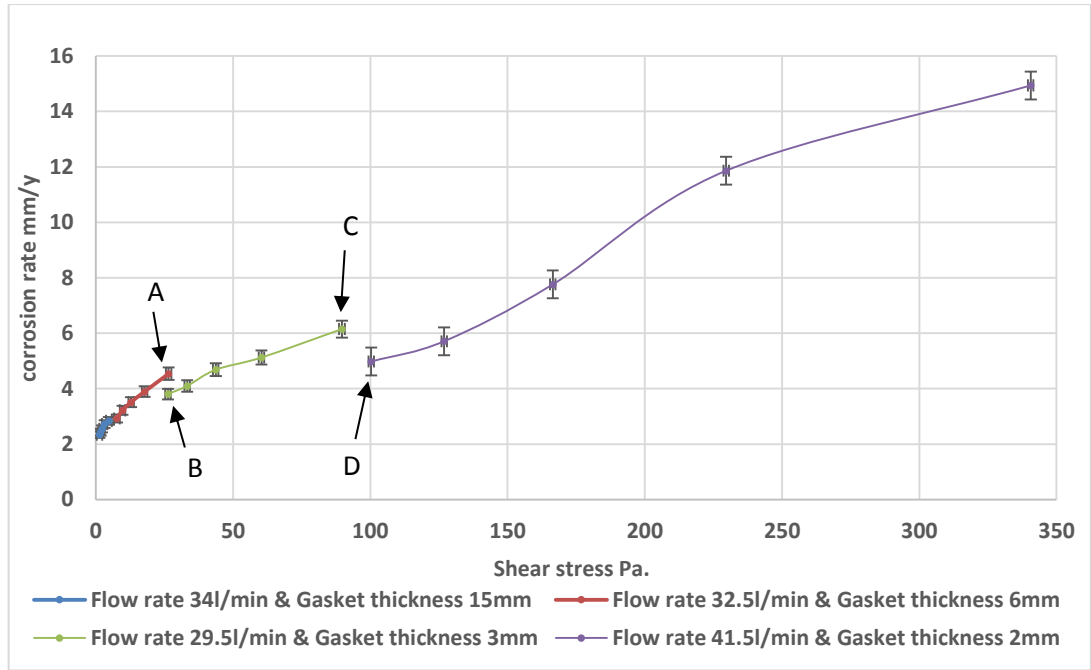


Figure 6-16. Corrosion rate as a function of flow shear stress – 6.6 pH, 80°C and 3% NaCl.

Furthermore, similar behaviour was observed at higher wall shear stress ≥ 90 Pa where another two different corrosion rates were recorded at points C & D as shown in Figure 6-16. Both points C & D were subjected to wall shear stress values of 90 and 100 Pa respectively. However, the corrosion rate at point C is higher than D although the wall shear stress at C is less than that at D. From Figure 6-17 Reynold`s number at point C is $\sim 89,800$ and at point D is $\sim 66,700$.

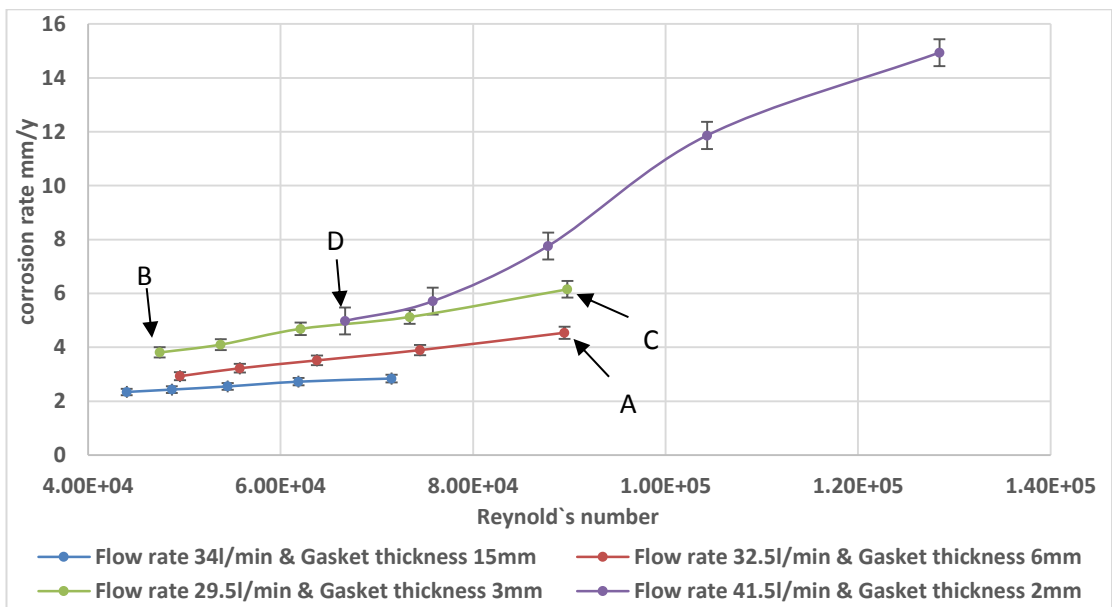


Figure 6-17. Corrosion rate as a function of Reynold`s number – 6.6 pH, 80°C and 3% NaCl.

Separate tests were performed to ensure whether samples 1 to 4 altered the corrosion rate at position 5. Figure 6-18 shows the outcome of the corrosion rate tests as a function of wall shear stress which represents points C & D in Figure 6-16. The first test was carried out using one exposed sample surface mounted as the fifth sample on the test section using flow rate 29.5 l/min and gasket thickness 3mm. The other four samples positions were filled with blank (plastic) samples. The second test was performed using one sample surface mounted as the first sample on the test section under a flow rate of 41.5 l/min and 2mm gasket thickness. The other four samples holders were filled with dummy samples. Corrosion rates at both points were similar to the corrosion rate values illustrated in Figure 6-16 of the same points/samples position, which indicated that the effect of first four samples on the corrosion behaviour of the fifth sample was negligible and the variation in corrosion rate at points A, B, C and D may be attributed to other factors which will be explained in detail in the discussion Chapter 10.

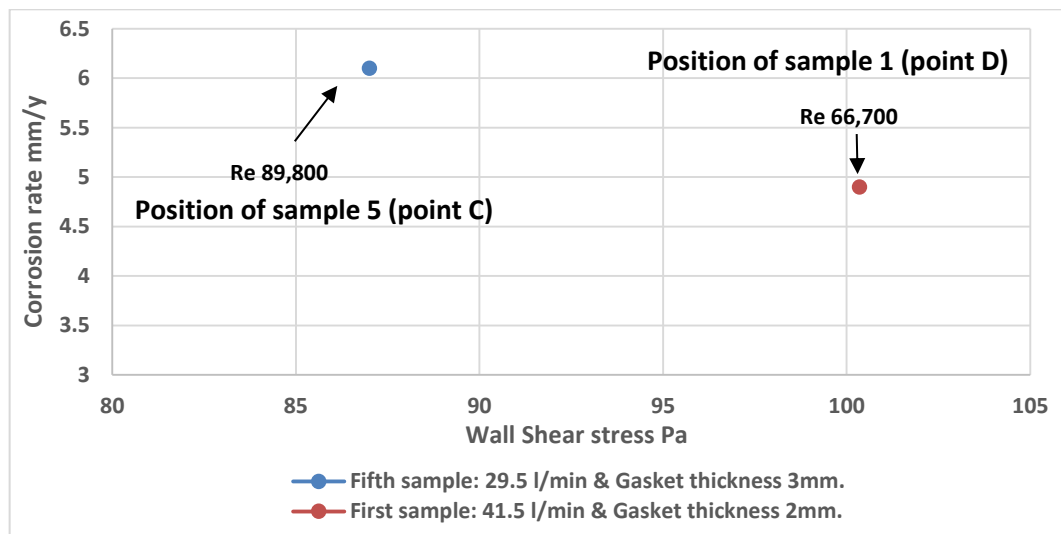


Figure 6-18. Points C & D: The effect of the samples on each other corrosion rates.

Furthermore, in order to investigate the effect of the flow velocity as a parameter on the corrosion behaviour, the corrosion rate was plotted versus the flow velocity as shown in Figure 6-19. The overall shape of the curve was in agreement with curve trend of the corrosion rate as a function of shear stress shown in Figure 6-16. Similar observation was recorded at 50°C.

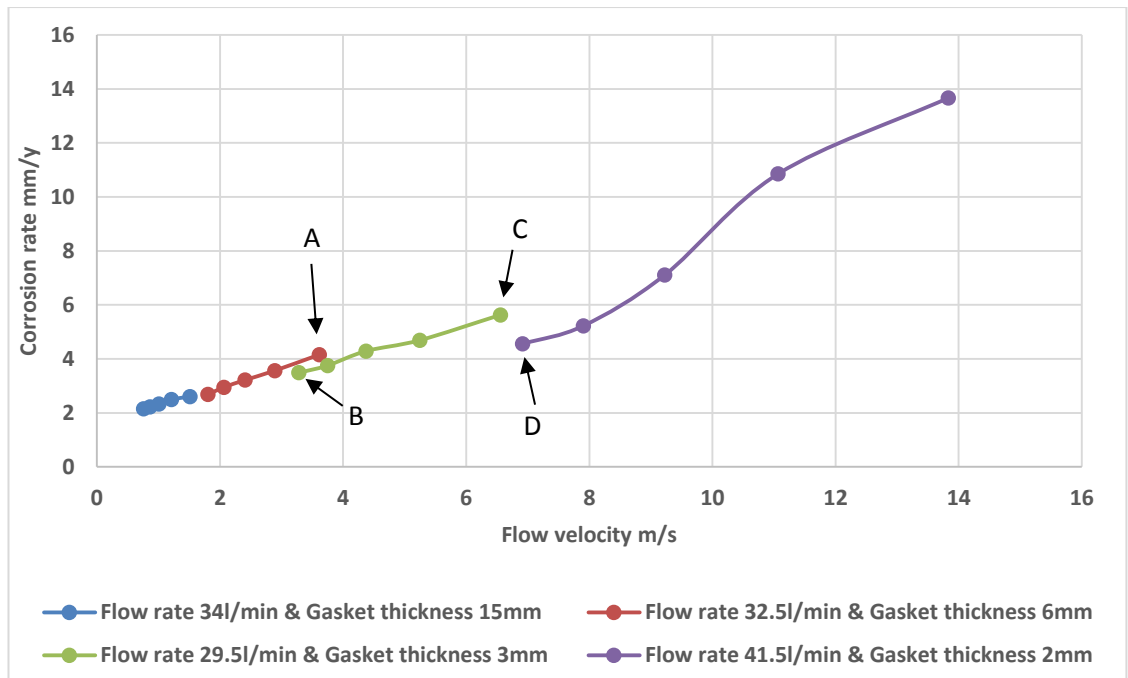


Figure 6-19. Corrosion rate as function of flow velocity – pH 6.6, 80°C and %3 NaCl

6.4.2.1 Cathodic sweep under flowing conditions at pH 6.6 and temperature 80°C

Figure 6-20 shows cathodic polarisation tests, carried out on samples that represent points C & D shown in Figure 6-16. Although point D was exposed to a higher wall shear stress/flow velocity; it had a lower corrosion rate than point C. The cathodic sweeps showed that the cathodic current density at C was higher than at D, which agreed well with the corrosion rate.

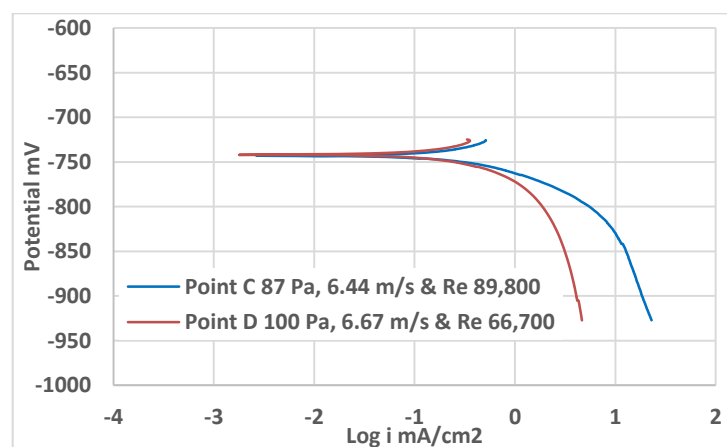


Figure 6-20. Cathodic sweep of point C & D at temperature 80°C, pH 6.6

Figure 6-21 shows cathodic sweeps conducted on X65 carbon steel samples under various shear stresses and Reynold`s numbers. The plots of the cathodic currents densities as a function of the potential explain well the corrosion rate behaviour at 80°C shown in Figure 6-16, where the cathodic current density increased as a function of the wall shear stress. Further discussion of these data will be presented in the discussion Chapter 10.

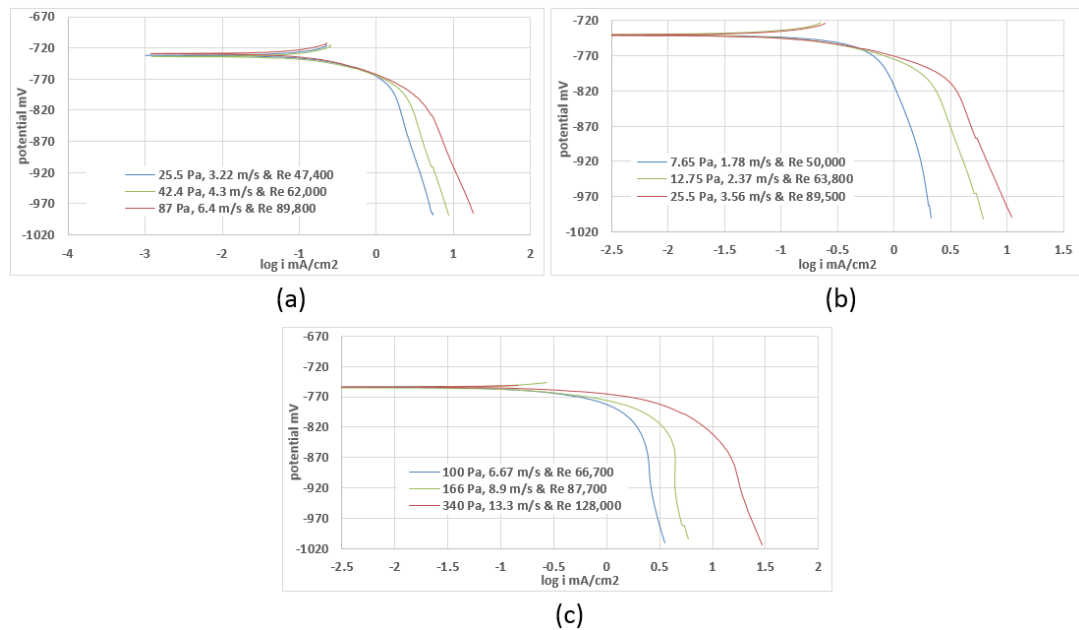


Figure 6-21. Cathodic sweeps carried out at temperature 80°C, pH 6.6 for wall shear stress/flow velocity: a- 7.65 to 25.5 Pa b- 25.5 to 87 Pa c-100 to 340 Pa.

6.5 Summary

Many studies and reviews have been published relating to investigating CO₂ corrosion on carbon steel under flow [22, 23, 49, 132, 149, 215]. However, the influence of flow parameters and solution conditions on the corrosion mechanism still raises many questions and debate due to its complex nature.

In this chapter, an investigation was conducted to examine the CO₂ corrosion behaviour in flowing conditions, in order to determine the influence of flow parameters and the temperature on the corrosion process at 6.6 pH solution on the corrosion behaviour of X65 carbon steel. At pH 6.6, the corrosion rate is flow dependent at both temperatures 50°C and 80°C. Corrosion rates at 80°C are higher than 50°C as expected. The corrosion rate is not solely a function of the flow

conditions of wall shear stress, and other flow parameters can govern the corrosion rate. This will be addressed in the discussion chapter.

Chapter 7. Results of X65 carbon steel bare surface under flowing conditions at pH 4

7.1 Introduction

In the previous chapter corrosion behaviour under flowing conditions at pH 6.6 where the concentration of species H^+ is low ($10^{-6.6}$ mol/l). In this chapter corrosion behaviour at low pH solution conditions were investigated under flowing conditions where the H^+ concentration is (10^{-4} mol/l at pH 4). The objective was to establish an understanding of the corrosion behaviour when the mass diffusion reactant of H^+ is present in a high concentration in the bulk solution and to determine which flow parameter the corrosion rate is best related to. In literature, corrosion behaviour of carbon steel at pH 4 is under a mass diffusion-controlled process, and as such, the corrosion rate shows a strong flow dependency [60, 121].

The tests have been performed at two temperatures of 50°C and 80°C. The experiments are divided into two parts; corrosion rate as a function of time, and corrosion rate as a function of wall shear stress.

7.2 Test matrix

Table 7-1 shows the matrix of the tests series of the X65 carbon steel surface under flowing conditions and pH 4.

Table 7-1. Test matrix of the corrosion tests at pH 4

Solution	pH 4	
Temperature °C	50 °C	80 °C
Duration of test (hrs)	5	
Range of flow velocity (m/s)	0.7 to 13.5	
Range of wall shear stress (Pa)	1.34 to 410	
Solution	3 wt. % NaCl	
Electrochemistry measurement	LPR	

Corrosion measurements are performed using LPR. Corrosion rate values under flowing conditions at both temperatures reached a stable rate within ≤ 5 hrs, therefore the test duration was limited to 5 hrs.

7.3 X65 carbon steel corrosion behaviour under flowing conditions at 50°C and pH 4

The corrosion tests were carried out at two temperatures, 50°C and 80°C. At each temperature, the tests series consists of four tests. Therefore corrosion behaviour was examined under four different flow turbulence, characteristic and geometry profiles. Consequently, the plot of the corrosion rate as a function of time under wall shear stress 1.6 to 410 Pa was divided into four plots. A similar procedure was followed in previous tests, detailed in paragraph 6.3.1.

7.3.1 Corrosion rate as a function of time at temperature 50°C and pH 4

The sequenced tests were performed under flowing conditions of wall shear stress range 1.6 to 410 Pa and temperature 50°C as detailed in Table 6-4. Figure 7-1 shows the corrosion behaviour at shear stress range 1.6 to 5.66. The initial corrosion rate under 1.6 Pa increased with time up to a stable level (steady state rate) within ~2.5 hrs to the end of the test. At shear stress 2 and 2.7 Pa corrosion rate showed different behaviour, where the initial corrosion increased and stabilised on the plateau after 1 hr. However, at shear stresses 3.75 and 5.66 Pa the stabilisation period was ~30 minutes.

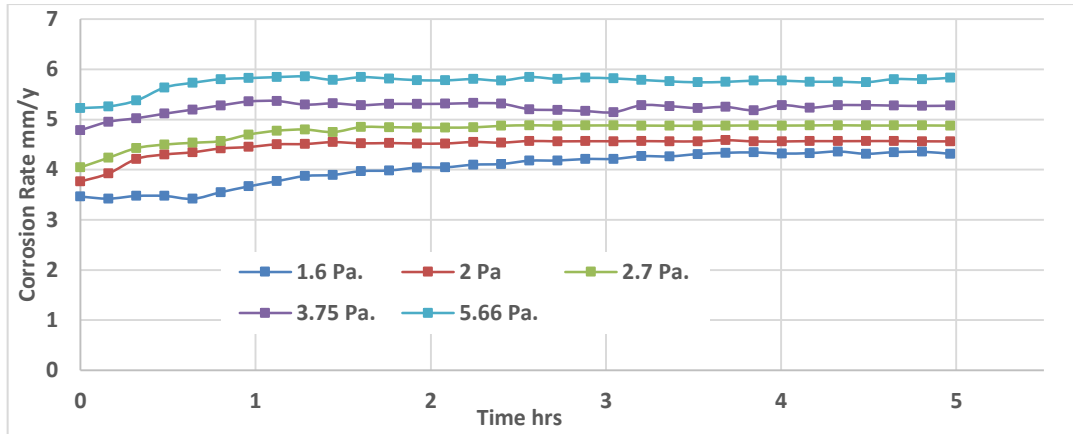


Figure 7-1. Corrosion rate as function of time under wall shear stress range of 1.6 to 5.66 Pa at temperature 50°C and pH 4

The second test was carried out at shear stresses ranging from 9 to 30 Pa. The corrosion behaviour showed different initial values, depending on the applied shear stress as shown in Figure 7-2. The initial corrosion rate under 9, 11 and 15 Pa increased within 30 minutes to stable values. Furthermore, at 20.5 and 30 Pa corrosion rate showed higher initial values and reached a plateau within ~15 minutes.

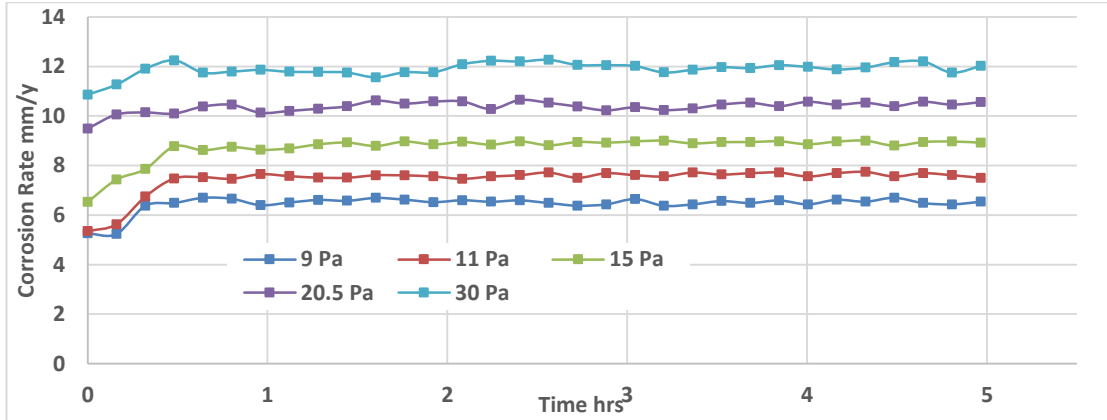


Figure 7-2. Corrosion rate as function of time under wall shear stress range of 9 to 30 Pa at temperature 50°C and pH 4

The tests were carried out under higher shear stresses in the range of 30 to 100 Pa as shown in Figure 7-3. The overall shape of the curves indicated that corrosion rate was at a steady value from the starting point. The corrosion rate of each sample was stable at steady state rate from the starting point to the end of the test. The corrosion rate throughout the test was a function of the applied wall shear stress.

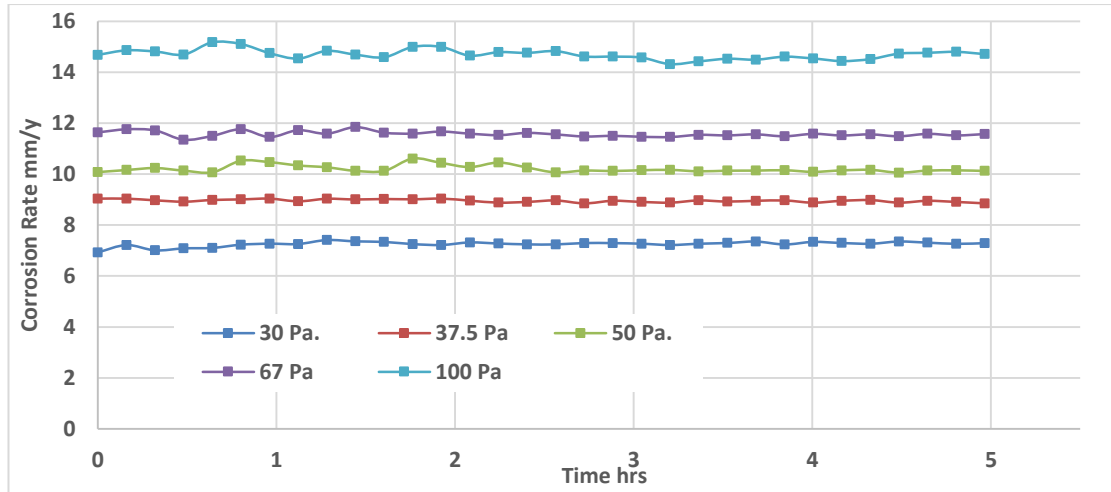


Figure 7-3. Corrosion rate as function of time under wall shear stress range of 30 to 100 Pa at temperature 50°C and pH 4

Figure 7-4 shows the same data at higher wall shear stresses 120 to 410 Pa. The corrosion behaviour as a function of shear stress was similar, where the corrosion rates of the five samples showed no increase throughout the 5 hrs exposure time.

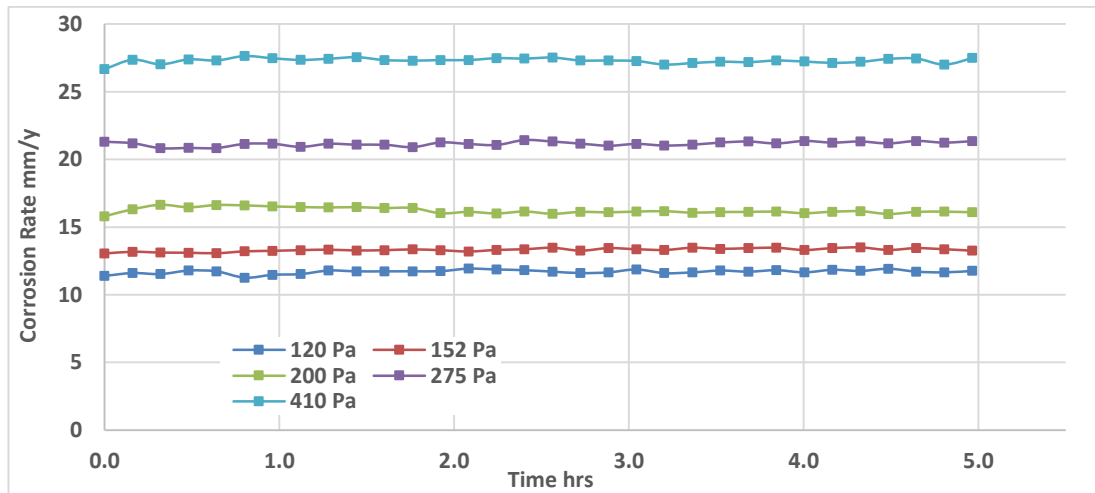


Figure 7-4. Corrosion rate as function of time under wall shear stress range of 120 to 410 Pa at temperature 50°C and pH 4

The outcome of the four tests showed that the tendency of the corrosion rate to increase under flowing conditions and fixed pH 4 can vary as a function of shear stress. At low range of wall shear stress, 1.6 to 5.66 Pa corrosion rate showed the highest flow sensitivity as shown in Figure 7-1. At higher wall shear stress ranges the flow dependency of the corrosion rate gradually decreased.

7.3.2 Corrosion rate as a function of flow at 50°C and pH 4

Corrosion behaviour of carbon steel under different flow parameters such as wall shear stress, velocity and Reynold`s number was examined at pH 4 and 50°C. The flow parameters were calculated using empirical correlations equations 5.1 to 5.10. The details of the test section geometry across the samples at each test and the wall shear stress levels are shown in Table 6-2. Figure 7-5 shows the relation between the corrosion rates and the wall shear stress at temperature 50°C. Similar to the previous test procedure in 6.3.2, the plot consists of four curves represent four tests. Wall shear stress range 1.6 to 30 Pa was generated through two tests; first tests represented as a blue curve and second tests as the red curve. At this range of shear stress, corrosion rates exhibited a linear relationship up to 30 Pa point, within this range of shear stress corrosion rate was directly proportional to shear stress.

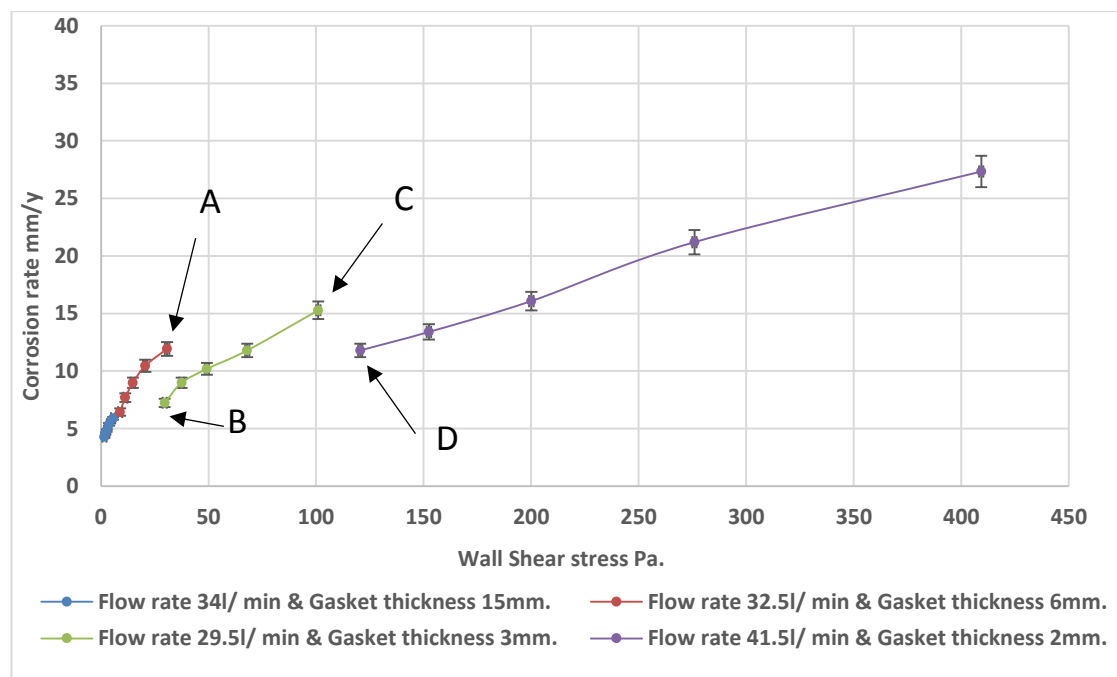


Figure 7-5. Corrosion rate as a function of flow shear stress – pH 4, 50°C and %3 NaCl.

Wall shear stress 30 Pa two corrosion rates were recorded at points A & B as shown in Figure 7-5. Although the wall shear stress and flow velocities were similar at both points, a higher corrosion rate at point A than at B was recorded. Similar behaviour was observed during the corrosion rate test at pH 6.6 and temperature 50°C and 80°C, however, under pH 6.6, the variation in corrosion rate at these points was much lower.

Corrosion rates were high flow dependent, showed significantly increased as a function of the flow (shear stress/flow velocity), indicating a mass diffusion-controlled reaction. At Shear stress range 30 to 100 Pa corrosion rate increased linearly with wall shear stress, however another variation in corrosion rate at two points was recorded at point C & D which was similar to the observation at point A & B where corrosion rates at point C were higher than the corrosion rate at point D despite both points were exposed to 100 & 120 Pa of wall shear stresses respectively.

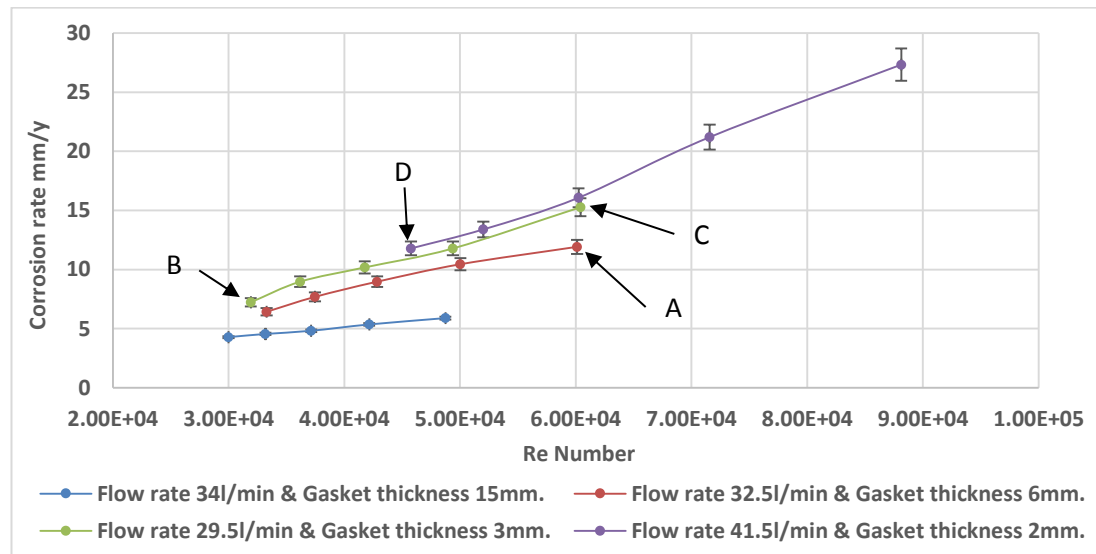


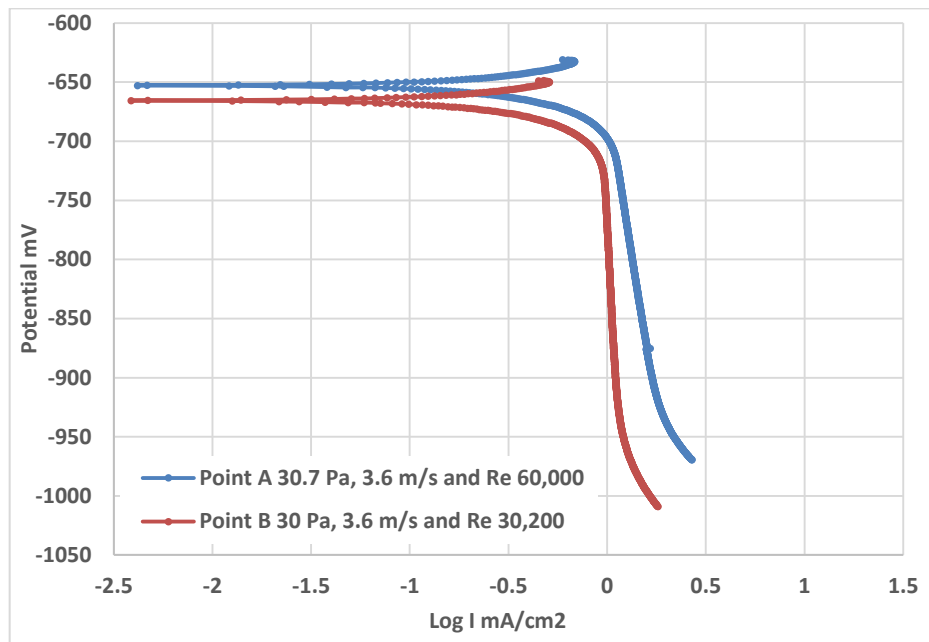
Figure 7-6. Corrosion rate as a function of Reynold`s number – pH 4, 50°C and %3 NaCl.

Figure 7-6 illustrates the plots of the corrosion rate as function Reynold`s number. It shows that corrosion rate at point A is associated with Reynold`s number ~60,000, where the Reynold`s number at point B is ~32,000. Similar behaviour at point C & D. The corrosion rate at point C than D is supported by higher Reynold`s number at C ~60,000 than at D ~45,800.

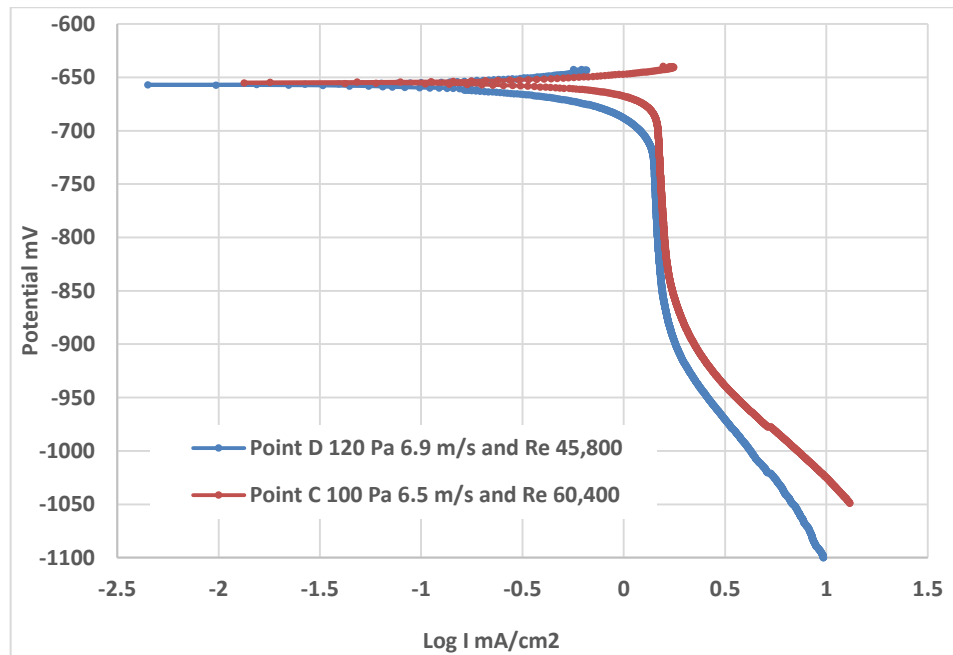
7.3.2.1 Cathodic sweep under flowing conditions at pH 4 and temperature 50°C

Potentiodynamic sweeps were carried out on the samples that are represented at points A & B and C & D under conditions of pH 4 and temperature 50°C as shown in Figure 7-7. The anodic branches were flow insensitive and showed a constant behaviour at different flow velocities at all tests, therefore it was not plotted.

Figure 7-7(a) shows the polarisation curves of points A & B, both curves show a clear mass diffusion controlled behaviour which is expected at such low pH conditions. The cathodic sweep of point A indicates a limiting current density that is higher than at point B. Similar behaviour was observed at points C & D in Figure 7-7(b). The overall shape of the curves indicates that point C has higher limiting current density than at point D, although point D was subjected to 20% higher wall shear stress than point C.



(a)



(b)

Figure 7-7. Cathodic sweep carried out at temperature 50°C and pH 4 for
a- points: Points A & B b- Points C & D

Additional potentiodynamic sweep tests were carried on at temperature 50°C and pH 4 solution at wall shear stresses range of 8.9 to 410 Pa as detailed in Figure 7-8. At wall shear stress (8.9 to 30 Pa) and (30 to 100 Pa) the cathodic current densities curves showed significant limiting current density regions, indicating a mass diffusion rate controlled process in all cases as shown in Figure 7-8(a & b).

The potentiodynamic sweeps continued under higher wall shear stress range of 120 to 410 Pa illustrated in Figure 7-8(c). Cathodic sweep under 120 and 200 Pa indicated a mass diffusion-controlled reaction. However, at highest wall shear stress of 410 Pa, the reduction reaction showed a mix controlled process of charge transfer and mass diffusion; the charge transfer rate was the limiting step and the mass diffusion rate showed minor effect.

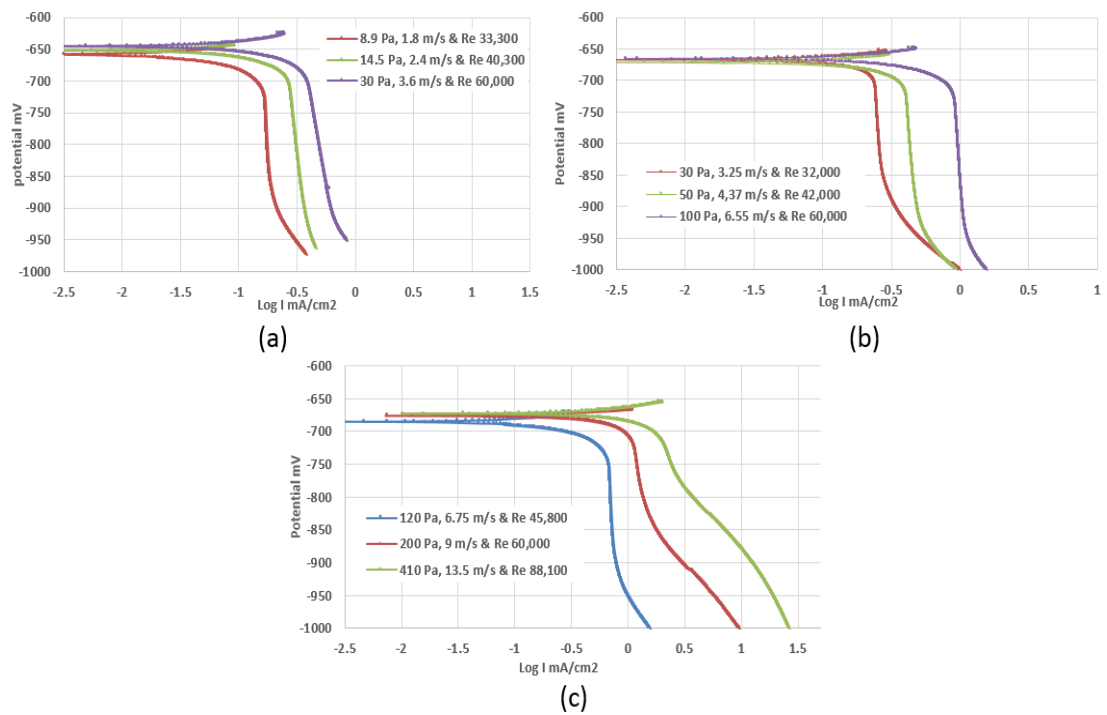


Figure 7-8. Cathodic sweeps carried out at temperature 50°C and pH 4 for wall shear stress/flow velocity: a- 8.9 to 30 Pa b- 30 to 100 Pa c- 120 to 410 Pa

7.4 X65 carbon steel corrosion behaviour under flowing conditions at 80°C and pH 4

7.4.1 Corrosion rate as function of time at temperature 80°C and pH 4

Corrosion behaviour of X65 carbon steel surface was further investigated as a function of time at pH 4 and temperature 80°C. In general, the corrosion behaviour at all tests was similar to the corrosion behaviour at temperature 50°C as shown in Figure 7-1 to Figure 7-4, where at both temperatures 50°C and 80°C corrosion rate under wall shear stress ≤ 25 Pa increased with the time from an initial value up to the plateau level. However, at higher wall shear stress > 25 Pa, corrosion rate was stable from the starting point to the end of the 5 hrs exposure to flow conditions. Nevertheless, the stabilisation period of the corrosion rate at temperature 80°C was shorter than at temperature 50°C.

At shear stress range of 1.35 to 4.75 Pa the corrosion rate curves are shown in Figure 7-9. At 1.35 and 1.75 Pa, the initial corrosion progressed up to steady state value within ~1.5 hrs. However, at higher shear stresses of 2.25 and 3.1 Pa the corrosion rates increased and stabilised within the 45 minutes. Whilst, at shear stress 4.75 Pa the initial corrosion rate increased and reached the plateau after only 30 minutes.

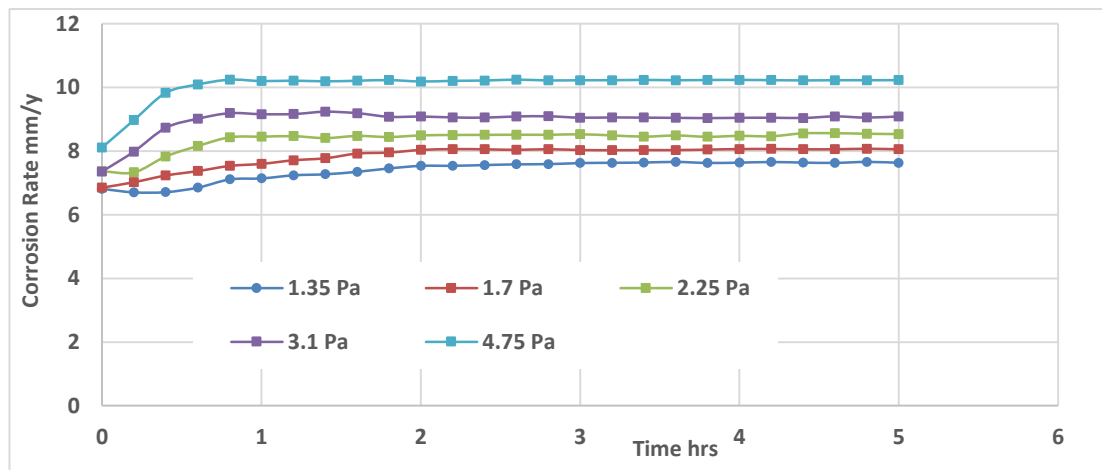


Figure 7-9. Corrosion rate as function of time under wall shear stress range of 1.35 to 4.75 Pa at temperature 80°C and pH 4

Figure 7-10 shows the plots of the corrosion rate at shear stresses of 7.65 to 25.5 Pa. The overall shape of the curves indicates a similar corrosion behaviour to the previous test for the first four samples. However the fifth curve at 25.5 Pa showed different behaviour, the corrosion rate was at steady state value from the starting point.

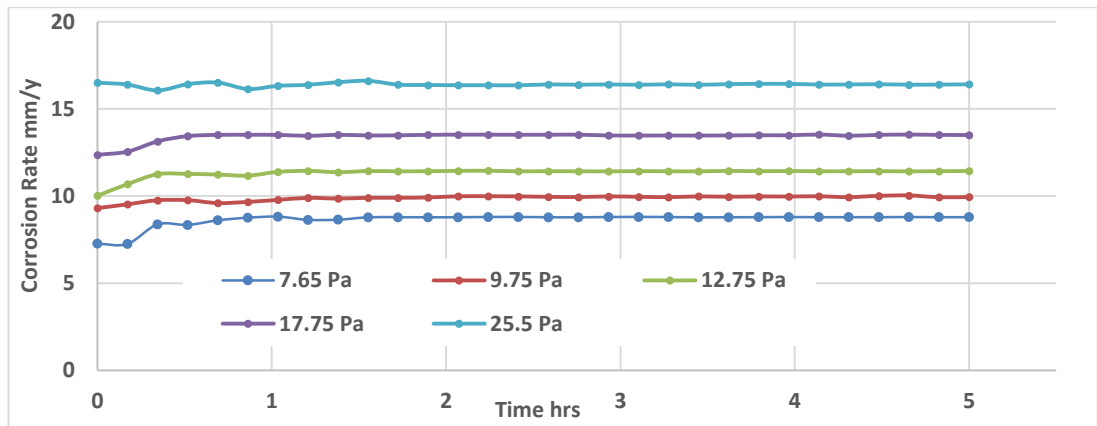


Figure 7-10. Corrosion rate as function of time under wall shear stress range of 7.65 to 25.5 Pa at temperature 80°C and pH 4

For the following tests, the shear stress ranges of 25.5 to 87 Pa was employed across the five samples. From Figure 7-11 corrosion rate showed no increase above the initial values during the test duration. However, corrosion behaviour showed lower flow sensitivity as a function of the wall shear stress than the previous two tests that are shown in Figure 7-9 and Figure 7-10.

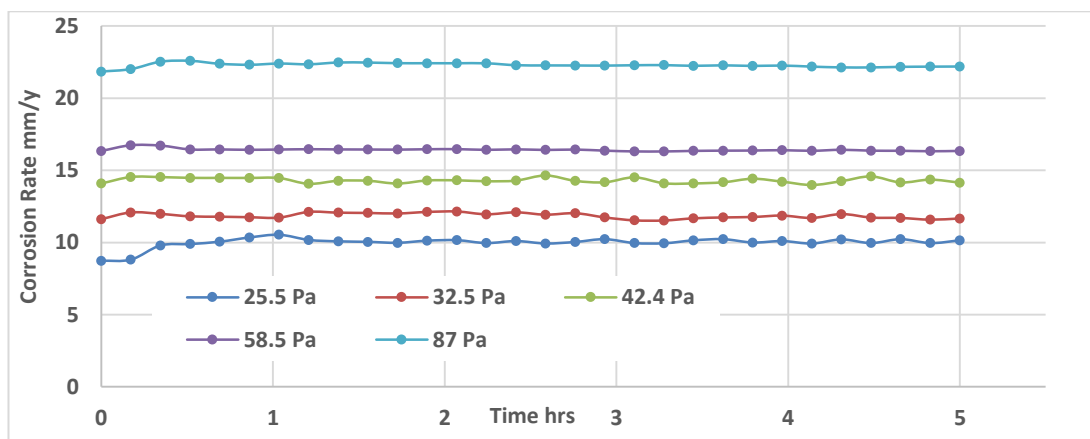


Figure 7-11. Corrosion rate as function of time under wall shear stress range of 25.5 to 87 Pa at temperature 80°C and pH 4

At shear stress range 100 to 340 Pa all the five samples showed a consistent and similar corrosion behaviour to the previous test. Where the corrosion rate was at steady state values throughout the test duration.

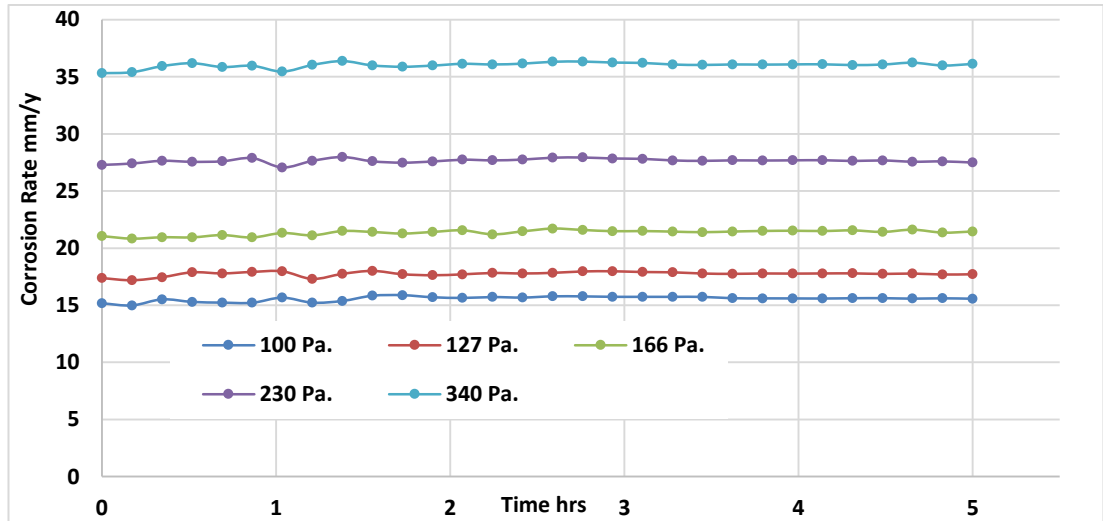


Figure 7-12. Corrosion rate as function of time under wall shear stress range of 100 to 340 Pa at temperature 80°C and pH 4

7.4.2 Corrosion rate as a function of flow at 80°C and pH 4

The tests procedure was similar to the sequence of the 50°C temperature tests. Tests matrix is detailed in Table 7-1. Corrosion rates were plotted as a function of the wall shear stress at 80°C and pH 4 and shown in Figure 7-13. The corrosion behaviour of the samples showed strong flow dependency at all the four tests. Corrosion rates increased rapidly with wall shear stress during the first test displayed as a blue curve. The fifth sample of the first test was subject to ~ 5 Pa, this sample is referred to as point A in Figure 7-13. The second test plot displayed as a red curve, start with the first sample that is represented by point B. Although the wall shear stress at point B is higher than the shear stress at point A, the corrosion rate at A is higher than it is at B.

Similar corrosion behaviour was observed during the 50°C and pH 4 at points A & B as shown in Figure 7-5. However, at 50°C, the variation in corrosion rates observed at a wall shear stress of ~30 Pa.

Whereas at 80°C, this variation occurred at a much lower wall shear stress ~ 4.75 Pa. This behaviour occurred again at wall shear stress ~25 Pa with two points share approximately similar wall shear stresses and showed different corrosion rates; these points are highlighted as C & D

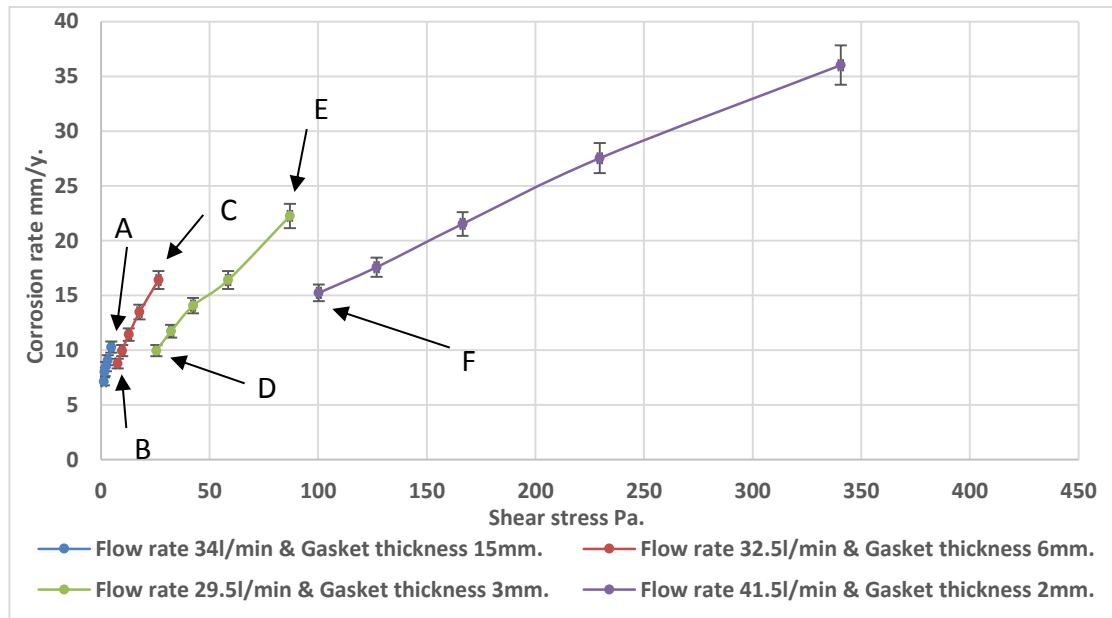


Figure 7-13. Corrosion rate as a function of flow shear stress –pH 4, 80°C and 3% NaCl.

Furthermore, points E & F confirm the previous two behaviours, where, the sample which is represented by point E and is exposed to ~87 Pa shows higher corrosion rate than the sample that is referred to as point F subjected to ~100 Pa.

As previously explained in 6.3.2 and 6.4.2 the variation in corrosion rate at points subjected to similar flowing conditions have occurred in tests at a higher pH level of 6.6. However, it becomes more significant at conditions of lower pH level and higher temperatures. This indicates that this behaviour is governed by a parameter that is highly affected by the temperature and the concentration of the cathodic species in the bulk solution.

Figure 7-13 illustrates the relationship between Reynold`s number and corrosion rate, where, corrosion rate increased as a function of the Reynold`s number at all the four tests. Nevertheless, at points that are referred to as (A & B), (C & D) and (E & F) Reynold`s number value showed variation between these points. Where the points with higher corrosion rate are always associated with higher Reynold`s number.

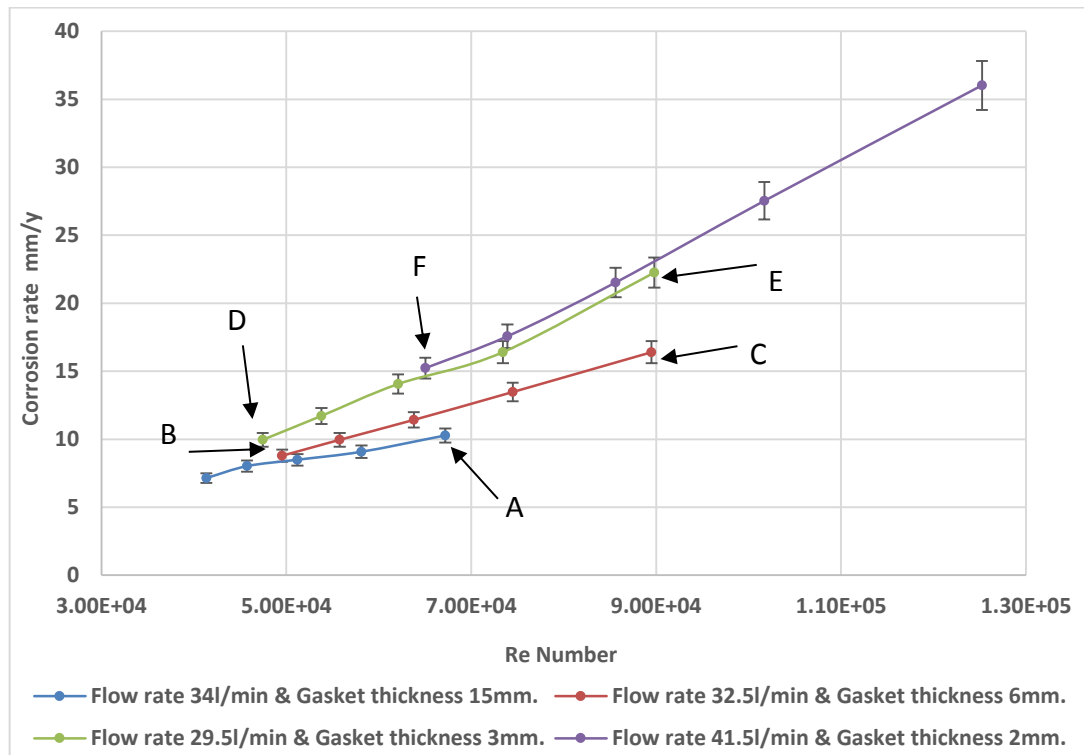
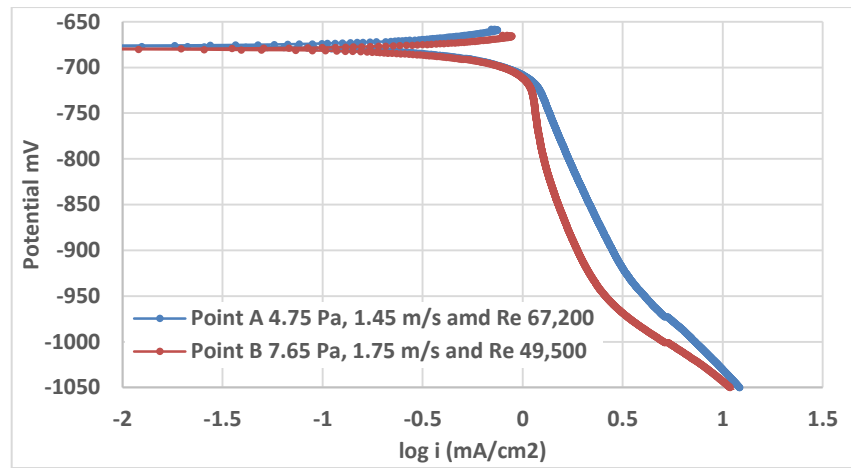


Figure 7-14. Corrosion rate Vs Reynold`s number – pH 4, 80°C and 3% NaCl

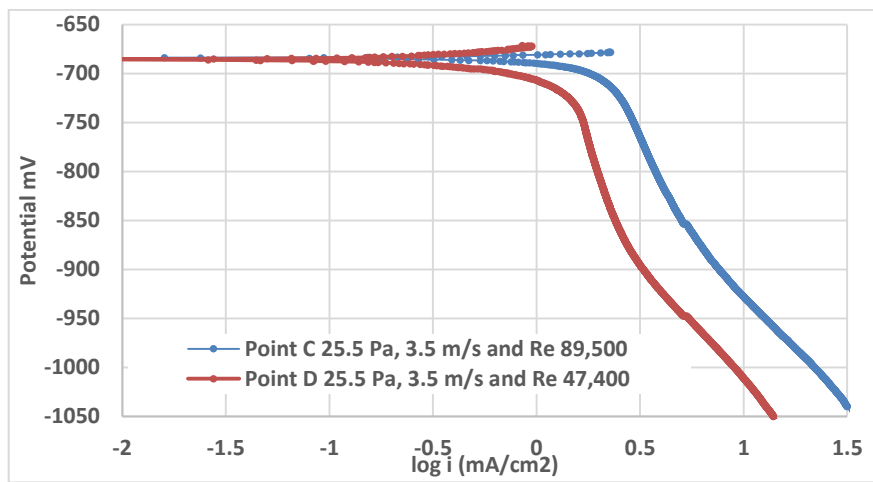
7.4.2.1 Cathodic polarisation curves under flowing conditions at pH 4 and temperature 80°C

A series of cathodic sweep tests were carried out at conditions of pH 4 and solution temperature 80°C. Figure 7-15 details the cathodic polarisation curve at points A, B, C, D, E and F which are shown in Figure 7-13. The limiting current density at point A is higher than at point B as shown in Figure 7-15(a). Similar behaviour was recorded at the cathodic sweeps of points C & D in Figure 7-15(b) the overall behaviour of both curves are mass transfer controlled.

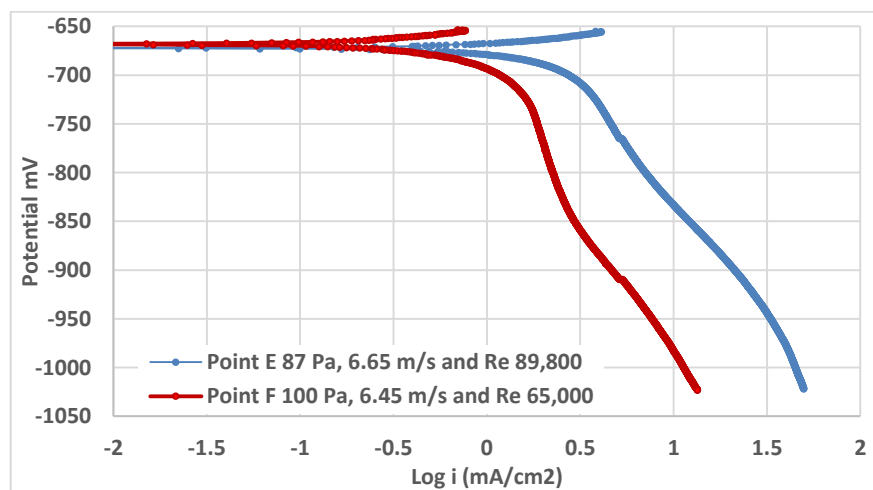
In other words, the wall shear stress and flow velocities at both points are similar, nevertheless, the limiting current densities generated from the sample that is referred to by point C is greater than the sample of point D. This observation is also applied to points F and E as shown in Figure 7-15(c).



(a)



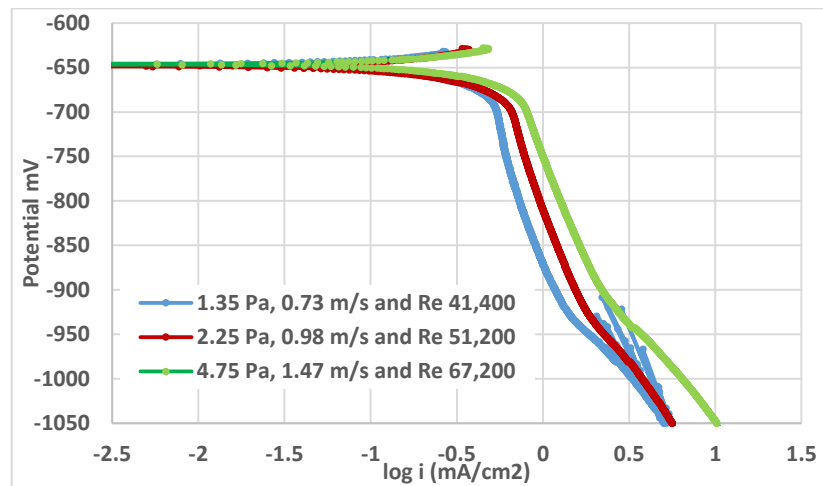
(b)



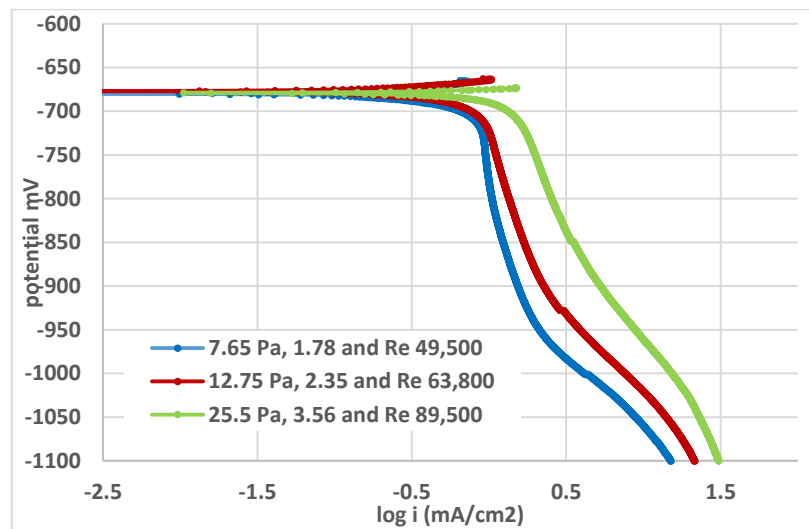
(c)

Figure 7-15. Cathodic sweep carried out at temperature 80°C, pH 4 for points:
a: Points A & B b: Points C & D c: Points E & F

Further cathodic sweep tests were carried out to examine the reduction process at shear stress 1.35 to 340 Pa. At low wall shear stress 1.35 to 4.75 Pa, the overall shapes of the curves indicate a mass diffusion controlled process, with a limiting current density, that is a function of the shear stress as shown in Figure 7-16(a). At higher wall shear stress 7.65 to 25.5 Pa, the cathodic reactions illustrate a further mass diffusion controlled process Figure 7-16(b).



(a)



(b)

Figure 7-16. Cathodic sweeps carried out at temperature 80°C, pH 4 for wall shear stress/flow velocity: a- 1.35 to 4.75 Pa b- 7.65 to 25.5 Pa.

The following cathodic polarisation tests were carried out under higher wall shear stress range 25.5, 42.4 and 87 Pa. Curves details are shown in Figure 7-17(a), the shape of the curves of the cathodic sweep at a wall shear stress 87 Pa illustrated a clear shift in the reduction process from mass transfer controlled reaction to a mixture of

charge and mass transfer controlled, where the rate determining step is the charge transfer rate. Similar observations were recorded in the 50°C & pH 4 tests that are mentioned previously. However, this behaviour at temperature 50°C occurred at much higher wall shear stress.

Moreover, the cathodic polarisation curves at shear stresses of 100, 166 and 340 Pa are shown in Figure 7-17(b). At shear stress 100 Pa the cathodic sweep indicates a mass transfer controlled process. This was an interesting behaviour, considering the shear stress at this point is higher than at the previous curve of 87 Pa at which the reduction process was mixed charge and mass transfer controlled as shown in Figure 7-17(a). Nevertheless, under 166 Pa wall, the cathodic sweep showed another mix controlled process. The cathodic reaction curve at 340 Pa shows a clear charge transfer controlled process with an insignificant effect on the mass diffusion rate on the species reduction process.

The previous data in Figure 7-5 to Figure 7-8 and Figure 7-13 to Figure 7-17 showed that the wall shear stress is not the only parameter governs the reduction rate, other flow parameters also have an influence on the corrosion behaviour as it will be discussed in the discussion Chapter 10.

The data of the corrosion rate at pH 4 and temperatures 50°C and 80°C showed that the highest flow sensitivity of the corrosion rate occurred at low shear stress ranges (1.35 to 4.75 Pa at temperature 80°C), and (1.66 to 5.66 Pa at temperature 50°C). Where the curves of the corrosion rate as a function of these shear stress ranges are steeper than at the higher shear stress ranges. A similar observation was recorded at corrosion rate tests as a function of shear stress at pH 6.6.

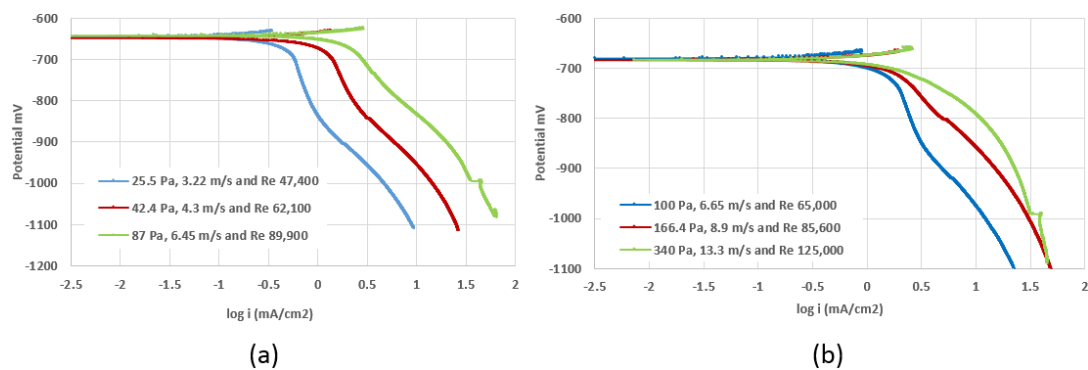


Figure 7-17. Cathodic sweeps carried out at temperature 80°C, pH 4 for wall shear stress/flow velocity: a- 25.5 to 87 Pa b- 100 to 340 Pa.

7.5 Summary

At both temperatures 50°C & 80°C, corrosion behaviour was under mass transfer controlled reduction process. Corrosion rates at temperature 80°C are relatively higher than 50°C. At high flow wall shear stress/velocities, the reduction reaction of the cathodic species switches from mass diffusion controlled process to mix charge transfer and diffusion controlled process, indicating a critical diffusion rate at which the reduction process reaches its limit. However, the critical wall shear stress at which the reaction shifted to charge transfer control varies depending on the temperature, flow characteristic and solution properties. Wall shear stress effect on the corrosion rate is linearly up to 30 Pa at temperature 50°C, and 4.75 Pa at 80°C. Corrosion rate showed a strong dependency on the diffusion rate of the cathodic species from/to surface of the surface.

Chapter 8. Results of X65 carbon steel protected surface under flowing conditions at temperature 50°C

8.1 Introduction

In this chapter, the stability of iron carbonate films under flowing conditions tests was examined. To achieve an understanding of the film stability and the removal process, two possible mechanisms were considered; chemical dissolution and flow hydrodynamic effects. It is appreciated that these two factors are often inextricably linked. In order to isolate and study the effect of flow parameters on the corrosion behaviour of the X65 carbon steel with the presence of iron carbonate films, the critical pH and wall shear stress at which the protective films exhibit no removal under flowing conditions are defined

As previously explained in 5.4, the testing cell was designed to generate increasing flow shear stresses along the solution flow direction, by which it was possible to test the effect of different levels of flow shear stress on the iron carbonate covered X65 carbon steel samples. The protective film in this study was pre-formed using a high-pressure autoclave.

The stability and protectiveness of the iron carbonate were tested under different solution conditions and flow shear stress up to values of 655 Pa. This range of wall shear stress represents the highest shear stress used in literature to examine the removal mechanisms of the protective film [16, 21, 22, 149, 152]. The results illustrate that films are subject to chemical dissolution at pH levels lower than a critical pH (the minimum pH level environment at which the protective films do not undergo a chemical dissolution at static conditions). Flow has an effect in accelerating the films dissolution and removal. Critical pH and wall shear stress were determined at 50°C.

8.2 Film formation rate as a function of various immersion times

This part of the chapter presents the formation mechanism of the protective film. The time required for the protective film to reach a stable, compact, dense structure was determined. The first five formation tests were carried out for different durations of 14, 24, 48, 96 and 192 hrs under a high-pressure CO₂ environment. The outcome of these five tests was used to select the critical immersion time at which the protective

films reach a stable thickness. This was then used as in the following formation tests. The test matrix is shown in Table 8-1.

Table 8-1. Formation test matrix

CO ₂ Pressure (bar)	100
Temperature (°C)	60
pH	3.25 to 3.45
Time (hrs)	14/24/48/96/192

Figure 8-1 shows the corrosion behaviour of X65 carbon steel under 100 bar CO₂ pressure and temperature 60°C for various periods of time; the corrosion rate was calculated using mass loss technique described in paragraph 5.4.1.8. From the shape of the curve, at the beginning of the test the corrosion rate was high and within the first 24 hrs, it dropped by 25% from starting point value. The decline in corrosion rate with the time associated with an increase in the mass loss of corrosion product curve indicated a pseudo passivation process occurring by forming a protective film on the sample surface. After 48 hrs, a further decline in corrosion rate was recorded and the total mass loss curves were stabilised, for the rest of the 198 hrs test.

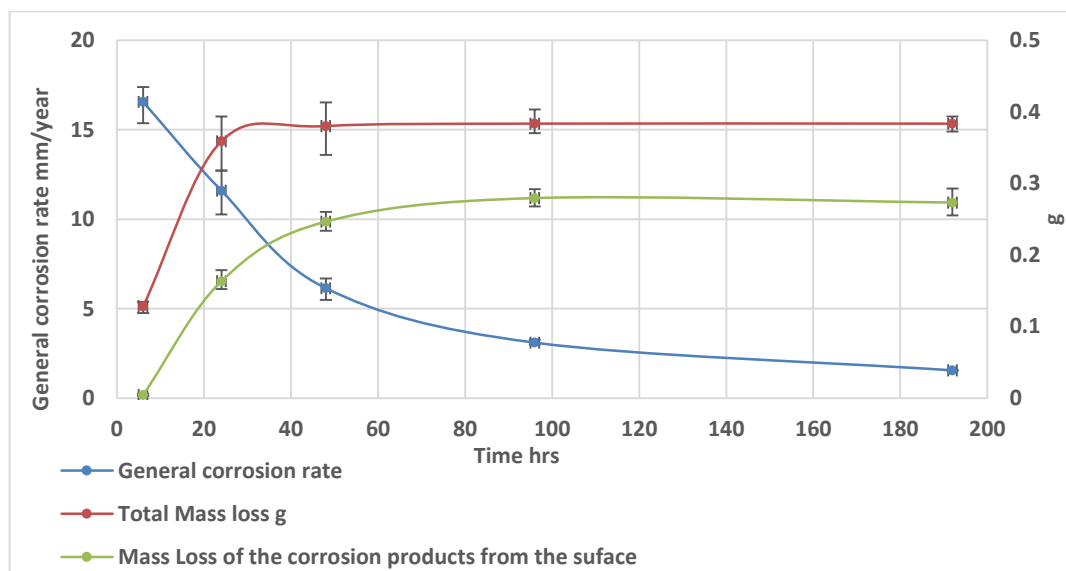


Figure 8-1. Corrosion behaviour of X65 under CO₂ pressure 100 bar and temperature 60°C as function of time

This can be attributed to the formation of thick and dense corrosion products on the surface preventing further mass loss from the surface. This shows that after 48 hrs the

thickness of the protective films had reached a critical value and no further increase of film formation is likely to occur. Therefore, the period of 48 hrs was selected as ‘formation duration time’ in the formation test. Figure 8-2 shows the SEM surface and cross-section images of the outcome of protective films formation test on the X65 carbon steel samples.

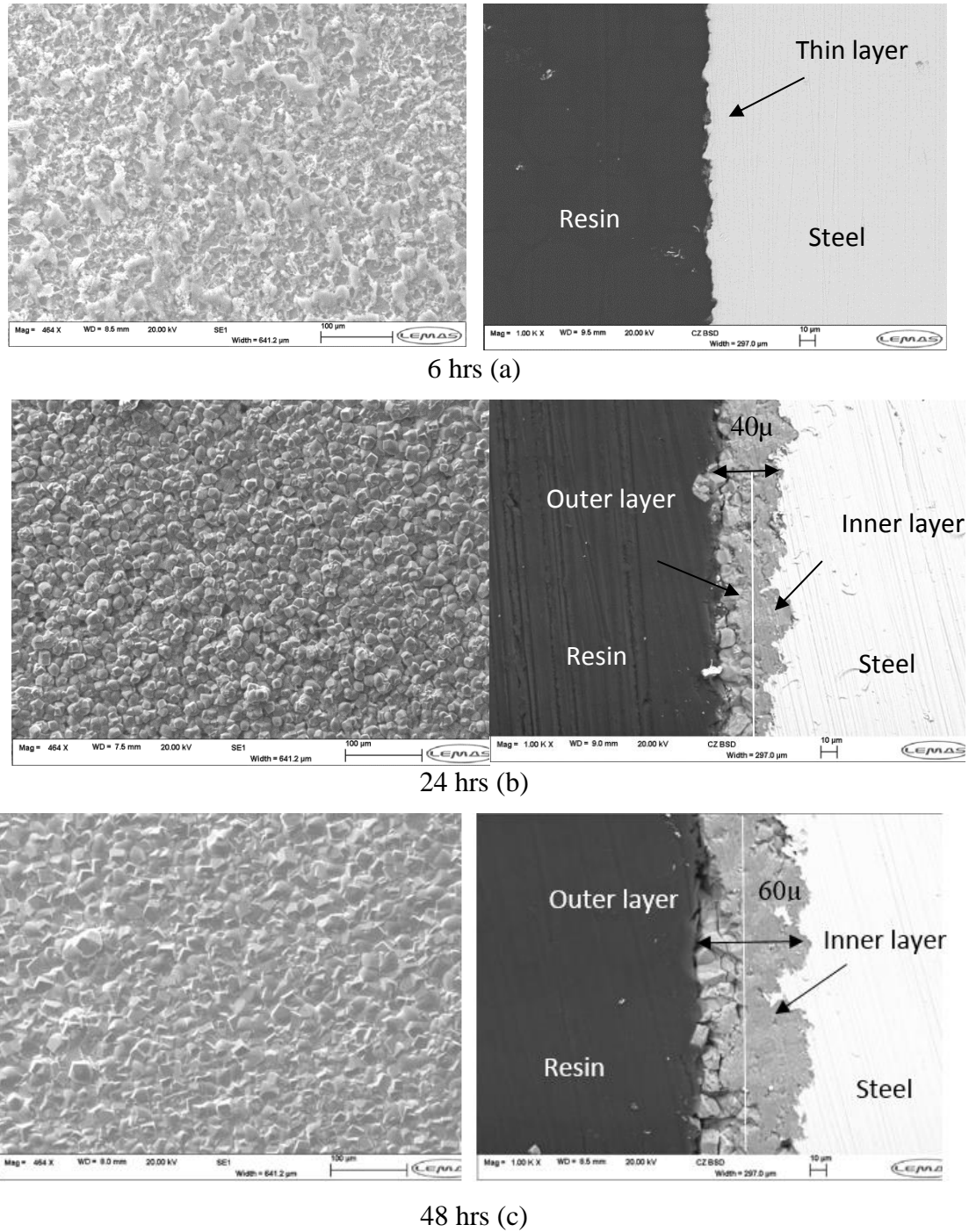


Figure 8-2. SEM images of the corrosion products morphology and thickness the X65 carbon steel surface formed at temperature 60°C and 100 bar CO₂ pressure

Surface analysis after 6 hrs immersion time Figure 8-2(a) shows the early stage of the protective films formation whereby, after 6 hrs most of the surface is still uncovered and exposed to the solution. The cross-section image shows a very thin layer of corrosion product. After 24 hrs Figure 8-2(b) the SEM analysis for the sample surface shows fully covered the surface with a prism-shaped crystal of iron carbonate. The cross-section image of the films agree with the surface SEM topography analysis, a clear film layer was observed with a thickness of $\sim 40\mu\text{m}$. From the analysis of the cross-section, the structure of the films consisted of two layers of the protective films, an inner layer and outer layer. However, after 48 hrs the SEM analysis of the surface indicates a dense and compact structure of corrosion film fully covered the surface as shown in Figure 8-2(c), the cross-section image revealed the thickness of protective film layer to be a $\sim 60\mu\text{m}$.

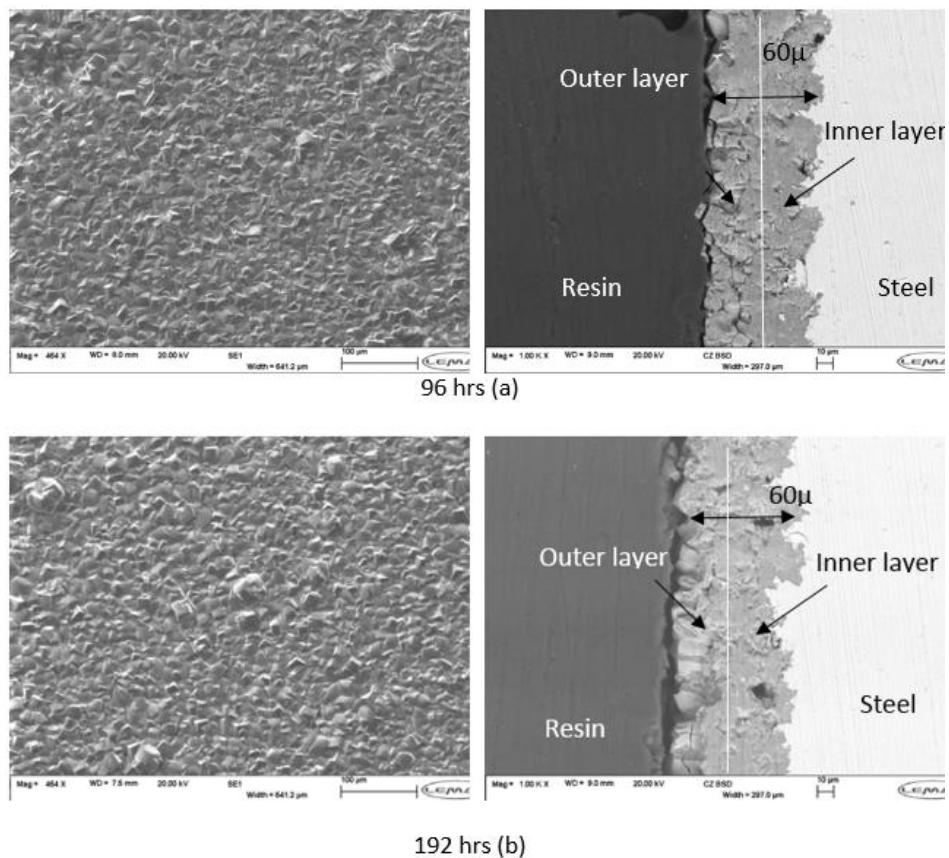


Figure 8-3. SEM images of the corrosion products morphology and thickness the X65 carbon steel surface formed at temperature 60°C and 100 bar CO_2 pressure for immersion time: a- 96 hrs b- 192 hrs

Furthermore, samples surfaces and cross sections were analysed using the SEM after 96 hrs immersion time as shown in Figure 8-3(a). The surface and the cross-section SEM images indicated a fully covered surface. Cross section images showed the structure and thickness of the films after 96 hrs is almost identical to that after 48 hrs indicating that no further accumulation or increase in films thickness than the $\sim 60\mu\text{m}$. Figure 8-3(b) shows the SEM analysis of the surface and the cross-section after 196 hrs immersion time. The surface image showed a fully covered and well compact iron film similar to the structure of the film formed after 48 and 96 hrs, no further increase in the thickness of the film layer than $\sim 60\mu\text{m}$. The surface analysis confirmed the corrosion behaviour curves in Figure 8-1 in which the total mass loss and mass loss of the corrosion product were stabilised and showed constant values after 48 hrs up to 196 hrs associated with a substantial decline in corrosion rate occurring during the duration of the test. Therefore, an immersion time of 48 hrs was selected as formation time for this study, and it would be employed in the following formation tests matrix. The thickness of the formed films after 48 hrs exposure agrees with the previous iron carbonate formation tests in the literature, where the average thickness of the formed iron carbonate was $\sim 60\mu\text{m}$ [112, 216]. Further surface analysis was carried out to confirm the films morphology on the sample surface. Figure 8-4 details XRD analysis to the X65 carbon steel surface after 48 hrs exposure to CO_2 saturated water at 60°C and 100 bar. The pattern of the XRD analysis indicates an iron carbonate layer crystal fully covers the sample surface.

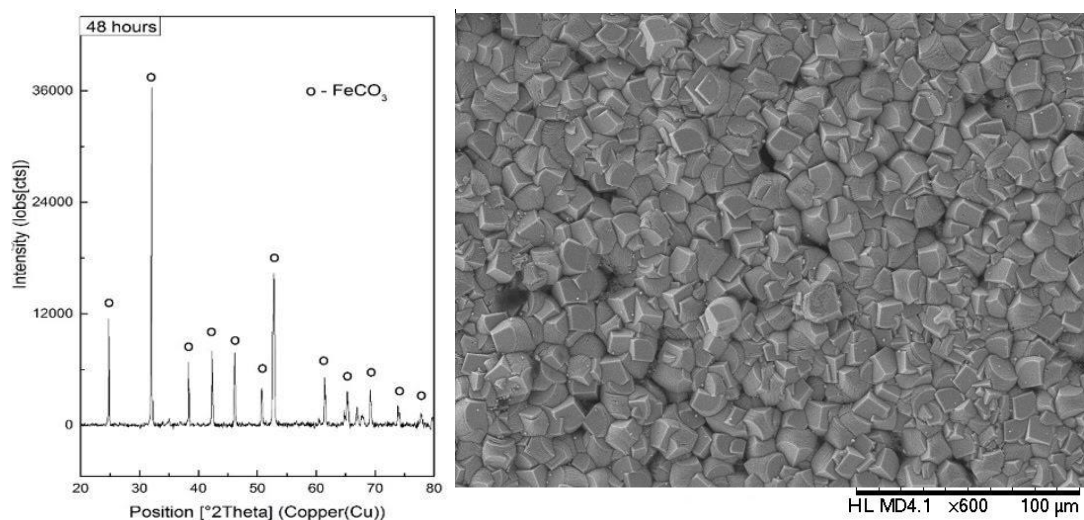


Figure 8-4. SEM image and XRD pattern of the formed films at conditions of CO_2 saturated water at temperature 60°C and partial pressure 100 bar for 48 hours.

8.3 Protective film removal under static conditions

Following the film formation tests, the protective films were exposed to the aqueous CO₂ solution to examine the stability of the film under static conditions at 50°C temperature. The samples preparation technique and test procedure are described in paragraphs 5.35.3.1 & 5.4.2 respectively. The test matrix is shown in Table 8-2.

Table 8-2. Static conditions test matrix

Pressure	Atom bar
Temperature (°C)	50
pH	4, 5 & 5.5
NaCl	3wt%
Saturation ratio (SR) of Fe ⁺	0
Time (hrs)	24

Three levels of pH were used in this experiment; 4, 5 and 5.5, in order to determine the extent of chemical dissolution and be able to select the pH value for the subsequent tests. Figure 8-5 shows the corrosion rates of the protected surfaces versus time at different pH values. At pH 4, the corrosion rate showed a rapid increase with time; after an immersion time of three hours, the corrosion rate increased, indicating of an iron carbonate film removal, enabling the underlying substrate to be corroded.

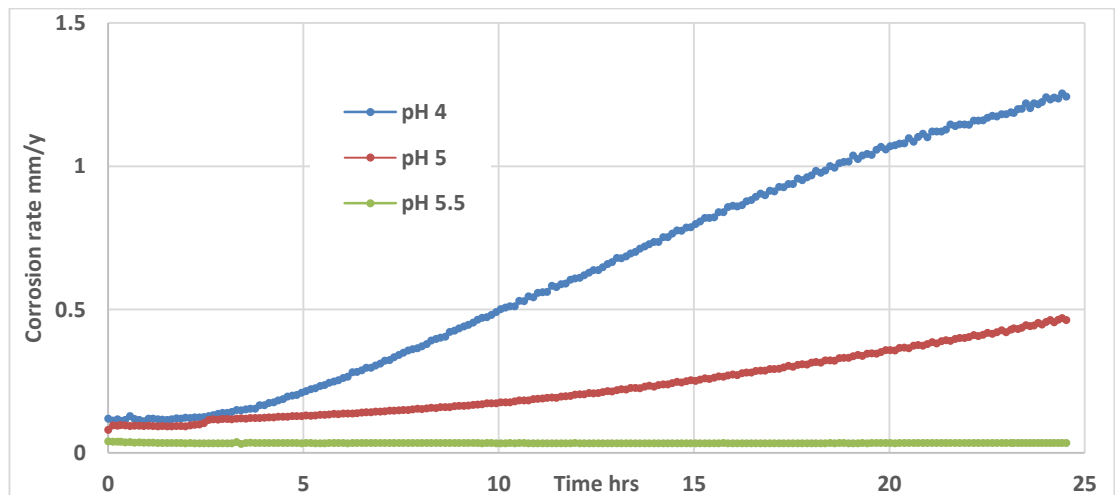


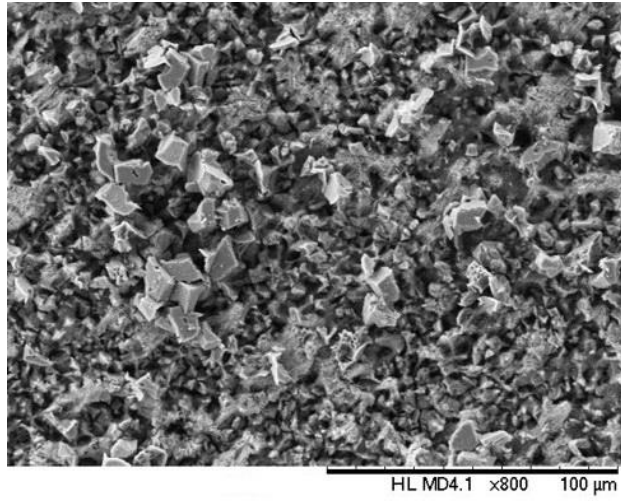
Figure 8-5. Corrosion rates of the covered surface with protective films at different pH values & temperature 50°C for 24 hrs

The corrosion rate curve at pH 5 was stable for first 6 hrs around the initial value. It then showed an increase with time in a linear trend. After 24 hr immersion time, a corrosion rate of 0.45 mm/y was recorded

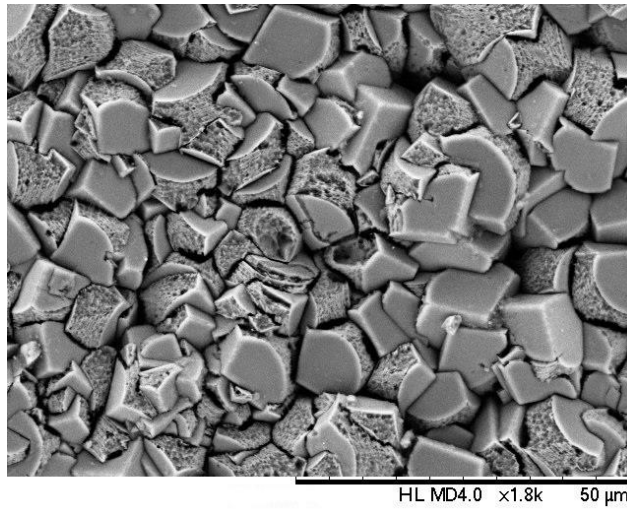
At pH 5.5 the corrosion rate was stable and constant throughout the 24 hr test period. The corrosion rate started with an initial rate and stabilised at this value to the end of the test. The constant corrosion rate at pH 5.5 and temperature 50°C indicated a stable level of protection throughout the immersion time offered by a compact and dense structure of a protective film.

Surface analysis using SEM images confirmed the corrosion rate. Figure 8-6(a) shows the protective films after 24 hrs immersion in a pH 4 solution. It is clear that the iron carbonate film exhibited severe chemical dissolution, where most of the prism-shaped crystals of iron carbonate were dissolved. The SEM image agrees well with the corrosion rate curve at the same pH in Figure 8-5. Figure 8-6(b) showed the image of the protective film after the exposure to pH 5 solution. Visually the protective films were in a better condition than after exposure to pH 4 for the same period of time, where no major gaps or empty pits were present on the surface, the film was almost covering the whole surface. However, there were signs of local film removal due to localised chemical dissolution. Most of the iron carbonate crystal edges were porous and damaged; this explains the rise in corrosion rate during the pH 5 static conditions test shown in Figure 8-5.

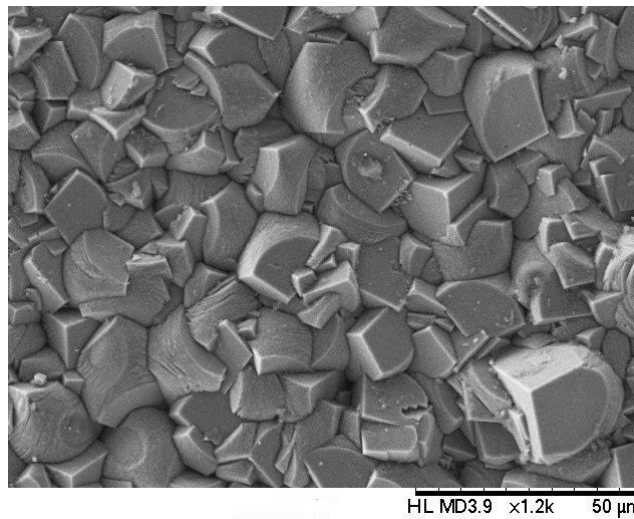
The SEM images of the surface of the protective film at pH 5.5 are shown in Figure 8-6(c). Visually, the film structure confirmed the outcome of the corrosion rate as function time curve in Figure 8-5, where no visual signs of films removal were present. Both the SEM image and the corrosion rate graph indicated that at 50°C temperature pH 5.5 level the structure of the protective film remained stable, and the overall process did not undergo removal throughout the test duration.



(a)



(b)



(c)

Figure 8-6. SEM images of the protective films on the X65 carbon steel surface at 50C after 24 hrs exposure to a- pH 4 b- pH 5 c- pH 5.5

8.4 Protective film removal under flowing conditions

Following the formation of the iron carbonate film, three tests were carried out under flowing conditions, to examine the effect of the wall shear stress on the stability of the protective film. By using three different gasket thicknesses associated with three different flow rates as shown in Table 8-3, it was possible to generate a range of wall shear stresses (10 to 655 Pa) resulting from a gradual increase of the flow velocity from 1.5 to 13.9 m/s.

Table 8-3. Tests sequence details for 50°C temperatures: Flow cell heights and flow rates

Tests Sequence	Gasket thickness (mm)	Flow rate (l/min)
1	2	41.5
2	3	29.5
3	6	32.5

Prior to the flowing condition tests, the surface roughness of the protective film was measured by a non-contact method using 3D optical microscopy based on white light interferometry. Figure 8-7 shows a 3D image of the protective films surface, from which the surface roughness was obtained to be $\sim 10\mu\text{m}$ in comparison to $\sim 0.5\mu\text{m}$ of the uncovered surface. The value of the surface roughness was used to calculate the friction factor and the wall shear stress across the samples. These correlations were described in the previous chapter equations 5.1 to 5.4. The calculated wall shear stress values across each sample are detailed in Table 8-4.

Using the same procedure for corrosion tests under flowing conditions described in 6.3.2 and 7.3.2, samples with protected surfaces were mounted on the test section and exposed to the wall shear stress. The shear stress was lowest at the 1st sample and stepped up in value on each followed sample up to the 5th sample where the highest shear stress was applied.

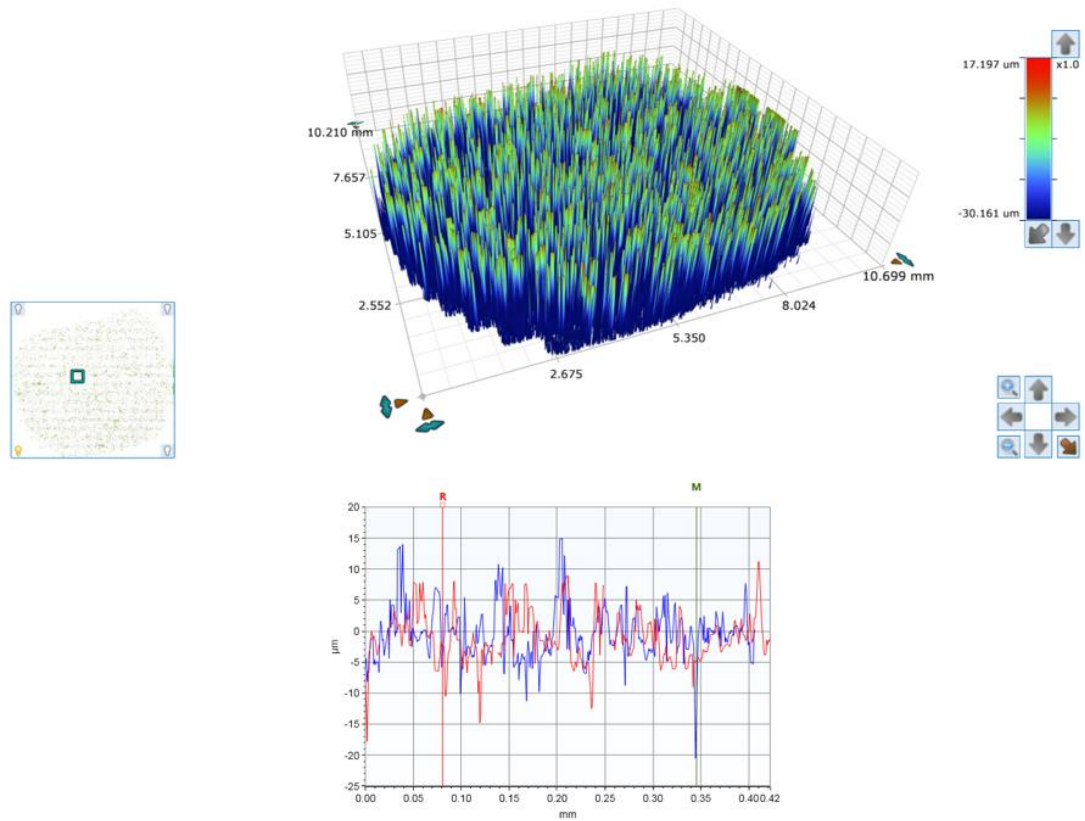


Figure 8-7. 3D analysis to the protected films surface roughness

Table 8-4. Cross section dimensions at every sample along the flow direction & flow cell height (gasket thickness) and the wall shear stress generated at each sample at temperature 50°C

Sample number	Width of the channel (mm)	Wall shear stress on sample		
		Channel height: 6mm Flow rate: 32.5 l/min	Channel height: 3mm Flow rate: 29.5 l/min	Channel height: 2mm Flow rate: 41.5 l/min
1	50.0	10 Pa	37 Pa	171 Pa
2	43.8	13 Pa	49 Pa	221 Pa
3	37.5	18 Pa	65 Pa	300 Pa
4	31.3	25 Pa	91 Pa	425 Pa
5	25.0	40 Pa	140 Pa	655 Pa

The flow condition test matrix is shown in Table 8-5. The pH of the solution was adjusted to the level of the 5.5 pH using NaHCO₃, at which the protective film exhibited no sign of removal at static conditions test. 5.5 pH level was used in the flowing conditions test to determine the effect of the hydrodynamics on the iron carbonate film, and whether the flow effect will accelerate the removal of the films or has no significant effect on the film removal. As has been suggested in the literature, mass transfer rate from/to the surface of the sample due to the flowing conditions has a limited effect on film removal process [39].

Studying the protective films removal under flowing conditions at critical pH will provide an opportunity to determine a critical wall shear stress and flow velocity at which the iron carbonate films remain protective and show no sign of removal at a temperature of 50°C.

Table 8-5. Test matrix of flowing condition test at temperature 50°C

pH	The critical value of the static test (pH 5.5)
Temperature (°C)	50
Time (hrs)	24
Range of flow velocity (m/s)	1.5 to 13.9
Range of wall shear stress (Pa)	10 to 655
Solution	3 wt. % NaCl
Electrochemistry measurement	LPR

8.4.1 Flow effects on the protective film removal

The protective film stability under flowing conditions test was examined using the matrix shown in Table 8-5. These films were formed following the procedure explained in 8.2. After films were formed, the samples were directly moved from the autoclave and placed in the test section of the flow loop. Each test was carried out using a freshly formed film. Figure 8-8 shows how the effect of the shear stress affects the corrosion rate and the stability of the protective films. The increase in corrosion rate at shear stress > 37 Pa is due to the enhanced removal of the films.

A rapid increase in corrosion rate was recorded under 655 Pa wall shear stress; the corrosion rate increased during the 24 hr test starting at 0.4 mm/y and reaching 4 mm/y at the end of the test, indicating a significant reduction in surface protection due to film removal process. At 300 Pa wall shear stress, the corrosion rate also increased with time. However, corrosion rate at the end of the test was much lower than 655 Pa.

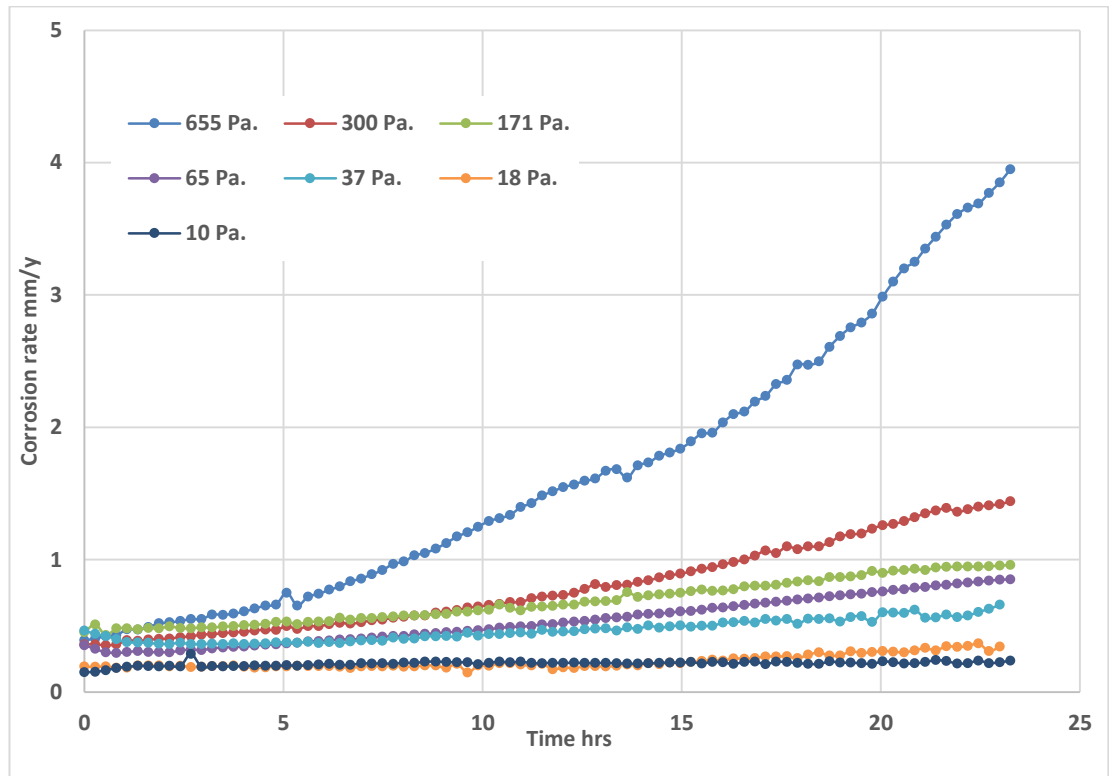


Figure 8-8. Corrosion rates of the protected surface under different levels of wall shear stress at pH 5.5 & temperature 50°C for 24 hrs.

The protective film was subjected to wall shear stress of 171 Pa, after 24 hrs exposure, corrosion rate increased to be ~ 1 mm/y. However, under 65 Pa wall shear stress corrosion rate was slightly less than the corrosion rate at 171 Pa, indicating a low flow sensitivity at shear stress range < 300 Pa. Where the flow sensitivity of the corrosion rate at shear stress > 300 Pa is much higher and showed a rapid increase with the flow.

The shape of the corrosion rate curves illustrate two different corrosion mechanisms; (a) at a high level of wall shear stress, a significant increase in corrosion rate due to the high removal rate of the protective film, and (b) at low level of wall shear stress below 300 Pa where the corrosion rate shows less flow dependency during the 24 hrs exposure time, suggesting a lower removal rate to the protective film.

In another word, at higher shear stress the removal rate is fast enough to reduce the protection degree of the iron carbonate film, allowing a higher rate of the cathodic species to diffuse to the surface. However, at lower shear stress < 300 Pa the removal rate is slower, leading to a lower increase in corrosion rate as a function of time. This behaviour was observed at 37 Pa shear stress. Where a minor increase in corrosion rate was recorded.

However, at wall shear stresses between 18 & 10 Pa corrosion rate showed a stable behaviour from the starting point up to the end of the test. After 24 hrs of exposure to both wall shear stresses, the corrosion rate did not show a significant increase, which indicates a full and constant protection of the surface by the iron carbonate films.

The SEM analysis of the surface and cross-section of the protective films after 24 hrs exposure to shear stress is shown in Figure 8-9. A clear film removal occurred at 655 Pa wall shear stress as shown in Figure 8-9(a). Large pieces of the protective film were removed from the covered surface leaving behind rough and deep holes and gaps which possibly became high turbulence zones on the surface leading to further removal. Therefore, the rapid increase in corrosion rate in Figure 8-8 at 655 Pa can be attributed to the high removal rate of the film from the surface. The cross-section SEM image of 655 Pa flowing condition confirm the removal of most of the outer layer of the protective films, where the thickness of the films decreased from $\sim 60\mu\text{m}$ to $\sim 5\mu\text{m}$.

An additional surface analysis is conducted to the cross-section of the iron carbonate films under 655 Pa was done using an element mapping technique as shown in Figure 8-10. This technique maps the distribution of the elements on the surface; each element is displayed using a different colour. The distribution of the elements on the cross section consists of Fe, O and C as expected. This is a clear indication that the thin bottom layer of the films was iron carbonate FeCO_3 .

Furthermore, SEM images of the protective film after exposure to 300 Pa showed similar observation to the surface at 655 Pa as shown in Figure 8-9(b) where, films were removed from some areas of the surface creating many gaps and rough pits on

the surface; however, it was much less than what was found at 655 Pa SEM image. Therefore the influence of flowing condition on corrosion rate under 300 Pa was not as significant as under 655 Pa as shown in Figure 8-8.

The cross-section at 300 Pa shear stress shows a thicker film than the previous 655 Pa readings, where the average thickness was $\sim 8\mu\text{m}$ almost twice the thickness of the films subjected to 655 Pa. This can explain the less dependency of the corrosion rate on the flowing conditions under 300 Pa shear stress. However, it also illustrates the high removal rate between shear stress 300 & 655 Pa.

Further SEM analysis revealed the removal of the compact films of iron carbonate was still occurring under 171 Pa shear stress. SEM image showed a small number of gaps/pits were present on the surface of the film as shown in Figure 8-9(c). Regardless of these few gaps and pits, the SEM image showed a uniform removal, where the whole iron carbonate layer was removed exposing the layer of iron carbonate films beneath it.

However, surface and the cross-section images under 65 Pa showed some crystals of iron carbonate were still present on the surface. The cross-section view indicates the thickness of the protective film is approximately twofold the thickness the film at 171 Pa. Similar surface analysis observation was recorded films under 37 Pa wall shear stress; however, in general, the films were slightly thicker as shown in Figure 8-11(a).

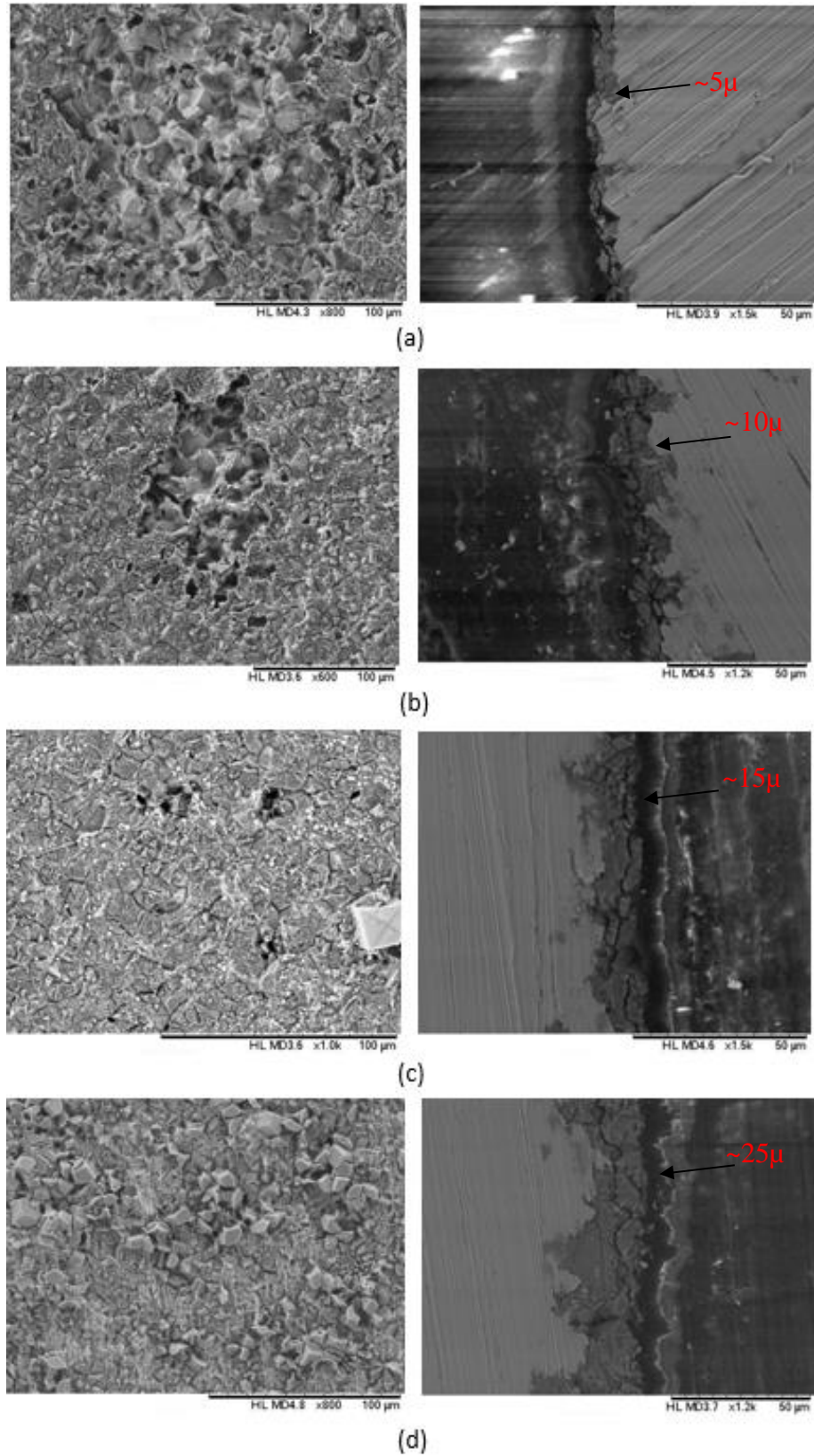


Figure 8-9. Surface and cross-section SEM images of the protective films after 24 hrs exposure to flowing conditions with various wall shear stresses: a- 655 Pa b- 300 Pa c- 171 Pa d- 65 Pa.

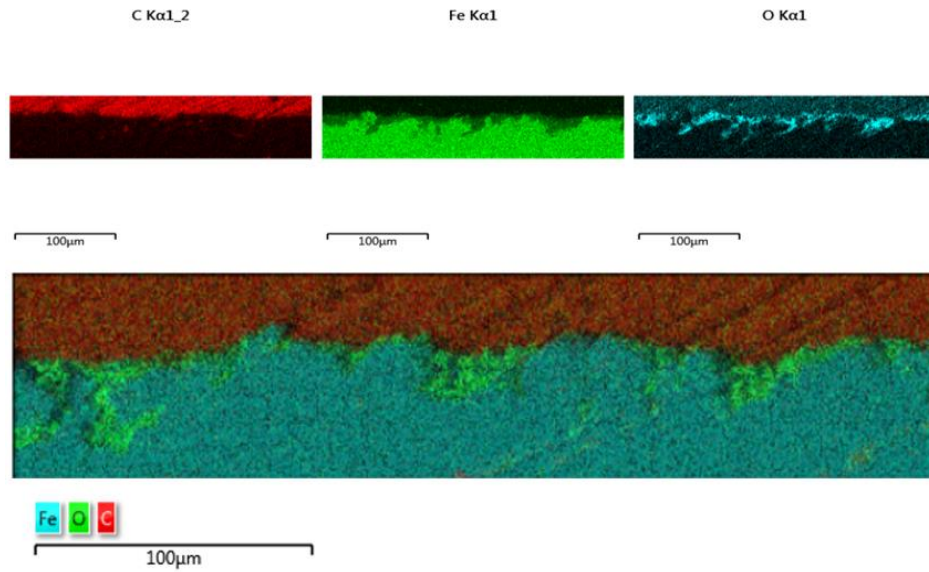


Figure 8-10. Element mapping profile of the cross-section of the iron carbonate films after exposure to 655 Pa shear stress

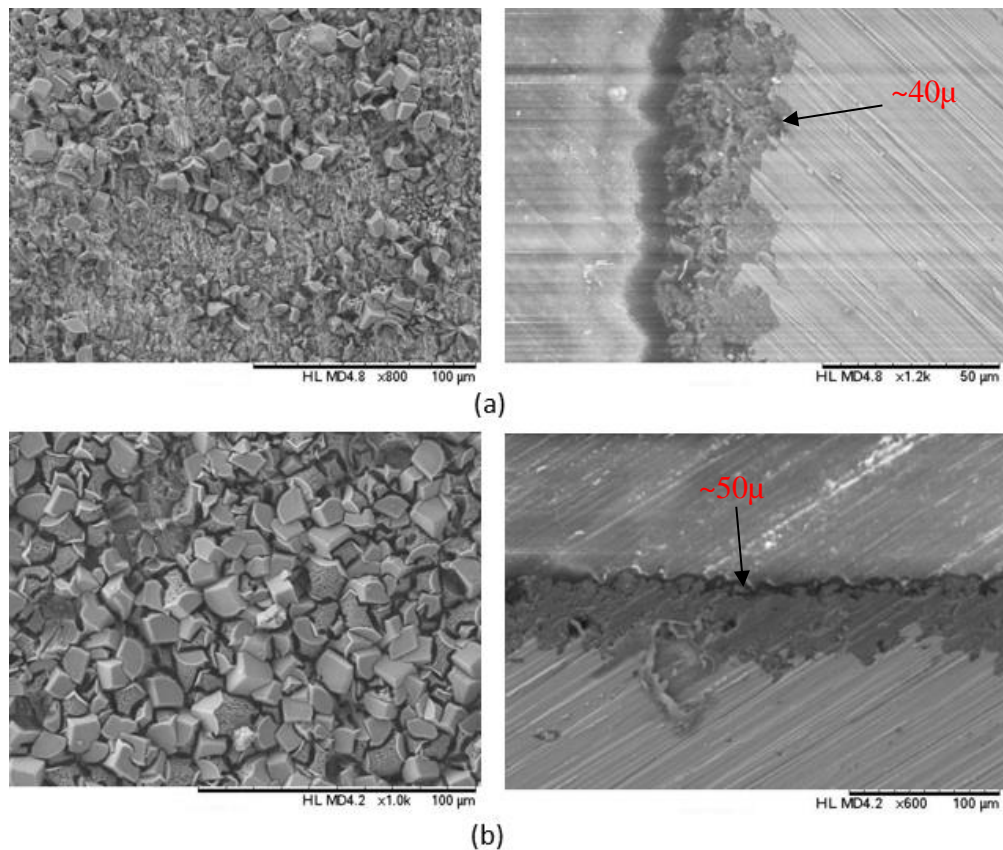


Figure 8-11. Surface and cross-section SEM images of the protective films after 24 hrs exposure to flowing conditions with various wall shear stresses:
a- 37 Pa b- 18 Pa

The SEM images of the surface and the cross-section view of the protective film subjected to 18 Pa are shown in Figure 8-11(b). In general, the SEM image showed a surface covered by iron carbonate film with few gaps and holes on the surface, in addition to porous and rough edges of some of the iron carbonate crystal. Figure 8-12 showed the protective film status under 10 Pa shear.

A fully covered surface with compact and dense prism-shaped crystals was observed on the surface. The cross-section view illustrates a layer of protective film with thickness $\sim 60\mu\text{m}$. Figure 8-12(b) shows a zoomed in image of the films confirming the stability of the films with no indication of removal. The cross-section views showed a $\sim 60\mu\text{m}$ as shown in Figure 8-2(c), film thickness which is similar to the thickness of the films before the exposure to the flowing condition.

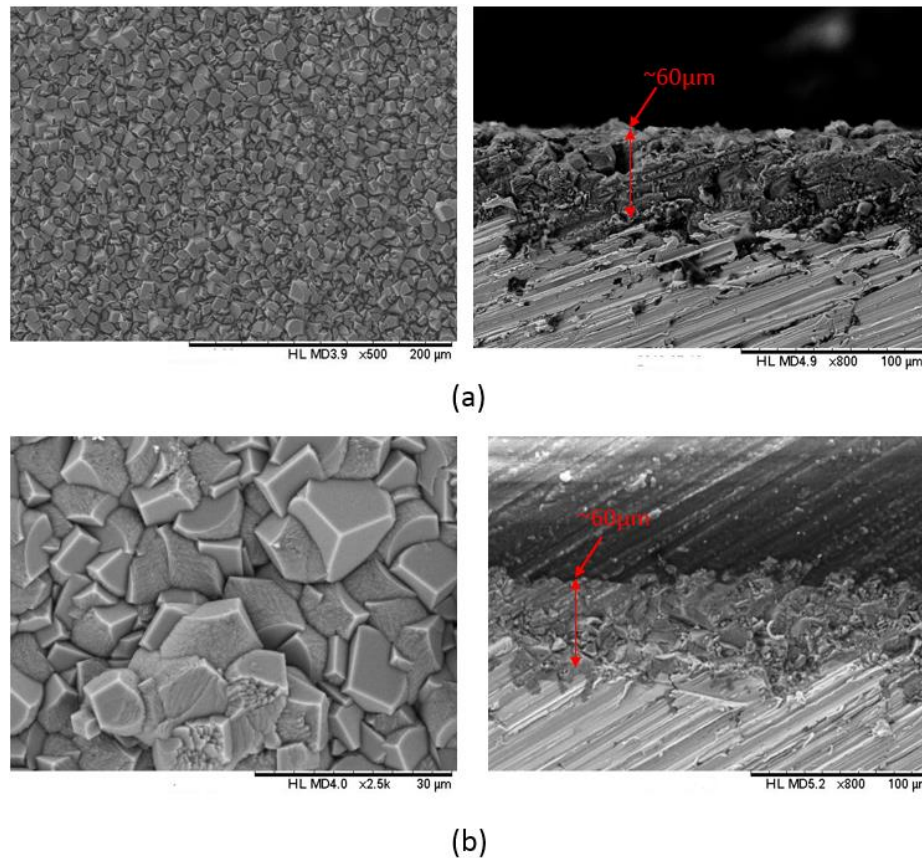


Figure 8-12. SEM images to the surface and cross-section of the protective films after 24 hrs exposure to 10 Pa wall shear stress at different zoom.

8.4.2 Mechanical effect of the flow (erosion) on the film removal

An additional test was carried out to investigate the mechanical effect of the flow on the overall protective film removal mechanism. The aim was to understand whether the hydrodynamic force of the flow is able to remove the protective film mechanically (erosion) or not. The test was conducted at a pH level of 6.9, at which the concentration of the cathodic species H^+ is extremely low in the bulk solution ($10^{-6.9}$ mol/l), this is to minimise the effect of the chemical dissolution process on the overall film removal mechanism. The solution temperature was set to 50°C. The wall shear stress was 655 Pa, which is the highest wall shear stress level across the protected surfaces generated by the flow loop. Figure 8-13 shows the corrosion rate as a function of time at wall shear stress 655 Pa. The corrosion rate at the starting point was ~0.009 mm/y, decreased slightly to ~0.007 mm/y and stayed stable to the end of the test, indicating that the surface protection level was maintained throughout the test.

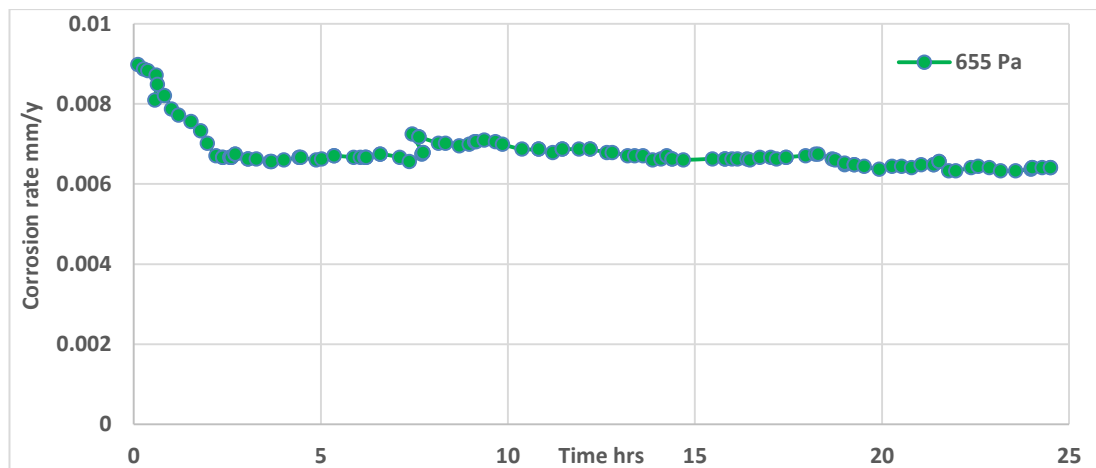


Figure 8-13. Corrosion rate at 655 Pa as a function of time, temperature 50°C, pH 6.9.

The SEM images agreed well with corrosion rate behaviour, Figure 8-14 shows the surface analysis of the film after 24 hrs exposure to 655 Pa shear stress. The images show a fully covered surface with compact structure of iron carbonate film, no sign of removal or gaps on the surface. The cross-section view indicated a ~60µm thick protective film similar to the thickness of the freshly formed film prior to the test. The LPR measurement and the surface analysis of the protective film confirmed that the mechanical removal (i.e. erosion) of the flow has a negligible effect on the overall film removal process. Further analysis of the film removal mechanisms is detailed in Chapter 10.

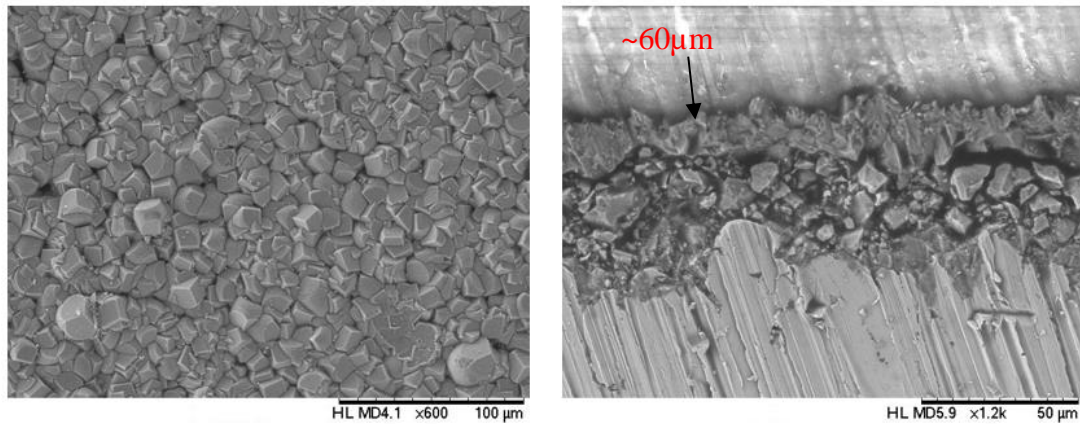


Figure 8-14. SEM images of the top view of the surface and the cross-section after 24 hrs exposure to wall shear stress 655 Pa at temperature 50°C and pH 6.9

8.5 Summary

At temperature 50°C iron carbonate films were formed on the X65 carbon steel samples using a high-pressure autoclave, the films were compact and dense with ~60μm thickness. Films stability was tested under different pH solutions and static conditions. Corrosion rates and SEM analysis to the surface and cross-section of the protective film helped to determine the minimum pH level at which the film maintain stability and a high degree of protection under static conditions (critical pH for temperature 50°C). Moreover, the film stability was examined under flowing conditions. Corrosion behaviour and surface analysis determined the maximum wall shear stress can apply without iron carbonate films exhibit a removal process at 50°C operating temperature.

The protective films removal rate was a function of wall shear stress, indicating a mass transfer controlled reaction. Critical pH and wall shear stress are the threshold conditions at which no films removal is likely to occur for an operating temperature of 50°C.

These findings may contradict with Yang et al [39] work, Yang concluded that the mass diffusion rate has limited effect on the mass loss rate of the protective film. However, Yang used low flow velocity range between 0.6 to 2 m/s to examine the effect of the mass transfer on the dissolution rate of the protective films. At this small range of flow velocities, the effect of the mass transfer is small and hard to observe, this assumption was confirmed during Ruzic et al [23] study, where the effect of the mass transfer on the film removal was small until the flow velocity became ≥ 1.2 m/s.

Chapter 9. Results of X65 carbon steel protected surface under flowing conditions at 80°C

9.1 Introduction

In this chapter, a further investigation was carried out to examine the iron carbonate films stability under flowing conditions at higher temperature environment of 80°C. At this temperature, iron carbonate protected surfaces exhibit different corrosion behaviour than at lower temperatures < 70°C [10], where the solubility of the iron carbonate films decreases at temperature 80°C [217]. It is well known that diffusion rate of the chemical reactants increases as a function of temperature [218]. Therefore the formation of compact protective films is faster at high temperatures than at lower temperatures. Dense and compact films provide better protection to the surface. However, the level of protection of these films may be decreased by the removal of these films due to hydrodynamic or chemical effects, inflicting a high corrosion threat and risk of failure on the exposed steel surface. The present study was carried out to investigate the protective film stability and removal at high temperature. Two removal mechanisms were studied; removal by chemical dissolution and by the hydrodynamic effect. The results show that films removal may occur at high pH level due to the chemical dissolution under static conditions, however, at flowing condition, the hydrodynamic effect accelerate the chemical dissolution on the surface causing films removal. The effect on high temperature was investigated on the removal process, where the results suggest that at high-temperature chemical dissolution occur at higher pH values than at lower temperature.

9.2 Iron carbonate FeCO₃ film formation

Iron carbonate films were formed using high-pressure CO₂ autoclave prior to each test. Films formation procedure was explained in paragraph 8.2. The outcome of each formation test showed a thick and dense iron carbonate film. Figure 9-1 shows the SEM & EDS analysis to the surface of the protective film.

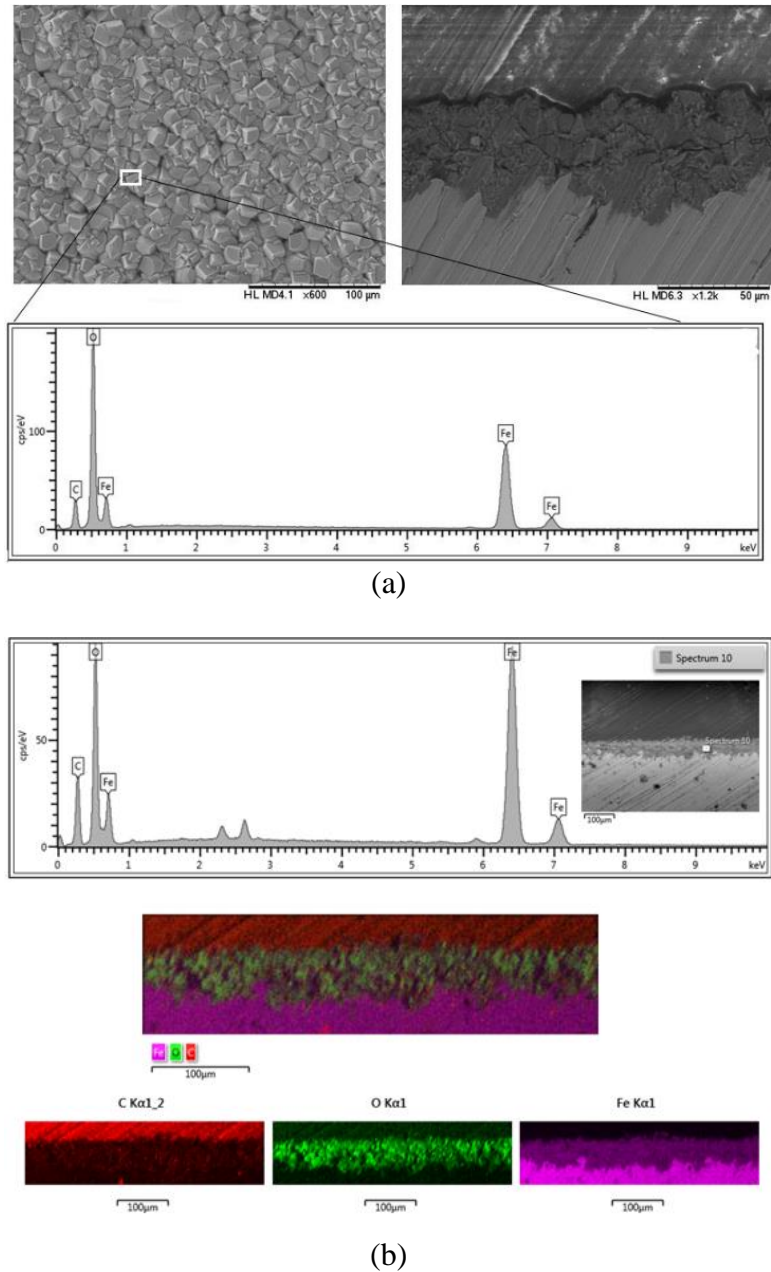


Figure 9-1. SEM & EDS analysis image of the surface and the cross-section of the iron carbonate films after the formation test.

9.3 Protective films removal under static conditions.

The stability of the iron carbonate films at various pH levels and 80°C temperature was examined under static conditions through a sequence of four tests, each test was carried out at different pH solution; 4, 5, 5.5 and 6, to determine the pH level at which no films removal reaction occur at 80°C temperature.

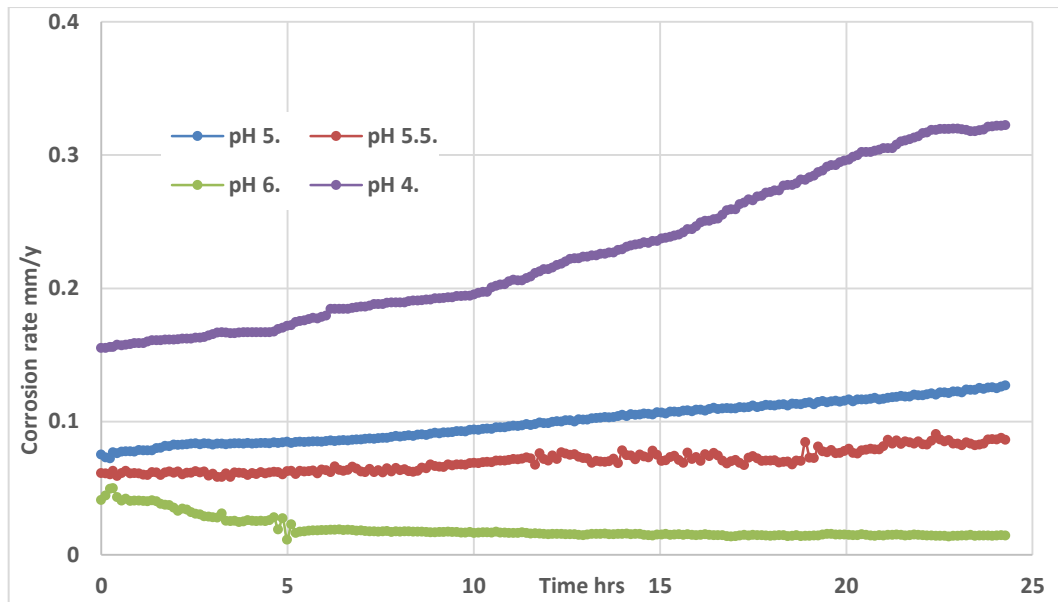


Figure 9-2. Corrosion rates of the covered surface with protective films at different pHs & temperature of 80°C for 24 hr

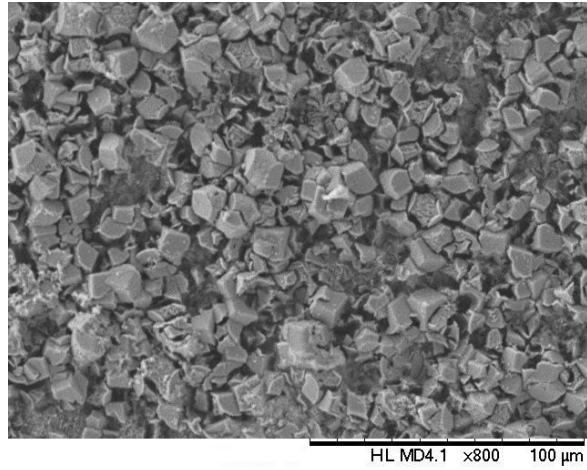
Figure 9-2 shows the corrosion behaviour of the protective films FeCO_3 at different solution pH values as a function of time. At pH 4 corrosion rate at the starting point was ~ 0.15 mm/y, the corrosion rate was stable within the first 4 hrs, which can be an initiation period of film dissolution process. After that, corrosion rate increased as a function of the time up to ~ 0.32 mm/y. At pH 5 solution, corrosion rate showed another increase with the time. At the beginning of the test, the corrosion rate was stable for ~ 6 hrs as an initiation period. However, after the 6 hrs, corrosion rate increased linearly to the end of the 24 hrs. The overall shape of the curve of pH 5.5 indicated an initiation period of films removal for the first 8.5 hrs, however, it increased slightly after 24 hrs. At pH 6, corrosion rate showed different behaviour than the previous three tests. For ~ 1.5 hr corrosion rate was stable around its initial value, however, corrosion rate then decreased down slightly to a lower rate and stabilised till the end of the test. This behaviour can be attributed to the stability of the protective films at pH 6 solution and temperature 80°C, where no film removal occurred and the surface of the carbon steel was fully protected throughout the test period under these conditions.

Subsequent to the film removal tests at static conditions, the surface analysis was carried out on the tested film surface using SEM technique, after 24 hrs exposure to a CO_2 saturated solution at three different pH solutions. Figure 9-3(a) illustrates the surface analysis of the protective film after 24 hr immersion in pH 4 solution.

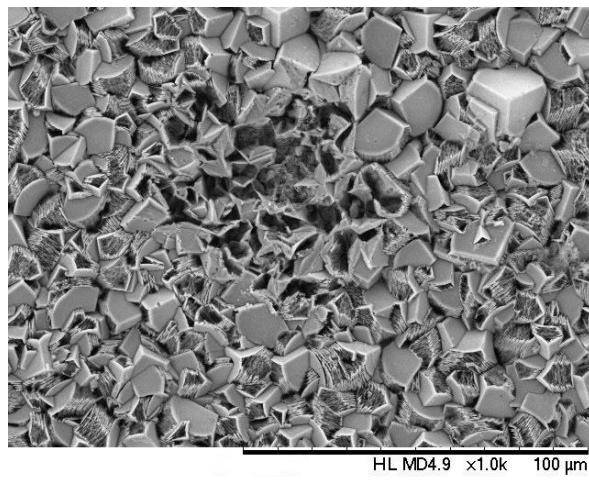
It was clear that many of the iron carbonate films were removed from the surface. However, the steel surface is still covered and no bare surface was exposed to the solution. The SEM surface analysis explained the corrosion rate curve at pH 4, where the corrosion rate at the end of the test was twofold higher than the initial value. Figure 9-3(b) shows a SEM image of the protective film immersed in pH 5 solution, many gaps and holes were observed on the surface which indicates film removal, where the prism-shaped crystals of iron carbonate were partially or fully dissolved.

Figure 9-3(c) shows the surface condition after exposure to a pH 5.5. It showed a fully covered surface with iron carbonate crystals. However, some of the protective film edges were porous and partially dissolved as resulted of a local chemical dissolution. The SEM analysis confirmed that, although the increase in corrosion rate at pH 5.5 was relatively low as shown in Figure 9-2, the iron carbonate crystals showed a significant deformation and removal, which may develop and progress to higher removal rate if exposed to pH 5.5 solution for longer durations.

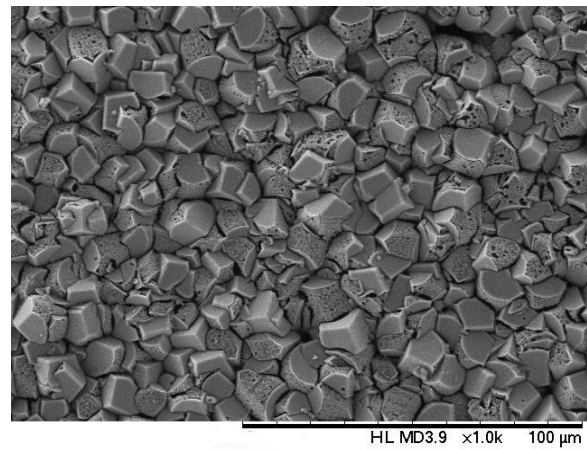
The SEM image at pH 6 solution is shown in Figure 9-4. Visually, the protective films were in good condition with no signs of film removal on the surface. It showed a fully covered surface with compact and dense structure of iron carbonate crystals. The surface analysis confirmed the corrosion behaviour at pH 6 in Figure 9-2, where it declined within the first 5 hrs down to its minimum value and stabilised till the end of the test. Both the corrosion rate curves and the surface analysis of the protective film indicate that; at static conditions environment, temperature 80°C and 3% wt. NaCl solution the critical pH level is 6, at which the protective films exhibit no films removal due to chemical dissolution.



(a)



(b)



(c)

Figure 9-3. SEM images of the protective films on the X65 carbon steel surface at temperature of 50°C after 24 hrs exposure to a- pH 4 b- pH 5 c- pH 5.5

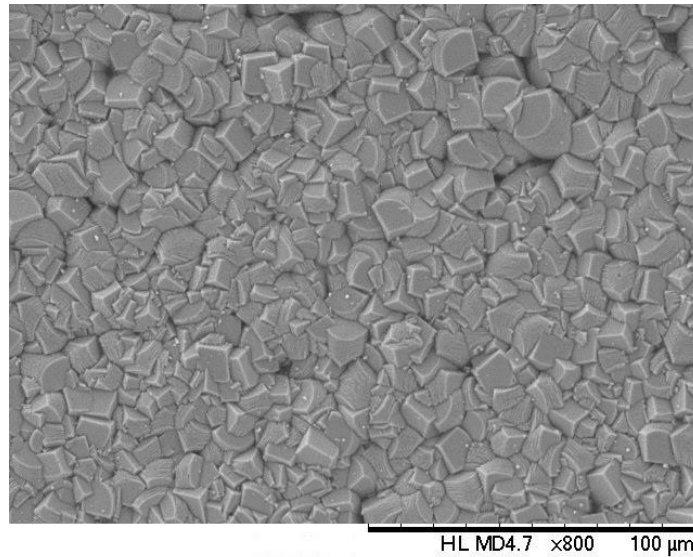


Figure 9-4. SEM images of protective films on the X65 carbon steel surface at 80°C after 24 hrs exposure to pH 6 solution

However, for more verification of this data, the test duration was extended from 24 hrs to 48 hrs to confirm whether or not the pH 6 is the critical pH level at 80°C where no chemical dissolution is likely to occur even after the first 24 hrs. Therefore the corrosion behaviour of the iron carbonate films at pH 6 and 80°C temperature was examined for 48 hrs immersion time. The outcome of this test confirms the data obtained from the 24 hrs, where the corrosion rate showed a stability at minimum value throughout the test period as shown in Figure 9-5

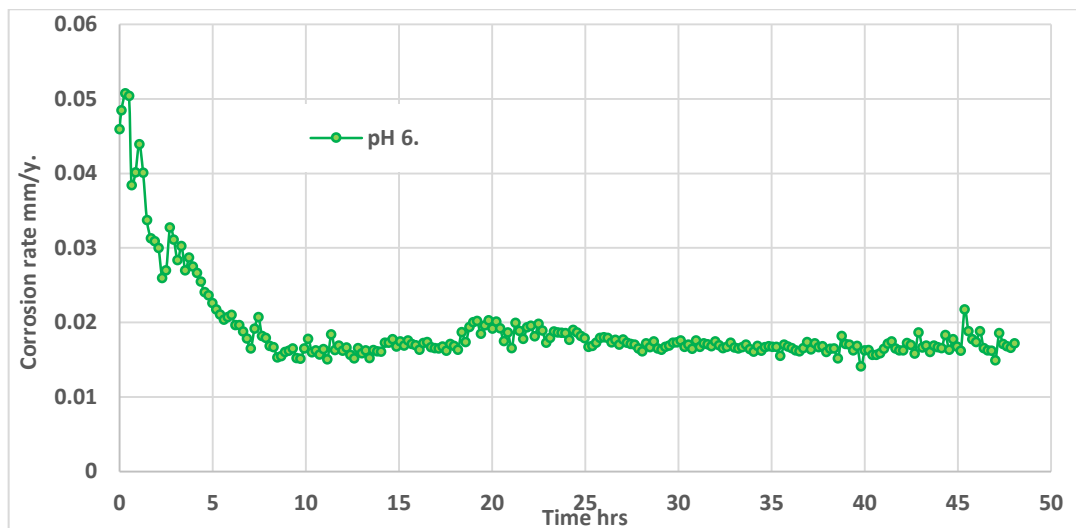


Figure 9-5. Corrosion rates of the covered surface with protective films at pH 6 and temperature of 80°C for 48 hrs exposure time.

The SEM analysis of the protective films surface after 48 hrs exposure is shown in Figure 9-6. The SEM image illustrates a fully covered surface with dense iron carbonate crystals with no visible sign of films removal may occur during the 48 hrs exposure time. The outcome of this test confirmed the previous test results which suggested that pH 6 is the critical pH level of the CO₂ saturated environment at a temperature of 80°C.

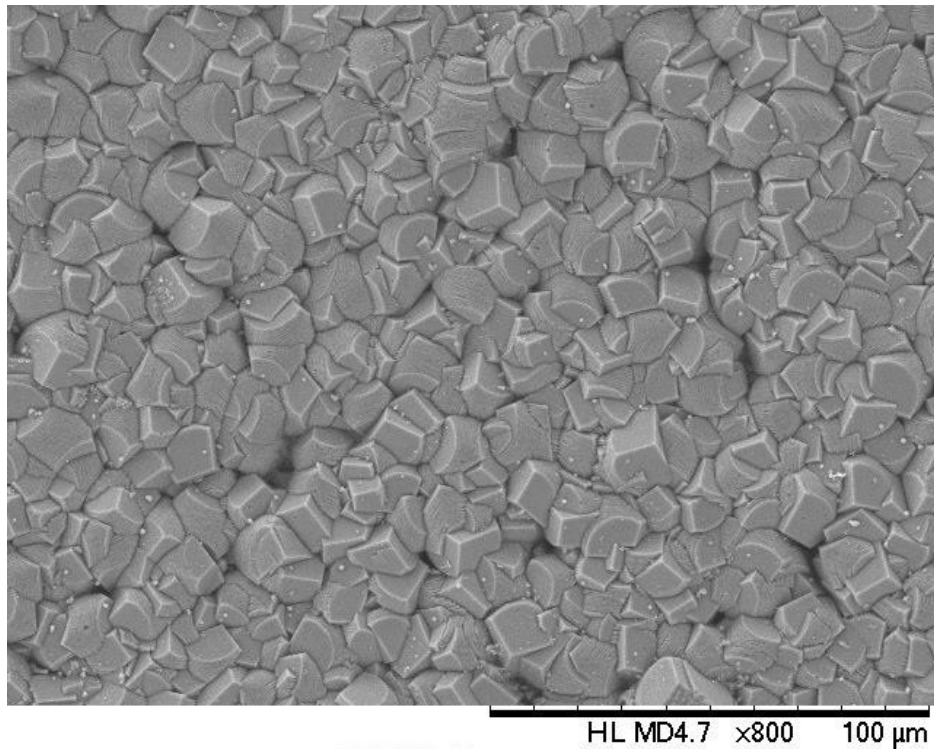


Figure 9-6. SEM image of the protective films surfaces at pH 6 & 80°C temperature for 48 hrs.

9.4 Protective film removal under flowing conditions at 80°C and the critical pH

Following the static tests series, the effect of the wall shear stress on the stability of the protective films were examined using the test matrix in Table 9-1. Iron carbonate films were formed prior to the flowing condition tests using the procedure explained in paragraph 8.2. Film stability test under shear stress was carried out to investigate the removal mechanism at a high temperature of 80°C and compare this with removal process of the protective film at temperature 50°C.

The pH of the aqueous solution was adjusted to the pH 6. This will determine whether the hydrodynamic force has any effect on the removal process. And if there was an influence from the hydrodynamic force on the removal of the film, it will be possible to identify the mechanisms of that effect.

The wall shear stress was generated using three different flow rates associated with three different gasket thicknesses as shown in Table 8-3, which generated a range of wall shear stresses 10 to 592 Pa and flow velocities 1.8 to 13.3 m/s. The flow parameters were calculated using the empirical relations which were described in the previous chapter equations 5.1 to 5.4.

Table 9-1. Test matrix of flowing condition test at a temperature of 80°C.

pH	The critical pH of the static test (pH 6)
Temperature °C	80
Time (hrs)	24
Range of flow velocity (m/s)	1.8 to 13.3
Range of wall shear stress (Pa)	10 to 592
Solution	3 wt. % NaCl
Electrochemistry measurement	LPR

The roughness of the protective films surface was measured using similar methodology explained in paragraph 8.4. Table 9-2 shows the calculated values of the wall shear stress across the protected surfaces under different flow conditions and temperature 80°C. Table 6-4 and Table 9-2 show the value of the wall shear stress across the samples, the former is for the clean surfaces and the latter is for the covered surfaces.

Table 9-2. Cross section dimensions at every sample along the flow direction & Flow cell height (gasket thickness) and the wall shear stress generated at each sample at temperature 80°C

Sample number.	Width of the channel mm	Wall shear stress on sample		
		Channel height: 6mm Flow rate: 32.5 l/min	Channel height: 3mm Flow rate: 29.5 l/min	Channel height: 2mm Flow rate: 41.5l/min
1	50	10 Pa	35 Pa	152 Pa
2	43.8	12 Pa	45 Pa	197 Pa
3	37.5	16 Pa	61 Pa	266 Pa
4	31.3	24 Pa	87 Pa	381 Pa
5	25	36 Pa	134 Pa	592 Pa

9.4.1 Flow effect on the protective film removal

The stability of the protective films was examined. Corrosion behaviour of the protected surface was tested under high wall shear stress 592 Pa and stepped down at each following tests down to 10 Pa. Figure 9-7 details the corrosion rate of the protective films surface, at 592 Pa corrosion rate increased with time. Throughout the first 20 hrs, corrosion rate increased slowly, then the corrosion rate increased rapidly where it doubled in value compared to initial value. This indicates that the first 20 of the 25 hrs divided into two regions, an initiation for 5 hrs and slow progress region for 15 hrs, and during the last 5 hrs film removal was accelerated rapidly leading to a fast increase the corrosion rate. At 266 Pa wall shear stress, corrosion rate showed similar behaviour.

Corrosion rate at 266, 152 and 61 Pa showed different initiation periods which was an inverse function of the applied shear stress, where it exhibited 10, 15 and 20 hrs respectively. The stable corrosion rate can be described solely as an initiation period of the films removal process, however, it progressed and accelerated during the second period of the test duration.

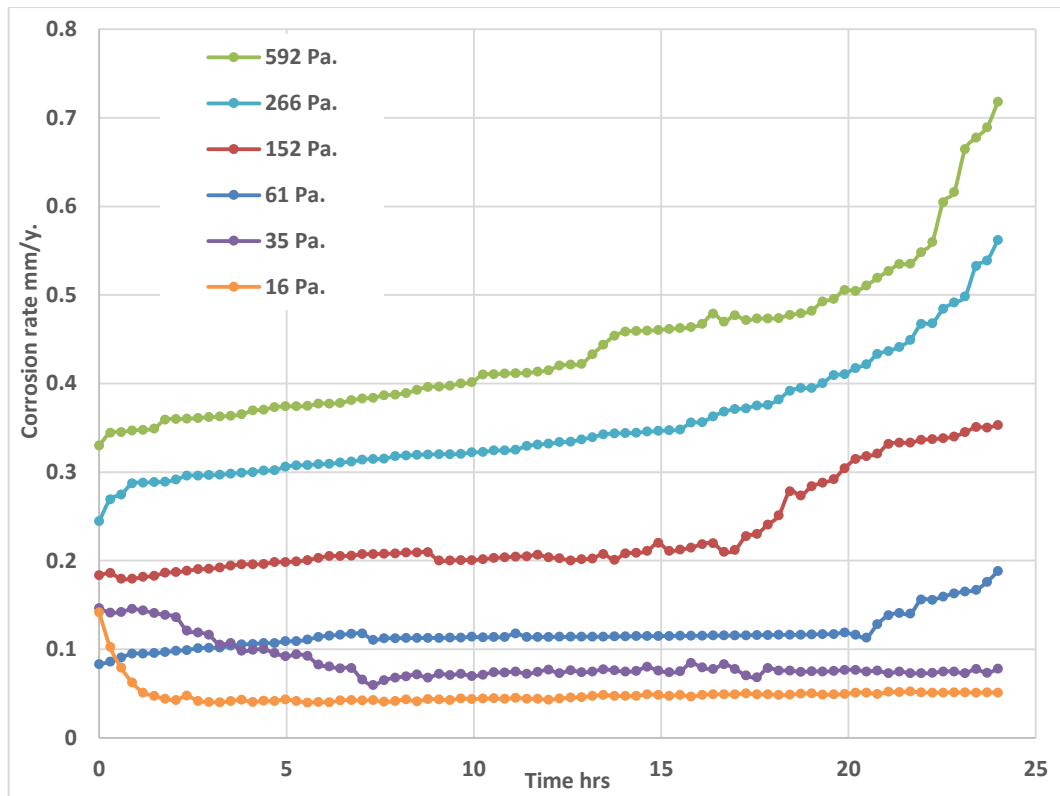


Figure 9-7. Corrosion rates of the protected surface under different levels of wall shear stress at pH 6, temperature 80°C and for 24 hrs.

However, at 35 Pa the corrosion rate of the protected surface showed different behaviour, where the corrosion rate at the beginning of the test was at an initial value, then it decreased down and stabilised to the end of the test. Moreover, corrosion rate at 16 Pa showed a similar behaviour of the corrosion rate under 35 Pa, where at 16 Pa the initial value of the corrosion rate decreased within 1.5 hrs and remained constant at until the end of the 24 hrs exposure time.

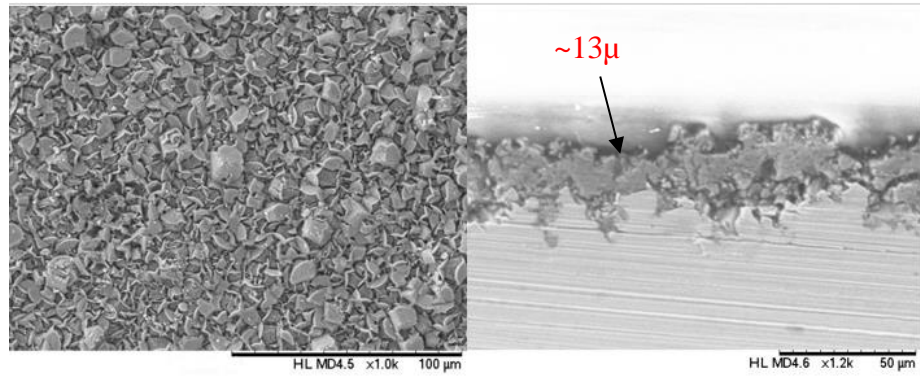
Therefore, from the overall shape of the corrosion rate curves, two wall shear stress levels of 35 & 16 Pa can be selected as the critical wall shear stress. At both 35 & 16 Pa corrosion rates showed a stable behaviour throughout the test period, indicating that the degree of protection of the iron carbonate films did not decrease as consequence of the exposure to the wall shear stress for 24 hrs.

SEM analysis was carried out on the surface and the cross-section after each test. Images are shown in Figure 9-8. The SEM image of the iron carbonate films after 24 hrs exposure to shear stress 592 Pa shows dissolution and removal, where most of the prism-shaped crystals of iron carbonate were damaged. The cross-section view indicates a reduction in the protective films thickness from $\sim 60 \mu\text{m}$ prior to the test to $\sim 13 \mu\text{m}$. The reduction of the protective layer thickness decreased the degree of the protection of the iron carbonate film, leading to an increase in corrosion rate.

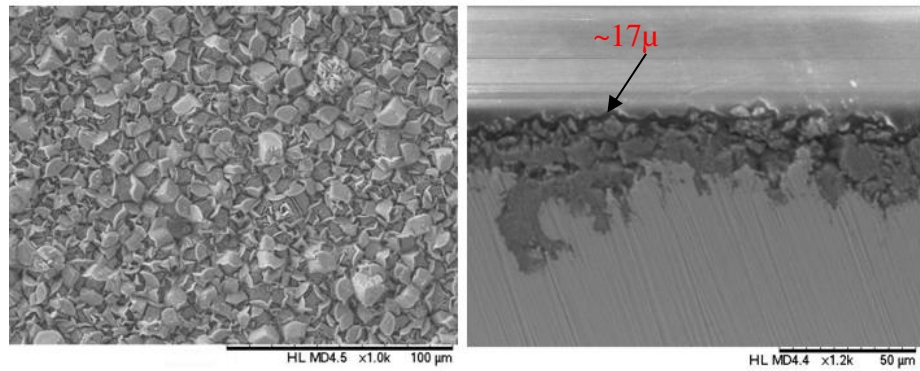
The SEM image under 266 Pa showed similar observation. Where the iron carbonate crystals were damaged and exhibited a removal process, consequently the thickness of the protective films was decreased to $\sim 25\%$ of what it was prior to the test. Further SEM analysis was carried out on the protected surface subjected to 152 Pa. The protective film was deformed and the appearance of the crystals was transformed from the prism to a non-uniform smaller shaped crystals. The SEM image of the cross-section view illustrated a $\sim 60\%$ reduction in the protective films thickness.

Surface analysis of the protective films at 61 Pa is shown in Figure 9-8. The SEM images of the surface and the cross-section showed again film removal, where a sharp edge crystals are present on the surface, which can be due to a local film dissolution. The cross-section view shows a $\sim 45\%$ decrease in the protective films thickness.

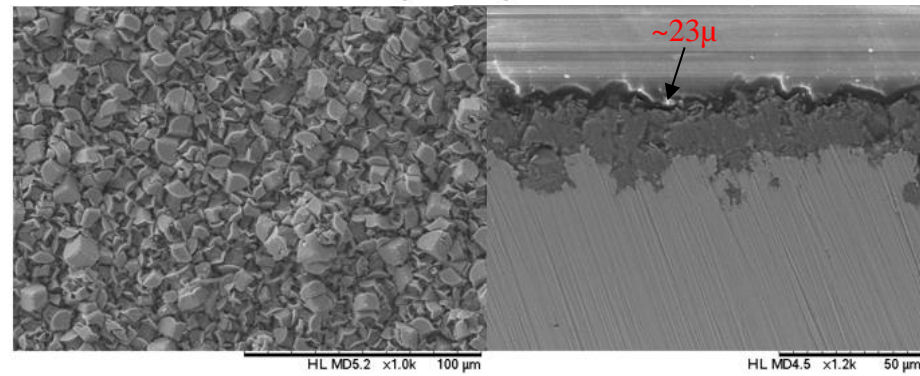
At 35 & 16 Pa the SEM images of the surface showed a fully covered surface with compact and fully prism-shaped iron carbonate crystals, with no visible gaps or holes present on the surface of the film. The cross-section view shows the thickness of the protective films as $\sim 60 \mu\text{m}$ which is similar to the thickness of the protective films before the exposure Figure 9-9.



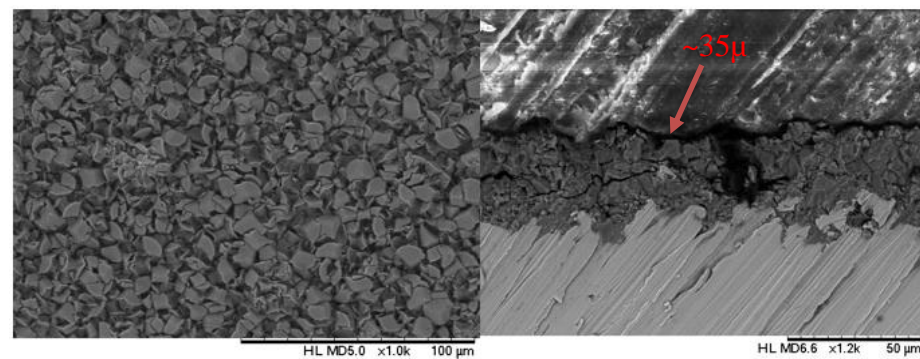
(592 Pa)



(266 Pa)



(152 Pa)



(61 Pa)

Figure 9-8. Surface and cross-section SEM images of the protective films after 24 hrs exposure to flowing conditions with various wall shear stresses at temperature of 80°C.

At 35 Pa the SEM image showed a fully covered surface with prism-shaped crystal of iron carbonate. However, some of the crystals appeared rough and porous indicating minor and local dissolution occurred at the crystals edges. The cross-section view showed a $\sim 60\mu\text{m}$ thickness of protective films which indicated that no reduction in the protective films thickness accrued throughout the 24 hrs exposure to 35 Pa.

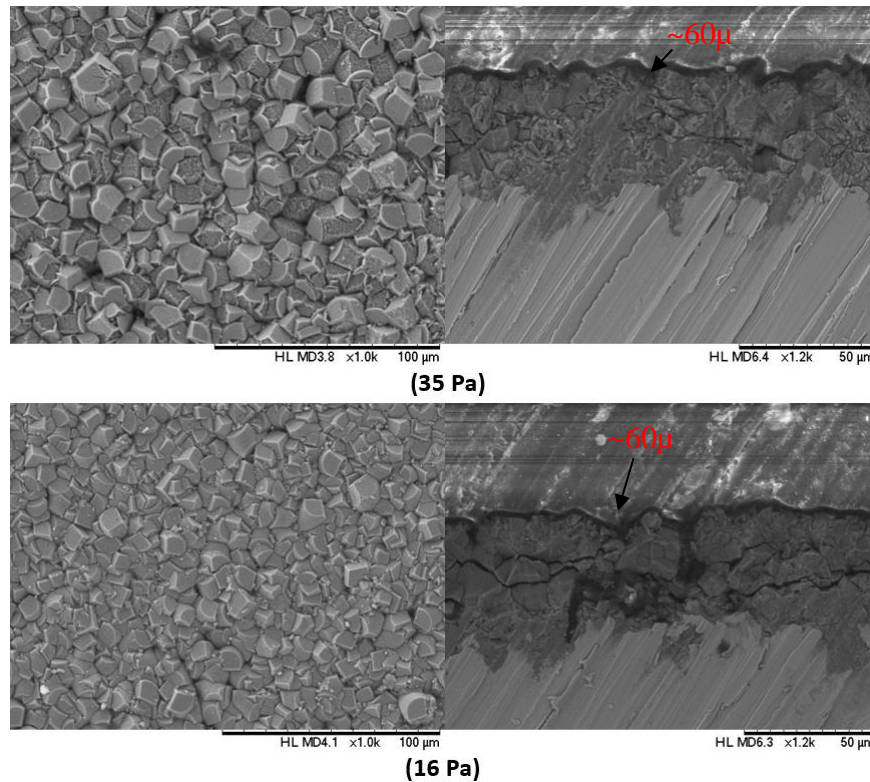


Figure 9-9. Surface and cross-section SEM images of the protective films after 24 hrs exposure to flowing conditions with wall shear stresses 35 & 16 Pa at temperature of 80°C

The SEM images of the surface and cross-section of the iron carbonate film at shear 16 Pa showed that at this wall shear stress value no films removal likely to occur. Therefore, under flowing conditions environment the 16 Pa is the wall shear at which the iron carbonate films exhibit a full protection to the carbon steel surface at 80°C temperature.

9.5 Summary

In the current study, the effect of high temperature on the stability of the protective films under flowing conditions was examined. To understand the removal mechanism at high-temperature environment, and to determine the pH and wall shear stress at the protective film maintains its compact structure without undergoing film removal under hydrodynamic force at 80°C.

The outcome of the protective films stability tests confirmed that Iron carbonate film removal under static condition occurs at pH solutions below pH 6. However at $\text{pH} \geq 6$ no films removal was observed. Iron carbonate stability was investigated under flowing conditions using the critical pH solution. The iron carbonate layers exhibited a significant films removal due to a uniform chemical dissolution reaction across the protected surface with no visible gaps or holes on the surface. The rate of the chemical dissolution reaction was a function of the flowing conditions. By testing the stability of the iron carbonate layer under various levels of wall shear stresses it was possible to determine the maximum wall shear stress can apply on the protective film without undergoing a removal process at 80°C.

Chapter 10. Overall Discussion

10.1 Introduction

In this chapter, an appraisal of the work done in this thesis is presented to highlight the contribution this research has made towards an understanding of the flow induced corrosion behaviour of X65 carbon steel. The results show the importance of the flow parameters, the nature of the starting surface and the fluid properties on the corrosion behaviour of the X65 carbon steel. The protective film removal and the mechanisms of such removal under flowing at different fluid temperatures are appraised.

10.2 What controls the corrosion of the unprotected surface of X65 under flowing conditions and pH 6.6?

An important finding from this work relates to the fact that, corrosion behaviour as a function of time at temperature 50°C & 80°C showed a clear flow dependency. Corrosion rate reached a steady state value at different times; at 1.6 Pa the corrosion rate took 5 hrs to stabilise, however at higher shear stresses the time required was 30 minutes as shown in Figure 6-12. The influence of the wall shear stress level on the corrosion rate was more significant at a higher temperature of 80°C.

The corrosion behaviour at a shear stress range 7.5 to 26.5 and at 80°C, showed that the corrosion rate ≥ 26.5 Pa exhibited no stabilisation period, with the final corrosion rate being equal to the initial value as shown in Figure 6-13. At < 26.5 Pa corrosion rate showed different length of stabilisation periods depending on the applied shear stress. Further confirmation to this proposal will be established by analysing the outcome of the corrosion behaviour tests at pH 4 and temperatures 50°C and 80°C.

10.2.1 Flow sensitivity of the corrosion rate

Corrosion rate in general as a function of wall shear stress/flow velocity at both temperatures 50°C & 80°C. The dependency of the corrosion rate at pH 6.6 environment on flow was an interesting behaviour since the diffusion limited species (i.e. H⁺) concentration in the bulk solution was low.

Nevertheless, low H⁺ concentration does not entirely eliminate the effect of hydrogen ions or other components of the carbonic acid H₂CO₃ diffusion rates to/from the steel surface, especially in the highly turbulent flow. Corrosion flow dependency at pH ≥ 6 is not a new phenomenon. Several previous studies investigated this behaviour and Table 10-1 summarises some of these studies.

Table 10-1. Summary of the studies in literature related to the corrosion flow sensitivity at high pH conditions.

The study	The observation	The given analysis
Vetter [219] 1967	Corrosion rate increased with flow at pH ≥ 6	The carbonic acid has a diffusion control effect
Schmitt et al [220] 1977	Corrosion rate increased with flow at pH ≥ 6	The carbonic acid has a diffusion control limiting current
Nesic et al [60, 221] 1995, 2010	Corrosion rate increased with flow at pH ≥ 6	The carbonic acid has a diffusion current limit component
Ferreira et al [27] 2015	Corrosion rate increased with flow at pH ≥ 6	Turbulence flow effect. No further details were given
The current study	Corrosion rate increased with flow at pH ≥ 6	-

Vetter [219] proposed that the reduction of the carbonic acid is not restricted to the chemical controlled reaction, but it can also be under diffusion control. The reduction of carbonic acid can only be under pure activation control in low flow velocity conditions, where the thickness of the diffusion boundary layer is greater than the reaction layer. The outcome of the Schmitt et al [220] study agreed with Vetter's conclusion, where Schmitt concluded that the carbonic acid H₂CO₃ has a diffusion-controlled limiting current in addition to its activation controlled cathodic reaction component.

Nesic et al [60, 221] demonstrated that the corrosion rate showed flow dependency in flowing conditions at pH ≥ 6 as shown in Figure 10-1. The author attributed the flow sensitivity to the diffusion behaviour of some of the carbonic acid components, with which the diffusion limited current effectively participates in the cathodic reaction rate.

The authors added that higher flow velocities accelerate the reduction of the carbonic acid by increasing the diffusion rate of the carbonic acid from the bulk solution to the surface. Nestic et al [60] carried out their study at 20°C and 1% NaCl solution, which can inflict a significant reduction in the diffusion coefficient and the chemical reactions rates resulting in less flow dependency. Ferreira et al [27] studied the influence of surface roughness on the corrosion rate at flowing conditions of up to 1m/s. The outcome showed that CO₂ corrosion has flow dependency at pH > 6 conditions are shown in Figure 10-2.

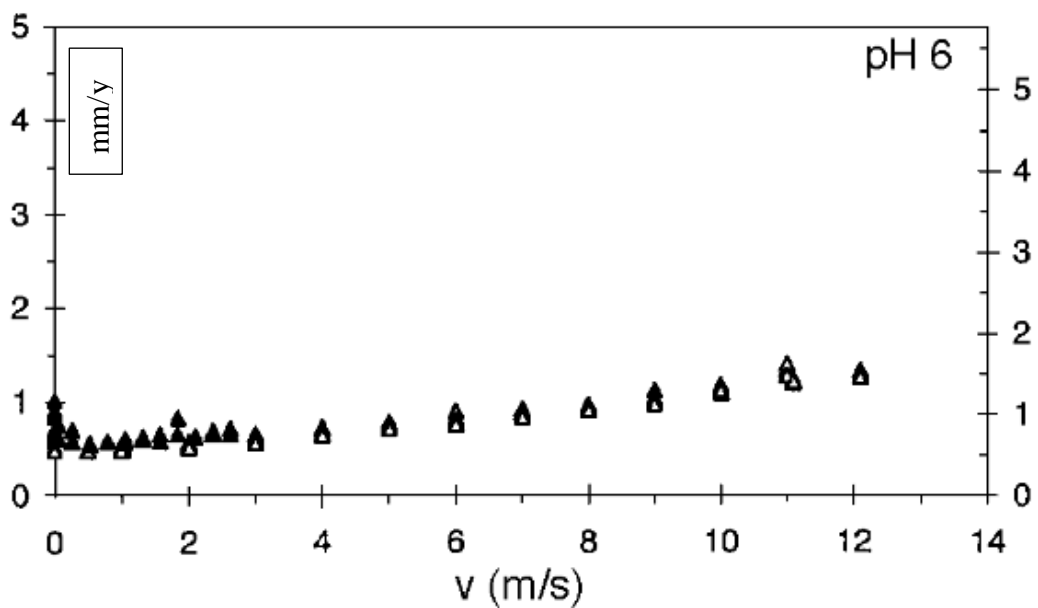


Figure 10-1. Data of corrosion rate as function of flow at temperature 20°C and 1% NaCl, from Nestic et al [60]

However, the studies by Nestic et al [60, 221], Schmitt et al [220], Vetter [219] and Ferreira et al [27] gave no further details about the composition or the nature of diffusion-limited component of the carbonic acid H₂CO₃. Moreover, these studies did not necessarily consider all the physical and chemical properties of the flow in their investigation, nor the effect of the geometry of the flow section on the corrosion process. Each study was limited to one or two parameters, therefore an adequate understanding of the effect of flow on corrosion in a high pH environment is still lacking.

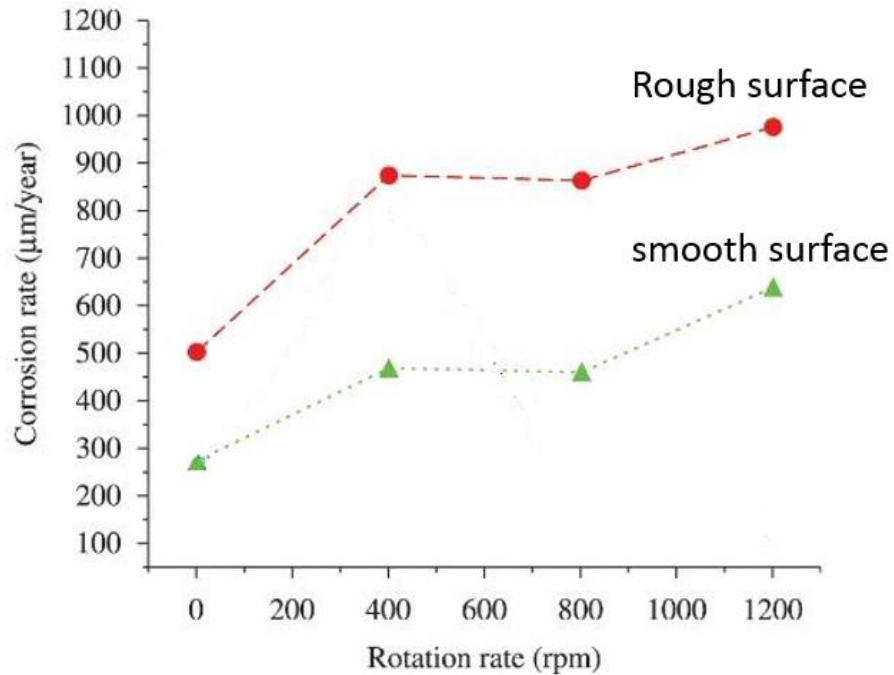


Figure 10-2. Data of corrosion rate as a function of flow and surface roughness at temperature 25°C and pH > 6, from Ferreira et al [27]

The current study outcome agrees with the studies mentioned in Table 10-1 with corrosion rate showed flow sensitivity at $\text{pH} \geq 6$ environments. Corrosion rate was plotted versus the flow velocity as shown in Figure 10-3. Corrosion rate was flow dependent at both temperatures 50°C & 80°C. The flow dependency showed variation with the shear stress/flow velocity. At wall shear stress/flow velocity 410 Pa/13.85 m/s corrosion rate increased several times higher than at 1.6 Pa/0.7 m/s as shown in Figure 10-3 and Figure 6-7. This is much higher than the corrosion rate presented in Nestic et al [60] in Figure 10-1. The current study was conducted at much higher NaCl concentration and temperatures which could have accelerated the species diffusion and the chemical reaction rates to a point where the flow-dependent corrosion behaviour becomes more evident. The increase in corrosion rate in the present study at pH 6.6 cannot be attributed solely to initial concentration of H^+ species in the bulk solution. Therefore, another source of cathodic species must be present and providing more diffusion limiting species H^+ to the bulk solution, with which the diffusion-limited current effectively participates in cathodic reactions rate.

Recently, another cathodic reaction proposed as a dominant cathodic reduction process [66-68] known as “Hydrogen buffering effect” in which the carbonic acid dissociation becomes an additional source of H^+ to the hydrogen-reduction process on the sample surface; details of these studies were presented in paragraph 2.1.4. In general, the outcome of this study indicated the presence of a source for the diffusion-limited species, feeds the bulk solution with additional H^+ when the concentration of H^+ depleted, due to the ongoing reduction process on the sample surface.

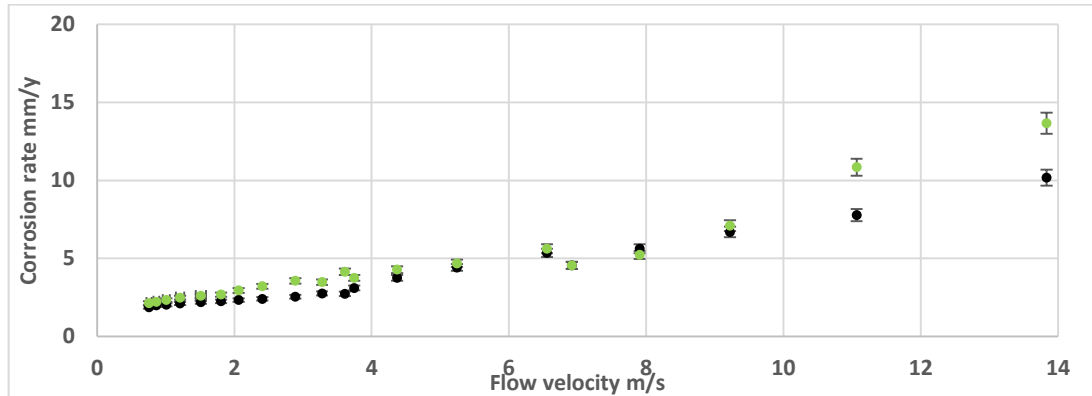


Figure 10-3. The data of the corrosion rate as a function of flow velocity from current study at pH 6.6: 50°C (Black dots) and 80°C (Green dots)

The cathodic polarisation curves at temperatures 50°C and 80°C showed an increase in the cathodic current density as a function of the shear stress as shown in Figure 6-10, Figure 6-11, Figure 7-7 and Figure 7-8. This introduced a possible flow effect on the dissociation rate of the carbonic acid. High dissociation rate increases the H^+ availability in the bulk solution and can explain the flow sensitivity of the cathodic current density.

Similar proposals are present in literature, where the authors suggest that higher flow velocities accelerate the reduction/dissociation rate of the carbonic acid [60, 221]. Therefore, the observed diffusion-limited current in this study at 50°C and 80°C at pH 6.6 can be a consequence of the solution buffering with H^+ from the dissociation of the carbonic acid.

In general, corrosion behaviour under flowing conditions factors that altered corrosion rate not restricted to wall shear stress/flow velocity and temperature. Other flow parameters such as the flow turbulence level and/or the parameters affect the transport rate of the cathodic species can play a significant role in determining the corrosion behaviour, especially in high wall shear stress/flow velocity environment.

10.2.2 How the flow and channel geometry influence the corrosion rate

The changes in corrosion rate as a function of shear stress showed variations at some points; although the points are subjected to a similar level of shear stress. Figure 6-7 shows the corrosion rate at point A is higher than at B despite the fact that point B was subjected to 120 Pa wall shear stress while point A was subject to 100 Pa. The difference in corrosion rates can be attributed to the variation in flow cell geometry at points A & B, where the characteristic length D (hydraulic diameter) at A is 1.5 times larger than D at point B due to the differences in the dimensions of the cross-section.

Flow parameters such as Reynold`s number is a function of flow cell dimensions (hydraulic diameter), flow velocity and fluid properties. Large hydraulic diameter generates high turbulent flow (Reynold`s number). From equation 4.3 Reynold`s numbers were calculated and plotted versus the corrosion rates as shown in Figure 6-8. Reynold`s number at point A is $\sim 60,000$ and at B is $\sim 45,000$. The mass transfer coefficient is described in equation 4.6 as the Sleicher and Rouse correlation [171] which is a function of Reynold`s number, water properties and flow geometry. This correlation can provide an insight into the main parameters controlling the mass transfer coefficient between the bulk solution and the sample surface [63, 171].

Mass transfer coefficient increases with flow turbulence (Re number) to the power of $Re^{0.87}$ [173]. Therefore any increase in Reynold`s number leads to an increase of the mass transfer coefficient which increases the diffusion rate of the cathodic species to/from the surface. This can explain the higher corrosion rate at A than at point B despite the former being exposed to a higher flow velocity and wall shear stress than the latter.

The cathodic polarisation analysis at point A & B as shown in Figure 6-10 shows the cathodic current density at point A is higher than at B. Consequently a thinner diffusion boundary layer thickness is generated at point A sample than at B. A thin diffusion boundary layer thickness prompts higher cathodic species rate to reach the sample surface for reduction or to diffuse from the surface to the bulk solution [60].

Figure 10-4 shows two corrosion rate curves plotted versus Reynold`s number. The flow rates and gasket thicknesses were adjusted to have similar Reynold`s number range across the five samples at both curves. However, the shear stress value in the

green curve is always $\times 3$ the equivalently positioned sample in the red curve. If corrosion's flow sensitivity was only a function a Reynold`s number, the corrosion rate at both curves should have similar flow sensitivity (slopes). Nevertheless, corrosion rate in the green curve exhibited a steeper flow dependency than the red curve. Therefore, a third parameter must be present and influence this behaviour.

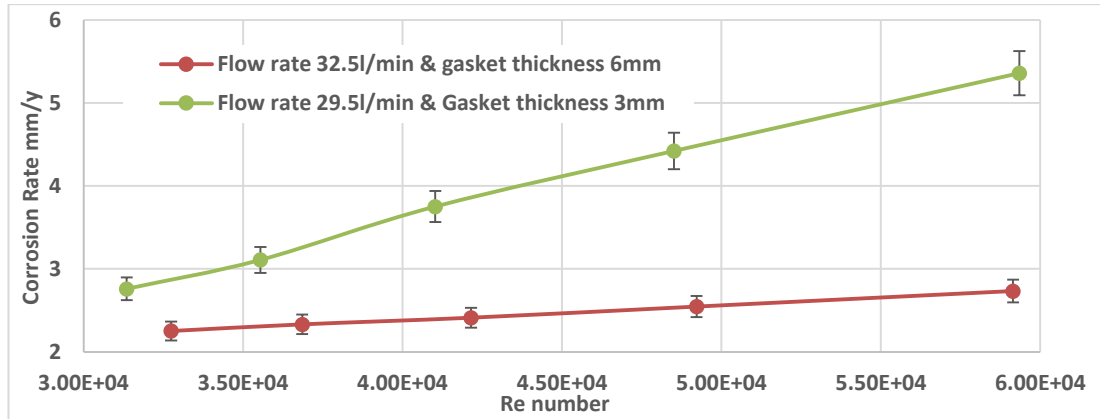


Figure 10-4. Reynold`s number effect and channel geometry on the corrosion behaviour at temperature 50°C and pH 6.6

This can be attributed to the direct effect of the geometry at both curves on the mass transfer coefficient. From Sleicher and Rouse correlation Equation 4.6 [171] the mass transfer coefficient is described as a function of flow turbulence and solution properties. It shows that the diffusion rate of cathodic species is an inverse proportion to the geometry (L_c) (L_c is a function of the thickness of the gasket). For the red curve test, the mass transfer coefficient has a characteristic length larger than the green curve test, resulting in less mass diffusion rate to/from the surface at the former than the latter. This shows that the corrosion behaviour under flowing conditions is not only a function of the flow characteristics and fluid properties, but the geometry of the flow channel has a significant effect on the diffusion rate of the cathodic species to/from the surface of the samples.

Figure 10-5 shows a diagram of the physical and chemical parameters that affect the corrosion rate. The characteristic length in the mass diffusion coefficient correlation was determined as a function of the gasket thickness [222-226].

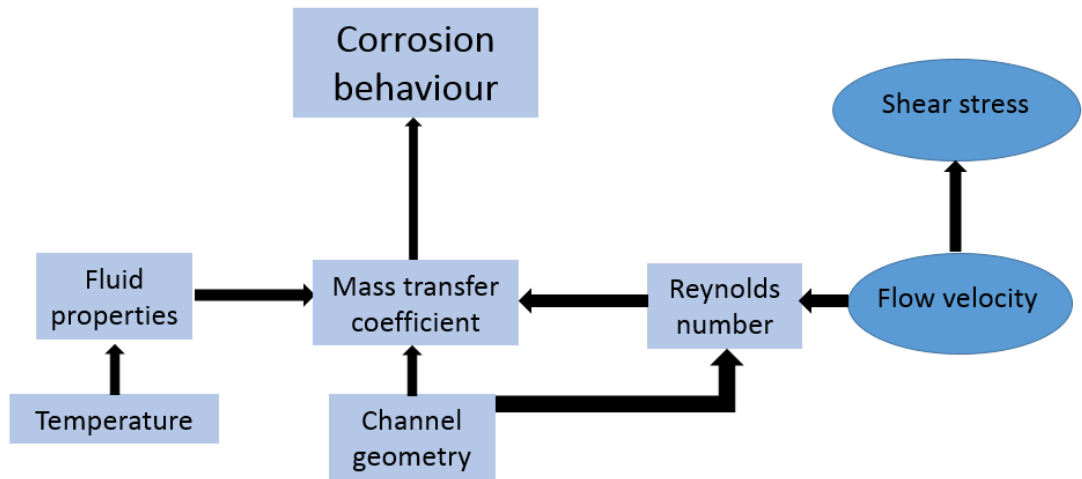


Figure 10-5. Sketch shows how the flow parameters and properties influence the corrosion rate

The data at 80°C provided a further confirmation of the prior analysis of the data at 50°C. Points with higher corrosion rate have Reynold`s number higher than the points with lower Reynold`s number. Therefore, mass transfer coefficient at the former is higher than the latter.

At both temperatures 50°C and 80°C the four curves of the corrosion rate as a function of the shear stress and flow velocity showed consistency, with no significant differences in corrosion rates at points A & B and C & D as shown in Figure 6-7 & Figure 6-9 and Figure 6-16 & Figure 6-19. The overall shape of the four curves combined showed one semi-continuous curve. However, corrosion rate as a function of flow turbulence (Reynold`s number) at Figure 6-8 and Figure 6-17 showed discontinuous curves. Therefore at pH 6.6 environment, the wall shear stress is a valid parameter to describe the corrosion behaviour of the X65 carbon steel at both low and high flow ranges. Other parameters such as the mass transfer coefficient are also valid. However at pH 6.6, using the mass transfer coefficient to describe the corrosion behaviour has its obstacles, whereas at pH > 4 the calculation of the actual mass transfer coefficient value is limited due to the difficulties of measuring the limiting current density at (pH levels > 4).

10.2.3 Temperature effect on the corrosion rate

High temperature accelerates chemical reaction rates and the diffusion of species to/from the surface, therefore high corrosion rates are expected at high-temperature environments [10, 119]. This agrees well with the current study where the corrosion rates at 80°C were relatively higher than at 50°C as shown in Figure 6-7 and Figure 6-16. The significant flow dependency of the corrosion rate at 80°C in comparison to 50°C can be attributed to the influence of temperature on the overall process. Figure 10-6 explains how the temperature influences the corrosion behaviour.

Corrosion rate sensitivity to flow indicates that the diffusion-controlled species are participating actively in the cathodic reaction. The effect of temperature can be comprehended by understanding the effect of the temperature on chemical reactions and the diffusion process of the cathodic species to/from the surface, in addition to the effect of the temperature on the fluid properties (i.e. viscosity & density).

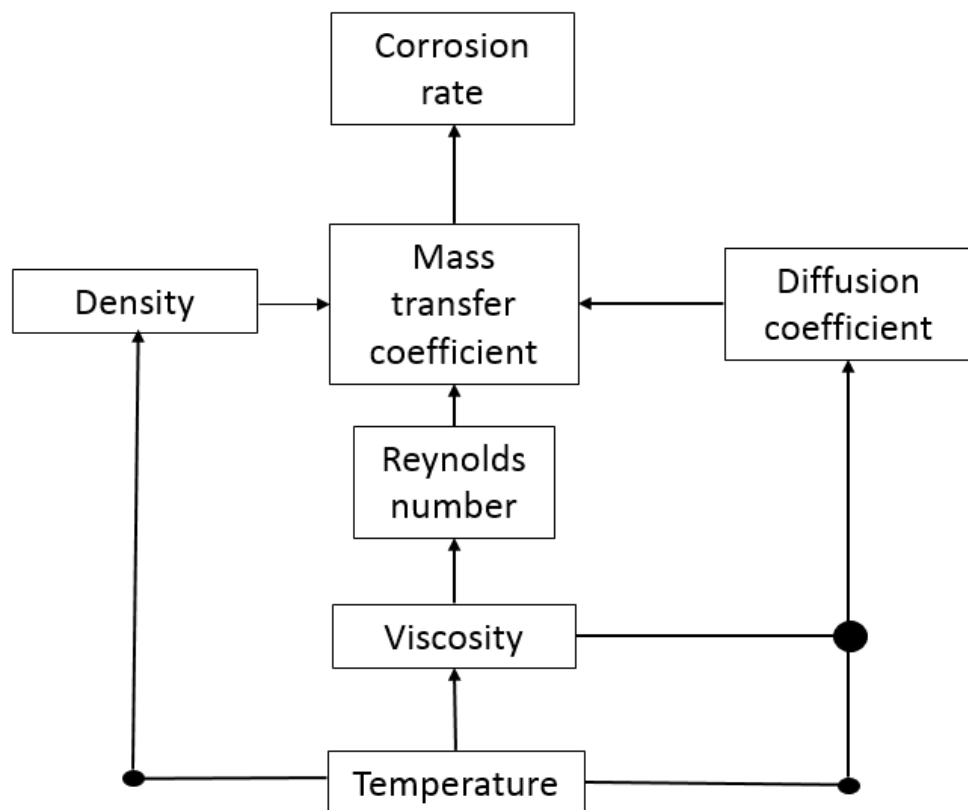


Figure 10-6. A diagram illustrates how the temperature affects the corrosion behaviour

At temperatures 50°C and 80°C different corrosion rates were recorded under similar shear stress; at 80°C this occurred under ~26 Pa, and at 50°C this behaviour started at a much higher wall shear stress ~100 Pa. This can be explained by the influence of the temperature on the diffusion coefficient (D) as given by Stokes-Einstein equation 4.5 [60]. It indicates that the diffusion coefficient is a function of the temperature and varies inversely with solution viscosity. Water viscosity decreases with temperature [214] which introduced a further increase in diffusion coefficient at high temperatures. The difference in the solution viscosity between temperatures 50°C & 80°C generates two different Reynold`s numbers at any given flow velocity. From equation 4.3 the water viscosity at temperature 80°C generates 50% higher Reynold`s number than at 50°C under the same flow velocities and channel geometry, in other words at temperature 80°C a ~ 90,000 Reynold`s number was generated with flow velocity 3.5 m/s at one sample in comparison to ~60,000 at 50°C under the same flow velocity. Consequently, at 80°C a higher mass transfer coefficient was expected at low wall shear stress/flow velocity ~26Pa/3.5m/s, whilst at temperature 50°C it was not possible to induce a similar magnitude of mass diffusion coefficient under this level of shear stress/flow velocity. However, it required much higher shear stress/flow velocity ~100Pa/6.5m/s to obtain a similar level of mass transfer coefficient. Consequently, the reduction in the diffusion boundary layer thickness (as described by equation 4.8) at temperature 80°C a thin diffusion boundary layer can be present under much lower wall shear stress/flow velocity than at 50°C.

10.3 An understanding of the effect of flow on the corrosion behaviour at pH 4 environment

At pH 4 the concentration of the H⁺ is 400 times higher than at pH 6.6, therefore the effect of the mass diffusion behaviour on the corrosion current density was more significant than at pH 6.6. Corrosion rate as a function of time was under strong mass diffusion control in all cases, in which the corrosion rate increased rapidly with the flow. The length of stabilisation period varied depending on the applied flowing conditions. The variation in the length of the stabilisation period as a function of shear stress is an interesting behaviour as shown in Figure 7-9 and Figure 7-12.

This behaviour can be explained by understanding the effect of the cathodic species diffusion on the stabilisation time. The diffusion rate is a function of temperature and

flow conditions [40]. At temperature 50°C, the length of the stabilisation period was inversely proportional to the shear stress, where it decreased from 2.5 hrs at 1.6 Pa down to 1 hr at 5.66 Pa as shown in Figure 7-1. However, at higher wall shear stress ≥ 30 Pa the corrosion rate was stable throughout the test duration. Indicating that the Rate-Determining Step (RDS) of the length of the stabilisation period is the charge transfer and not the diffusion rate of the cathodic species. At temperature 80°C, the time required for the corrosion rate to reach a steady state value was much shorter than at 50°C. However, at shear stress ≥ 26 Pa the corrosion rate showed no stabilisation period, similar to the observation at 50°C.

In general, at the starting point of a test under low shear stress, the diffusion rate of the cathodic species is gradually increased with the time, until it reaches the diffusion limit under that level of shear stress, at which the corrosion rate reaches steady-state value. The length of the stabilisation time is therefore expected to vary as a function of the applied shear stress. At shear stress < 26 Pa corrosion rate increased as a function of the time from an initial value up to the plateau. However, at shear stress ≥ 26 Pa the hydrodynamic force is high enough at the starting point to supply high rate of the cathodic species from the bulk solution to the surface to be reduced. The diffusion rate was enough to reach a diffusion limit in a short period of time. Therefore, no stabilisation period was required to reach a steady state corrosion rate at high shear stress range.

One can argue that at 80°C the diffusion coefficient is higher, and thus the corrosion behaviour should show no stabilisation period at much lower shear stress than at 50°C. This argument is valid if the effect of the flow cell geometry was eliminated. At 50°C the corrosion rate showed steady-state value from the beginning of the test at shear stress 30 Pa with a characteristic length that is half of the characteristic length of the flow cell at 80°C and shear stress ~ 26 Pa. With smaller characteristic length the diffusion coefficient increased, and therefore corrosion rate exhibited a stable rate throughout the test at both temperatures 50°C and 80°C at approximately the same range of shear stress.

10.3.1 How the mass transfer coefficient controls the corrosion behaviour

It is well known that at low pH solutions the main cathodic reaction is the reduction of hydrogen ions in a process known as cathodic hydrogen evolution [18, 40, 48, 119]. The corrosion behaviour is highly influenced by the transport rate of the cathodic species from/to samples surface. Corrosion rate as a function of wall shear stress at temperature 50°C was shown in Figure 7-5. The variation in corrosion rate values at points A & B and C & D was attributed to variation in flow turbulence as detailed in section 10.3.1. Figure 7-7 illustrates the cathodic sweeps at points A & B and C & D. The cathodic sweep branches confirmed the limiting current at point A & C are higher than at point B & D. Therefore, greater corrosion rate at points A & C can be linked to the higher mass transfer coefficient at these points than at points B & D.

In order to confirm this hypothesis, a further analysis was carried out on the corrosion behaviour, by calculating the mass transfer coefficient at these points using empirical correlation equations 10.1. From Figure 7-7 it was possible to measure the limiting current of the samples at point A & B and C & D, therefore the mass transfer coefficient at these points was empirically calculated using [60, 227]

$$K_m = \frac{I_{lim}}{F \times 10^{-pH}} \quad 10.1$$

Where K_m is mass transfer coefficient m/s, I_{lim} is limiting current density A/m² and F is Faraday's number 96485 C/mol.

Figure 10-7 shows the mass transfer coefficient as function of the wall shear stress at points A & B and C & D. It is clear that the calculated mass transfer coefficient values are in agreement with the corrosion rate readings in Figure 7-5, where the mass transfer coefficient at point A is approximately twofold higher than at B and at point C is 34% greater than at D.

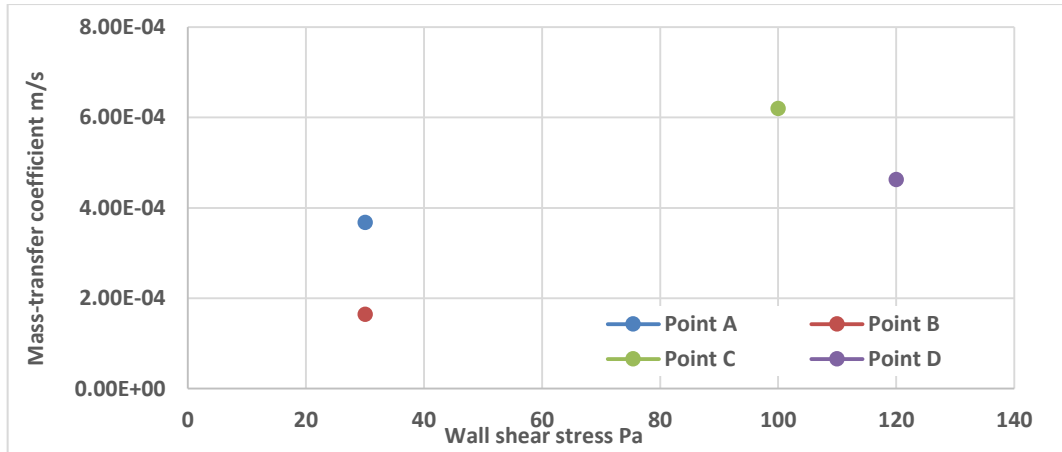


Figure 10-7. Mass transfer coefficient as a function of the wall shear stress at points A, B, C and D at pH 4 & temperature 50°C

Using the limiting current density to calculate the mass transfer coefficient by equation 10.1 provided an opportunity to examine the corrosion behaviour as a function of the mass transfer coefficient. This allowed examination of how the mass transfer coefficient correlates with the corrosion behaviour at fixed pH 4 level. Figure 10-8 shows the corrosion rate of the samples as a function of the mass transfer coefficient at pH 4 and temperature 50°C.

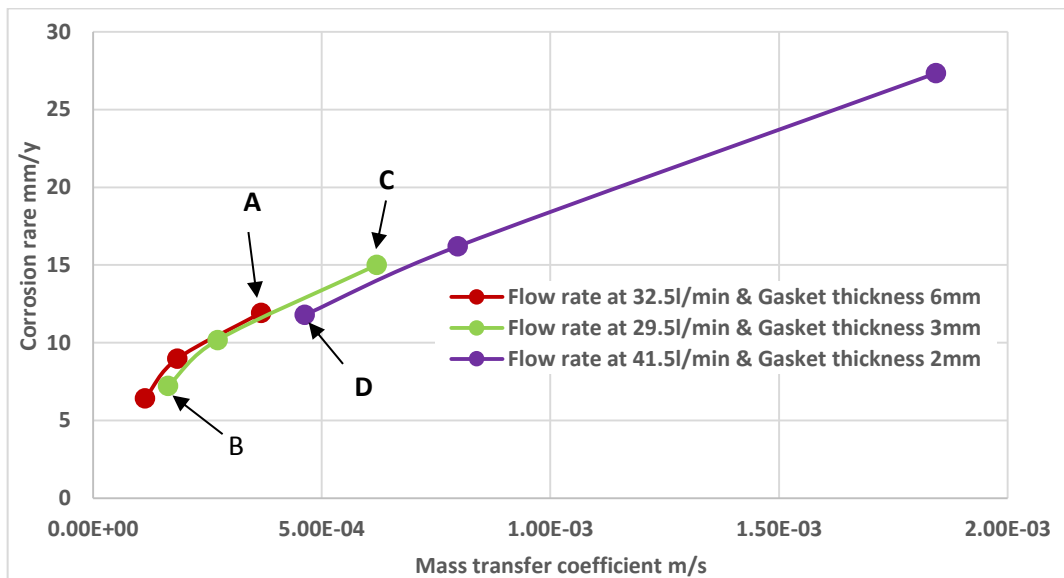


Figure 10-8. Corrosion rate as function of mass transfer coefficient at pH 4 and temperature 50°C calculated using the limiting current density

The overall shape of the curves showed that the corrosion rate is a direct function of the mass transfer value. The boundary diffusion layer thickness across the samples of points A & B and C & D was calculated using the mass transfer coefficient and the

diffusion coefficient from equation 10.1 and equation 4.5. The boundary diffusion layer thickness showed that the layer at point B is twofold thicker than at point A, whilst the thickness of point D is 50% greater than at C. Therefore, the variation in corrosion rate at these points can be attributed and linked to the difference in mass coefficient.

In addition, further analysis of the cathodic sweep curves at pH 4 and temperature 50°C revealed an interesting behaviour. Figure 7-8 illustrates that the reduction process is a mass transfer controlled reaction (a clear limiting current density region on the curve, at which the polarisation process becomes an independent of the current density) up to wall shear stress 200 Pa, however at 410 Pa the cathodic reduction was under mixed control of mass diffusion and charge-transfer (the limiting current density region decreased, and the polarisation process becomes current density dependent). The shift from mass diffusion to mix controlled can be attributed to the high diffusion rate of the cathodic species reaching the surface through the diffusion boundary layer. Figure 10-9 shows that the mass transfer coefficient at the sample subject to 410 Pa is more than twofold higher than the sample under 200 Pa, which reduces the thickness of the diffusion boundary layer from $\sim 20\mu\text{m}$ at 200 Pa to $\sim 9.7\mu\text{m}$ at shear stress 410 Pa. The thickness of the diffusion boundary layer was calculated using equation 4.8 as a function of mass transfer coefficient and diffusion coefficient. This accelerated the rate of the cathodic reaction until it reached a point at which the charge transfer rate could not keep up with the diffusion rate of the species, therefore the reaction switches from mass diffusion control to charge transfer control. Similar observations were reported in [228-230].

A similar observation was recorded at 80°C, the cathodic polarisation curves as a function of shear stress are shown in Figure 7-16 and Figure 7-17. The reduction process showed two different behaviours, at shear stress < 87 Pa (point E) the cathodic process remained as a mass diffusion controlled reaction, however at higher shear stress 100 Pa (point F) the reaction becomes mixed controlled.

At wall shear stress 87 Pa and flow turbulent Reynold's number $\sim 89,900$ (Point E) the reduction process was under mixed mass and charge transfer controlled reaction as shown in Figure 7-16(b). At shear stress 100 Pa (Point F) with flow turbulent Reynold's number $\sim 65,000$, the reduction process was under mass diffusion controlled with negligible effect of charge transfer controlled reaction. This is because

the Reynold's number at point F is not high enough to increase the diffusion rate of the species higher than the diffusion limit, and thus the cathodic reaction remains a mass diffusion controlled, although it was subjected to higher shear stress.

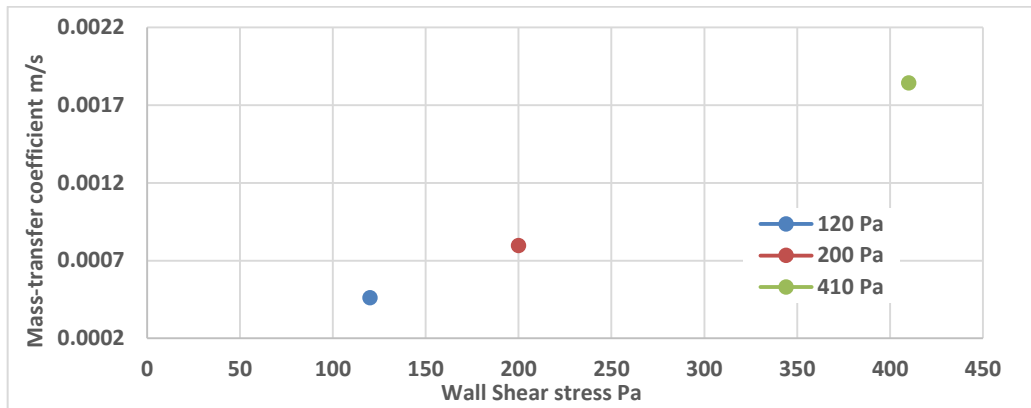


Figure 10-9. Mass transfer coefficient as function of the wall shear stress at pH 4 & temperature 50°C

The mass diffusion coefficient and the thickness of the diffusion boundary layer were calculated using equations 10.1 and 5.8. The corrosion rate as a function of the mass transfer coefficient at temperature 80°C is shown in Figure 10-10. The overall shape of the curves is shown another linear relation between the corrosion rate and the mass transfer coefficient similar to the curve of this data at temperature 50°C.

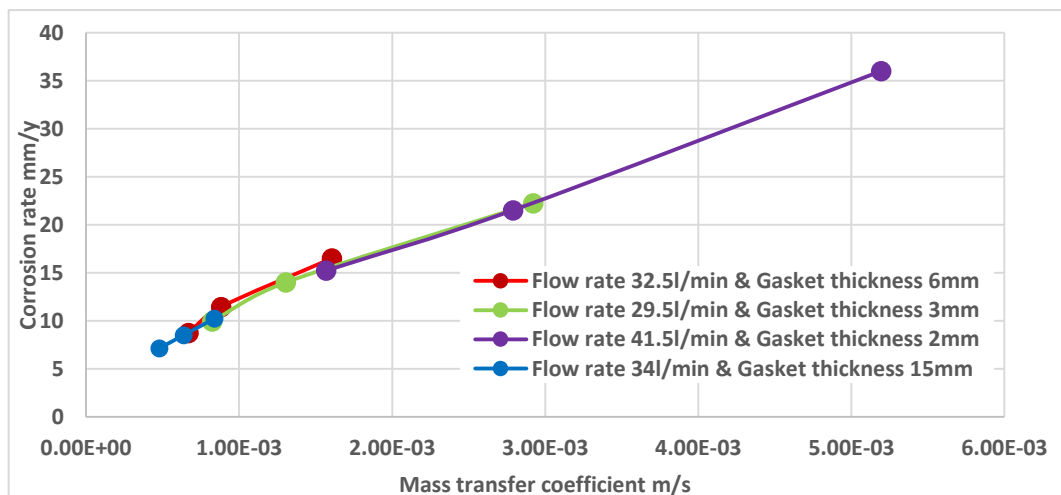


Figure 10-10. Corrosion rate as function of mass transfer coefficient at pH 4 and temperature 80°C calculated using the limiting current density

Figure 10-11 shows the mass transfer coefficient as a function of the wall shear stress at points E & F. The diffusion boundary thickness at the sample represented by point E is $\sim 10\mu\text{m}$, whilst the diffusion boundary thickness at point F $\sim 18\mu\text{m}$. This illustrated interesting phenomena, where the cathodic process switched to a mixed controlled reaction when the diffusion boundary layer thickness decreased to $\sim 10\mu\text{m}$. A similar observation occurred at 50°C and diffusion boundary thickness $\sim 9.7\mu\text{m}$, although at 50°C the reduction process switched to mix controlled reaction at higher wall shear stress 410 Pa, which can be attributed to the difference in fluid properties and mass diffusion behaviour at between temperature 50°C and 80°C .

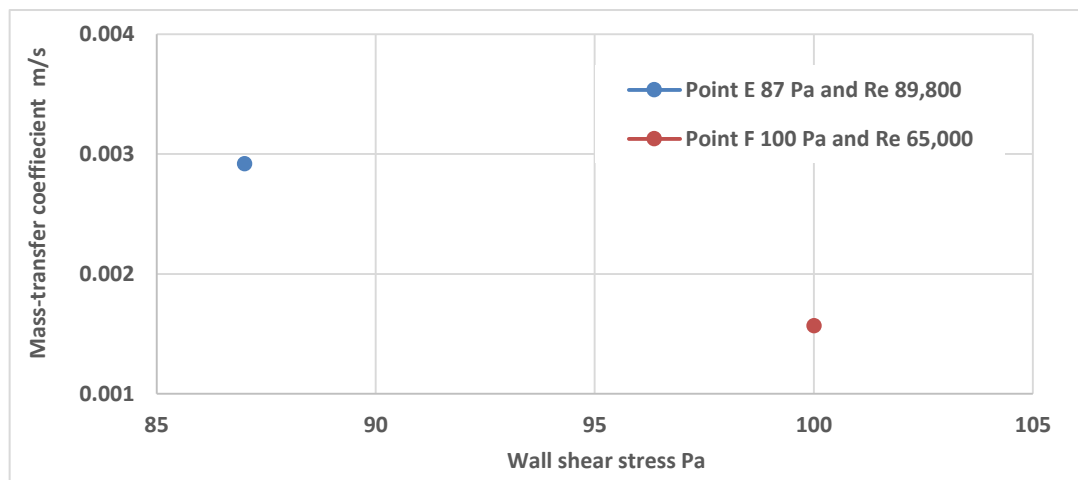


Figure 10-11. Mass transfer coefficient as function of the wall shear stress of points E & F at pH 4 & temperature 80°C

Therefore, from the cathodic polarisation tests at pH 4 and temperatures 50°C & 80°C , the diffusion boundary thickness of $10\mu\text{m}$ can be identified as a threshold thickness. Where, at diffusion boundary thickness $\leq 10\mu\text{m}$, the diffusion rate of the cathodic species increased to the level at which the charge transfer rate reaches its limit, and consequently the cathodic reduction reaction becomes a mixed diffusion and charge transfer controlled.

The plots of the corrosion rate versus the shear stress at both temperatures 50°C and 80°C in Figure 7-5 and Figure 7-13, the overall shape of the four curves indicates a discontinuous relationship, whereas corrosion rate showed a significant variation at several points. These points were subjected to similar wall shear stress/flow velocity. This suggests that using wall shear stress as a parameter to correlate and describe the

corrosion behaviour of carbon steel, without considering the other physical and chemical parameter, does not always produce accurate results.

The outcome of this study, emphasizes the importance of the mass diffusion coefficient as a parameter to understand the corrosion behaviour of the X65 carbon steel. Therefore the calculations of the mass transfer coefficient can be a millstone to understand the effect of the flowing conditions on the corrosion behaviour of the X65 carbon steel at pH 4 environment. The calculated mass transfer coefficient was plotted and shown in Figure 10-8 and Figure 10-10 at temperatures 50°C and 80°C respectively.

The overall shape of the curves combined showed a linear behaviour, with which the corrosion rate is a direct function of the mass transfer value. Therefore, at pH 4 environment, the mass transfer coefficient is more valid parameter than other flow characteristics to describe the corrosion rate at any given wall shear stress/flow velocity. And by understanding the variables that affect the mass transfer coefficient it will be possible to predict the corrosion behaviour at pH 4 and flowing conditions.

10.4 Understanding to the corrosion behaviour of protected surfaces

10.4.1 In static conditions

At 50°C, Figure 8-5 showed the corrosion rate at three different pH levels 4, 5 and 5.5. At pH 4 and 5 there was an initiation period of ~3 and 6 hrs respectively, followed by rapid increase in corrosion rate, which was confirmed by the SEM images of the surface as shown in Figure 8-6(a & b). During the initiation period, a gap or pit was created on the surface due to local dissolution resulted in a decline in the degree of protection and an increase in corrosion rate. The further the chemical dissolution progresses the more gaps and pits will present on the surface leading to further increase in corrosion rate. However, under pH 5.5, the corrosion rate of the protected surface was stable throughout the immersion time, with no sign of reduction in the films protectiveness. This was confirmed by the SEM image of both the surface and the cross-section, where no reduction in the thickness of the film was noticed as shown in Figure 10-12. Therefore pH 5.5 was selected as the critical pH level at temperature 50°C.

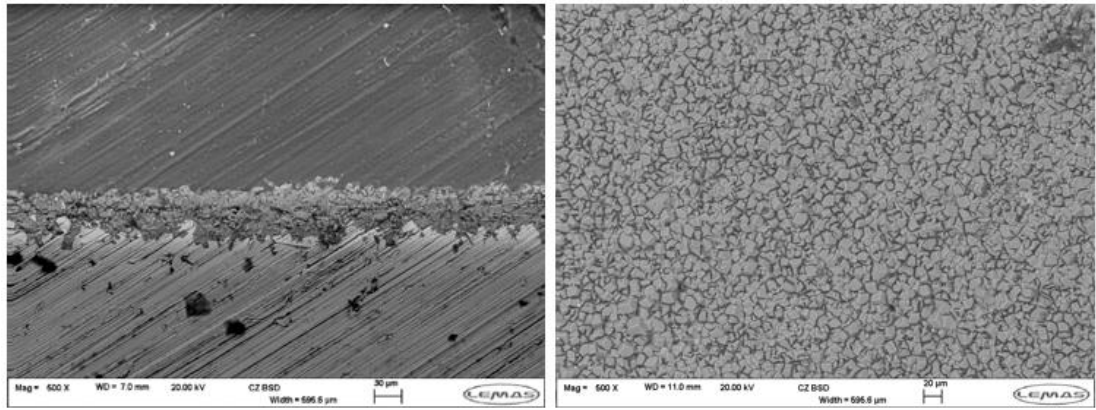


Figure 10-12. SEM image of the surface and cross-section of the protective film after 24 hrs exposure in pH 5.5 solution

However, at 80°C, corrosion rate in static conditions test series carried out under four pH levels 4, 5, 5.5 and 6. The outcome of the tests showed, that the critical pH level at which no sign of removal was observed was pH 6. Surface analysis of the protective films after each test confirm that at pH 6 the protected surface exhibited no films removal as shown in Figure 9-4.

10.4.2 In flowing conditions

At temperature 50°C and the critical pH of 5.5. The protective film was subject to a ranged wall shear stress values from 10 to 655 Pa. Corrosion rate increased with time at all the applied wall shear stress values between 655 to 37 Pa as shown in Figure 8-8. However, at wall shear stress 18 and 10 Pa corrosion rate showed no significant increase and was almost stable throughout the test duration. The SEM analysis of the surface and the cross-section of the protective films as shown in Figure 8-9, agreed well with the outcome of the corrosion rate curves in Figure 8-8. At shear stress of 655 Pa, several iron carbonate crystals disappeared due to chemical dissolution and mechanical effect of the flow, leaving behind gaps and cavities on the surface as shown in Figure 10-13. These gaps create high flow turbulent zones, promoting further films removal and consequently severe corrosion attack due to the exposure of the bare surface of the carbon steel to the corrosive environment.

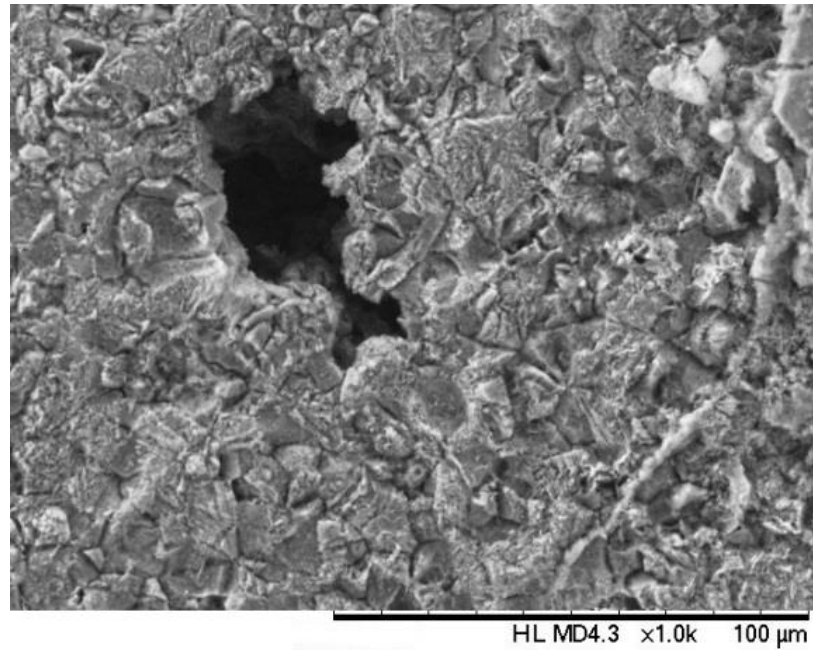


Figure 10-13. Gaps/holes on the surface of the protective film at shear stress 655 Pa, 50°C and pH 5.5

A similar observation was recorded by Ruzic et al [22], where the SEM images showed gaps are present on the surface after exposure to the rotational velocity of 10,000 rpm at pH environment of 6.9 as shown in Figure 10-14(a). The author attributed these gaps to the mechanical effect of high flow turbulence, however, Ruzic did not eliminate the possibility of the centrifugal force acting as an additional effect to remove the film, at such high rotation rate. Nevertheless, the outcome of the current study contradicts with the Ruzic findings, whereas, no film removal was observed at pH environment of 6.6 under a shear stress of 655 Pa at 50°C and 592 at 80°C which is equal to flow velocity of 13.8m/s as shown in Figure 10-14(b & c).

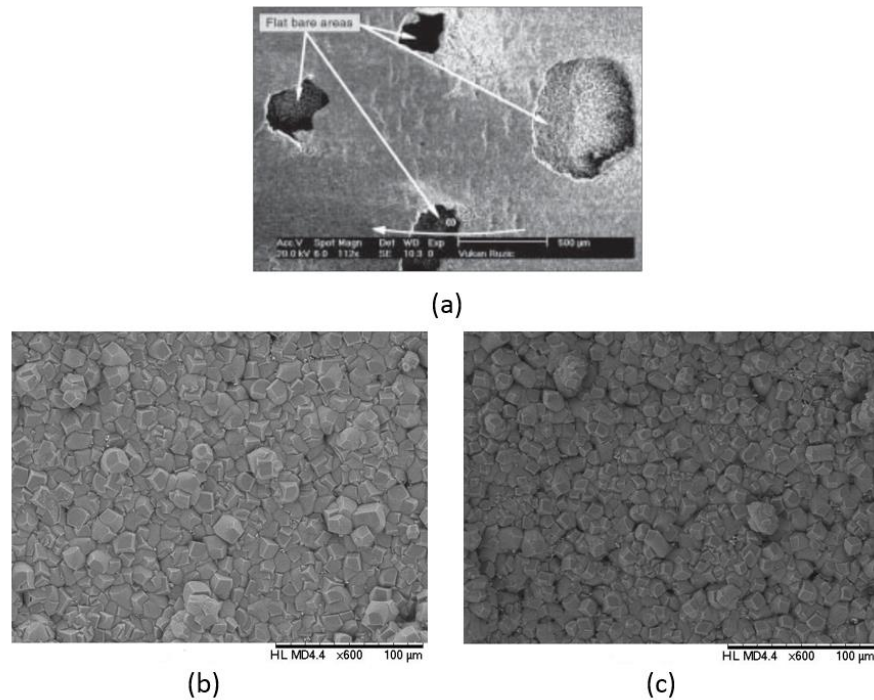


Figure 10-14. SEM images from a- Data from Ruzic et al [22] show gaps on the surface as consequence of mechanical removal from at 10,000 rpm (466 Pa) b- from this thesis, shows the surface after exposure to 655 Pa at 50°C c- from this thesis, at 592 Pa at 80°C

The contradiction here can be attributed to the difference in flow systems, Ruzic employed an RCE rig with rotation rate up to 10,000 rpm. At such high speed, the effect of the vibration of the sample in addition to the centrifugal force can effectively participate in the mechanical removal process of the film. This study a flow loop was used to generate a realistic flow profile with no additional mechanical forces, other than the wall shear stress and the flow turbulence represented by the Reynold's number.

At temperature 80°C, corrosion rate tests carried out using the critical pH of 6 and at shear stress range of 16 to 592 Pa. Corrosion rate under wall shear stress of 592 to 61 Pa increase with time throughout the immersion time. The SEM analysis showed that at shear stress range of 592 to 61 Pa the protective film exhibited different degrees of removal depending on the applied shear stress. However, no gaps or holes were observed on the surface, indicating that at 80°C the overall removal mechanism was a uniform removal.

10.5 The critical shear stress at temperature 50°C and 80°C

At 50°C, the SEM images illustrated different levels of removal behaviour at shear stress > 10 Pa. At 10 Pa the corrosion rate was stable throughout the test. This was confirmed by the SEM images shown in Figure 8-12 of the surface and the cross-section of the protective film, where the surface was fully covered with no visible removal of the iron carbonate film, at the thickness of the cross-section was $\sim 60\mu\text{m}$ similar to the thickness of the protective films prior to the test. Therefore, shear stress of 10 Pa was selected as the wall shear stress level at which no films removal occurred at 50°C and $\text{pH} \geq 5.5$.

At 80°C, the corrosion rate at shear stress 35 and 16 Pa decreased during the first ~ 3 hrs and the curves were stable throughout the next ~ 21 hrs immersion time, indicating that the surface was fully protected. The SEM image confirmed the outcome of the electrochemistry measurement of the corrosion rate test as shown in Figure 9-9, with no reduction in the thickness of the film, and the surface is fully covered with iron carbonate crystals. SEM images showed that under shear stress 35 Pa, iron carbonate films suffered a minor removal at the edges of the crystals. The removal was not significant enough to reduce the protection of the X65 surface during the corrosion rate tests. Therefore, wall shear stress of 16 Pa was selected as the level of wall shear stress at which no film removal is likely to occur at temperature 80°C under pH 6.

10.6 A categorisation of the corrosion behaviour of the protective surface throughout the 24 hr immersion time

The corrosion of the protected surface at static and flowing conditions showed different behaviours during the 24 hrs duration time. These behaviours were illustrated on the curve as regions. Each curve can consist of one or multi-regions.

The initial values of the corrosion rate at static conditions and 50°C showed an interesting behaviour as shown in Figure 8-5. Although the initial corrosion rate at all cases was small, however at pH 4 and 5 the initial values were relatively higher than at pH 5.5. The difference in the initial corrosion rate signifies the importance of the concentration of the cathodic species in the bulk solution during the diffusion process through the protective film.

Despite how compact and dense was the structure of the protective film, at higher concentration of these species H^+ (i.e. pH 4 & 5) the corrosion rate was greater than at lower concentration environment. Figure 10-15 illustrates how the corrosion rate curve of the protective film exhibited different behaviours throughout the exposure time.

At pH 4 and 5, the curves of the corrosion rate can be divided into two different regions. First, a stable corrosion rate at the initial value, and second, a linear increase with the time. During the first region, the corrosion rate was at plateau indicating a stable diffusion rate across the protective film thickness. However, another active reaction was occurring, which is the dissolution of the iron carbonate crystal due to the accelerated acidity level near the surface. The rate of the dissolution is slow and an ongoing process, therefore the corrosion rate was stable for the first few hrs at which the thickness of the protective film is constantly decreasing until it reached a low degree of protection allowing higher cathodic species to reach the carbon steel surface. At this stage, the second region on the corrosion behaviour curve starts, with the corrosion rate increase rapidly, as consequence of the ongoing film dissolution and thus the reduction in the degree of the surface protection. At pH 5.5 corrosion rate curve showed a single region consisted of one stable behaviour at plateau throughout the immersion time.

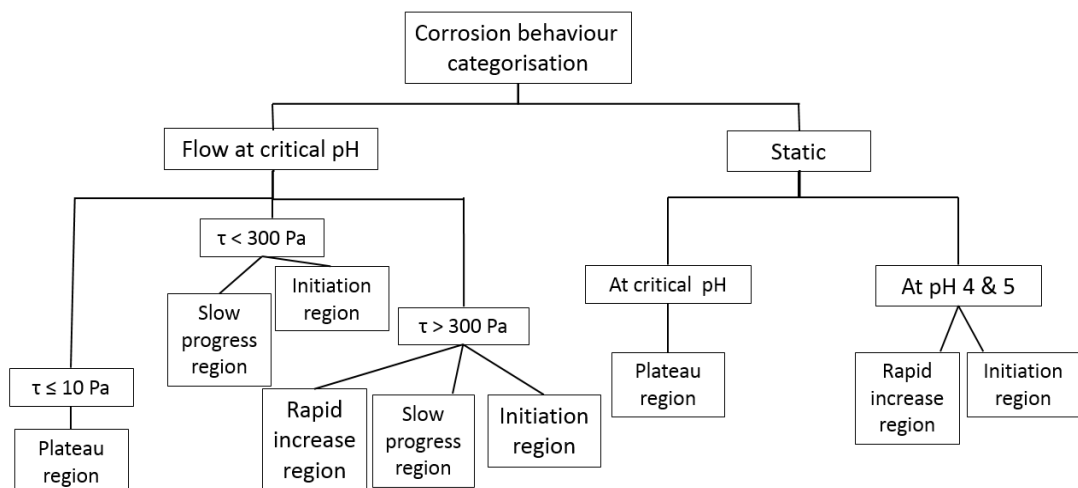


Figure 10-15. A categorisation of the corrosion behaviour of the protective surface throughout a 24 hrs immersion time

Similar behaviour occurred at static conditions and temperature 80°C. However, the initiation period (first region) was much longer than at temperature 50°C under the same pH levels, this can be attributed to the effect of temperature the iron carbonate stability. At higher temperature, the solubility of the iron carbonate decreased [231], and therefore the dissolution rate decreases, which leads to increase the initiation period at such environment. However, the overall reaction is still in favour to the dissolution process, and the protective film was removed at the end of the test.

At flowing conditions, fixed pH at the critical level and temperature 50°C and 80°C. The curve of the corrosion rate as a function of the shear stress showed more diversity in corrosion behaviours than at static conditions. At shear stress 655 Pa the corrosion rate curve divided into three regions. First, an initiation period where the corrosion rate was at initial value for 1.5 hrs, second region between 1.5 to 15 hrs where the removal process progresses and gradually increased, the third region between 15 and 24 hrs at which the corrosion rate showed a rapid increase indicating the severe removal of the protective film, which was confirmed by the SEM images of the surface and the cross-section. At lower shear stress levels 300 to 37 Pa, corrosion rate curves showed only two regions, the initiation and progress regions. Nevertheless, at shear stress 18 to 10 Pa the curve indicates a stable behaviour consists of one region at the plateau level.

10.7 How durable is the iron carbonate layer, and what are the removal mechanisms?

10.7.1 At temperature 50°C

From both the static and flowing condition tests, film removal occurred under both conditions at 50°C temperature. However, under each condition, film removal can be attributed to a different parameter. At static condition tests, it was reported by [23, 39] at pH 3.8 & 3 that the removal of the films was determined by the chemical dissolution reaction rate. In the present study, the dissolution of the protective films was examined at different pH 4 to 5.5 solutions. At pH 4 the removal of the films was significant, which was a sign that a fast chemical dissolution reaction occurred on the protective films. At higher pH levels, the effect of the chemical dissolution rate on the film removal was decreased to a minimum level.

Specifically at pH 5.5 at which no sign of removal by chemical dissolution was observed, therefore it was selected as critical pH level. The outcome of this study indicates that the dissolution reaction is mass-transfer controlled. During the static condition tests at the critical pH solution (i.e. 5.5), no film dissolution was observed. However, under the flowing condition test using the same critical pH solution, the film dissolution rate increased as a function of the applied wall shear stress/flow velocity. This was also confirmed by the surface analysis carried out using SEM images showing the effect of the flowing conditions on the dissolution rate. The previous study by Ruzic et al [23] showed that the dissolution process of the protective film is mass-transfer controlled. However later, Yang et al [39] proposed that the mass transfer rate has a limited effect on the dissolution of the iron carbonate. Figure 10-16(a) shows a comparison between these data.

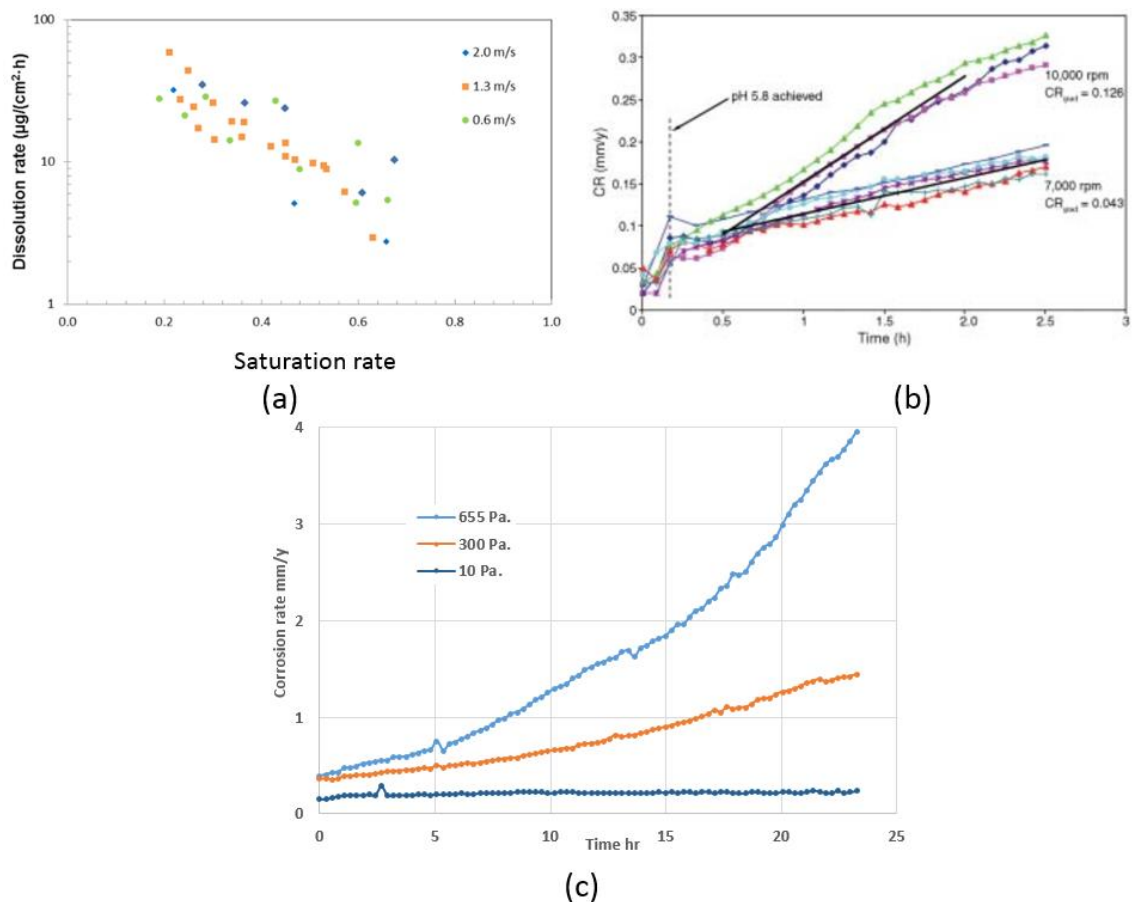


Figure 10-16. Data show the effect of mass transfer on the dissolution of the protective film from a- Yang et al [39] b- Ruzic et al [23] c- the current study

Ruzic et al [23] data showed a clear mass transfer effect on the dissolution process. However, the author conducted his work at pH 5.8 and 80°C as shown in Figure 10-16(b), Ruzic attributed the removal process solely to the chemical dissolution effect. The author did not give a clear explanation about how he eliminated the mechanical effect of the flow. Considering the current study findings of the critical pH level to be at 6, where at $\text{pH} < 6$ the chemical dissolution occurred at static conditions spontaneously, therefore testing the chemical dissolution effect at such pH (i.e. 5.8) can give inaccurate results, at which the mechanical effect of the flow of the dissolution process cannot be eliminated.

Yang et al [39] dismissed the effect of flow on the film dissolution, proposing that the flow velocity showed a limited effect on the dissolution rate as shown in Figure 10-16(a). This can be attributed to the low range of flow velocity Yang et al [39] used, at which the effect of flow is small.

Previous studies were conducted to examine the mechanical effect of the flow on the removal process of the protective film [22, 33, 35, 143] and there was general understanding that the wall shear stress magnitude generated by the flowing conditions was well below the shear required to remove the protective films from the surface mechanically.

However in the current study, a clear film removal occurred at shear stress 655 Pa and the critical pH level, film removal was observed even at lower wall shear stresses down to 10 Pa, at this level no sign of removal was recorded. Therefore, the flow must have an effect on the film removal process, not necessarily a direct mechanical effect, but it can accelerate the chemical dissolution process by reducing the supersaturation level near the surface. This can initiate a chemical dissolution reaction leading to the removal of the films. Additionally, chemical dissolution can create a gap or pit on the surface as the iron carbonate crystals dissolve under the flowing conditions. These pits generate local high turbulent zones and any further chemical dissolution can weaken the adhesive force between the crystals around these pits/gaps. The high turbulent flow around these zones can accelerate the crystals removal by flushing the films with a weak adhesion bind with the films layer. Nevertheless, at lower shear stress levels ≤ 300 Pa corrosion rate showed lower flow sensitivity with little increase in comparison to the ≥ 650 Pa, which can attribute to the effect of the hydrodynamic on the mass diffusion and the durability of the film.

Three mechanisms can be identified to describe the film removal under static and flowing conditions at 50°C temperature.

- I. Film removal by chemical dissolution, likely to occur at static conditions or low flow velocities under low pH solutions < 5.5 conditions.
- II. Film removal by chemical dissolution accelerated by hydrodynamic effects under flowing conditions under critical pH solution.
- III. Film removal by a synergistic effect of chemical dissolution and mechanical effect. This mechanism occurs at high flow velocities/wall shear stress, when the chemical dissolution increases in the mass-transfer rate, the dissolved iron carbonate film leave behind gaps and pits, these gaps play as high turbulent zones, at which the mechanical effect of the flowing condition will be high enough to wash away any crystal at these zones with a weakened adhesive force, due to the ongoing chemical dissolution process.

10.7.2 At 80°C

At higher temperature, corrosion behaviour under static and flowing conditions confirmed that films removal can occur under both conditions. Two mechanisms of films removal can be identified from the current study.

In static conditions, film removal occurred at pH levels below the critical value, where, at pHs 5 & 5.5 solutions the iron carbonate films were removed due to a uniform chemical dissolution across the protected surface. At pH 6, the corrosion behaviour was different where no film removal was observed. Under flowing conditions and temperature 80°C, another film removal reaction was determined as second possible mechanisms.

At 80°C temperature, two mechanisms can describe the film removal process under static and flowing conditions.

- I. Film removal by chemical dissolution, this mechanism can occur at the static condition at pH solution < than the critical pH.
- II. Film removal by accelerated chemical dissolution, where the film dissolution reaction initiated by the effect of the flow on the diffusion rate from/to the protective films surface.

This mechanism can occur at $\text{pH} \geq$ the critical pH level. The flow increases the concentration of the mass-diffusion species near the surface. This decreases the local pH below the critical level and initiates a chemical dissolution reaction. Therefore, the removal rate of the protective films by chemical dissolution becomes a function of the flow.

In both mechanisms the removal process of the protective films was uniform with no holes or gaps left on the surface as results of localised high turbulence zones, indicating that the mechanical effect of the flow had a limited effect on the removal process.

Chapter 11. Conclusions and recommendations for future work

This thesis has contributed to an understanding of the corrosion behaviour of the protected/unprotected surface of the X65 carbon steel under flowing conditions. The tests series was carried out using flow loop, the flow cell was designed to provide a realistic fluid flow simulating the flow dynamics in transport pipelines, and to generate from low to high flow shear stresses. Based on the findings of this research, the following conclusions can be summarised:

11.1 Corrosion behaviour of X65 carbon steel under flowing conditions and temperature 50°C & 80°C

11.1.1 At pH 6.6

X65 carbon steel corrosion behaviour was evaluated under flowing conditions at pH 6.6 and temperatures 80°C & 50°C. The following general conclusions can be drawn from the analysis of the outcome of the corrosion behaviour:

- Corrosion rate showed flow dependency at both temperatures 50°C & 80°C. The increase in corrosion rate was significant, where corrosion rate at temperature 80°C was higher than at 50°C. Corrosion rate flow dependency shows that the cathodic current which is generated by the mass diffusion controlled reaction is actively participating in the total cathodic current density. At low shear stress range of 1.3 to 5.66 Pa corrosion rate showed higher flow sensitivity at higher shear stress ranges.
- The increase in cathodic current density as a function of wall shear stress despite the low H⁺ concentration at pH 6.6, indicates that there is an additional source of H⁺ feeding the bulk solution throughout the test. This can be attributed to the “hydrogen buffering” effect on the cathodic reduction process of the diffusion controlled species. Whereas the dissociation of the carbonic acid H₂CO₃ become a source of the diffusion of the cathodic species H⁺.
- Wall shear stress is a valid parameter to describe the corrosion behaviour under flowing conditions at pH 6.6, where corrosion rate was a direct function to the wall shear stress. Whilst other parameters such as; Flow turbulence level (Reynold`s number) illustrated a discontinue relationship with corrosion rate, where corrosion

rate showed different values at the same Reynold`s number. The mass transfer coefficient cannot be used to describe the corrosion behaviour due to the difficulties of mass transfer calculations at $\text{pH} > 4$. Therefore at $\text{pH} 6.6$ conditions, having the knowledge of only the wall shear stress range is sufficient to predict the corrosion behaviour of the X65 carbon steel.

11.1.2 At pH 4

The aim of the study presented has focused on understanding the corrosion behaviour of the X65 carbon steel subjected to wall shear stress at high concentration of cathodic species. From the test series at 4 pH solution, the following conclusion can be made:

- Corrosion behaviour is under pure mass transfer controlled reduction process at both temperatures 50°C & 80°C . Corrosion rates at 80°C are higher than 50°C due to the higher diffusion rate at 80°C and lower solution viscosity.
- Corrosion behaviour was a function of the wall shear stress under both temperature 50°C and 80°C . However, corrosion rate showed significant variation in values at some points subjected to the same wall shear stress range, the variation range was 35% at temperature 50°C and $\sim 50\%$ at 80°C . It is difficult to describe the corrosion behaviour of the X65 carbon steel solely by the wall shear stress level.
- In general, at $\text{pH} 4$ the corrosion rate showed a linear relationship with the mass transfer coefficient of the cathodic species. The calculation of the mass transfer coefficient is relatively easy at $\text{pH} \leq 4$ due to the possibility of the direct measurement of the limiting current density. Therefore at $\text{pH} 4$ environment, mass transfer coefficient is a valid parameter to describe the corrosion behaviour. Other parameters such as flow characteristic, fluid properties and channel geometry affect the corrosion rate by influencing the mass transfer coefficient from/to the surface of the X65 samples.
- The cathodic reduction reaction of the species switches from pure mass diffusion controlled process to mixed mass diffusion and charge transfer controlled process, this change is a function of the boundary diffusion layer thickness. The critical boundary diffusion layer thickness is $\sim 10\mu\text{m}$ at which the reaction shifts from pure mass diffusion to mass diffusion and charge transfer controlled. At lower boundary diffusion layer thickness, the reduction process becomes pure charge

transfer controlled. This behaviour occurred at different wall shear stress level, at temperature 50°C the cathodic reduction switches to mix controlled reaction at 410 Pa, whereas at temperature 80°C this occurred at 87 Pa.

11.2 Corrosion behaviour of the protected X65 carbon steel under static and flowing conditions

11.2.1 At 50°C

This study was carried out in two parts; first was the formation process of the iron carbonate films at static and high CO₂ pressure environment, and the second part covered the aspect of the corrosion behaviour of the protected surface under both static and flow conditions. To achieve an understanding to the formation of the protective films under high CO₂ pressure, and the corrosion behaviour of the protected surface of the X65 carbon steel and the removal mechanism of the iron carbonate films FeCO₃ under static and flowing conditions. The main conclusions which can be drawn from this study are:

- Iron carbonate films were formed on the X65 carbon steel samples using a high-pressure autoclave. The thickness of the protective films during the formation process increased with immersion time up to ~60µm after 48 hrs of exposure, the films were compact, dense and fully covered the surface. No further increase in the thickness of the film was observed when the immersion time increased to 96 and 192 hrs. This indicates a protective films thickness threshold, where with ~60µm thickness of compact FeCO₃ films, the formation process reached its limit no further accumulation occurs.
- Films stability was tested under different pH solutions and static conditions. Corrosion rates and SEM analysis to the surface and cross-section of the protective films confirmed the dissolution of the protective films at pH 4 & 5 environment. The dominant films removal mechanism at static conditions was by chemical dissolution of the iron carbonate films. However, at pH 5.5, no film removal was observed after 24 hrs immersion time. Therefore, pH 5.5 was selected as the critical pH at static conditions and temperature 50°C.

- Film stability was examined under the flowing condition and the critical pH. The protective films exhibited a various level of removal depending on the applied wall shear stress. The corrosion rate measurement and the surface & cross section analysis showed different film removal mechanisms. The wall shear stress accelerated the chemical dissolution process, and the hydrodynamic force increased the removal process by flushing away the weakened and less adherent iron carbonate crystal, leaving behind holes and gaps on the surface which can generate high flow turbulence zones and promote further iron carbonate films removal. The critical wall shear stress was determined at which no films removal occurred under flowing conditions and 50°C operating temperature.
- The protective film's removal rate by chemical dissolution reaction was a function of the wall shear stress. This confirmed that the films removal reaction was under mass transfer controlled.
- Critical pH and wall shear stress are the threshold conditions at which no films removal is likely to occur for operating temperature of 50°C

11.2.2 At 80°C

Further investigation was carried out on the corrosion behaviour of the protective surface of the X65 carbon steel at temperature 80°C. The iron carbonate films were formed prior to each test using 100 bar CO₂ pressure. The tests series under static and flowing conditions showed different values of critical pH and wall shear stress than at temperature 50°C. From this study, the following conclusions can be made:

- Iron carbonate films removal under static condition occurs at pH solutions below a critical level. At pH solution \geq the critical pH no film removal was observed. pH 6 is the critical pH at temperature 80°C which is higher than the critical pH at 50°C. This indicated that at temperature 80°C the dissolution rate of the iron carbonate crystals at pH 5.5 (i.e. the critical pH at temperature 50°C) is higher than the formation rate. However, at pH 6 which is the critical pH level and 80°C the rates of the dissolution and accumulation of the iron carbonate crystals was balanced at which the structure of the film remains stable and compact with no reduction in the protective films thickness occurred after 24 hrs immersion time at pH 6 environment.

- Following the tests series under static conditions, the stability of the protective films was investigated under flowing conditions using the critical pH level. The iron carbonate FeCO_3 crystals exhibited a significant films removal due to a uniform chemical dissolution reaction across the protected surface with no visible gaps or holes on the surface. Films removal at temperature 80°C was limited to films removal due to chemical dissolution at static conditions and $\text{pH} < \text{the critical level}$, however under flowing conditions and at the critical pH level, the dominate films removal mechanism was accelerated chemical dissolution by the wall shear stress/flow velocity. By testing the stability of the iron carbonate layer under various levels of wall shear stresses it was possible to determine the critical wall shear stress at 80°C temperature environment.
- The corrosion rate curves can be divided into different regions, at which the corrosion behaviour exhibited different mechanisms. At the starting point the diffusion of the cathodic species through the protective film resulting with steady state corrosion rate. Further diffusion of species from the bulk solution to the surface increases the concentration of the H^+ near the surface and the local acidity level, promoting the dissolution reaction rate of the protective film. The dissolution of the protective film increases the local saturation rate, high saturation rate favours the reformation of the protective film. However, at low pH environment the dissolution reaction rate is greater than the formation rate, and therefore a reduction in the degree of the protection occurred.
- The rate of the chemical dissolution reaction was a function of the flowing conditions. Therefore, films removal by chemical dissolution reaction was controlled by the mass diffusion rate.

11.3 Recommendations for future work

This research used flow loop combined with an electrochemical monitoring to investigate the corrosion behaviour of the unprotected/protected surface of the X65 carbon steel under flowing conditions. The outcome of this study opens the way to further investigations of corrosion behaviour of the carbon steel under different flowing conditions and environment. Specific recommended suggestions for future work include:

- Modify the flow loop to work under high CO₂ pressure conditions (up to 10 bar). To investigate the corrosion behaviour of the X65 carbon steel at a high CO₂ pressure under realistic flowing conditions at different pH level environment. This will illustrate the effect of the hydrogen buffering effect and the direct reduction of the carbonic acid in the total cathodic current.
- Investigate the corrosion behaviour of the X65 carbon steel in presence of inhibitors under realistic flowing conditions. To achieve an understanding to the effect of the wall shear stress on the corrosion behaviour of the inhibited surface of the X65 carbon steel at different temperatures and pCO₂.
- Add sand load to the solution to investigation the degradation mechanisms that take place during erosion-corrosion damage of protected/unprotected X65 carbon steel surface at different sand load and temperatures under flowing conditions.
- Study the formation of the iron carbonate crystals FeCO₃ from the initial stage under flowing conditions using live feed camera. The transparent top part of the test section provides the opportunity to fit HD camera on top of each sample to record the crystallisation and growth of the iron carbonate crystals under different wall shear stress levels. This will generate enough data to identify the critical wall shear stress at which the formation of the iron carbonate crystals exhibits the highest rate.

References

1. Marcus, P., Corrosion mechanisms in theory and practice. 2011. Page 243-255: CRC Press.
2. Grabke, H., R. Krajak, and J. Nava Paz, On the mechanism of catastrophic carburization: 'metal dusting'. Corrosion Science, 1993. **35**(5): p. 1141-1150.
3. Sato, N., 1989 Whitney Award Lecture: Toward a More Fundamental Understanding of Corrosion Processes. Corrosion, 1989. **45**(5): p. 354-368.
4. Jones, D.A., Principles and prevention of corrosion (2nd ed'96). 1996.
5. Shaw, B.A. and R.G. Kelly, What is corrosion? Interface-Electrochemical Society, 2006. **15**(1): p. 24-27.
6. Craig, B.D., Fundamental aspects of corrosion films in corrosion science. 1991: Springer.
7. Sanchez, M., N. Hernandez, and G. Gonzalez, Designing and building an electrochemical cell to measure corrosion rate in flow lines. Corrosion Reviews, 2001. **19**(2): p. 157-174.
8. Koch, G.H., M.P. Brongers, N.G. Thompson, Y.P. Virmani, and J.H. Payer, Corrosion cost and preventive strategies in the United State. 2002.
9. Dobmann, G., J. Kurz, A. Taffe, and D. Streicher, Development of automated non-destructive evaluation (NDE) systems for reinforced concrete structures and other applications. Non-destructive Evaluation of Reinforced Concrete Structures, 2010. **1**: p. 39.
10. Kermani, M. and A. Morshed, Carbon dioxide corrosion in oil and gas production-A compendium. Corrosion, 2003. **59**(8): p. 659-683.
11. Dugstad, A., Fundamental Aspects of CO₂ Metal Loss Corrosion-Part 1: Mechanism. CORROSION 2006, 2006.
12. Dugstad, A., L. Lunde, and K. Videm, Parametric study of CO₂ corrosion of carbon steel. A. Dugstad, L. Lunde, and K. Videm, Paper, 1994(14).
13. Sun, W. and S. Nešić, Kinetics of Corrosion Layer Formation: Part 1-Iron Carbonate Layers in Carbon Dioxide Corrosion. Corrosion, 2008. **64**(4): p. 334-346.
14. Nestic, S., Effects of Multiphase Flow on Internal CO₂ Corrosion of Mild Steel Pipelines. Energy & Fuels, 2012. **26**(7): p. 4098-4111.
15. Hu, X. and A. Neville, CO₂ erosion–corrosion of pipeline steel (API X65) in oil and gas conditions—A systematic approach. Wear, 2009. **267**(11): p. 2027-2032.
16. Akeer, E., B. Brown, and S. Nestic, The Influence of Mild Steel Metallurgy on the Initiation of Localized CO₂ Corrosion in Flowing Conditions. 2013.
17. Schmitt, G. and B. Rothmann, Studies on the corrosion mechanism of unalloyed steel in oxygen-free carbon dioxide solutions, part 2: kinetics of iron dissolution. Werkstoffe Und Korrosion, 1978. **29**: p. 153-166.
18. Dugstad, A., Fundamental Aspects of CO₂ Metal Loss Corrosion, Part I: Mechanism. CORROSION 2015. NACE International, 2015.
19. From: <http://projects.propublica.org/pipelines/>.
20. Efird, K., Disturbed flow and flow-accelerated corrosion in oil and gas production. Journal of energy resources technology, 1998. **120**(1): p. 72-77.
21. Ruzic, V., M. Veidt, and S. Nestic. Mechanisms of protective FeCO₃ film removal in single-phase flow-accelerated CO₂ corrosion of mild steel. in Corrosion and Prevention 2005. 2005. Australasian Corrosion Association (ACA).

22. Ruzic, V., M. Veidt, and S. Nešić, Protective iron carbonate films-Part 1: Mechanical removal in single-phase aqueous flow. *Corrosion*, 2006. **62**(5): p. 419-432.
23. Ruzic, V., M. Veidt, and S. Nešić, Protective iron carbonate films-Part 2: Chemical removal by dissolution in single-phase aqueous flow. *Corrosion*, 2006. **62**(7): p. 598-611.
24. Palacios, C. and J. Shadley, CO₂ corrosion of N-80 steel at 71°C in a two-phase flow system. *Corrosion*, 1993. **49**(8): p. 686-693.
25. Villarreal, J., D. Laverde, and C. Fuentes, Carbon-steel corrosion in multiphase slug flow and CO₂. *Corrosion science*, 2006. **48**(9): p. 2363-2379.
26. Slayman, Q.J. and B.O. Hasan, Study on corrosion rate of carbon steel pipe under turbulent flow conditions. *The Canadian Journal of Chemical Engineering*, 2010. **88**(6): p. 1114-1120.
27. Ferreira, L.R.M., H.A. Ponte, L.S. Sanches, and A.C.T.G. Abrantes, CO₂ Corrosion in the Region Between the Static and Turbulent Flow Regimes. *Materials Research*, 2015. **18**(2): p. 245-249.
28. Revie, R.W. and H.H. Uhlig, *Uhlig's corrosion handbook*. 3rd ed. Vol. 51. 2011. Pages 229: John Wiley & Sons.
29. Dugstad, A., Mechanism of protective film formation during CO₂ corrosion of carbon steel. *CORROSION* 98, 1998.
30. Zheng, J. and Z. Lu, A study of mechanism and influencing factors of carbon dioxide corrosion. *Acta petrolei sinica*, 1995. **16**: p. 134-139.
31. Nordsveen, M., S. Nešić, R. Nyborg, and A. Stangeland, A mechanistic model for carbon dioxide corrosion of mild steel in the presence of protective iron carbonate films-Part 1: Theory and verification. *Corrosion*, 2003. **59**(5): p. 443-456.
32. Cabrini, M., S. Lorenzi, T. Pastore, and M. Radaelli, Corrosion rate of high CO₂. 2014.
33. Yang, Y., B. Brown, S. Nešić, M.E. Gennaro, and B. Molinas, Mechanical strength and removal of a protective iron carbonate layer formed on mild steel in CO₂ corrosion. *CORROSION* 2010, 2010.
34. Schmitt, G., T. Simon, and R. Hausler, CO₂ Erosion Corrosion and its Inhibition under Extreme Shear Stress. I. Development of Methodology. *CORROSION/90*, paper, 1990(22).
35. Schmitt, G.A. and M.A. Mueller, Critical wall shear stresses in CO₂ corrosion of carbon steel. *CORROSION* 99, 1999.
36. Ige, O., R. Barker, X. Hu, L. Umoru, and A. Neville, Assessing the Influence of Shear Stress and Particle Impingement on Inhibitor Efficiency through the Application of In-situ Electrochemistry in a CO₂-Saturated Environment. *Wear*, 2013.
37. Nešić, S. and J. Postlethwaite, Hydrodynamics of disturbed flow and erosion—corrosion. Part I—Single-phase flow study. *The Canadian Journal of Chemical Engineering*, 1991. **69**(3): p. 698-703.
38. Dawson, J. and C. Shih, Corrosion under flowing condition--An overview and model. 1993.
39. Yang, Y., B. Brown, and S. Nestic, Study of Protective Iron Carbonate Layer Dissolution in a CO₂ Corrosion Environment. *CORROSION* 2013.
40. Nestic, S., J. Postlethwaite, and S. Olsen, An electrochemical model for prediction of corrosion of mild steel in aqueous carbon dioxide solutions. *Corrosion*, 1996. **52**(4): p. 280-294.

41. Zhang, G., M. Lu, Y. Qiu, X. Guo, and Z. Chen, The Relationship between the Formation Process of Corrosion Scales and the Electrochemical Mechanism of Carbon Steel in High Pressure CO₂-Containing Formation Water. *Journal of The Electrochemical Society*, 2012. **159**(9): p. C393-C402.
42. Sun, J., G. Zhang, W. Liu, and M. Lu, The formation mechanism of corrosion scale and electrochemical characteristic of low alloy steel in carbon dioxide-saturated solution. *Corrosion Science*, 2012. **57**: p. 131-138.
43. Place Jr, M. Corrosion control-Deep sour gas production. in *SPE Annual Technical Conference and Exhibition*. 1979.
44. Liu, Z. and S. He, Experiment investigation of superfine deep hole drilling mechanism for high temperature alloy 718. *Materials research innovations*, 2013. **17**: p. S229-S233.
45. Perez, T.E., Corrosion in the Oil and Gas Industry: An Increasing Challenge for Materials. *JOM*, 2013. **65**(8): p. 1033-1042.
46. From: <http://www.gateinc.com/>.
47. Rajeev, P., A. Surendranathan, and C.S. Murthy, Corrosion mitigation of the oil well steels using organic inhibitors—A review.
48. Choi, Y.-S., S. Nestic, and S. Ling, Effect of H₂S on the CO₂ corrosion of carbon steel in acidic solutions. *Electrochimica Acta*, 2011. **56**(4): p. 1752-1760.
49. Barker, R., X. Hu, A. Neville, and S. Cushnaghan, Flow-induced corrosion and erosion-corrosion assessment of carbon steel pipework in oil and gas production. *CORROSION 2011*, 2011.
50. Bardal, E., *Corrosion and protection*. 2004: Springer.
51. Yean, S., H. Alsaiani, A. Kan, and M. Tomson. Ferrous carbonate nucleation and inhibition. in *SPE International Oilfield Scale Conference*. 2008.
52. Revie, R.W. and H.H. Uhlig, *Uhlig's corrosion handbook*. Vol. 51. 2011.. Page 232: John Wiley & Sons.
53. De Yoreo, J.J. and P.G. Vekilov, Principles of crystal nucleation and growth. *Reviews in mineralogy and geochemistry*, 2003. **54**(1): p. 57-93.
54. Aifantis, K.E., S.A. Hackney, and R.V. Kumar, *High energy density lithium batteries*. 2010: Wiley. com.
55. Revie, R.W., *Corrosion and corrosion control*. 2008: John Wiley & Sons.
56. Sherif, E.-S.M. and A.A. Almajid, Anodic Dissolution of API X70 Pipeline Steel in Arabian Gulf Seawater after Different Exposure Intervals. *Journal of Chemistry*, 2014. **2014**.
57. Bockris, J.M., D. Drazic, and A. Despic, The electrode kinetics of the deposition and dissolution of iron. *Electrochimica Acta*, 1961. **4**(2-4): p. 325-361.
58. Nestic, S., A Critical Review of CO₂ Corrosion Modelling in the Oil and GAS Industry. 10th Middle East Corrosion Conference, 2004.
59. Revie, R.W. and H.H. Uhlig, *Uhlig's corrosion handbook*. 3rd ed. Vol. 51. 2011. Pages 229-249: John Wiley & Sons.
60. Nešić, S., G.T. Solvi, and J. Enerhaug, Comparison of the rotating cylinder and pipe flow tests for flow-sensitive carbon dioxide corrosion. *Corrosion*, 1995. **51**(10): p. 773-787.
61. Garsany, Y., D. Pletcher, D. Sidorin, and W. Hedges, Quantifying the acetate-enhanced corrosion of carbon steel in oilfield brines. *Corrosion*, 2004. **60**(12): p. 1155-1167.
62. De Waard, C. and D. Milliams, Carbonic acid corrosion of steel. *Corrosion*, 1975. **31**(5): p. 177-181.

63. Nor, A., The Effect of Turbulent Flow on Corrosion of Mild Steel in High Partial CO₂ Environments in Engineering and Technology. Ohio University.
64. Bonis, M. and J. Crolet, Basics of the Prediction of the Risks of CO₂ Corrosion in Oil and Gas Wells. M. R. Bonis and J. L. Crolet, CORROSION 89/466, NACE, Houston, TX. Per Copy\$, 1989.
65. Linter, B. and G. Burstein, Reactions of pipeline steels in carbon dioxide solutions. Corrosion science, 1999. **41**(1): p. 117-139.
66. Tran, T., B. Brown, and S. Nescic, Corrosion of Mild Steel in an Aqueous CO₂ Environment—Basic Electrochemical Mechanisms Revisited. CORROSION/2015, 2015.
67. Kahyarian, A., M. Singer, and S. Nescic, Modeling of Uniform CO₂ Corrosion of Mild Steel in Gas Transportation Systems: a Review. Journal of Natural Gas Science and Engineering, 2016.
68. Remita, E., B. Tribollet, E. Sutter, V. Vivier, F. Ropital, and J. Kittel, Hydrogen evolution in aqueous solutions containing dissolved CO₂: quantitative contribution of the buffering effect. Corrosion Science, 2008. **50**(5): p. 1433-1440.
69. Hurlen, T., S. Gunvaldsen, R. Tunold, F. Blaker, and P. Lunde, Effects of carbon dioxide on reactions at iron electrodes in aqueous salt solutions. Journal of electroanalytical chemistry and interfacial electrochemistry, 1984. **180**(1): p. 511-526.
70. Turgoose, S., R. Cottis, and K. Lawson, Modeling of electrode processes and surface chemistry in carbon dioxide containing solutions, in Computer Modeling in Corrosion. 1992, ASTM International.
71. Javaherdashti, R., C. Nwaoha, and H. Tan, Corrosion and materials in the oil and gas industries. 2013. Page 515: CRC Press.
72. Lyons, W.C. and G.J. Plisga, Standard handbook of petroleum and natural gas engineering. 2011. Page 509: Gulf Professional Publishing.
73. Baboian, R., Corrosion Tests and Standards application and interpretation. 2nd ed. 2005. Page 205-210.
74. Sun, Y. and S. Nescic, A parametric study and modeling on localized CO₂ corrosion in horizontal wet gas flow. CORROSION/2004, paper, 2004(380).
75. From: http://www.amteccorrosion.co.uk/m_corrosionresistantship.html.
76. From: <https://preservall.com/blog/>.
77. From: <http://met-engineering.blogspot.co.uk/2009/06/forms-of-corrosion.html>.
78. Leckie, H. and H. Uhlig, Environmental factors affecting the critical potential for pitting in 18–8 stainless steel. Journal of the Electrochemical Society, 1966. **113**(12): p. 1262-1267.
79. Frankel, G., Pitting corrosion of metals a review of the critical factors. Journal of the Electrochemical Society, 1998. **145**(6): p. 2186-2198.
80. Eldevik, F., B. Graver, L.E. Torbergsen, and O.T. Saugerud, Development of a guideline for safe, reliable and cost efficient transmission of CO₂ in pipelines. Energy Procedia, 2009. **1**(1): p. 1579-1585.
81. Noothout, P., F. Wiersma, O. Hurtado, P. Roelofsen, and D. Macdonald, CO₂ pipeline infrastructure. Report, Global CCS Institute, IEA Greenhouse Gas R&D Programme (IEAGHG), 2014.
82. Roberge, P.R., Handbook of corrosion engineering. 2000: McGraw-Hill.
83. Buit, L., M. Ahmad, W. Mallon, and F. Hage, CO₂ EuroPipe study of the occurrence of free water in dense phase CO₂ transport. Energy Procedia, 2011. **4**: p. 3056-3062.

84. Sun, W., K. Chokshi, S. Nesic, and D.A. Gulino, A Study of Protective Iron Carbonate Scale Formation in CO₂ Corrosion. Ohio University, USA, 2004.
85. Briggs, J., level Course in Chemistry. 2002. Page 539: Pearson Education South Asia.
86. Gadag, R., Engineering Chemistry. 2010. Page 134: IK International Pvt Ltd.
87. Berntsen, T., M. Seiersten, and T. Hemmingsen, Effect of FeCO₃ Supersaturation and Carbide Exposure on the CO₂ Corrosion Rate of Carbon Steel. CORROSION 2011, 2011.
88. Hernandez, J., A. Muñoz, and J. Genesca, Formation of iron-carbonate scale-layer and corrosion mechanism of API X70 pipeline steel in carbon dioxide-saturated 3% sodium chloride. AFINIDAD, 2014. **69**(560).
89. Gao, M., X. Pang, and K. Gao, The growth mechanism of CO₂ corrosion product films. Corrosion Science, 2011. **53**(2): p. 557-568.
90. Ferreira, L.R., S.M. Klok, H.d.A. Ponte, and F. Farelas, The formation of protective iron carbonate films and the control of CO₂ corrosion in turbulent flow. Química Nova, 2016. **39**(9): p. 1027-1033.
91. Wang, H., H. Shi, T. Hong, C. Kang, and W. Jepson, CORROSION2001. 2001.
92. Mora-Mendoza, J. and S. Turgoose, Fe₃C influence on the corrosion rate of mild steel in aqueous CO₂ systems under turbulent flow conditions. Corrosion Science, 2002. **44**(6): p. 1223-1246.
93. Schmitt, G. and M. Horstemeier, Fundamental aspects of CO₂ metal loss corrosion-Part II: Influence of different parameters on CO₂ corrosion mechanisms. CORROSION 2006, 2006.
94. Nesic, S. and L. Lunde, Carbon dioxide corrosion of carbon steel in two-phase flow. Corrosion, 1994. **50**(9): p. 717-727.
95. Nesic, S., D. Drazic, N. Thevenot, and J.L. Crolet, Electrochemical properties of iron dissolution in the presence of CO₂-basics revisited. CORROSION 96, 1996.
96. Herbsleb, G., R.K. Poepperling, and W. Schwenk, Occurrence and prevention of hydrogen induced stepwise cracking and stress corrosion cracking of low alloy pipeline steels. Corrosion, 1981. **37**(5): p. 247-256.
97. Ogundele, G. and W. White, Some observations on corrosion of carbon steel in aqueous environments containing carbon dioxide. Corrosion, 1986. **42**(2): p. 71-78.
98. Lopez, D., T. Perez, and S. Simison, The influence of microstructure and chemical composition of carbon and low alloy steels in CO₂ corrosion. A state-of-the-art appraisal. Materials & design, 2003. **24**(8): p. 561-575.
99. Shibaeva, T.V., V.K. Laurinavichyute, G.A. Tsirlina, A.M. Arsenkin, and K.V. Grigorovich, The effect of microstructure and non-metallic inclusions on corrosion behavior of low carbon steel in chloride containing solutions. Corrosion Science, 2014. **80**: p. 299-308.
100. Abiodun, R.K., Effect of iron-carbonate film on erosion-corrosion of pipeline steel. 2011.
101. Kazmierczak, T., M. Tomson, and G. Nancollas, Crystal growth of calcium carbonate. A controlled composition kinetic study. The Journal of Physical Chemistry, 1982. **86**(1): p. 103-107.
102. Nancollas, G.H., The growth of crystals in solution. Advances in colloid and interface science, 1979. **10**(1): p. 215-252.

103. Greenberg, J. and M. Tomson, Precipitation and dissolution kinetics and equilibria of aqueous ferrous carbonate vs temperature. *Applied geochemistry*, 1992. **7**(2): p. 185-190.
104. Tomson, M. and M. Johnson. How ferrous carbonate kinetics impacts oilfield corrosion. in *SPE International Symposium on Oilfield Chemistry*. 1991.
105. Nielsen, A.E. Mechanisms and rate laws in electrolyte crystal growth from aqueous solution. in *Geochemical Processes at Mineral Surfaces*, eds. JA Davis & KF Hayes, ACS Symp. Ser. 1986. ACS Publications.
106. Van Hunnik, E., B.F. Pots, and E. Hendriksen, The Formation of Protective Fe₃CO₂ Corrosion Product Layers in CO₂ Corrosion. *CORROSION* 96, 1996.
107. Chen, T., A. Neville, and M. Yuan, Calcium carbonate scale formation—assessing the initial stages of precipitation and deposition. *Journal of Petroleum Science and Engineering*, 2005. **46**(3): p. 185-194.
108. Ueda, M. and H. Takabe, Effect of environmental factor and microstructure on morphology of corrosion products in CO₂ environments. *CORROSION* 99, 1999.
109. Nestic, S., J. Lee, and V. Ruzic, A mechanistic model of iron carbonate film growth and the effect on CO₂ corrosion of mild steel. *CORROSION* 2002, 2002.
110. Tanupabrungsun, T., B. Brown, and S. Nestic, Effect of pH on CO₂ Corrosion of Mild Steel at Elevated Temperatures.
111. SK, M.H., A.M. Abdullah, M. Ko, N. Laycock, B. Ingham, and D.E. Williams, Effects of Flow on Scales Formation in a CO₂ Saturated Brine Environment. *ECS Transactions*, 2017. **75**(30): p. 17-31.
112. Farelas, F., B. Brown, and S. Nestic, Iron Carbide and its Influence on the Formation of Protective Iron Carbonate in CO₂ Corrosion of Mild Steel. 2013.
113. Liu, Z., X. Gao, L. Du, J. Li, Y. Kuang, and B. Wu, Corrosion behavior of low-alloy steel with martensite/ferrite microstructure at vapor-saturated CO₂ and CO₂-saturated brine conditions. *Applied Surface Science*, 2015. **351**: p. 610-623.
114. Guo, Y.-b., C. Li, Y.-c. Liu, L.-m. Yu, Z.-q. Ma, C.-x. Liu, and H.-j. Li, Effect of microstructure variation on the corrosion behavior of high-strength low-alloy steel in 3.5 wt% NaCl solution. *International Journal of Minerals, Metallurgy, and Materials*, 2015. **22**(6): p. 604-612.
115. Nafday, O. and S. Nestic, Iron carbonate scale formation and CO₂ corrosion in the presence of acetic acid. *CORROSION* 2005, 2005.
116. Kennell, G.F., K.L. Heppner, and R.W. Evitts, Modelling carbon dioxide corrosion with film crystallization and erosion. *The Canadian Journal of Chemical Engineering*, 2007. **85**(3): p. 350-359.
117. GREENBERG, J.L., High Temperature Kinetics of Precipitation and Dissolution of Ferrous-carbonate. ETD <http://hdl.handle.net/1911/13221>, 1987.
118. Johnson, M.L., Ferrous Carbonate Precipitation Kinetics-A Temperature Ramped Approach. 1991, Ph. D. Thesis, Rice University, Houston, Texas.
119. Honarvar Nazari, M., S. Allahkaram, and M. Kermani, The effects of temperature and pH on the characteristics of corrosion product in CO₂ corrosion of grade X70 steel. *Materials & Design*, 2010. **31**(7): p. 3559-3563.
120. L. Gray, B.A., M Tremaine, Effect of pH and Temperature on the Mechanism of Carbon Steel Corrosion by Aqueous Carbon Steel Corrosion by Aqueous Carbon Dioxide, in *Nace Corrosion*. 1990. p. 90.

121. L Gray, b.A., M Tremaine, Mechanism of Carbon Steel Corrosion in Brines Containing Dissolved Carbon Dioxide at pH 4, in Nace, Corrosion. 1989.
122. Fajardo, V., C. Canto, B. Brown, and S. Nestic. Effect of organic acids in CO₂ corrosion. in Proceedings of the NACE International Conference and Exposition CORROSION. 2007.
123. Dugstad, A., The importance of FeCO₃ supersaturation on the CO₂ corrosion of carbon steels. A. Dugstad, Paper, 1992(14).
124. Malka, R., S. Nešić, and D.A. Gulino, Erosion–corrosion and synergistic effects in disturbed liquid-particle flow. *Wear*, 2007. **262**(7): p. 791-799.
125. SK, M.H., A.M. Abdullah, N. Laycock, D.E. Williams, and B. Ingham. Effects of Flow on Protective Scales Formation in a CO₂ Saturated Brine Environment. in Meeting Abstracts. 2016. The Electrochemical Society.
126. Barton, L., D. Sandana, R. Ladwa, P. Birkinshaw, and J. Soltis. Assessment of pipeline internal corrosion of challenging pipelines through the integration of flow modelling and corrosion risk assessments. in 10th North American Conference on Multiphase Technology. 2016. BHR Group.
127. Shi, L., C. Wang, and C. Zou, Corrosion failure analysis of L485 natural gas pipeline in CO₂ environment. *Engineering Failure Analysis*, 2014. **36**: p. 372-378.
128. Heitz, E., Chemo-mechanical effects of flow on corrosion. *Corrosion*, 1991. **47**(2): p. 135-145.
129. den Toonder, J. and F. Nieuwstadt, Reynold`s number effects in a turbulent pipe flow for low to moderate Re. *Physics of Fluids*, 1997: p. 3398-3409.
130. DEN TOONDER, J. and F. NIEUWSTADT, Reynold`s number effect in a turbulent pipe flow for low to moderate Re. *Physics of fluids*, 1997. **9**(11): p. 3398-3409.
131. From: <http://me.queensu.ca/People/Sellens/PowerLaw.html>.
132. Efir, K., Flow effects on corrosion. *Uhlig's Corrosion Handbook*, 2011. **51**: p. 203.
133. Videm, K. and A. Dugstad, Effect of flow rate, pH, Fe²⁺ concentration and steel quality on the CO₂ corrosion of carbon steel. K. Videm and A. Dugstad, Institute of Energy Technology, P. O. Box 40, N-2007 Kjeller, Norway, Corrosion 87/42, NACE, Houston, TX, Per Copy\$ 4. 00, 1987.
134. N Zara, K., H. Mas Ayu, T. Siti Haryani, and I. Sudin, Study of Flow and Temperature Effect on Carbon Steel in Oil and Gas Environment. 2015.
135. Barmatov, E., T. Hughes, and M. Nagl, Efficiency of film-forming corrosion inhibitors in strong hydrochloric acid under laminar and turbulent flow conditions. *Corrosion Science*, 2015. **92**: p. 85-94.
136. Guo, P., Z. Wang, Y. Xu, and J. Du, Research on Molecular Diffusion Coefficient of Gas-Oil System Under High Temperature and High Pressure.
137. Wang, H., J.Y. Cai, C. Bosch, W.P. Jepson, and T. Hong, Enhanced mass transfer and wall Shear Stress in multiphase slug flow. *CORROSION* 2002, 2002.
138. Galvan-Martinez, R., R. Orozco-Cruz, J. Mendoza-Flores, A. Contreras, and J. Genesca, Study of the Mass Transport on Corrosion of Low Carbon Steel Immersed in Sour Solution Under Turbulent Flow Conditions.
139. Wang, F., Modelling of aqueous carbon dioxide corrosion in turbulent pipe flow. 1999.
140. Denpo, K. and H. Ogawa, Fluid flow effects on CO₂ corrosion resistance of oil well materials. *Corrosion*, 1993. **49**(6): p. 442-449.

141. Ruzic, V., M. Veidt, and S. Nešić, Protective iron carbonate films—part 3: simultaneous chemo-mechanical removal in single-phase aqueous flow. *Corrosion*, 2007. **63**(8): p. 758-769.
142. Efid, K., Effect of fluid dynamics on the corrosion of copper-base alloys in sea water. *Corrosion*, 1977. **33**(1): p. 3-8.
143. Schmitt, G.A., T.A. Gudde, and E. Strobel-Effertz, Fracture mechanical properties of CO₂ corrosion product scales and their relation to localized corrosion. *CORROSION* 96, 1996.
144. Yang, K.S., J.Y. Hwang, K. Bremhorst, and S. Nestic, Numerical investigation of turbulent flow around a rotating stepped cylinder for corrosion study. *The Canadian Journal of Chemical Engineering*, 2003. **81**(1): p. 26-36.
145. Nichols, D.A., H. Thomson, C. Simpson, and G.M. Graham. Scale and Corrosion Inhibitor Evaluation under High Shear Flow Conditions. in *SPE International Conference on Oilfield Chemistry*. 2017. Society of Petroleum Engineers.
146. Zhang, G., D. Liu, Y. Li, and X. Guo, Corrosion behaviour of N80 carbon steel in formation water under dynamic supercritical CO₂ condition. *Corrosion Science*, 2017.
147. Li, J., Z. Liu, C. Du, X. Li, R. He, Y. Xing, and W. Huangfu, Study on the corrosion behaviours of API X65 steel in wet gas environment containing CO₂. *Corrosion Engineering, Science and Technology*, 2017: p. 1-7.
148. Zheng, L., J. Landon, N.S. Matin, and K. Liu, FeCO₃ Coating Process toward the Corrosion Protection of Carbon Steel in a Postcombustion CO₂ Capture System. *Industrial & Engineering Chemistry Research*, 2016. **55**(14): p. 3939-3948.
149. Li, W., Y. Xiong, B. Brown, K.E. Kee, and S. Nestic, Measurement of wall shear stress in multiphase flow and its effect on protective FeCO₃ corrosion product layer removal. *CORROSION/2015*, 2015: p. 5922.
150. Crocker, M., P. Fairhurst, and D. Wilson, Model experiments of crystalline scale removal. *ICHEME RESEARCH EVENT*, 1996: p. 853-855.
151. Yang, Y., Removal Mechanisms of Protective Iron Carbonate Layer in Flowing Solutions 2012. .
152. Yang, Y., Removal Mechanisms of Protective Iron Carbonate Layer in Flowing Solutions 2012. Page 85.
153. Islam, M.A. and Z.N. Farhat, The Synergistic Effect between Erosion and Corrosion of API Pipeline in CO₂ and Saline Medium. *Tribology International*, 2012.
154. Rincon, H., J. Shadley, K. Roberts, and E. Rybicki, Erosion-Corrosion of Corrosion Resistant Alloys Used in the Oil and Gas Industry. *CORROSION* 2008, 2008.
155. Demoz, A. and T. Dabros, Relationship between shear stress on the walls of a pipe and an impinging jet. *Corrosion Science*, 2008. **50**(11): p. 3241-3246.
156. From: <http://www.corrosionlab.com/>.
157. Bai, Y. and Q. Bai, Subsea pipelines and risers. 2005: Access Online via Elsevier.
158. Yu, B., D. Li, and A. Grondin, Effects of the dissolved oxygen and slurry velocity on erosion-corrosion of carbon steel in aqueous slurries with carbon dioxide and silica sand. *Wear*, 2013.
159. Neilson Jr, R., P. Colombo, and B. Vyas, Corrosion of mild steel waste form containers. *Trans. Am. Nucl. Soc.:(United States)*, 1979. **32**(CONF-790602-(Summ.)).

160. Johnson, J., J. Nicholls, R. Hurst, and P. Hancock, The mechanical properties of surface scales on nickel-base superalloys—II. Contaminant corrosion. *Corrosion Science*, 1978. **18**(6): p. 543-553.
161. Jervis, T. and J.-P. Hirvonen, Tribology and surface mechanical properties of the oxide film formed by excimer laser surface treatment of AISI 304 stainless steel. *Wear*, 1991. **150**(1): p. 259-265.
162. Hancock, P., J. Nicholls, and K. Mahmood, The influence of imposed strain rate on fracture of surface oxides. *Corrosion science*, 1993. **35**(5): p. 979-987.
163. Armitt, J., R. Holmes, M. Manning, D. Meadowcroft, and E. Metcalfe, Spalling of steam-grown oxide from superheater and reheater tube steels. Technical planning study 76-655. Final report. 1978, Central Electricity Research Labs., Leatherhead (UK).
164. Zacoeb, A. and K. Ishibashi, Point load test application for estimating compressive strength of concrete structures from small core. 2006.
165. Dean, R., Reynold`s number dependence of skin friction and other bulk flow variables in two-dimensional rectangular duct flow. *Journal of Fluids Engineering*, 1978. **100**(2): p. 215-223.
166. Menon, E.S., *Transmission Pipeline Calculations and Simulations Manual*. 2014. Page 207: Gulf Professional Publishing.
167. Mah, R., M. Shacham, and T. Drew, *Advances in Chemical Engineering*. *Advances in Chemical Engineering*, 1978. page 256.
168. Han, Y., N. Shikazono, and N. Kasagi, Measurement of liquid film thickness in a micro parallel channel with interferometer and laser focus displacement meter. *International Journal of Multiphase Flow*, 2011. **37**(1): p. 36-45.
169. Young, T.J. and K. Vafai, Convective flow and heat transfer in a channel containing multiple heated obstacles. *International Journal of Heat and Mass Transfer*, 1998. **41**(21): p. 3279-3298.
170. Li, W., B. Pots, B. Brown, K.E. Kee, and S. Nestic, A direct measurement of wall shear stress in multiphase flow—Is it an important parameter in CO₂ corrosion of carbon steel pipelines? *Corrosion Science*, 2016. **110**: p. 35-45.
171. Sleicher, C. and M. Rouse, A convenient correlation for heat transfer to constant and variable property fluids in turbulent pipe flow. *International Journal of Heat and Mass Transfer*, 1975. **18**(5): p. 677-683.
172. Nor, A.M., M. Suhor, M. Mohamed, M. Singer, and S. Nestic. Corrosion of Carbon Steel in High CO₂ Containing Environments-the Effect of High Flow Rate. in *CORROSION 2012*. 2012. NACE International.
173. Nor, A.M., M. Suhor, M. Mohamed, M.M. Singer, and S.M. Nestic, Corrosion of Carbon Steel in High CO₂ Environment: Flow Effect. *CORROSION 2011*, 2011.
174. Coulson, J. and J. Richardson, *Chemical Engineering: Fluid Flow*. Vol. 1. 1964: Pergamon.
175. Zheng, Y., J. Ning, B. Brown, and S. Nešić, Electrochemical Model of Mild Steel Corrosion in a Mixed H₂S/CO₂ Aqueous Environment in the Absence of Protective Corrosion Product Layers. *Corrosion*, 2014. **71**(3): p. 316-325.
176. Stern, M. and A.L. Geary, Electrochemical polarization I. A theoretical analysis of the shape of polarization curves. *Journal of the electrochemical society*, 1957. **104**(1): p. 56-63.
177. Tu, J., G.H. Yeoh, and C. Liu, *Computational fluid dynamics: a practical approach*. 2012. Page 1-5: Butterworth-Heinemann.
178. Wesseling, P., *Principles of computational fluid dynamics*. Vol. 29. 2009. Page 227-235: Springer Science & Business Media.

179. Singh, K., J. Mathur, V. Ashok, and D. Chakraborty, Computational fluid dynamics in aerospace industry in India. *Defence Science Journal*, 2010. **60**(6).
180. Hirsch, C., Numerical computation of internal and external flows: The fundamentals of computational fluid dynamics. 2007. Page 70-85: Butterworth-Heinemann.
181. Ferziger, J.H. and M. Peric, Computational methods for fluid dynamics. 2012: Springer Science & Business Media.
182. Wendt, J., Computational fluid dynamics: an introduction. 2008. Page 3-15: Springer Science & Business Media.
183. Tu, J., G.H. Yeoh, and C. Liu, Computational fluid dynamics: a practical approach. 2012. Page 275-350: Butterworth-Heinemann.
184. Norton, T. and D.-W. Sun, An overview of CFD applications in the food industry. *Computational Fluid Dynamics in Food Processing*, 2007: p. 1-43.
185. Hughes, T.J. and L.P. Franca, A new finite element formulation for computational fluid dynamics: VII. The Stokes problem with various well-posed boundary conditions: symmetric formulations that converge for all velocity/pressure spaces. *Computer Methods in Applied Mechanics and Engineering*, 1987. **65**(1): p. 85-96.
186. Gnanavelu, A.B., A geometry independent integrated method to predict erosion wear rates in a slurry environment, in *Mechanical engineering*. 2010, University of Leeds.
187. Tu, J., G.H. Yeoh, and C. Liu, Computational fluid dynamics: a practical approach. 2012. Page 30-50: Butterworth-Heinemann.
188. Multiphysics, C., Modeling Software. COMSOL Inc., version, 2016. **5**.
189. Hirsch, C., Numerical computation of internal and external flows: The fundamentals of computational fluid dynamics. Vol. 1. 2007: Butterworth-Heinemann.
190. Johnson, C., Numerical solution of partial differential equations by the finite element method. 2012: Courier Corporation.
191. Dick, E., Introduction to finite element methods in computational fluid dynamics, in *Computational Fluid Dynamics*. 2009, Springer. p. 235-274.
192. Ruiz, M.J.G., J.F.D. Lombana, and P. Boulanger, Development of a light preprocessor for Interactive CFD Simulations. 2008.
193. Sayma, A., Computational fluid dynamics. 2009: BookBoon.
194. Rao, S.S., The finite element method in engineering. 2010. Page 266: Elsevier.
195. Rao, S.S., The finite element method in engineering. 2010. Page 559-600: Elsevier.
196. Hinton, E. and B. Irons, Least squares smoothing of experimental data using finite elements. *Strain*, 1968. **4**(3): p. 24-27.
197. Versteeg, H.K. and W. Malalasekera, An introduction to computational fluid dynamics: the finite volume method. 2007: Pearson Education.
198. Gnanavelu, A.B., A geometry independent integrated method to predict erosion wear rates in a slurry environment. 2010, The University of Leeds.
199. Wilcox, D.C., Turbulence modeling for CFD. Vol. 2. 1998: DCW industries La Canada, CA.
200. Sodja, J., Turbulence models in CFD. University of Ljubljana, 2007.
201. Murakami, S., Overview of turbulence models applied in CWE-1997. *Journal of Wind Engineering and Industrial Aerodynamics*, 1998. **74**: p. 1-24.
202. Speziale, C.G., On nonlinear kl and k- ϵ models of turbulence. *Journal of Fluid Mechanics*, 1987. **178**: p. 459-475.

203. Alpert, S.M., Evaluation of Computational Fluid Dynamics (CFD) for Modeling UV-Initiated Advanced Oxidation Processes. 2009. Page 173: ProQuest.
204. Paul, E.L., V.A. Atiemo-Obeng, and S.M. Kresta, Handbook of industrial mixing: science and practice. 2004. Page 266: John Wiley & Sons.
205. Basile, A., Handbook of Membrane Reactors: Fundamental Materials Science, Design and Optimisation. Vol. 1. 2013. Page 547: Elsevier.
206. Oberlack, M., A unified approach for symmetries in plane parallel turbulent shear flows. *Journal of Fluid Mechanics*, 2001. **427**(1): p. 299-328.
207. Landau, L. and E. Lifshitz, *Hydrodynamics: Theoretical Physics [in Russian]*, Vol. 6. 1988, Nauka, Moscow.
208. Ocon, J.D., L. Jirkovsky, R.L. de Leon, and A. Muriel, Theory-derived law of the wall for parallel flat-plates turbulent flow. *CFD Letters*, 2012. **4**(3): p. 93-101.
209. Hua, Y., R. Barker, and A. Neville, Effect of temperature on the critical water content for general and localised corrosion of X65 carbon steel in the transport of supercritical CO₂. *International Journal of Greenhouse Gas Control*, 2014. **31**: p. 48-60.
210. 7.1, M., MultiScale 7.1 is a commercial software package from Expro Group International Ltd., for more information see: <http://multiscale.no/>.
211. Hua, Y., R. Barker, and A. Neville, Comparison of corrosion behaviour for X-65 carbon steel in supercritical CO₂-saturated water and water-saturated/unsaturated supercritical CO₂. *The Journal of Supercritical Fluids*, 2015. **97**: p. 224-237.
212. Standard, A., Standard practice for preparing, cleaning, and evaluating corrosion test specimens. American Society for Testing and Materials G1-03, 2004.
213. Hua, Y., R. Barker, and A. Neville, The effect of O₂ content on the corrosion behaviour of X65 and 5Cr in water-containing supercritical CO₂ environments. *Applied Surface Science*, 2015. **356**: p. 499-511.
214. El-Dessouky, E., *Fundamentals of sea water Desalination 2002*. p. Appendix A: Thermodynamic Properties.
215. Efir, K.D., *Flow accelerated corrosion testing basics*. CORROSION 2006, 2006.
216. Rajappa, S., R. Zhang, and M. Gopal. Modeling the diffusion effects through the iron carbonate layer in the carbon dioxide corrosion of carbon steel. in Nace. Engineering annual conference. 1998. NACE.
217. Dugstad, A., Mechanism of protective film formation during CO₂ corrosion of carbon steel. 1998, NACE International, Houston, TX (United States).
218. Brezonik, P.L., *Chemical kinetics and process dynamics in aquatic systems*. 1993. Page 101: CRC Press.
219. Vetter, K.J., *Electrochemical kinetics: theoretical aspects*. 1967. Page 235.: Elsevier.
220. Schmitt, G. and B. Rothmann, Studies on the Corrosion Mechanism of Unalloyed Steel in Oxygen-Free Carbon Dioxide Solutions, Part I. Kinetics of the Liberation of Hydrogen. *Werkstoffe und Korrosion*, 1977. **28**: p. 816-822.
221. Nestic, S. and W. Sun, Corrosion in acid gas solutions. *Shreir's corrosion*, 2010. **2**: p. 1270-1298.
222. Forrest, E.C., L.-W. Hu, J. Buongiorno, and T.J. McKrell, Convective Heat Transfer in a High Aspect Ratio Minichannel Heated on One Side. *Journal of Heat Transfer*, 2016. **138**(2): p. 021704.

223. Nguyen, N.-T., *Micromixers: Fundamentals, Design and Fabrication (Micro & nano technologies)*. 2008. Page 36: William Andrew Publishing.
224. Shah, R.K., E.C. Subbarao, and R.A. Mashelkar, *Heat transfer equipment design*. 1988. Page 232: CRC Press.
225. Duffie, J.A. and W.A. Beckman, *Solar engineering of thermal processes*. Vol. 3. 2013. Page 161: Wiley New York.
226. Kandlikar, S., S. Garimella, D. Li, S. Colin, and M.R. King, *Heat transfer and fluid flow in minichannels and microchannels*. 2005. Page 40: elsevier.
227. Nešić, S., Key issues related to modelling of internal corrosion of oil and gas pipelines—A review. *Corrosion Science*, 2007. **49**(12): p. 4308-4338.
228. Kelly, R.G., J.R. Scully, D. Shoesmith, and R.G. Buchheit, *Electrochemical techniques in corrosion science and engineering*. 2002. Pages: 135-150: CRC Press.
229. Threthewey, K.R. and P. Roberge, *Modelling aqueous corrosion: from individual pits to system management*. Vol. 266. 2012. Pages:327-329: Springer Science & Business Media.
230. Haynes, G.S. and R. Baboian. *Laboratory corrosion tests and standards*. 1985. Pages: 375-380. American Society for Testing and Materials.
231. Hernandez, J., A. Muñoz, and J. Genesca, Formation of iron-carbonate scale-layer and corrosion mechanism of API X70 pipeline steel in carbon dioxide-saturated 3% sodium chloride. *Afinidad*, 2012. **69**(560).

Appendix A

This section presents the details of the calculation of the flow parameters carried out using the empirical correlations and relations listed in paragraph 4.2.

Clean surface flow parameter calculations:

At temperature 50°C and 3% NaCl water properties are:

Viscosity = 0.000587 Pa*S.

Density = 1009.68 Kg/m³.

Diffusion Coefficient = 1.75E-08 m²/s (D_{ref} of H⁺ at 20°C = 9.31 × 10⁻⁹).

Schmidt number = 33.18

Channel height = to the gasket thickness.

The calculation of flow parameters at flow rate 34 l/min and gasket thickness 15mm and 50°C

Sample	Channel width (mm)	Cross section area m ²	Flow velocity m/s	Hydraulic diameter m	Reynold's number	Friction factor	Wall shear stress N/m ²
1	50	7.50E-04	0.76	0.023076923	3.00E+04	5.55E-03	1.60
2	43.8	6.56E-04	0.86	0.022340426	3.32E+04	5.41E-03	2.04
3	37.5	5.63E-04	1.01	0.021428571	3.71E+04	5.26E-03	2.69
4	31.3	4.69E-04	1.21	0.02027027	4.21E+04	5.09E-03	3.76
5	25.0	3.75E-04	1.51	0.01875	4.87E+04	4.91E-03	5.66

The calculation of flow parameters at flow rate 32.5 l/min and gasket thickness 6mm and 50°C

Sample	Channel width (mm)	Cross section area m ²	Flow velocity m/s	Hydraulic diameter m	Reynold's number	Friction factor	Wall shear stress N/m ²
1	50	3.00E-04	1.81	0.010714286	3.33E+04	5.40E-03	8.90
2	43.8	2.63E-04	2.06	0.010552764	3.75E+04	5.25E-03	11.28
3	37.5	2.25E-04	2.41	0.010344828	4.28E+04	5.07E-03	14.85
4	31.3	1.88E-04	2.89	0.010067114	5.00E+04	4.88E-03	20.57
5	25.0	1.50E-04	3.61	0.009677419	6.01E+04	4.66E-03	30.69

The calculation of flow parameters at flow rate 29.5 l/min and gasket thickness 3mm and 50°C

Sample	Channel width (mm)	Cross section area m ²	Flow velocity m/s	Hydraulic diameter m	Reynold`s number	Friction factor	Wall shear stress N/m ²
1	50	1.50E-04	3.28	0.005660377	3.19E+04	5.46E-03	29.62
2	43.8	1.31E-04	3.75	0.005614973	3.62E+04	5.29E-03	37.50
3	37.5	1.13E-04	4.37	0.005555556	4.18E+04	5.11E-03	49.24
4	31.3	9.38E-05	5.24	0.005474453	4.94E+04	4.90E-03	68.00
5	25.0	7.50E-05	6.56	0.005357143	6.04E+04	4.66E-03	101.02

The calculation of flow parameters at flow rate 41.5 l/min and gasket thickness 2mm and 50°C

Sample	Channel width (mm)	Cross section area m ²	Flow velocity m/s	Hydraulic diameter m	Reynold`s number	Friction factor	Wall shear stress N/m ²
1	50	1.00E-04	6.92	0.003846154	4.58E+04	4.99E-03	120.55
2	43.8	8.75E-05	7.90	0.003825137	5.20E+04	4.83E-03	152.49
3	37.5	7.50E-05	9.22	0.003797468	6.02E+04	4.66E-03	200.07
4	31.3	6.25E-05	11.07	0.003759398	7.16E+04	4.46E-03	275.96
5	25.0	5.00E-05	13.83	0.003703704	8.81E+04	4.24E-03	409.31

At temperature 80°C the 3% NaCl water properties are:

Viscosity = 0.000382 Pa*S.

Density = 993.67 Kg/m³.

Diffusion Coefficient = 2.9E-08 m²/s (D_{ref} of H⁺ at 20°C = 9.31 × 10⁻⁹).

Schmidt number = 13.28

Channel height is equal to the gasket thickness.

The calculation of flow parameters at flow rate 34 l/min and gasket thickness 15mm and 80°C

Sample	Channel width (mm)	Cross section area m ²	Flow velocity m/s	Hydraulic diameter m	Reynold's number	Friction factor	Wall shear stress N/m ²
1	50	7.50E-04	0.76	0.023076923	4.54E+04	5.00E-03	1.42
2	43.8	6.56E-04	0.86	0.022340426	5.02E+04	4.88E-03	1.81
3	37.5	5.63E-04	1.01	0.021428571	5.62E+04	4.74E-03	2.39
4	31.3	4.69E-04	1.21	0.02027027	6.37E+04	4.59E-03	3.34
5	25.0	3.75E-04	1.51	0.01875	7.37E+04	4.43E-03	5.03

The calculation of flow parameters at flow rate 32.5 l/min and gasket thickness 6mm and 80°C

Sample	Channel width (mm)	Cross section area m ²	Flow velocity m/s	Hydraulic diameter m	Reynold's number	Friction factor	Wall shear stress N/m ²
1	50	3.00E-04	1.81	0.010714286	5.03E+04	4.87E-03	7.89
2	43.8	2.63E-04	2.06	0.010552764	5.66E+04	4.73E-03	10.01
3	37.5	2.25E-04	2.41	0.010344828	6.48E+04	4.58E-03	13.18
4	31.3	1.88E-04	2.89	0.010067114	7.57E+04	4.40E-03	18.25
5	25.0	1.50E-04	3.61	0.009677419	9.09E+04	4.20E-03	27.24

The calculation of flow parameters at flow rate 29.5 l/min and gasket thickness 3mm and 80°C

Sample	Channel width (mm)	Cross section area m ²	Flow velocity m/s	Hydraulic diameter m	Reynold's number	Friction factor	Wall shear stress N/m ²
1	50	1.50E-04	3.28	0.005660377	4.83E+04	4.93E-03	26.29
2	43.8	1.31E-04	3.75	0.005614973	5.47E+04	4.77E-03	33.28
3	37.5	1.13E-04	4.37	0.005555556	6.32E+04	4.60E-03	43.70
4	31.3	9.38E-05	5.24	0.005474453	7.47E+04	4.42E-03	60.34
5	25.0	7.50E-05	6.56	0.005357143	9.14E+04	4.20E-03	89.65

The calculation of flow parameters at flow rate 41.5 l/min and gasket thickness 2mm and 80°C

Sample	Channel width (mm)	Cross section area m ²	Flow velocity m/s	Hydraulic diameter m	Reynold's number	Friction factor	Wall shear stress N/m ²
1	50	1.00E-04	6.92	0.003846154	6.92E+04	4.50E-03	106.98
2	43.8	8.75E-05	7.90	0.003825137	7.87E+04	4.36E-03	135.33
3	37.5	7.50E-05	9.22	0.003797468	9.11E+04	4.20E-03	177.55
4	31.3	6.25E-05	11.07	0.003759398	1.08E+05	4.02E-03	244.90
5	25.0	5.00E-05	13.83	0.003703704	1.33E+05	3.82E-03	363.25

Covered surface (protected) flow parameter calculations:

At temperature 50°C and 3% NaCl water properties are:

Viscosity = 0.000587 Pa*S.

Density = 1009.68 Kg/m³.

Surface roughness = 10µm

Channel height = to the gasket thickness.

The calculation of flow parameters on covered surface at flow rate 32.5 l/min and gasket thickness 6mm and 50°C

Sample	Channel width (mm)	Cross section area m ²	Flow velocity m/s	Hydraulic diameter m	Reynold's number	Friction factor	Wall shear stress N/m ²
1	50	3.00E-04	1.81	0.010714286	3.33E+04	6.38E-03	10.50
2	43.8	2.63E-04	2.06	0.010552764	3.75E+04	6.27E-03	13.48
3	37.5	2.25E-04	2.41	0.010344828	4.28E+04	6.16E-03	18.02
4	31.3	1.88E-04	2.89	0.010067114	5.00E+04	6.04E-03	2546
5	25.0	1.50E-04	3.61	0.009677419	6.01E+04	5.93E-03	39.9

The calculation of flow parameters on covered surface at flow rate 29.5 l/min and gasket thickness 3mm and 50°C

Sample	Channel width (mm)	Cross section area m ²	Flow velocity m/s	Hydraulic diameter m	Reynold's number	Friction factor	Wall shear stress N/m ²
1	50	1.50E-04	3.28	0.005660377	3.19E+04	6.92E-03	37.52
2	43.8	1.31E-04	3.75	0.005614973	3.62E+04	6.81E-03	49.27
3	37.5	1.13E-04	4.37	0.005555556	4.18E+04	6.71E-03	65.67
4	31.3	9.38E-05	5.24	0.005474453	4.94E+04	6.60E-03	91.64
5	25.0	7.50E-05	6.56	0.005357143	6.04E+04	6.50E-03	140.93

The calculation of flow parameters on covered surface at flow rate 41.5 l/min and gasket thickness 2mm and 50°C

Sample	Channel width (mm)	Cross section area m ²	Flow velocity m/s	Hydraulic diameter m	Reynold's number	Friction factor	Wall shear stress N/m ²
1	50	1.00E-04	6.92	0.003846154	4.58E+04	7.08E-03	171.07
2	43.8	8.75E-05	7.90	0.003825137	5.20E+04	7.01E-03	221.20
3	37.5	7.50E-05	9.22	0.003797468	6.02E+04	6.94E-03	299.04
4	31.3	6.25E-05	11.07	0.003759398	7.16E+04	6.87E-03	424.90
5	25.0	5.00E-05	13.83	0.003703704	8.81E+04	6.81E-03	655.64

At temperature 80°C and 3% NaCl water properties are:

Viscosity = 0.000382 Pa*S.

Density = 993.7 Kg/m³.

Surface roughness = 10µm

Channel height = to the gasket thickness.

The calculation of flow parameters on covered surface at flow rate 32.5 l/min and gasket thickness 6mm and 80°C

Sample	Channel width (mm)	Cross section area m ²	Flow velocity m/s	Hydraulic diameter m	Reynold's number	Friction factor	Wall shear stress N/m ²
1	50	3.00E-04	1.81	0.010714286	5.03E+04	5.99E-03	10
2	43.8	2.63E-04	2.06	0.010552764	5.66E+04	5.91E-03	12.50
3	37.5	2.25E-04	2.41	0.010344828	6.48E+04	5.83E-03	16.77
4	31.3	1.88E-04	2.89	0.010067114	7.57E+04	5.74E-03	23.81
5	25.0	1.50E-04	3.61	0.009677419	9.09E+04	5.67E-03	36.72

The calculation of flow parameters on covered surface at flow rate 29.5 l/min and gasket thickness 3mm and 80°C

Sample	Channel width (mm)	Cross section area m ²	Flow velocity m/s	Hydraulic diameter m	Reynold's number	Friction factor	Wall shear stress N/m ²
1	50	1.50E-04	3.28	0.005660377	4.83E+04	6.58E-03	35.12
2	43.8	1.31E-04	3.75	0.005614973	5.47E+04	6.50E-03	45.35
3	37.5	1.13E-04	4.37	0.005555556	6.32E+04	6.43E-03	61.00
4	31.3	9.38E-05	5.24	0.005474453	7.47E+04	6.35E-03	86.81
5	25.0	7.50E-05	6.56	0.005357143	9.14E+04	6.28E-03	134.16

Appendix B

This section presents the details of the relationship between the corrosion rate and the shear stress derived as a function of velocity, Reynold`s number and geometry.

The wall shear stress can be a function of $Re^{1.75}$ only when the hydraulic diameter D value is a constant throughout the test section. Figures C and D show the corrosion rate as function of Re^n ($n = 1.75$ and 0.85), the curves trends/behaviour is similar to the behaviour of the corrosion rate vs Re curve in Figure B. Knowing that the hydraulic diameter D at this study varies across the samples due to the complex shape of the test section.

The relation of the shear stress $\propto Re^{1.75}$ can be rearranged to (wall shear stress $\propto v^{1.75} \times D^{-0.25}$).

Where:

$$\tau = \frac{C_f \times v^2 \times \rho}{2}$$

$$C_f = 0.073 \times Re^{-0.25}$$

$$Re = \frac{D \times v \times \rho}{\mu}$$

These three equations can be rearranged to:

$$\tau = \left(0.073 \times \left(\frac{D \times v \times \rho}{\mu} \right)^{-0.25} \right) \times \frac{v^2 \times \rho}{2}$$

$$\tau = \underbrace{\left(0.073 \times \left(\frac{\rho}{\mu} \right)^{-0.25} \times \frac{1}{2} \right)}_{\text{(Constant)}} \times D^{-0.25} \times v^{1.75}$$

\therefore

$$\tau \propto D^{-0.25} \times v^{1.75}$$

Figure (E) shows the relationship of the corrosion rate Vs $v^{1.75} \times D^{-0.25}$. The overall shape of the curves indicates a similar behaviour/trend to the curves of corrosion rate Vs wall shear stress in Figure A.

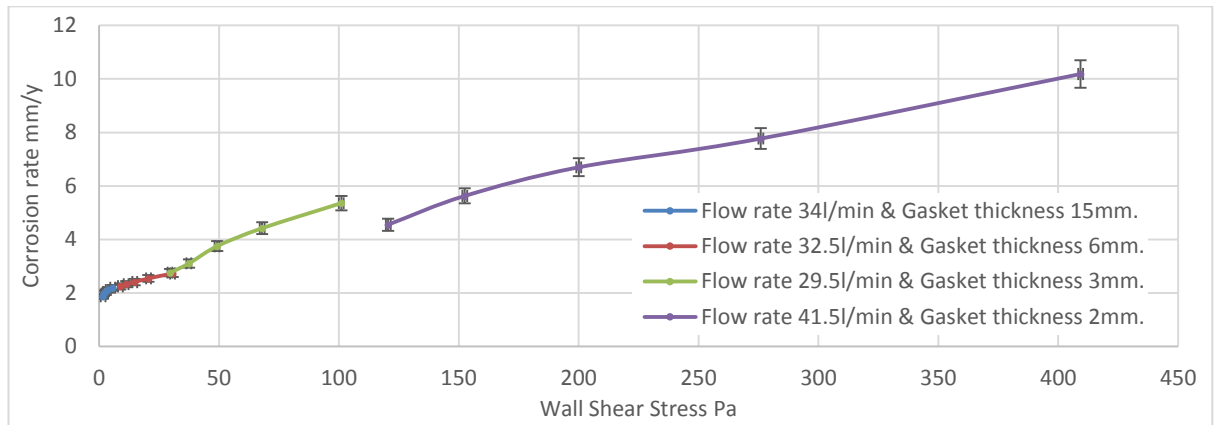


Figure A. Shear stress Vs Corrosion rate 50°C and pH 6.6

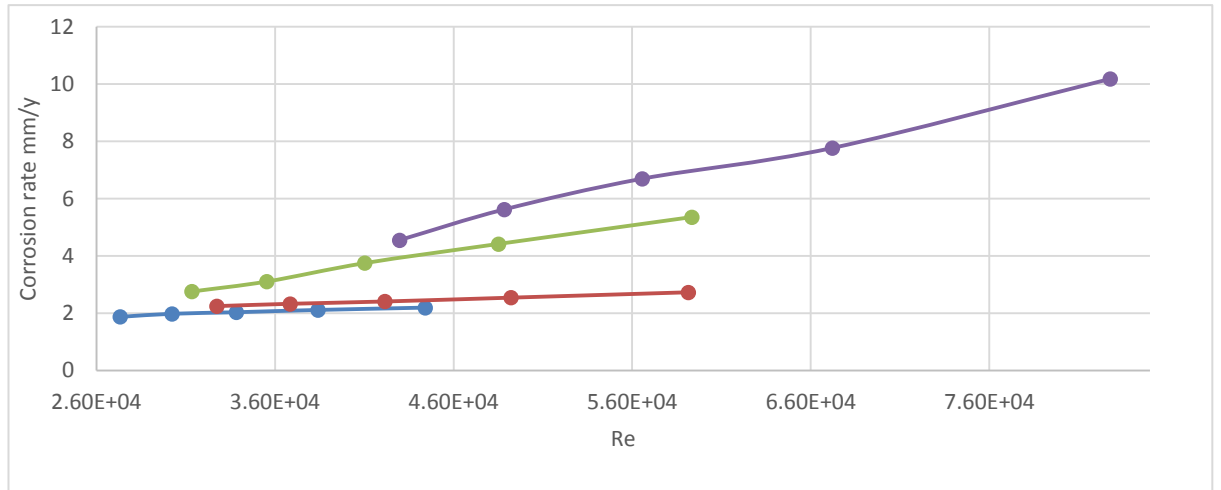


Figure B. Re Vs Corrosion rate 50°C and pH 6.6

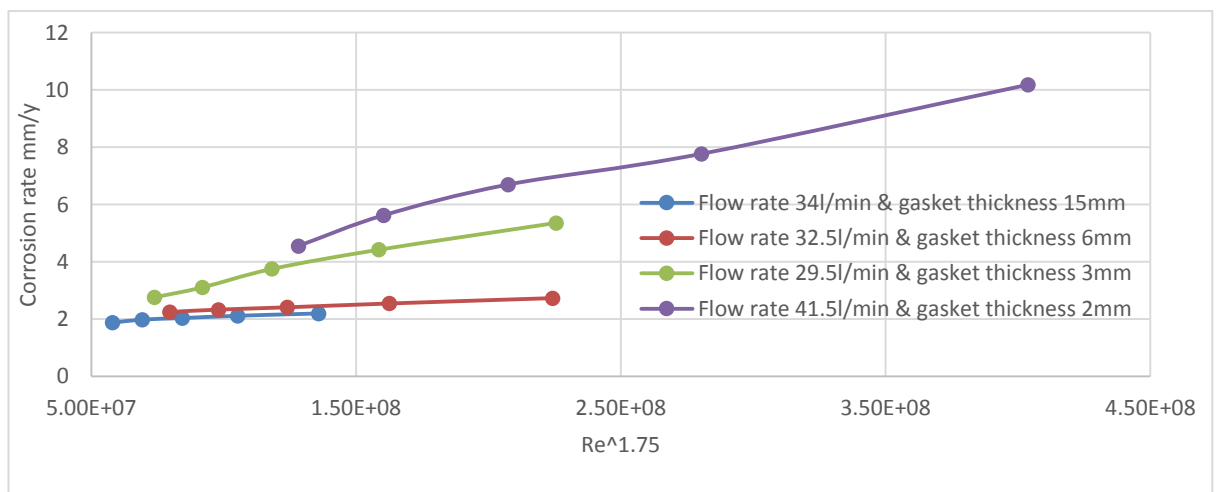


Figure C. $Re^{1.75}$ Vs Corrosion rate 50°C and pH 6.6

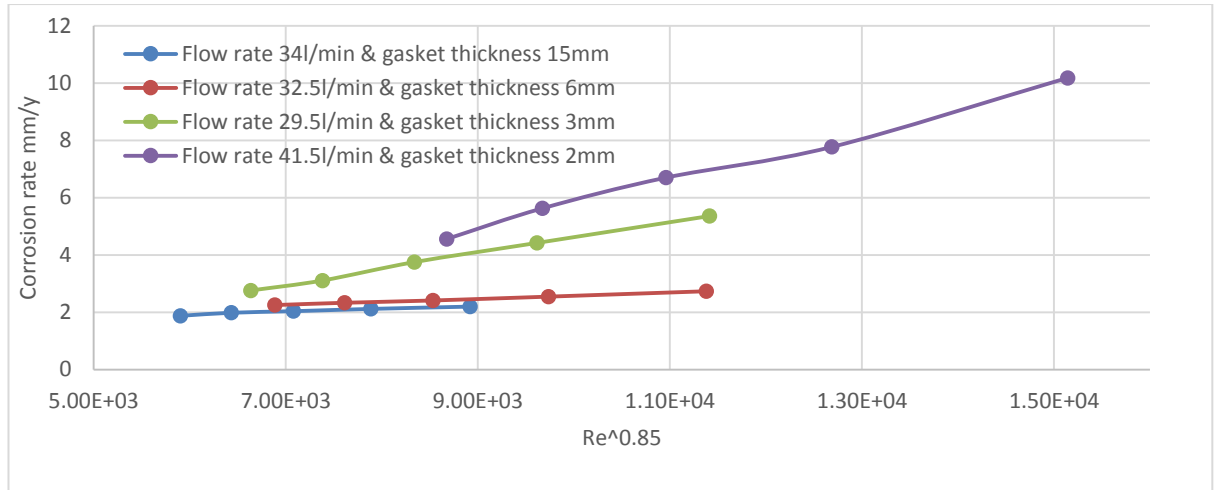


Figure D. $Re^{0.85}$ Vs Corrosion rate 50°C and pH 6.6

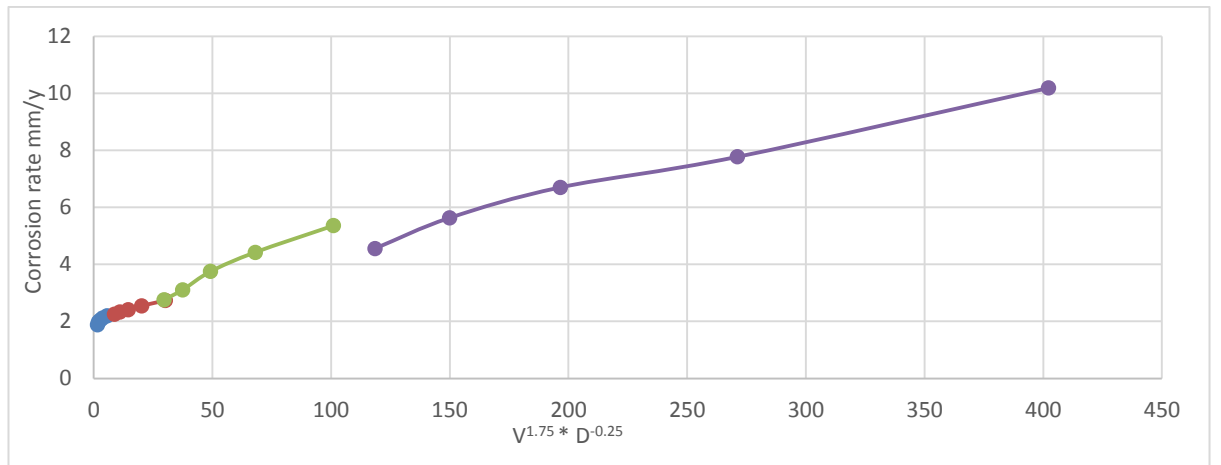


Figure E. $(V^{1.75} * D^{-0.25})$ Vs Corrosion rate 50°C and pH 6.6